Robustness of the parameterization of sub-grid scale wind variability on sea-surface fluxes

by

Kota Endo

B.Sc., University of Alberta, 2019

A Thesis Submitted in Partial Fulfillment of the
Requirements for the Degree of

MASTER OF SCIENCE

in the School of Earth and Ocean Sciences

University of Victoria

Robustness of the parameterization of sub-grid
scale wind variability on sea-surface fluxes

by

Kota Endo

B.Sc., University of Alberta, 2019

Supervisory Committee

Dr. Adam Monahan, Supervisor
School of Earth and Ocean Sciences

Dr. Roberta Hamme, Departmental Member
School of Earth and Ocean Sciences

Dr. William Merryfield, Departmental Member
School of Earth and Ocean Sciences

Abstract

Numerical models of the atmosphere discretize space and time, and are unable to resolve processes smaller than model resolution. As such, the aggregate effects of these sub-grid scale processes must be parameterized when their effects are manifest at resolved grid scale. However, it is known that the enhancement of sea-surface fluxes by sub-grid scale wind variations is difficult to appropriately parameterize deterministically. This limitation can be realized in a numerical model by the use of stochasticity, explicitly accounting for the randomness in how sea surface wind variability enhances sea-surface fluxes.

The robustness of stochastically parameterizing sea surface flux enhancement due to wind speed variability is investigated by applying an established statistical model to coarse grained global convection permitting numerical model output from six different numerical models and four different geographical regions, to determine if there exists any sensitivities to region, time period, or model type. The sensitivity of the deterministic part of a surface flux parameterization studied is quantified via correlation, where different ten-day periods have the highest correlations and thus the least sensitivity, followed by differences in numerical models and differences in geographical regions. Results suggest that the choice of cumulus parameterization employed by a numerical model may contribute to statistical model sensitivity and consequent regression fit portability. The robustness of a Gaussian process fit applied to the stochastic part of the sea-surface flux enhancement parameterization reveals spatial non-stationarity, which provides insight into the potential for further improvements to the sea-surface flux parameterization studied. Results suggest that the stochastic parameterization studied is broadly robust, supporting implementation of such sea surface flux parameterization in operational weather and climate models. Results are also used to identify specific methods that may be utilized for improvements of the stochastic parameterization.

Table of Contents

List of Tables

List of Figures

Acknowledgements

I am grateful for the constructive feedback on the project received from my supervisor Adam Monahan; supervisory committee members Roberta Hamme and Bill Merryfield; and collaborators Julie Bessac, Hannah Christensen, and Nils Weitzel, all of which greatly improved this manuscript.

Cascade data may be obtained from the Centre for Environmental Data Analysis (CEDA) Archives, part of the United Kingdom Natural Environment Research Council (NERC) Environmental Data Service (EDS), viz. from the dataset published by Lister and Woolnough (2008).

DYAMOND data management was provided by the Deutsches Klimarechenzentrum (DKRZ) and supported through the projects ESiWACE and ESiWACE2. The projects ESiWACE and ESiWACE2 have received funding from the European Union's Horizon 2020 research and innovation programme under grant agreements No 675191 and 823988. This work used resources of the Deutsches Klimarechenzentrum (DKRZ) granted by its Scientific Steering Committee (WLA) under project IDs bk1040 and bb1153.

Finally, I wish to thank my family for their support, especially during these trying times.

Chapter 1

Introduction

Numerical models of the atmosphere have seen remarkable improvement in the last 70 years, benefiting from both the increase in knowledge and understanding of atmospheric processes and the increase in computational power. Nevertheless, numerical models that attempt to simulate atmospheric processes are still limited by both empirical knowledge and computational power, and thus must make approximations. The representation of sub-grid scale processes that are not fully resolved by the atmospheric model, such as sea-surface fluxes, is such a limitation.

Traditionally, this limitation in computing sea-surface fluxes has been addressed by parameterizing sea-surface flux as a deterministic function of the resolved state. However, such an assumption requires scale separation between the unresolved sub-grid scale processes and the resolved atmospheric model grid-box, an assumption not necessarily the case where the length scales of the unresolved process approaches that length scale of the grid. In the absense of scale separation, stochastic parameterization that includes an explicitly random component is appropriate.

This study intends to improve the approximations made while computing sea-surface flux in numerical models by recognizing that the true sea-surface flux in a model grid-box is not a deterministic function of the resolved state, such that numerical models see the benefit of a better representation of physics in sea surface interactions. In particular, this

work expands on previous works of Bessac et al. (2019, 2021), which used a regional fine resolution model of the Indo-Pacific Warm Pool region as an approximation to the state of a coarse resolution model 'truth' to investigate the stochastic enhancement of sea-surface fluxes by coarse graining model output. In particular, this study extends their analyses to a larger set of models and regional domains.

The present work will be organized as follows. This chapter will introduce the background information necessary for the analysis methods employed in this study. In Chapter 2 the specific features of the numerical and statistical models considered in this study will be outlined. Chapter 3 will present the results obtained, and Chapter 4 will discuss their implications. Concluding remarks will be presented as section 4.3.

1.1 Convection permitting models

The paradigmatic General Circulation Model (GCM) discretizes space and time onto grids, with the state variables in each spatial grid-box evolving with each progressing time-step. Such a representation of the atmosphere directly translates to the need for sufficient computational memory and processing speed in order to solve the governing equations across all model grid boxes.

Numerical models at the highest resolution allow for full resolution of all hydrodynamical processes relevant for the evolution of the fluid state. These Direct Numerical Simulations (DNS) require model resolution in the centimetre to decimetre range and are thus not realistic when constructing global models of the atmosphere. Although not to the extreme of a DNS, large-eddy simulations and cloud resolving models also have the fine model resolutions that allow for explicit representation of at least some of the turbulence (e.g. convective processes). Although such models may be employed for regional models of the atmosphere, they remain computationally expensive and are not yet practical for operational global models.

At coarser resolutions, the model resolution approaches the length scales of convective processes. At such resolution, convection is not fully resolved, but convective elements

are also not sufficiently small for them to be treated as small, unresolved processes. Such convection permitting models allow for partial resolution of the larger convective processes, but must otherwise account for the contributions made by smaller convective systems that are not resolved at model resolution. Even such convection permitting models, sometimes referred to as a storm resolving or cloud system resolving models, require resolutions in the three kilometre range and are thus finer in resolution than typical global models currently operating in the 20 – 200 km range. As such, convection permitting models are operationally limited to regional models. Expansion of these models to the global domain is an area of active experimentation.

Comprehensive reviews of recent developments in high resolution atmospheric models include Guichard and Couvreux (2017) and Satoh et al. (2019).

1.2 Gustiness parameterizations

Exchanges between the modeled atmosphere and ocean occur at the sea surface in the form of sea surface fluxes, e.g. energy, momentum, and gas exchange. These fluxes are oftentimes expressed for Reynolds averaged quantities[1] using the bulk flux formulation

$$F_x = \overline{\rho_a}\,\overline{s} c_x(\overline{s})(\overline{X_s} - \overline{X_a}) \tag{1.1}$$

with F_x the surface flux for some quantity x (in amount of x per area per unit time), ρ_a the air density, s the wind speed, c_x the exchange coefficient for x, and X_s, X_a the amount of x per atmospheric mass at the surface and at some specified height, respectively.

[1]The Reynolds mean averages over temporal scales relevant for turbulence, in particular averaging over a sufficiently long time scale T such that

$$\overline{s} = \frac{1}{T}\int_0^T s(t)\ \mathrm{d}t$$

Note that on Reynolds averaged scales, the vertical component of wind velocity becomes negligibly small compared to the horizontal components.

Jensen's inequality applied to wind fields, viz. for scalar mean wind $\overline{s}$ and vector mean wind s_v, where the overline denotes temporal averaging, implies that

$$s_v = \sqrt{\overline{u}^2 + \overline{v}^2} \leq \overline{\sqrt{u^2 + v^2}} = \overline{s} \tag{1.2}$$

where u, v, are the horizontal wind components. As such, the mean wind speed computed from mean vector components is always an underestimate of the true wind mean speed. Since global and regional models represent Reynolds averaged variables, numerical models must use Reynolds averaged wind vector components instead of scalar mean wind $\overline{s}$ when computing surface flux and thus sea-surface flux computed by a numerical model is also an underestimate. Compensation for such error associated with wind speeds computed at model resolution is usually achieved by introduction of the so-called wind gustiness s_g (e.g. Jabouille et al. (1996))

$$\overline{s}^2 = s_v^2 + s_g^2 \tag{1.3}$$

where s_g must be parameterized using quantities resolved by the numerical model. More specifically, this term represents the effects of small scale surface flow such as those due to shallow convection, and is oftentimes parameterized using the form

$$s_g = \beta \left(\frac{g}{\theta_v} \overline{\theta_v' w'} z_L \right)^{1/3} \tag{1.4}$$

with constant[2] β of order unity, g the gravitational acceleration, θ_v the virtual potential temperature, $\overline{\theta_v' w'}$ surface buoyancy flux, and z_L the boundary layer height (usually set to 1000 m). However, there exist other parameterizations for s_g that make use of other model variables, e.g. precipitation, which accounts for deep convection as well (Deardorff 1970; Godfrey and Beljaars 1991; Mahrt et al. 2021; Miller et al. 1992; Redelsperger et al. 2000; Zeng et al. 2002).

The above scheme to correct for unresolved turbulence in time averaging can be expanded to spatial averaging following Mahrt and Sun (1995), where time averaged fine-scale wind

[2]For example, Redelsperger et al. (2000) recommends $\beta = 0.65$, whereas Beljaars (1995) suggests 1.2. A common choice for β is unity (e.g. Miller et al. (1992) and Zeng et al. (1998, 2002)).

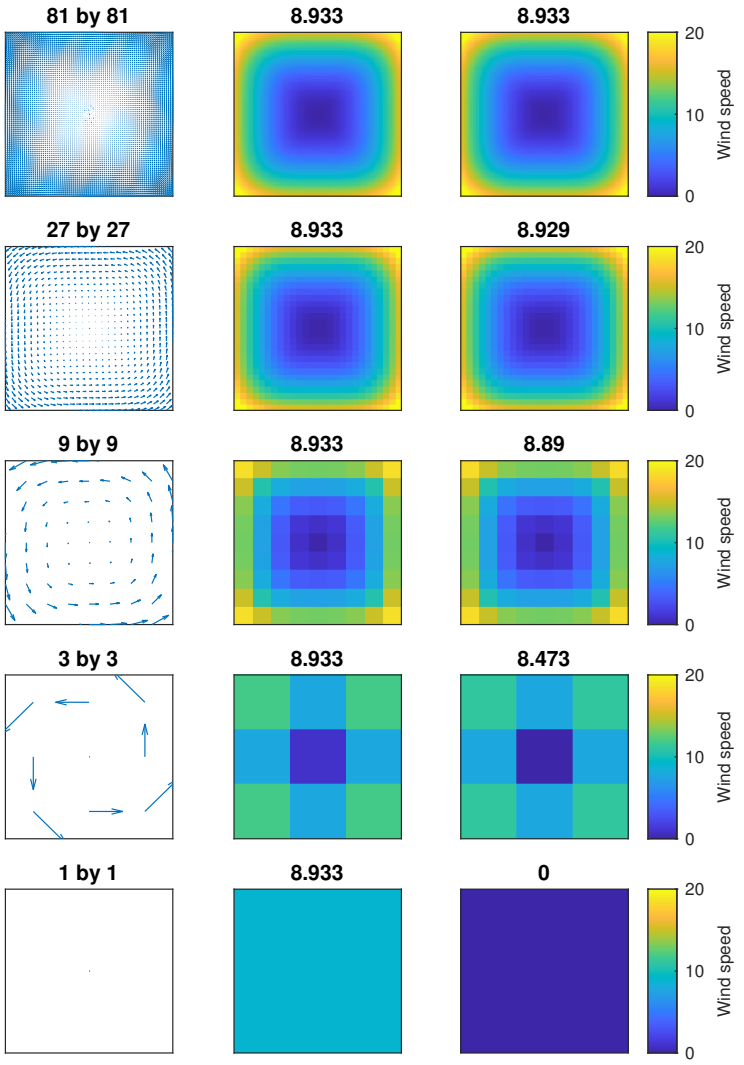

Figure 1.1: An illustrative example of the effects of coarsening resolution (i.e. averaging over boxes with given size, viz. 3-by-3, 9-by-9, 27-by-27, and 81-by-81, each corresponding to rows 2, 3, 4, and 5) of wind vector $(\langle u \rangle, \langle v \rangle)$ (left) on the mean true wind speed $\langle s \rangle$ over the domain (centre) and on vector means $\sqrt{\langle u \rangle^2 + \langle v \rangle^2}$ (right). Titles indicate means over entire field. Observed are the 'model resolutions' (rows 2–5, right column, norm of the mean of the vector components) underestimating the 'true' (top row) mean of the wind speeds at fine resolution, as well as the 'true' mean of the wind speeds at coarser resolutions (rows 2–5, centre column, mean of the vectoral norms). Note that the size of quiver plots are relative and not absolute to each other.

components $\overline{u}$, $\overline{v}$, are expressed as a sum of space-time averaged wind components $\langle\overline{u}\rangle$, $\langle\overline{v}\rangle$ and their local deviations u_*, v_*. Hence

$$\overline{u} = \langle\overline{u}\rangle + u_* \tag{1.5}$$

$$\overline{v} = \langle\overline{v}\rangle + v_* \tag{1.6}$$

$$\langle\overline{u}^2 + \overline{v}^2\rangle = \langle\langle\overline{u}\rangle^2 + 2\langle\overline{u}\rangle u_* + u_*^2 + \langle\overline{v}\rangle^2 + 2\langle\overline{v}\rangle v_* + v_*^2\rangle \tag{1.7}$$

$$= \langle\overline{u}\rangle^2 + \langle u_*^2\rangle + \langle\overline{v}\rangle^2 + \langle v_*^2\rangle \tag{1.8}$$

$$= \langle\overline{u}\rangle^2 + \langle\overline{v}\rangle^2 + s_*^2 \tag{1.9}$$

with $s_*^2 = \langle u_*^2\rangle + \langle v_*^2\rangle$, since $\langle u_*\rangle = \langle v_*\rangle = 0$. As with time averaging, spatial averaging of components results in an underestimate of the true spatial mean wind speed: such effects due to Jensen's inequality $\langle\overline{u}\rangle^2 + \langle\overline{v}\rangle^2 \leq \langle\overline{u}^2 + \overline{v}^2\rangle$, are illustrated in Figure 1.1.

1.3 Stochastic parameterizations

As discussed in the preceding sections, a numerical model computing sea-surface fluxes should account for the difference between the 'model wind speed' and the 'true wind speed.' However, a deterministic parameterization of this difference assumes sufficient scale separation such that the sub-grid scale processes parameterized are 'in the thermodynamic limit,' where there exists a sufficient number of individual processes that allow for fluctuations to be assumed small compared to the mean. This assumption is not necessarily true, since some atmospheric processes have length scales that approach model resolution, and as such cannot be deterministically parameterized. The lack of scale separation can, however, be accounted for by use of a stochastic parameterization.

The effects of using stochastic parameterizations for sub-grid scale processes are well established in the literature, a recent and comprehensive review being Berner et al. (2017). In particular, stochastic air-sea fluxes with vanishing time-means are known to be capable of causing noise-induced drift on the climate, as a consequence of an asymmetry in the influence rendered by positive and negative surface buoyancy fluxes (Williams 2012). This fact means

that the evolution of an atmospheric model with stochastic parameterizations of sub-grid scale processes can be expected to be different from the evolution of a comparable model with deterministic parameterizations, and thus the development and evaluation of stochastic parameterizations are of great importance to the Earth System modelling community, as discussed by Zadra et al. (2018). Furthermore, potential increase in ensemble spread introduced by explicit stochasticity may be of interest for the improvement of prediction capabilities (e.g. Palmer et al. (2009)). Vidale et al. (2021) discusses the use of stochastic model physics as a cost efficient substitute to increasing model resolution.

1.4 Idealized flux formulation

Sea-surface flux of some arbitrary quantity can be expressed using the previously discussed bulk flux formulation[3]

$$F_x = \rho_a s c_x(s)(X_s - X_a) \tag{1.1}$$

where the overbars denoting Reynolds averaging have been omitted, as this averaging is assumed for all quantities hereafter. A common simplified representation of surface flux (e.g. gas diffusion in Atamanchuk et al. (2020)) takes the form

$$F_x = \rho_a k(s)(X_s - X_a) \tag{1.10}$$

with $k(s)$ some function of wind speed. In the present work, the surface wind dependent part of some sea surface flux is expressed using the idealized, dimensionless form

$$F(s) = \left(\frac{s}{s_0}\right)^n \tag{1.11}$$

where s denotes the surface wind speed and $s_0 = 1$ m/s a scaling factor. This non-dimensional quantity expressed as Equation 1.11 will be referred to as 'the flux' hereafter for brevity, albeit only being a part of the quantities that control the full surface flux. Such simplification

[3]Albeit formulated as an air-side controlled flux the formulation is equally applicable for water-side controlled fluxes.

of surface flux in a numerical model grid box, which neglects sub-grid scale variations in density and concentration differences, is reasonable because the sub-grid scale variability of wind velocity contributes the majority of errors in the surface flux otherwise unaccounted for by resolved variables (Blein et al. 2020). Albeit being a simplification of the bulk flux formulation that removes dependence of flux on variables other than wind and concentration differences, it has been shown that the formulation of Equation 1.11 can be useful in the parameterization of both gas exchange (Wanninkhof 2014) and of whitecap coverage[4], a quantity useful for computing sea surface gas fluxes (e.g. Goddijn-Murphy et al. (2011)). Neglecting the speed dependence of the exchange coefficient, the flux of energy or water vapour is represented with $n = 1$; momentum, with $n = 2$; and (using the parameterization of Wanninkhof (2014)[5]) CO_2, with $n = 2$.

The effects of averaging are investigated by using convection permitting model output to generate a representation of a coarse scale model by coarsening of model output wind fields, and finding the difference between the fluxes computed at the raw (taken to be the 'truth') and coarsened resolutions. In particular,

$$\varepsilon_{N,n} = \log_{10}\left(F^{(T)}_{N,n} - F^{(R)}_{N,n}\right) \tag{1.12}$$

is the base 10 logarithm of the flux enhancement due to sub-grid scale wind variations, where N denotes the averaging scale for coarsening of the fine-resolution model output. Here

$$F^{(T)}_{N,n} = \left\langle \left(\frac{\sqrt{u^2 + v^2}}{s_0} \right)^n \right\rangle_N \tag{1.13}$$

$$F^{(R)}_{N,n} = \left(\frac{\sqrt{\langle u \rangle_N^2 + \langle v \rangle_N^2}}{s_0} \right)^n \tag{1.14}$$

[4]In K. Zhang et al. (2016), for example, the surface wind speed dependent flux appears within the parameterization of sea salt emission with $n = 3.41$, resulting from the parameterization of whitecap coverage (Monahan and Muircheartaigh 1980) being carried into the expression.

[5]As with many other parameterizations, a range of values have been proposed for n. For example, Kihm and Körtzinger (2010) found $n = 3$ to produce better fits working with O_2 data from the Labrador Sea.

are the 'true' and 'resolved' fluxes, respectively. Following Bessac et al. (2019, 2021) the linear regression

$$\varepsilon_{N,n} = (A_{N,n})_0 + \sum_{k=1}^{3} (A_{N,n})_k \left(\log_{10} F_{N,n}^{(R)}\right)^k + \sum_{l=1}^{4} (B_{N,n})_l P_N^{l/4} + \psi_{N,n} \tag{1.15}$$

with regression coefficients A, B, and resolved precipitation rate P_N the fine scale precipitation rate averaged over the coarse grid box is used as a statistical parameterization of $\varepsilon_{N,n}$. The quantity

$$\mu_{N,n} = \varepsilon_{N,n} - \psi_{N,n} \tag{1.16}$$

is defined as the deterministic part of $\varepsilon_{N,n}$, computed entirely from resolved variables $F_{N,n}^{(R)}$, P_N, whereas $\psi_{N,n}$ is the statistical residual, modelled to be stochastic and independent of resolved variables. This statistical model thus assumes that the regression fit captures all of the dependence of $\varepsilon_{N,n}$ on resolved variables $F_{N,n}^{(R)}$, P_N. It is also noteworthy that the magnitude of the stochastic residual has been reported by Bessac et al. (2019) to be over 10 percent of the magnitude of $F_{1^\circ,1}^{(R)}$ in 10 percent of the bottom quartile of surface fluxes (i.e. for small flux magnitudes). The analysis of this work will study the spatiotemporal fields $\log_{10} F_{N,n}^{(R)}$, P_N, $\varepsilon_{N,n}$, and $\psi_{N,n}$ in four geographical regions using output from six numerical models to determine the robustness of the stochastic parameterization (both $\mu_{N,n}$ and $\psi_{N,n}$) of sea-surface flux enhancement due to sea-surface wind.

1.5 Objectives

The object of this study is to expand on Bessac et al. (2019), which found that the missing part of sea-surface flux due to sub-grid scale wind speed variations conditioned on both resolved scale sea surface flux and precipitation was stochastic in nature, since the error process $\varepsilon_{N,n}$ exhibited a spread of possible values instead of one deterministic value for given magnitudes of resolved flux and precipitation. Bessac et al. (2019) analyzed the model output from the Cascade project, which studied the Indo-Pacific Warm Pool for nine days during an active Madden-Julian Oscillation (MJO) event, limiting the application of the

relevant statistical models to one atmospheric model in one geographical region for a single nine-day period. This study will expand on this work by applying their proposed statistical model to thirty days of model output in a variety of geographical regions, extending from the equatorial regions to the extratropics, simulated by a set of global convection permitting atmospheric models participating in the DYAMOND (DYnamics of the Atmospheric general circulation Modeled on Non-hydrostatic Domains) initiative. Such variety in model output will allow for an investigation of the robustness of stochastically parameterizing sea surface flux enhancement due to wind speed variability, by identifying sensitivities to model construction or geographical location and time period.

Chapter 2

Models and methods

The DYnamics of the Atmospheric general circulation Modeled on Non-hydrostatic Domains (DYAMOND) initative described by Stevens et al. (2019) provides forty days' (August 1 – September 9, 2016) worth of high resolution global numerical model output produced from identical initial conditions using a number of different models, and thus can be used to investigate the robustness of a statistical model obtained from dynamical model output. This chapter presents an overview of the similarities and differences of the models considered in the present study.

Note that the 'Cascade' experiment (Holloway et al. 2012; Love et al. 2011) considered in this study for comparison with Bessac et al. (2019, 2021) is not part of DYAMOND, but a separate project that used the UK Met Office Unified Model, a DYAMOND participant that will be described below. The fact that the Cascade project modeled a time-period different from DYAMOND (April 6 – 15, 2009) allows for a test of robustness with respect to time periods. Coming from the same model, it is expected that Cascade and the UM contribution to DYAMOND will have many similarities: specific differences between Cascade and UM will be noted where appropriate. For brevity and consistency, hereinafter 'Cascade' will denote the Cascade experiment whereas the shorthand 'UM' will denote the UM contribution to DYAMOND. Note also that the first day of the Cascade simulation and the first ten days of the DYAMOND simulations are discarded as spin-up.

Although the models participating in the DYAMOND initiative are global convection permitting models, this study will consider several specific geographical regions in the analysis. Discussion of these geographical regions will be presented in section 3.1. The specific computations performed on the DYAMOND output, viz. the zonal and meridional components of the 10 metre wind and total precipitation, are described in section 1.4.

2.1 Model configurations

Numerical models represent the atmospheric state on a grid. Model dynamics, which consist of the large-scale processes that are resolved by the numerical model, are governed by the dynamical core of the model; whereas model physics, which consist of the sub-grid scale processes that cannot be resolved by the model, are parameterized. This section will discuss the similarities and differences of dynamical cores utilized in the models considered in this study. Model physics will be discussed in the following section.

The Finite-Volume Cubed-Sphere dynamical core (FV3), initially developed at the United States National Aeronautics and Space Administration (NASA) Goddard Space Flight Center, was developed by the United States National Oceanic and Atmospheric Administration Geophysical Fluid Dynamics Laboratory (NOAA GFDL) situated in Princeton University. The model uses the cubed-sphere grid originally of Sadourny (1972), which has the benefit of being quasi-uniform and singularity-free: the benefits of a quasi-uniform grid cf. a latitude-longitude grid are discussed in de Grandpré et al. (2016). FV3 for DYAMOND solves the non-hydrostatic Euler equations using a finite-volume, vertically Lagrangian scheme (Satoh et al. 2019). With a column height of 39 km (Stevens et al. 2019), or 3 hPa (ESiWACE n.d.), it is the only low-top model (as defined by Charlton-Perez et al. (2013)) considered in this study. Technical documentation for FV3 includes Harris et al. (2020), Lin and Rood (1996, 1997), and Lin (2004).

The Goddard Earth Observing System (GEOS) is the model in use by the NASA Global Modelling and Assimilation Office. As GEOS uses the FV3 core, many of the dynamical

configurations for GEOS are identical to those of FV3. Technical references include Putman and Lin (2007) and Putman and Suarez (2011).

The Integrated Forecast System (IFS) of the European Centre for Medium-Range Weather Forecasts (ECMWF) is the only hydrostatic model in DYAMOND (Stevens et al. 2019), and is also the only spectral model in this study. The model operates on a reduced Gaussian grid and utilizes a semi-implicit, semi-Lagrangian scheme. Technical documentation includes ECMWF (2020a), Malardel et al. (2016), and Wedi (2014).

The Non-hydrostatic ICosahedral Atmospheric Model (NICAM) is a model developed by a Japanese consortium including the Japan Agency for Marine-Earth Science and Technology (JAMSTEC) and the University of Tokyo. NICAM uses an icosahedral grid, which is constructed by subdividing each of the twenty triangles that constitute the sides of an icosahedron until the desired spatial resolution is obtained. Notwithstanding the use of this grid in the model, model output is remapped to and reported on the latitude-longitude grid by use of SCRIP for CDO (Spherical Coordinate Remapping and Interpolation Package, Jones (1998, 1999); Climate Data Operator, Schulzweida (2020)). The model is governed by Euler's equations (Tomita and Satoh 2004), and uses a split-explicit, vertically implicit scheme (Satoh et al. 2019). Technical references for NICAM include Satoh et al. (2008, 2014).

The Unified Model (UM) of the United Kingdom's Meteorological Office (UK Met Office) is the operational model of the meteorological service of the United Kingdom. The dynamical core uses a semi-implicit semi-Lagrangian scheme on a latitude-longitude grid, and has the coarsest resolution of the DYAMOND participants (Stevens et al. 2019). Technical references includes Walters et al. (2017) and Wood et al. (2014).

An overview of the similarities and differences of each of the models considered in this study, as well as their resolutions, is summarized as Table 2.1. Further discussion and analysis of the strengths and shortcomings of the various grid schemes that are available to model spherical domains is presented in Williamson (2007). Further discussion of semi-Lagrangian advection schemes is presented in Staniforth and Côté (1991).

Configuration	FV3	GEOS	IFS	NICAM	UM
Grid construction	○	○			
Grid resolution (km)	3.3	3.3	4.8	3.5	7.8
Time integration	○	○	⋆		⋆
Non-hydrostatic	○	○		○	○
Column height		○	○	○	○

Table 2.1: Table of similarities between model constructions, for the models considered in this study. With the exception of grid resolution, sets of models with identical symbols within a given row have relatively similar construction for that aspect of the model. The lack of any symbol identifies model construction different from all other models. Grid resolution is as reported in Stevens et al. (2019).

2.2 Model parameterizations

The DYAMOND initiative allows for the intercomparison of results derived from global convection permitting models with different parameterizations governing their sub-grid scale tendencies, as summarized in Table 2 of Stevens et al. (2019). This section will explore model parameterizations to provide the background information relevant to assessing how the differences in parameterization between models may potentially contribute to differences in sub-grid scale flux enhancement characteristics.

It is important to note here that the effects of any parameterization are ultimately model-specific. For example, Martin et al. (2006) applied the same parameterization to a newer and older version of a model from the same centre[1] and found that the newer model benefited more from the same parameterization. As such, one must exercise caution when evaluating

[1]The Hadley Centre Global Environmental Model (HadGEM1) and the Third Hadley Centre Coupled Ocean-Atmosphere General Circulation Model (HadCM3), respectively.

the effects of two different models using similar parameterizations, since the same parameterizations need not influence model output in the same way for different models.

2.2.1 Cloud microphysics

Processes that govern cloud formation, dissipation, precipitation, and other related processes have length and time scales smaller than those that can practically be used in global numerical models. As such, these processes cannot be explicitly computed but must be parameterized. The appropriateness of said parameterizations are of great importance for the models, since cloud related processes influence convective transports, to be discussed later in this chapter, and furthermore influences atmospheric energetics. Examples of such energy-related processes include latent heat transfer, as considered in Grabowski (1998); ice crystal size distribution influencing shortwave albedo, as predicted by Heymsfield and Miloshevich (1991) and reported in Jensen et al. (1994); similar reported effects due to cloud condensate particle number density, as per, for example, Chen et al. (2000); and convective transport, as reported by Nasuno (2021).

The simplest form of such parameterization considers the interactions between water vapour, cloud condensate, and precipitation[2]. However, the global convection permitting models used in the DYAMOND initiative are well past the stage of having only three microphysical variables. In fact, all models involved in the DYAMOND initiative represent either five or six microphysical variables (Stevens et al. 2019): FV3 uses water vapour, cloud water, cloud ice, rain, snow, and graupel (L. Zhou et al. 2019); NICAM uses a scheme based on the same variables, as outlined in Seifert and Beheng (2006) and implemented as reported in Seiki and Nakajima (2014); IFS uses the same variables less graupel (ECMWF 2020b); and UM uses a six variable (Stevens et al. 2019) scheme based on Wilson and Ballard (1999) that

[2]Indeed such protocol, with a minimal number of microphysical variables, was the standard used in numerical models during the first decade of the 21st century: NICAM used parameterizations based on Grabowski (1998) until 2007 (Satoh et al. 2014); and IFS used a scheme based on Tiedke (1993) until 2010 (ECMWF 2020b).

accounts for water vapour, cloud water, rain, ice, snow, and graupel (Lean et al. 2008). The Cascade simulation used the three variable version of the UM scheme consisting of ice/snow, liquid water, and prognostic rain (Holloway et al. 2012).

Molod et al. (2015) reports that the scheme used in GEOS is that of Bacmeister et al. (2006), which uses one phase and two species of cloud condensate. In particular, GEOS tracks large-scale condensate, anvil condensate, large-scale precipitation, anvil precipitation, and convective precipitation, where each of the precipitation types have different representative particle sizes, fall speeds etc. but whose phase is determined from temperature and not tracked independently.

The number of microphysical variables and processes tracked indicate that the models considered all have cloud microphysics implemented to a comparable level of sophistication. The most different parameterization scheme considered in this subsection is, then, the scheme employed by GEOS which uses a set of hydrometeors fundamentally different from the other models.

2.2.2 Cumulus parameterization

Numerical models of the atmosphere generally consider two types of clouds depending on their generation mechanisms: large-scale clouds, which have the physical properties of stratiform clouds, generated in non-convective processes[3]; and cumuliform clouds, attributed to moist convection (Arakawa 2004; Wilson et al. 2008). Alternatively, Arakawa (2004) describes stratiform clouds as clouds of layered processes (e.g. Sundqvist (1978)) and cumuliform clouds to be vertical column processes (e.g. Arakawa and Schubert (1974)). As another alternative perspective, Xu and Krueger (1991) describes stratiform clouds to be inactive

[3]In reality, stratiform clouds may be generated from convective processes, but in the context of numerically modelling the atmosphere, the source of the cloud condensate (and their microphysical properties associated with their generation mechanism) is what motivates tracking each cloud type separately. Stratiform clouds produced from detraining convection are specifically referred to as anvils (Bacmeister et al. 2006; Xu and Krueger 1991).

processes in the sense of cloud generation, whereas cumuliform clouds are active processes. Note that this use of terminology makes the notion of 'cloud types' in atmospheric modelling to be quite different from its counterpart in observational meteorology (e.g. Warren et al. (2007)).

Classically, a cumulus parameterization scheme assumes the existence of moist updrafts (cumulus clouds) within a slowly sinking dry background (e.g. Arakawa and Schubert (1974) and Randall et al. (2003)). It is assumed that the moist convection occurs within a small fraction of the grid-box that is considered and thus classical cumulus parameterizations model the existence of convective systems within a primarily clear grid-box, e.g. Rosenthal (1978) and Yamasaki (1977, 1983). As a consequence of this assumption, cumulus parameterization schemes break down when the size of the grid-box approaches the size of the convective systems that are modelled: that is, these parameterizations fail in the so-called *terra incognita* (e.g. B. Zhou et al. (2014)), more commonly known as the grey zone. The challenges introduced by the grey zone are of great importance for convection permitting models such as the global models participating in the DYAMOND initiative.

Due to the difference in length scales for deep and shallow convection[4], it becomes necessary to consider treating the two processes separately. In particular, the convection-permitting resolutions used in the DYAMOND initiative allow for partial resolution of deep convection. Shallow convection, a process with considerably smaller length scales, continues to be an unresolved process for most model resolutions considered.

The only model considered in this study that has no cumulus parameterization is NICAM (Stevens et al. 2019), since NICAM attempts to explicitly resolve tropical convection. As

[4]Under the steady plume hypothesis, deep convection warms and dries the surrounding environment as a consequence of water loss due to precipitation (and thus not reevaporated from cloud top) and by subsidence of warm dry air from aloft (as per the assumptions of RAS), whereas shallow convection is a non-precipitating process that moistens (by cloud water reevaporation) and cools the environment. As with many other atmospheric processes, the two processes should be understood to be coupled (Yano and Plant 2012). Another distinction is the cloud thickness, where deep convection has cloud thickness exceeding 200 hPa whereas shallow convection is convective but has thickness less than 200 hPa (Becktold 2019).

such, their Chikira and Sugiyama (2010) cumulus parameterization scheme is not enabled (Noda et al. 2015; Satoh et al. 2014).

In contrast, the only model that used a full cumulus parameterization was GEOS (Stevens et al. 2019), which uses the Relaxed Arakawa-Schubert (RAS) scheme developed by Moorthi and Suarez (1992) (Molod et al. 2015). RAS is able to consider an arbitrary spectrum of cloud types with given detrainment pressure levels when computing precipitation from the moisture carried up by the cloud: that is, mass flux is computed for each different iterated cloud type and not in bulk. The Bacmeister et al. (2006) implementation for GEOS used 30 cloud types for their RAS scheme.

The other models, viz. IFS, FV3, and UM, employ cumulus parameterization for shallow convection and do not parameterize deep convection. Thus, differences that distinguish FV3, IFS and UM from the other models may potentially be attributed to cumulus parameterization. It is also necessary to note here that in the Cascade project cumulus parameterization was turned down, which forced most of the convection to be explicit (Love et al. 2011).

2.2.3 Fractional cloudiness

Notwithstanding the rare deviations discussed in, e.g. Pruppacher and Klett (2010), clouds are spatial regions with relative humidity at or near 100 percent. It is unrealistic to expect the concentration of water vapour in a model grid-box to be homogeneous: rather, clouds can be expected to be distributed unevenly within a grid-box. As such, some sub-grid scale regions within a grid-box may have higher relative humidity than the surrounding background within the same grid-box. Consequently, even a grid-box with low relative humidity may have a fraction of the grid-box cloudy, and the rest clear. Such situation must be manifested in numerical models by means of parameterization.

The only model considered in this study that does not parameterize fractional cloudiness is NICAM (Stevens et al. 2019), which, instead of using cloud fractions to represent the existence of sub-grid sized clouds, attempts to explicitly represent the smaller cloud systems (Satoh et al. 2018).

The parameterizations used in the other models are as follows: FV3 follows Rotstayn et al. (2000), a scheme based on the prognostic Smith (1990) scheme (Zhao et al. 2018); IFS uses the stochastic Räisänen et al. (2004) cloud generator with prognostic cloud cover based on Tiedke (1993) (ECMWF 2020b); GEOS uses the prognostic Bacmeister et al. (2006) scheme (Molod et al. 2015); and UM uses the Tiedke-like Wilson et al. (2008) extension to Smith (1990) (Walters et al. 2017, 2019). It can be noted here that all models considered use prognostic approaches to modelling cloudiness: that is, the models track cloud condensate explicitly. It should also be noted that Bacmeister et al. (2006) and Tiedke (1993) make assumptions similar to each other and different from Smith (1990) (Molod 2012).

2.2.4 Boundary layer parameterization

The planetary boundary layer (PBL) parameterization scheme represents vertical mixing within the lowest part of the troposphere, determining the exchange of energy, momentum, moisture, and trace gases between the atmosphere and the surface. Despite the numerous approaches available for the parameterization of boundary layer processes, all models considered in this study used what Stevens et al. (2019) classified as a parameterization that uses diagnostic eddy diffusivity.

In fact, FV3 (Zhao et al. 2018), GEOS (Molod et al. 2015), and UM (Walters et al. 2017, 2019) all use schemes based on Lock et al. (2000). This scheme computes a diffusion coefficient profile that depends on height, and has been attributed to a better simulation of lower clouds when compared against satellite observations and other models with different planetary boundary layer parameterizations (M. Zhang et al. 2005).

As all models considered in this study use the same general approach to model vertical mixing within the atmosphere, it is not anticipated that the model specific boundary layer parameterization will result in major differences between the considered models.

2.2.5 Gravity wave drag

The paradigmatic explanation of gravity waves consists of air moving over orography, say a mountain range, launching waves that propagate. The launch and subsequent breaking of gravity waves transport momentum within the atmosphere, making gravity waves an important process when modelling the atmosphere. The effects of sub-grid scale orography are parameterized in numerical models to ensure that the effects of gravity waves are represented appropriately, even if geographic features cannot be resolved at model grid scale. Such parameterizations of orographic gravity wave drag reduce wind near mountainous regions, and have been found to be important for quantifying mountainous precipitation correctly (as per personal communication from A. Zadra quoted in Mo et al. (2019); also note Zadra et al. (2003)). FV3 uses a parameterization scheme based on Garner (2005) (Zhao et al. 2018); UM uses a scheme based on Lott and Miller (1997) and improved by Vosper (2015) (Walters et al. 2017, 2019); GEOS, a scheme based on McFarlane (1987) (Molod et al. 2015); NICAM uses no parameterization, and IFS uses a scheme based on Lott and Miller (1997) (Stephan et al. 2019b). Although the direct influence of orographic gravity wave drag on sea-surface flux enhancement is likely small over open ocean, it may be substantial in the vicinity of land.

Non-orographic sources of gravity wave drag include those that originate from convective, jet flow, and frontal systems (e.g. Fritts and Alexander (2003) and Stephan et al. (2019b)), and carry momentum aloft into the stratosphere (e.g. Walters et al. (2019) and Zhao et al. (2018)). This effect is parameterized in numerical models by adding a time-invariant momentum flux source at model grid points in the troposphere, independent of other model variables (Bushell et al. 2015)[5]. Since it has been established that cumulus parameterization

[5]The use of globally uniform and solely latitude dependent parameterizations of non-orographic gravity wave drag is a consequence of the lack of constraints on parameters relevant for the generation and propagation of these types of gravity waves (Fritts and Alexander 2003). A classic example of such launch spectrum parameterization is proposed by Fritts and VanZandt (1993). This parameterization is subsequently used in, for example, Warner and McIntyre (1996).

influences gravity wave generation (e.g. Müller et al. (2018), Stephan et al. (2019a)), and since gravity wave propagation has been shown to influence convection both in the form of enhancement and suppression (Love et al. 2011), non-orographic gravity wave drag can be expected to be of importance when comparing parameterizations used in the models under consideration[6]. The particulars are as follows: FV3 follows Alexander and Dunkerton (1999), based on Lindzen (1981) (Zhao et al. 2018); UM uses Scaife et al. (2002) (Walters et al. 2017, 2019); GEOS, using Garcia and Boville (1994) (Molod et al. 2015); NICAM again using no parameterization, and IFS, based on Scinocca (2003) (Stephan et al. 2019b). Note here that both Scaife et al. (2002) and Scinocca (2003) are operational solutions to the computationally expensive Warner and McIntyre (1999), a parameterization built on Warner and McIntyre (1996), which itself is a so-called Lindzen-type parameterization (Fritts and Alexander 2003).

In conclusion, both orographic and non-orographic gravity wave drag parameterization schemes between IFS and UM are the most similar, whereas NICAM has the formulation most different from the others, using no parameterization.

2.2.6 Summary

This section considered five sets of processes that are unresolved or partially resolved in modern global convection permitting models, and are thus parameterized. Cloud microphysics, fractional cloudiness, cumulus parameterization, boundary layer parameterization, and gravity wave drag were discussed in order to identify similarities and differences between models considered in this study, as a background to investigating differences in model behaviour.

It was found that FV3 and UM have relatively similar parameterization schemes; NICAM has more explicit representations over parameterization; and that GEOS uses noticeably

[6]One specific example of convection causing gravity wave propagation is the so-called 'release of heat' due to precipitation under deep convection. Becktold (2019) describes this process as being analogous to waves on a disturbed water surface.

Parameter	FV3	GEOS	IFS	NICAM	UM
Cloud microphysics	∘		⋆	⋆	∘
Fractional cloudiness	⋆	∘	∘	–	⋆
Cumulus parameterization	∘		∘	–	∘
Boundary layer	∘	∘			∘
Gravity wave drag			∘	–	∘

Table 2.2: Table of similarities between parameterization schemes employed for each model considered in this study. Sets of models with identical symbols have relatively similar parameterizations. A dash indicates the lack of parameterization for the corresponding parameter. The lack of any symbol identifies parameterization schemes different from all other models.

different parameterization schemes when compared with the other models. A summary of parameterization similarities and differences is presented in Table 2.2.

Notwithstanding the facts presented above, it is important to note that the parameterizations considered herein constitute only a small subset of the parameterizations made in numerical models of the atmosphere. Other parameterizations that were not explicitly considered above, such as those associated with radiative transfer, atmospheric chemistry (e.g. ozone, methane oxidation, aerosol), and land surfaces (e.g. snow, soil), are anticipated to be of lesser importance for the comparisons made in this study.

2.3 Modelling Gaussian fields

Practical estimation of the deterministic part of the error process $\varepsilon_{N,n}$ in Equation 1.15 is a relatively straightforward regression calculation by means of a least squares solution. Similarly, numerical generation of the stochastic part $\psi_{N,n}$ is not a foreign concept: for example, the so-called revised SPPT (Stochastically Perturbed Parameterization Tendencies)

scheme uses random complex numbers[7], with real and complex parts drawn from Gaussian distributions, to perturb model physics (Palmer et al. 2009).

Since random processes in geophysical systems are oftentimes correlated in space and time, it is a practical necessity to generate a correlated Gaussian random field when implementing stochastic parameterizations in a numerical model. This is also a straightforward process by use of a 'square root' of covariance matrices: for example, the γ-exponential covariance matrix K for characteristic length scale ℓ that consists of individual matrix elements

$$K(x_i, x_j) = \exp\left(-\left(\frac{||x_i - x_j||}{\ell}\right)^{\gamma}\right) \tag{2.1}$$

with matrix elements x_i, x_j, and $\gamma \in]0, 2]$ some roughness factor represents a vector of correlated random variables ζ via

$$\zeta = \text{w chol } K \tag{2.2}$$

where w is a vector of Gaussian noise, and chol the Cholesky decomposition. This discussion of Gaussian random processes motivates the use of Gaussian process regression for results analysis[8] in section 3.4. For further discussion of Gaussian process modelling, one may consult Rasmussen and Williams (2006).

In practice, obtaining a correlated random field with known covariance is not anticipated to be computationally expensive, especially in light of recent developments by Chen and Stein (2021) and Tsyrulnikov and Gayfulin (2017), the former improving computation cost of covariance matrices and the latter being an alternative spatio-temporal pseudo-random Gaussian field generator.

[7]More specifically, Palmer et al. (2009) generates random fields on a sphere correlated in space and time by use of a transformation involving spherical harmonics. The use of an auto-regressive process of first order (which approximates the continuous-time Ornstein-Uhlenbeck process) to describe spectral coefficients ensure correlation of the pertubation in space and time.

[8]Realizations of such Gaussian processes were generated in Bessac et al. (2019) and agreed well with the 'true' fluxes.

Chapter 3

Results

This chapter will present the results of applying the previously described analysis on different models, regions, and time periods. The implications of these results, in the context of global or regional modelling, will be discussed in the following chapter. In particular, the analysis in this chapter will place emphasis on the following:

1. Assessment of the log 10 error process $\varepsilon_{N,n}$ conditioned on $F_{N,n}^{(R)}$ and P, as per Equation 1.15 and by using the 10 metre wind vectors and total precipitations available from the DYAMOND model outputs;

2. The statistical features of $\psi_{N,n}$, the stochastic residual of $\varepsilon_{N,n}$, conditioned on $F_{N,n}^{(R)}$ and P, computed using all points in a selected domain over a choice of time period;

3. Robustness of the regression model used to estimate the deterministic part of $\varepsilon_{N,n}$, estimated from the variables resolved by the numerical model; and

4. The features of the Gaussian process fit applied to the stochastic part of $\varepsilon_{N,n}$, quantifying the space-time covariance structure of the random scalar field.

Analysis of the results with emphasis on the aforementioned features will allow for evaluation of the robustness of the regression model and the structure of the stochastic spatiotemporal field $\psi_{N,n}$.

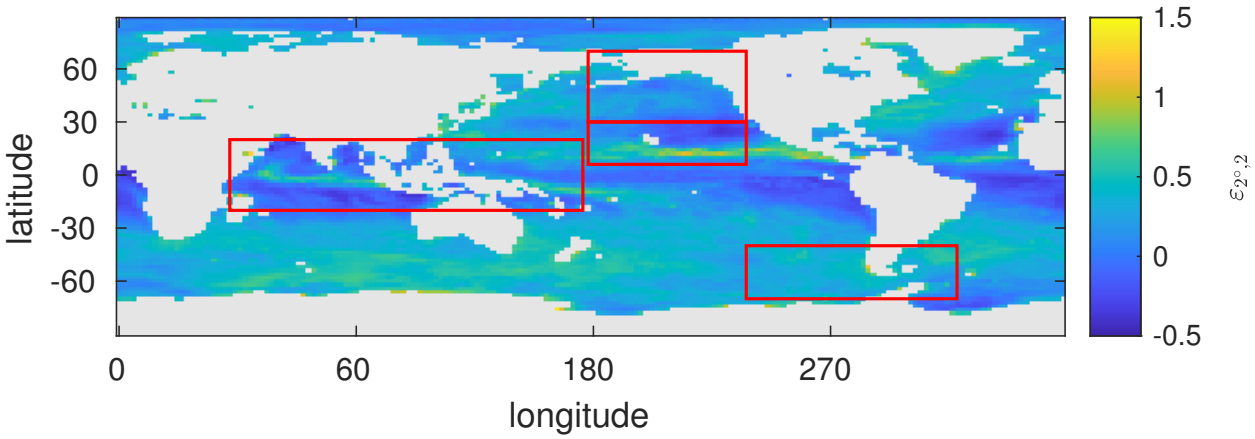

Figure 3.1: Global $\varepsilon_{2^\circ,2}$ means with land masked out in grey. Results from the IFS model are shown as a representative sample: plots of $\varepsilon_{2^\circ,2}$ and precipitation means for all models are included in the appendix as Figures A.1 to A.8. The regions considered in this study are outlined in red. A resolution coarser than those used in the remainder of this study is shown for computing reasons.

Specifically, the analysis will focus on $n = 1$ and $n = 2$, corresponding respectively to energy or freshwater fluxes and to momentum fluxes[1]; and will primarily be reported for the coarsening resolution $N = 0.4°$, with $N = 0.76°$ to be reported in the appendix. The choice of these resolutions allows for comparison with Bessac et al. (2021).

3.1 Regional error processes

This study will investigate four distinct geographical regions in the ten day period from August 11 to August 20[2] in order to establish the robustness of the statistical models of Bessac et al. (2019, 2021) across regions. In particular, this study considers the Indo-Pacific Warm Pool, subarctic Northeast Pacific, subtropical Northeast Pacific, and a region of the

[1]Recall that as per the representation made in Equation 1.11, the resolved flux $F^{(R)}_{N,n}$ considered in this study is the wind dependent part of the sea-surface flux represented by a chosen n value.

[2]A ten day period is used both for comparison with Bessac et al. (2019, 2021) and for computational simplicity. The weak sensitivity to taking different ten day periods for the presented results is shown in section 3.3.

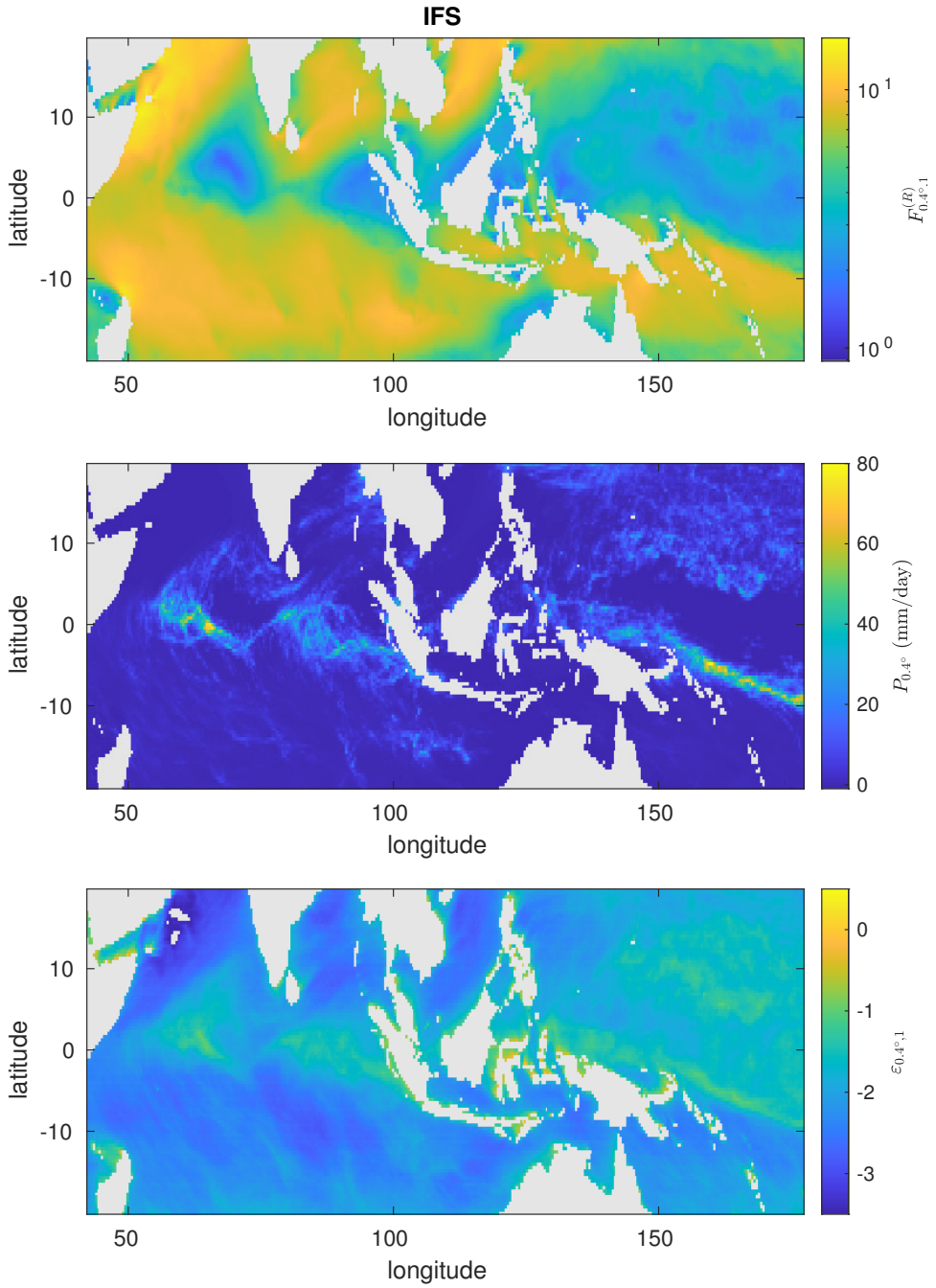

Figure 3.2: Time means of $F^{(R)}_{0.4°,1}$, $P_{0.4°}$, and $\varepsilon_{0.4°,1}$ for the IFS Indo-Pacific Warm Pool. Simulations by the other models are included in the appendix as Figures A.9 to A.14. Vertical axis denotes latitude, whereas the horizontal axis denotes longitude.

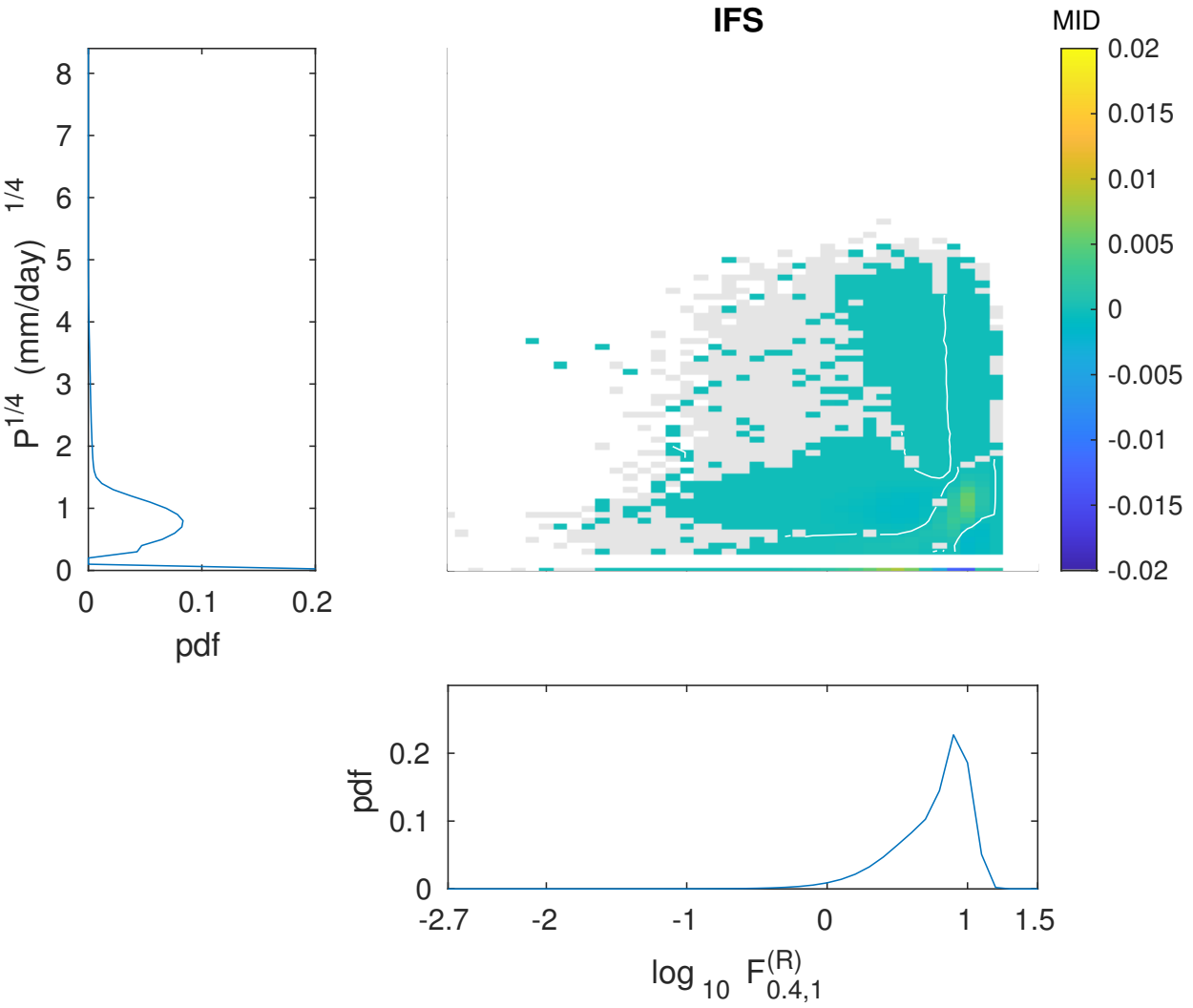

Figure 3.3: Distribution of precipitation and resolved flux for the Indo-Pacific Warm Pool for IFS, plotted as a mutual information density and respective marginal densities, with $N = 0.4°$, $n = 1$. Equivalent figures for all models are included in the appendix as Figures A.27 to A.32. Significant values of the mutual information density (at the five percent significance level with a two-tail test) are shown in colour. The white contour indicates a value of zero.

Southern Ocean encompassing the Drake Passage, to provide a set of different precipitation and wind climatologies. The regions are outlined in Figure 3.1. Time means of the resolved flux, precipitation, and the error processes for $N = 0.4°$ and $n = 1$ within the studied regions are presented as Figures 3.2, 3.4, 3.6, and 3.8. Results from the IFS model will be discussed in depth: differences and deviations present in other models will be discussed collectively afterwords. Note that for all analysis hereinafter coarsened grid-boxes that include land points are excluded.

The Indo-Pacific Warm Pool region considered herein is bounded by the 20° N and 20° S parallels and by the 42° E and 177° E meridians. Land masses within the region include the Maritime Continent, as well as northern Australia, the Horn of Africa, and South Asia. Being a region with substantial convection and resulting small scale wind variability, the region is expected to have relatively large values of $\varepsilon_{N,n}$. Furthermore, the choice of this region allows for direct comparison between this study and the results of Bessac et al. (2019, 2021), since the domain is identical to the domain used in the Cascade experiment. Note however that, unlike the Cascade experiment that modelled a ten day period in April, the DYAMOND initiative models the atmosphere during late Northern Hemisphere summer. As such, time means of precipitation and wind in the region may be different between the two model runs for reasons other than model differences: both because the model runs are short time periods and also due to different background climatologies.

It is also necessary to study the probability densities of resolved flux and precipitation, the variables utilized in the parameterization of the deterministic part of $\varepsilon_{N,n}$, since they may be different across models, spatial domains, and time periods. Specifically, the statistics of resolved flux and precipitation individually may be expressed as their respective marginal probability distributions. The marginal probability densities for precipitation and resolved flux, $p(P_{N,n})$ and $p(F^{(R)}_{N,n})$ respectively, and their joint probability density $p(P_{N,n}, F^{(R)}_{N,n})$, can be used to compute a mutual information density

$$\mathrm{MID}(P_{N,n}, F^{(R)}_{N,n}) = p(P_{N,n}, F^{(R)}_{N,n}) \log \left(\frac{p(P_{N,n}, F^{(R)}_{N,n})}{p(P_{N,n}) \cdot p(F^{(R)}_{N,n})} \right) \tag{3.1}$$

which characterizes statistical dependence by indicating whether a joint probability density is larger or smaller than the density resulting from the product of the marginal probabilities. In particular, a positive mutual information density in a region indicates a higher probability than if each variable was independent, whereas a negative mutual information density indicates a smaller probability than would be the case for independent variables.

Figure 3.2 shows maps of the time mean resolved flux, precipitation, and $\varepsilon_{0.4^\circ,n=1}$ for the Indo-Pacific Warm Pool, while Figure 3.3 shows the corresponding marginal probability distributions and mutual information density with estimated probabilities aggregated over space and time. Statistical significance of the MID is assessed at the five percent significance level, using a two-tailed test. Specifically, realizations from the null hypothesis distribution of independent $(P_{N,n}, F^{(R)}_{N,n})$ are generated via resampling, i.e. from 200 random permutations of the sets P_N and $F^{(R)}_{N,n}$. Such resampling preserves marginal distributions while removing dependence between variables. The null hypothesis is not rejected when the observed $\mathrm{MID}(P_N, F^{(R)}_{N,n})$ is no less than 2.5 percent and no more than 97.5 percent of the MID of the null hypothesis distribution. Such MID values are indicated in grey. Together, these figures offer insight into the relationship between sea surface flux, precipitation, and the sea surface flux enhancement in the Warm Pool.

It can be observed from Figure 3.2 that there appear to be similarities between the geographical distribution of time mean resolved flux, precipitation, and $\varepsilon_{N,n}$, which suggest some form of dependence between the variables. Such dependence may emerge from the stronger influence of $\varepsilon_{N,n}$ in regions of smaller $F^{(R)}_{N,n}$ (i.e. increased cancellation of vector winds within a grid box results in smaller $F^{(R)}_{N,n}$ and larger $\varepsilon_{N,n}$) and stronger convection (thus higher P_N, as a proxy of convection and thus convergent flow), relative location to nearby land (topography may disrupt large-scale flow and increase $\varepsilon_{N,n}$ on the lee side), and regional climatologies (e.g. relative strength of convection). This fact further motivates construction of a regression model $\mu(F^{(R)}_{N,n}, P_N)$ which represents the part of $\varepsilon_{N,n}$ that can be expressed in a deterministic manner. From the MID shown in Figure 3.3, the two predictors P_N, $F^{(R)}_{N,n}$ are not linearly dependent. The mutual information density exhibits lower proba-

bility densities for bands of $(F^{(R)}_{N,n}, P_N)$ combinations with moderate resolved flux and high precipitation as well as for moderate precipitation and small resolved wind, which indicates dependence between the variables, where certain rates of precipitation having favoured wind speeds, and vice versa. While this fact indicates that precipitation and resolved flux are not completely independent, the fact that the joint probability distribution indicates the two variables are also not linearly dependent justifies their construction as separate predictors for the purpose of constructing a regression model for $\mu_{N,n}$. Turning to the marginal distribution of precpitation in Figure 3.3, of particular note are the two peaks indicating a strong separation between a large number of space time points with no precipitation and a large number of points with appreciable precipitation.

Similar to the Indo-Pacific Warm Pool, the IFS model subtropical Northeast Pacific received a considerable amount of precipitation during the DYAMOND simulation, as shown in Figure 3.4. The region is bounded by the 5° N and 30° N parallels and the 120° W and 180° W meridians, the only substantial land mass in this region being Hawaii. The inclusion of this region is beneficial for comparison with the Indo-Pacific Warm Pool and with the adjacent subarctic Northeast Pacific domains, both being different wind and precipitation regimes. In particular, the strong, steady easterlies in this region contrast with the weak winds of the Warm Pool and the strong but variable winds of the midlatitude regions, to be discussed below. Furthermore, analyzing this region may be useful for quantification of sub-averaging scale fluxes in observational data, since air-sea fluxes in the region are well studied in the literature (e.g. Fagan and Mackenzie (2007)). The IFS model mutual information density for this region is presented as Figure 3.5, where it is observed that the mutual information density for the subtropical Northeast Pacific is similar to that of the Indo-pacific Warm Pool, demonstrating comparable dependence between wind and precipitation despite the different dominant meteorological processes in the regions as reflected in the marginal distributions. For example, the steady wind in this region manifests itself in the resolved flux marginal distribution, presenting a narrower probability distribution when compared

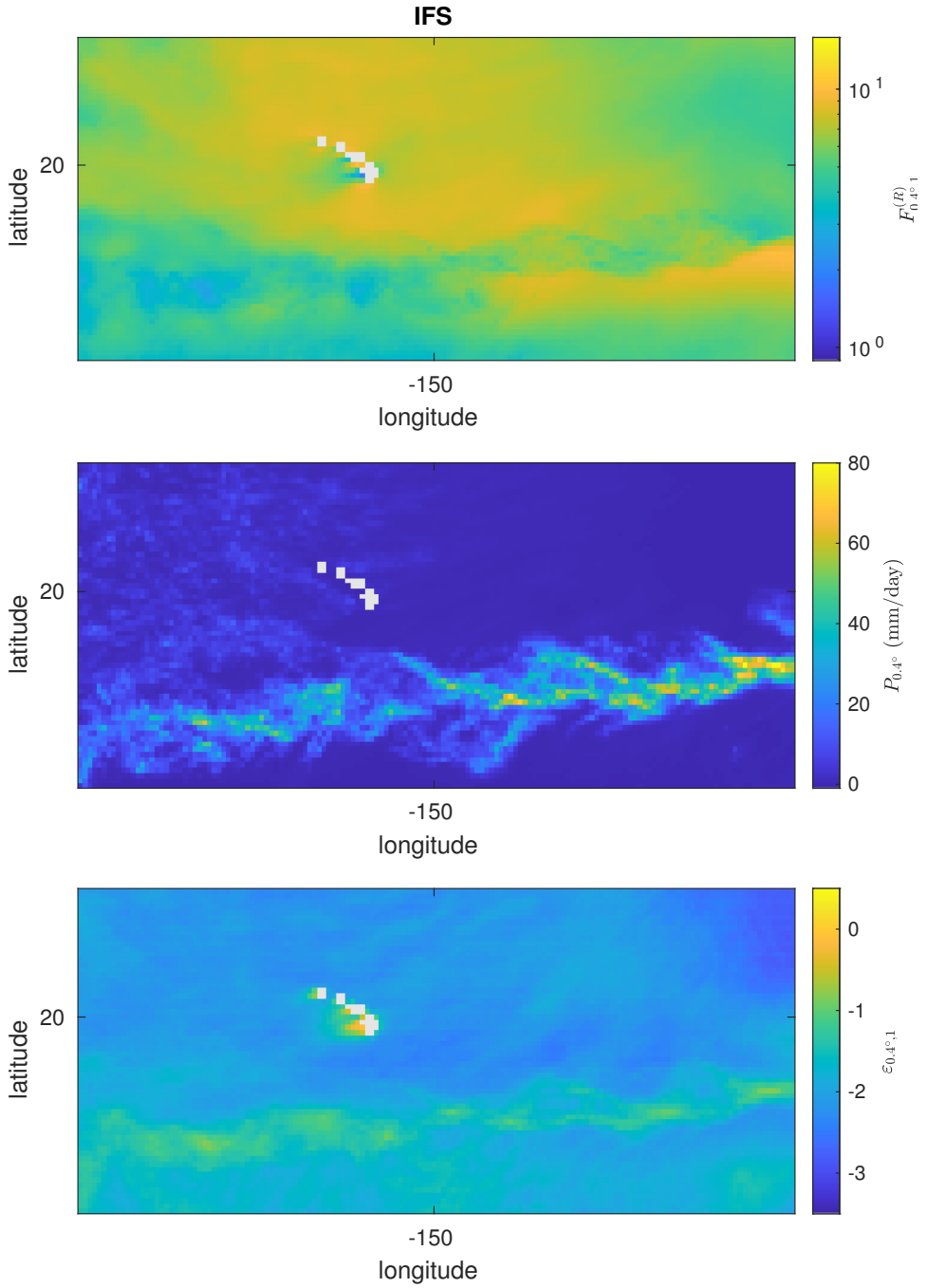

Figure 3.4: Time means of $F^{(R)}_{0.4^\circ,1}$, $P_{0.4^\circ}$, and $\varepsilon_{0.4^\circ,1}$ for the IFS subtropical Northeast Pacific. Simulations by the other models are included in the appendix as Figures A.15 to A.18. Vertical axis denotes latitude, whereas the horizontal axis denotes longitude.

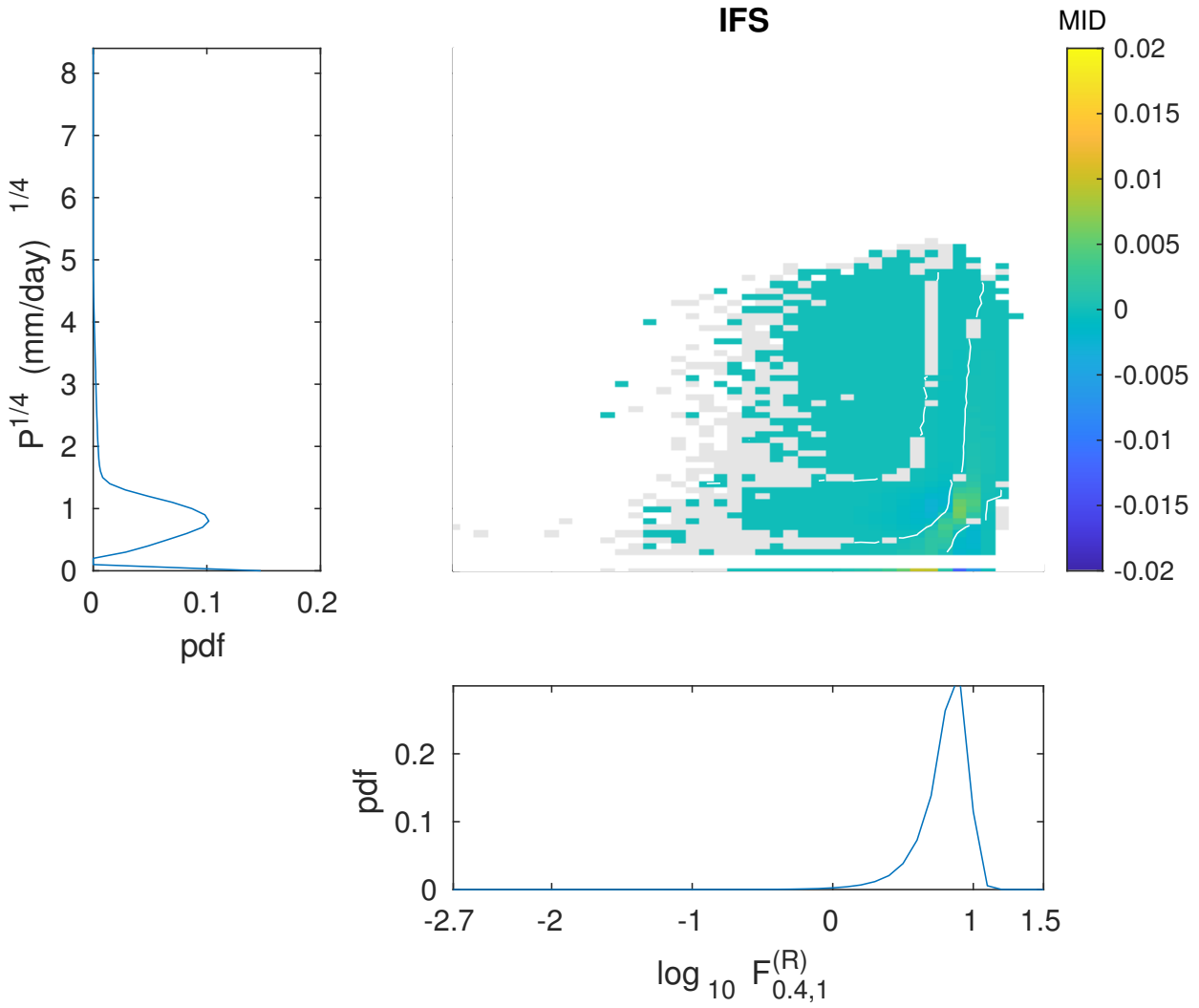

Figure 3.5: Distribution of precipitation and resolved flux in the subtropical Northeast Pacific, for IFS with $N = 0.4°$, $n = 1$. Other models included as Figures A.33 to A.36. Significant values of the mutual information density (at the five percent significance level with a two-tail test) are shown in colour. The white contour indicates a value of zero.

against the resolved flux marginal probability distribution in the Indo-Pacific Warm Pool. As with the Warm Pool, a large number of grid points are absent of precipitation.

The subarctic Northeast Pacific domain is adjacent to the subtropical Northeast Pacific domain, and is bounded by the 30° N and 70° N parallels and the 120° W and 180° W meridians. The region includes the west coast of North America including Alaska and the Aleutian Islands, as well as the Russian Far East. This region has different wind and precipitation climatologies compared to the Indo-Pacific Warm Pool and the subtropical Northeast Pacific, since the region has highly variable winds due to synoptic-scale storm activity (albeit relatively weak in August). Quantification of the error process in this well observed region is expected to be useful for analysis of observational data, such as those from Station P or Line P (e.g. Franco et al. (2021)). Maps of resolved flux, precipitation, and $\varepsilon_{N,n}$ are shown as Figure 3.6, and the precipitation and resolved flux probability distributions in Figure 3.7. During the simulation period, the region is largely absent of precipitation, unlike what is observed in the Warm Pool and subtropical Northeast Pacific. Despite the different marginal distributions, in particular the lower precipitation recognizable by the reduced tail in the higher precipitation range and the narrow resolved flux marginal distribution, the mutual information density plot is again similar to that of the other domains.

The region of the Southern Ocean considered is bounded by the 40° S and 70° S parallels and by the 40° W and 120° W meridians and includes Patagonia, the Antarctic Peninsula, and the Drake Passage region. Studying this region allows for the application of the analysis herein to a region of strong variable winds such as those known as the roaring forties, and may be useful for error quantification of datasets originating from the Drake Passage, such as the observations studied in Rees et al. (1997). Maps of mean resolved flux, precipitation, and $\varepsilon_{N,n}$ are presented in Figure 3.8, and the marginal distributions and mutual information densities are presented in Figure 3.9. Note the stronger winds in the region indicated by the marginal distribution for resolved flux, shifted to the right when compared against the other regions, and the weaker precipitation, shifted down compared against the other regions. Despite

these differences in the marginal distribution, the mutual information density maintains the features similar to those of the other regions' mutual information densities.

The four regions selected for this study, viz. the Indo-pacific Warm Pool, subtropical Northeast Pacific, subarctic Northeast Pacific, and a region of the Southern Ocean, offer a variety of wind and precipitation marginal distributions. Despite this fact, the mutual information densities for the regions are remarkably similar, indicating similar dependence between resolved flux and precipitation. Such similarity is part of the justification of the use of the same statistical model in all regions. Inclusion of these regions in the analysis will ensure that a wide range of possible precipitation and resolved flux marginal distributions are considered for the study, thus allowing for a comprehensive evaluation of the robustness of the employed methods.

Marginal distributions of resolved flux and precipitation rate between the models are noticeably different, even for identical regions (Figure 3.10). In particular, NICAM output does not display the non-zero 'precipitation peak' present in the other models and instead has a single 'peak' at the low end of precipitation. Notwithstanding the differences in the marginal distributions, a reasonable degree of similarity in MID structure is present across the different models studied for this analysis. Figure 3.10 also shows the mutual information densities for the Warm Pool region modeled by four different numerical models, and shows the noteworthy similarities between the different models, as well as the slight differences in precipitation-flux dependencies between models. In particular, the similarity of MID structure is remarkable even between models with the most dissimilar marginal distributions, such as those contributed by NICAM. Such similarity between the MID is important because it shows that the relationship between variables is similar between models, even if the marginal distributions of the variables show differences. A prominent example of a difference between models is the region of negative MID flanking strong positive MID, since the negative region is absent for NICAM but present for all other model outputs. When comparing marginal distributions, it is important to note that differences may be introduced by differences in

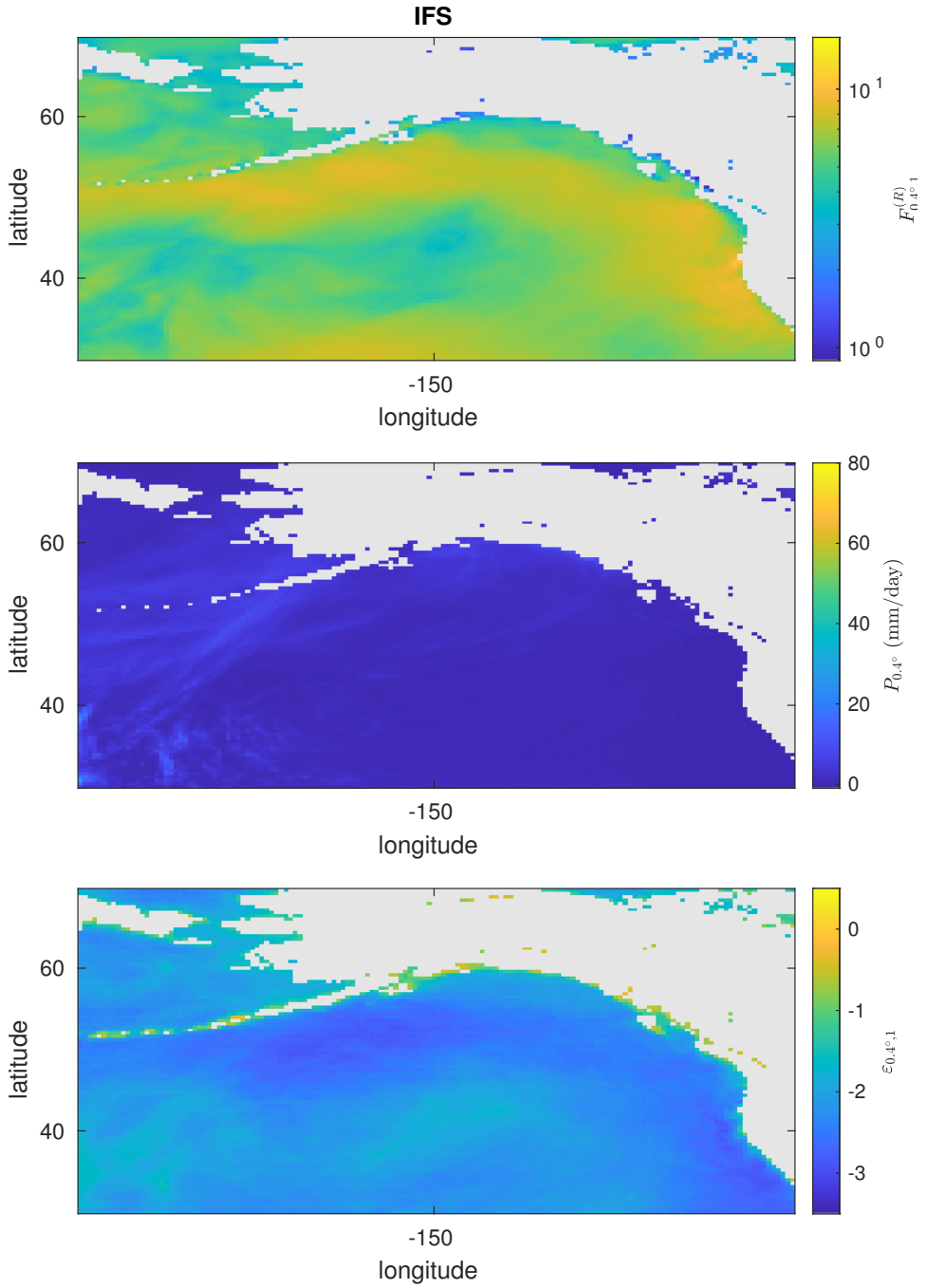

Figure 3.6: Time means of $F^{(R)}_{0.4^\circ,1}$, $P_{0.4^\circ}$, and $\varepsilon_{0.4^\circ,1}$ for the IFS subarctic Northeast Pacific. Simulations by the other models are included in the appendix as Figures A.19 to A.22. Vertical axis denotes latitude, whereas the horizontal axis denotes longitude.

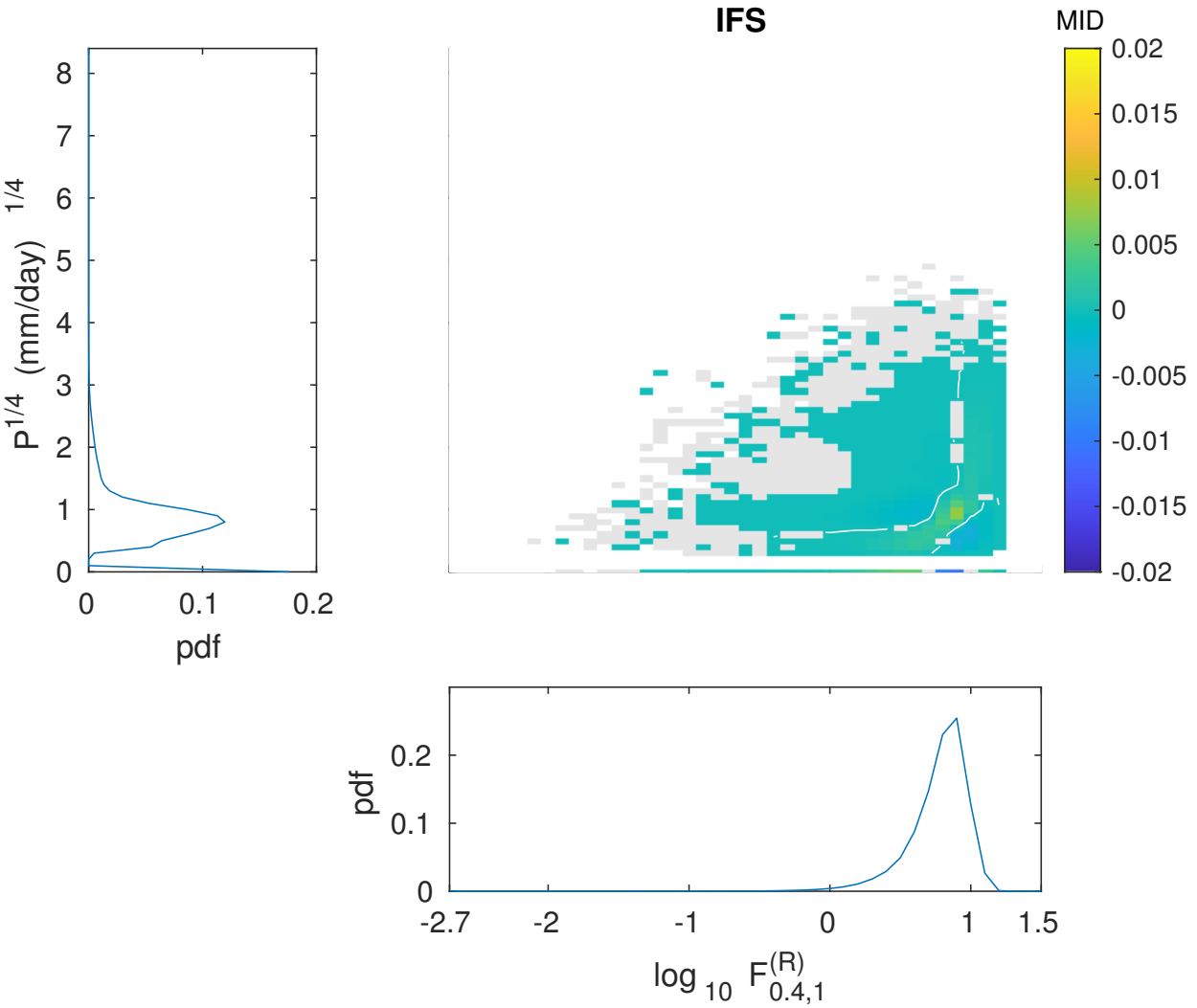

Figure 3.7: Distribution of precipitation and resolved flux in the subarctic Northeast Pacific, for IFS with $N = 0.4°$, $n = 1$. Other models included as Figures A.37 to A.40. Significant values of the mutual information density (at the five percent significance level with a two-tail test) are shown in colour. The white contour indicates a value of zero.

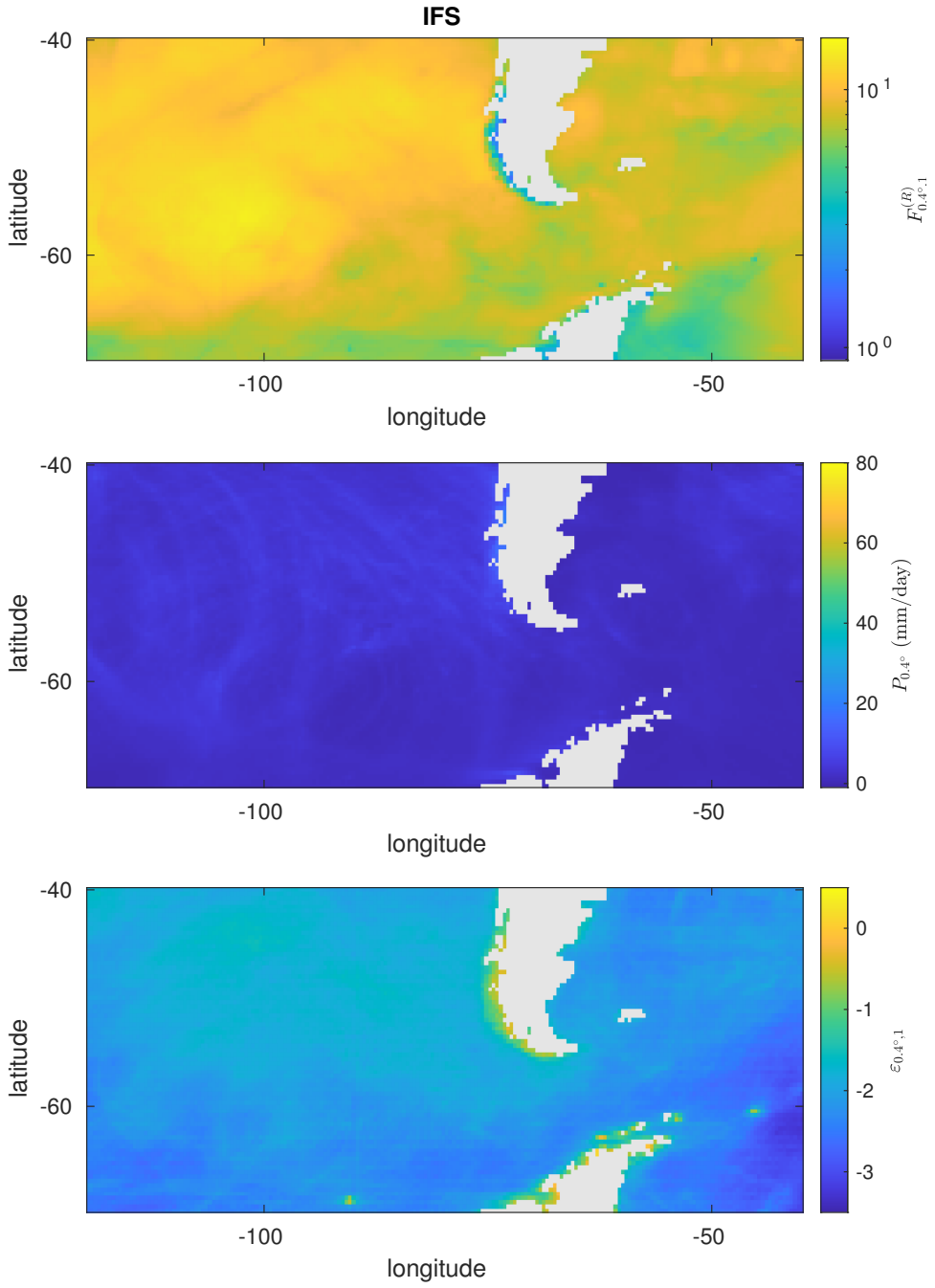

Figure 3.8: Time means of $F^{(R)}_{0.4^\circ,1}$, $P_{0.4^\circ}$, and $\varepsilon_{0.4^\circ,1}$ for the IFS Southern Ocean. Simulations by the other models are included in the appendix as Figures A.23 to A.26. Vertical axis denotes latitude, whereas the horizontal axis denotes longitude.

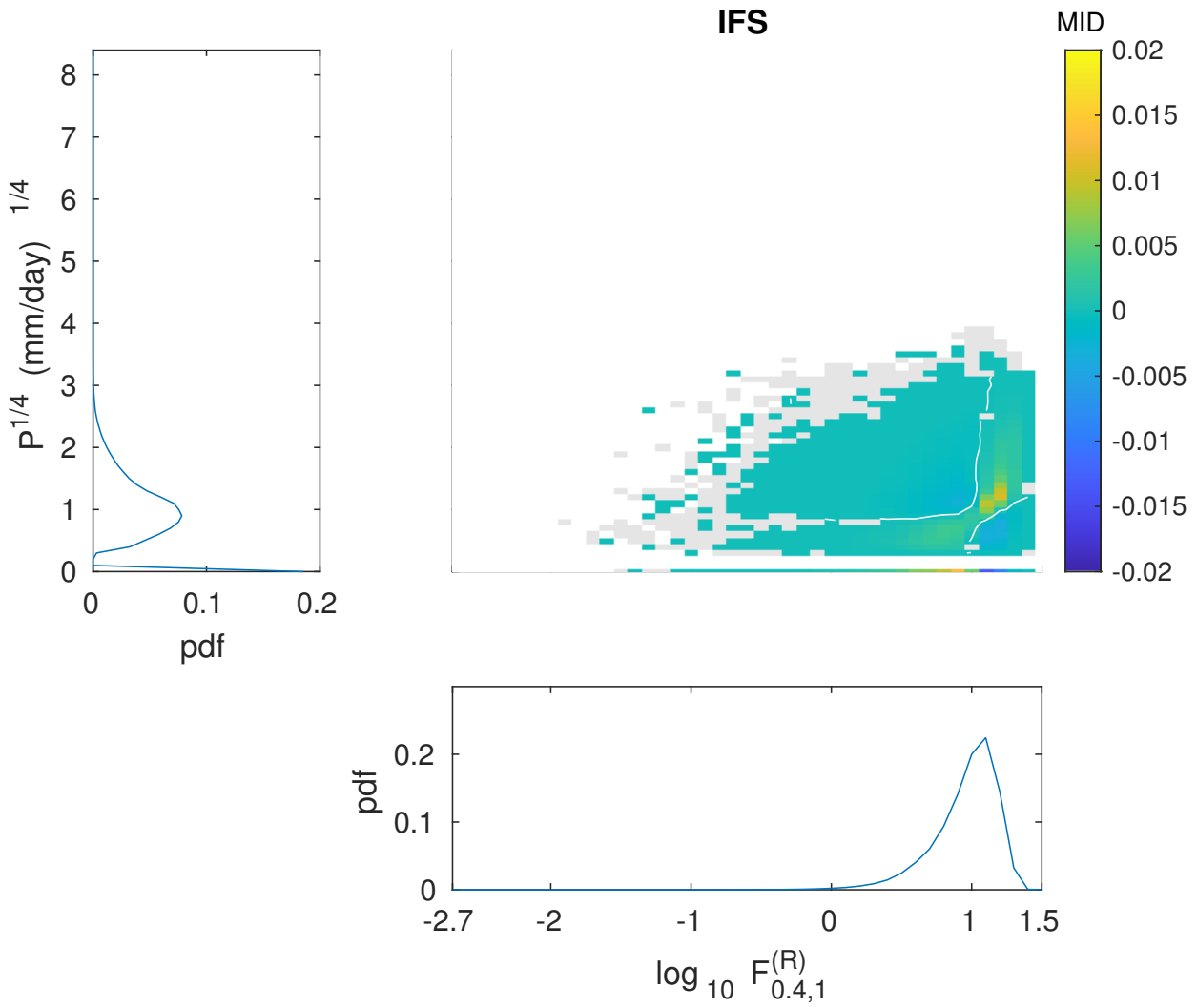

Figure 3.9: Distribution of precipitation and resolved flux in the Southern Ocean, for IFS with $N = 0.4°$, $n = 1$. Other models included as Figures A.41 to A.44. Significant values of the mutual information density (at the five percent significance level with a two-tail test) are shown in colour. The white contour indicates a value of zero.

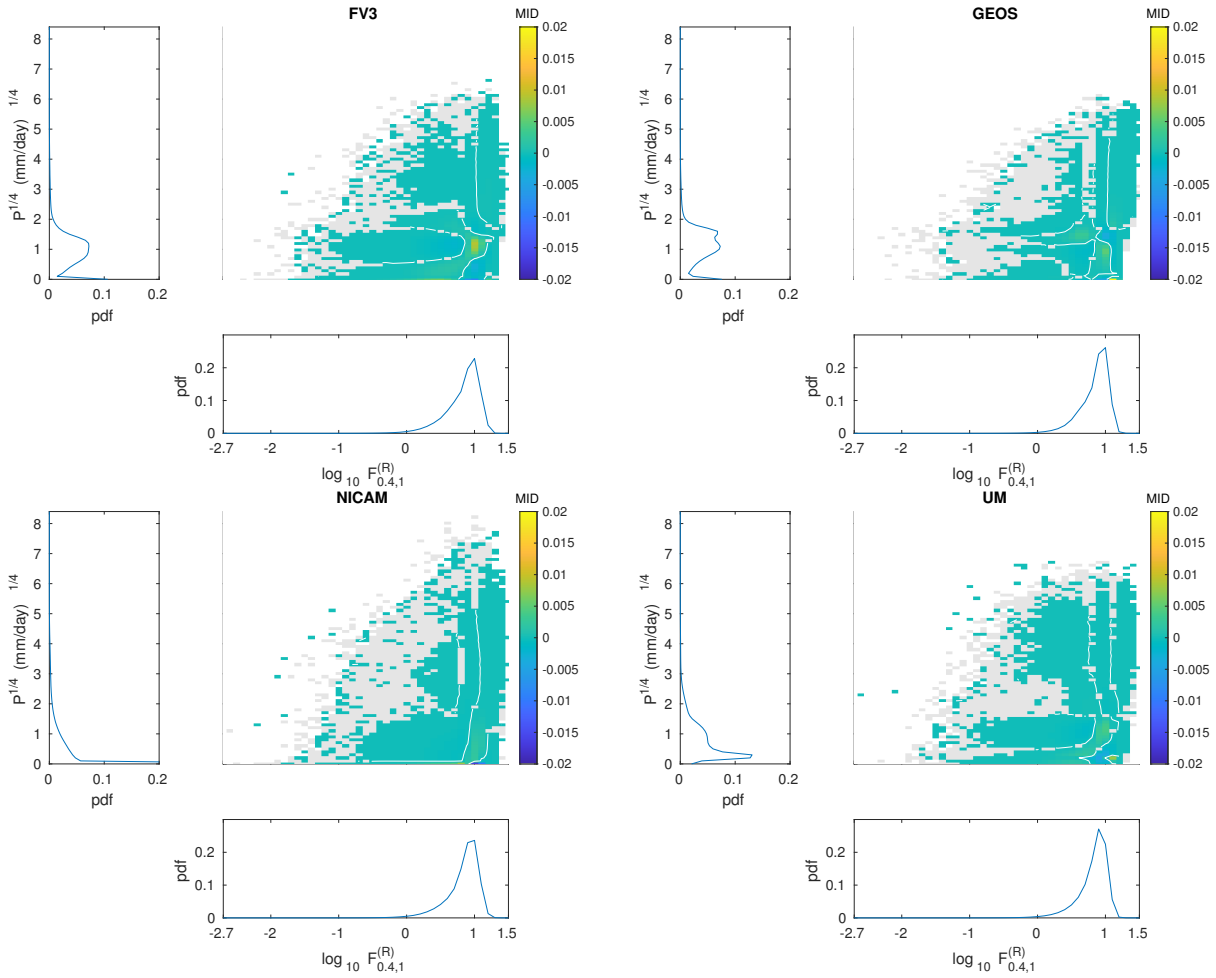

Figure 3.10: Warm Pool marginal distributions for resolved flux and precipitation, and mutual information density plots for four different numerical models. $N = 0.4°$, $n = 1$. White contour indicates a value of zero.

the models' representations of physical processes, by internal variability (i.e. differences in model weather realizations), or both.

Notwithstanding differences in marginal distributions of precipitation and resolved flux, the mutual information densities for these variables are thus concluded to be robust across different numerical models and geographical regions.

3.2 Conditioned distributions

As discussed in Chapter 1, this study applies the regression model of Bessac et al. (2019, 2021)

$$\varepsilon_{N,n} = (A_{N,n})_0 + \sum_{k=1}^{3}(A_{N,n})_k \left(\log_{10} F_{N,n}^{(R)}\right)^k + \sum_{l=1}^{4}(B_{N,n})_l P_N^{l/4} + \psi_{N,n} \tag{1.15}$$

to the error process in order to characterize the influence of resolved flux and precipitation on the error process $\varepsilon_{N,n}$. Note that regression coefficients $(A_{N,n})_0 \ldots (B_{N,n})_4$ are fit at the regional level (i.e. separately for each of the four domains described above): all spatial and temporal points included in a given region are included in the regional regression fit. This regression is intended to capture the dependence of $\varepsilon_{N,n}$ on $F_{N,n}^{(R)}$ and P_N, which can be visualized by use of conditional distributions.

Figures 3.11 and 3.12 present plots of the probability densities of $\varepsilon_{0.4^\circ,n}$ conditioned on the resolved flux and precipitation percentiles (which allows for comparison across different models with different precipitation biases while reducing effects due to the skewed distributions of resolved flux and precipitation) for $n = 1$ and 2 for different models. In particular, it is observed that $\varepsilon_{0.4^\circ,n}$ depends on both resolved flux and precipitation, with a form broadly consistent across different models and, to a lesser degree, locations. Important observations that can be made from the conditional distributions include:

1. $\varepsilon_{N,1}$ conditioned on $F_{N,1}^{(R)}$ decreases with increased resolved flux, whereas this structure is not prominent when $n = 2$; and

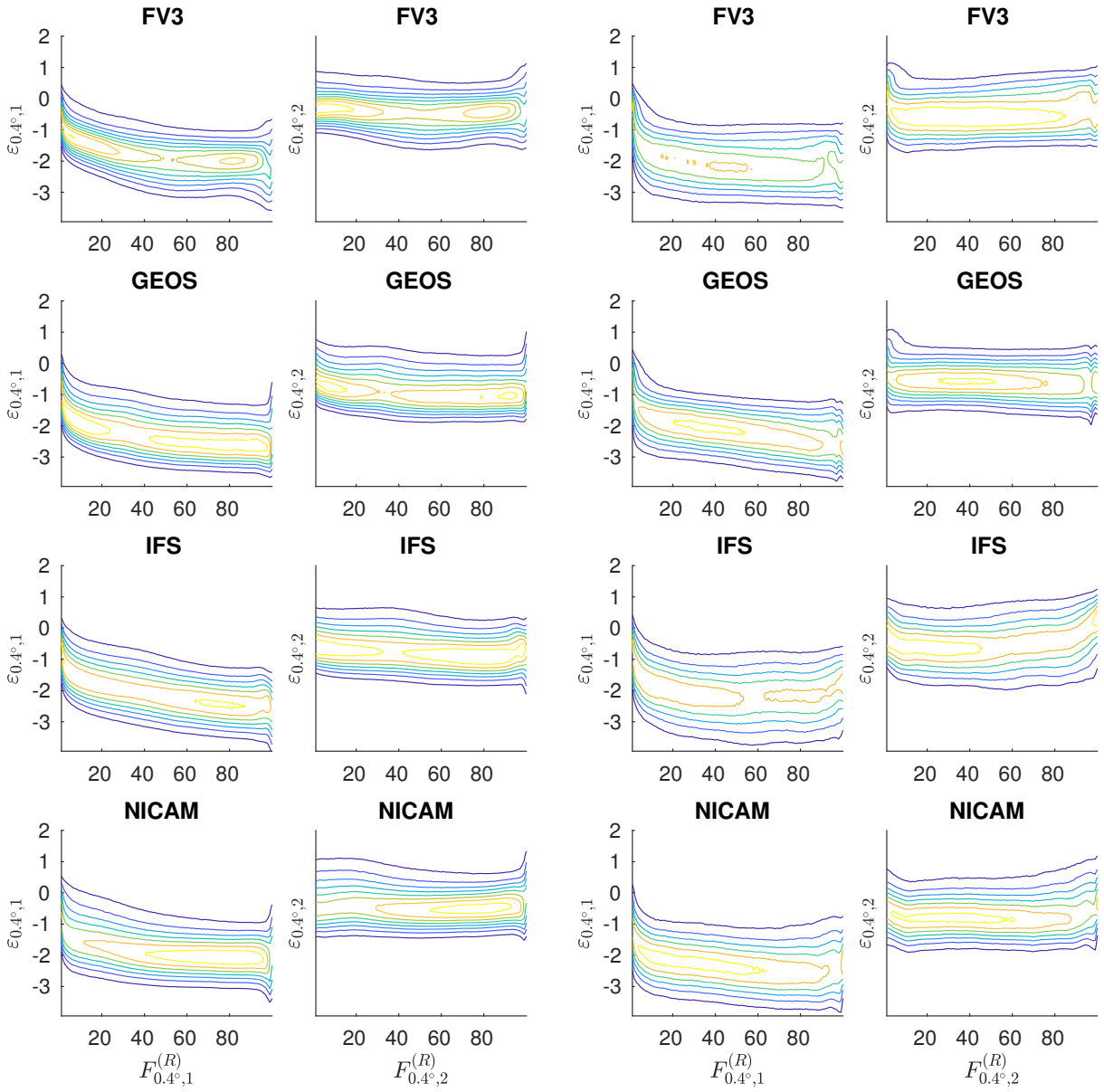

(a) $N = 0.4°$, $n = 1$ (left) and $n = 2$ (right). Warm Pool.

(b) $N = 0.4°$, $n = 1$ (left) and $n = 2$ (right). Southern Ocean.

Figure 3.11: Probability density function contours of the log 10 error processes conditioned on resolved flux. Horizontal axis values are model-specific percentiles. Other models and regions are included as Figures A.45 to A.64.

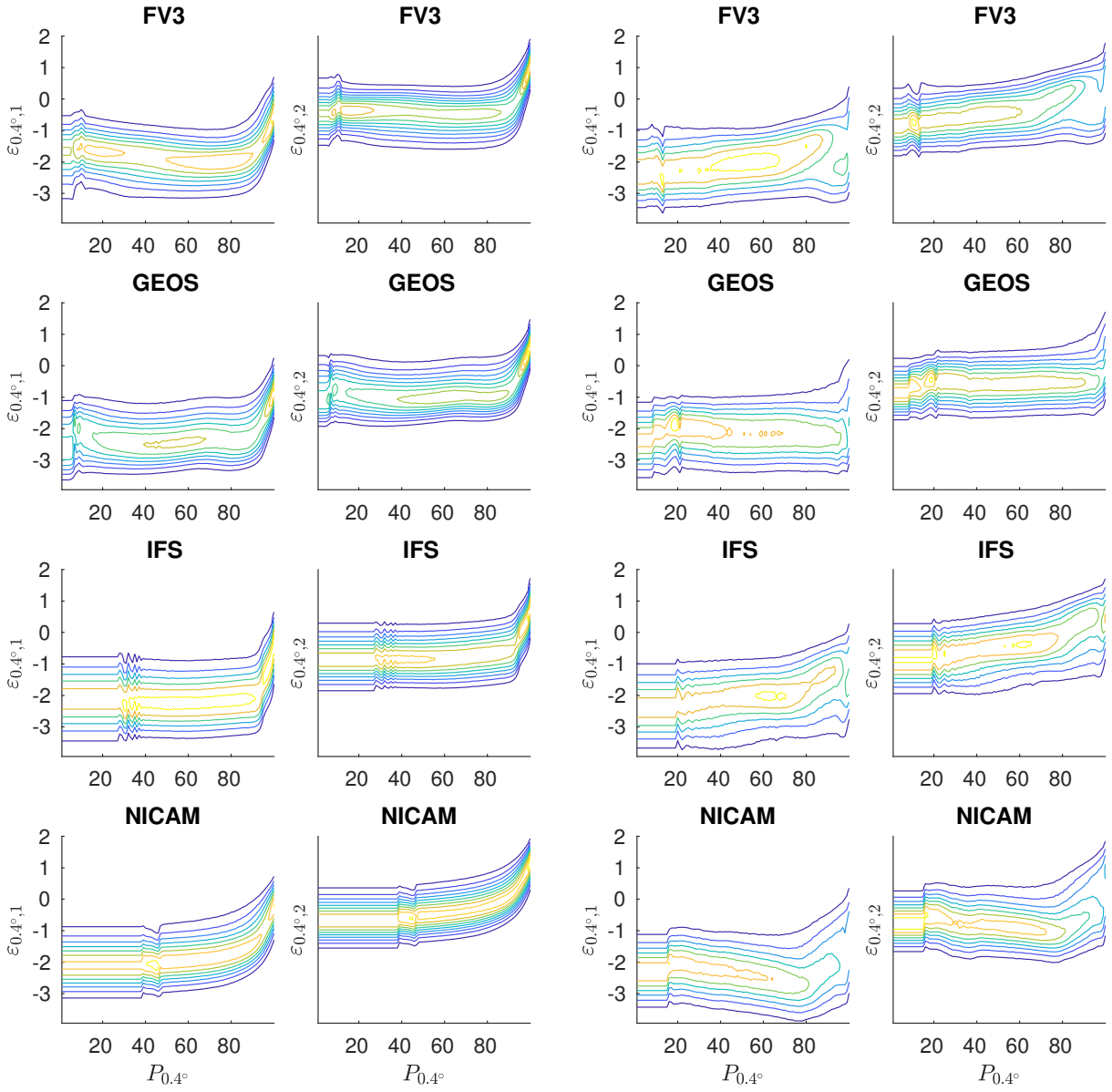

(a) $N = 0.4°$, $n = 1$ (left) and $n = 2$ (right). Warm Pool.

(b) $N = 0.4°$, $n = 1$ (left) and $n = 2$ (right). Southern Ocean.

Figure 3.12: Probability density function contours of the log 10 error processes conditioned on precipitation. Horizontal axis values are model-specific percentiles. Other models and regions are included as Figures A.45 to A.64.

2. the spread of $\varepsilon_{N,n}$ conditioned on P_N narrows with higher precipitation in the Warm Pool and the subtropical Northeast Pacific, but widens in the subarctic Northeast Pacific and the Southern Ocean (relatively weaker for $n = 2$).

Note that the contour disruptions in the low precipitation range of Figure 3.12 occur due to the existence of zero precipitation grid boxes.

The similarities of the conditional motivates the use of the same regression fit (i.e. Equation 1.15) for different models and locations, and is consistent with what was previously reported by Bessac et al. (2019). This conclusion is not substantially affected by the slight differences in conditional distributions observed in, for example, NICAM precipitation rate in the Southern Ocean (Figure 3.12) for $n = 1$, which sees a decrease in $\varepsilon_{N,n}$ distribution for intermediate quantiles of precipitation contrary to the other models that consistently increase with increased precipitation rate.

Again, of particular note is the similarity of the broad conditional distributions across models and regions, since this similarity supports the use of the same regression form for different models and regions.

3.3 Portability of the regression model

A regression fit using Equation 1.15 generates regression coefficients $A_0, \ldots, B_4$ which are specific to the realized values of the predictor-predictand set $P, F^{(R)}, F^{(T)}$ used in the regression. It is thus necessary to determine if these regression models are portable across models, geographical regions, or time periods, since an operational parameterization of $\varepsilon_{N,n}$ must be robust, in the sense that it must be able to generate accurate estimates of $\mu_{N,n}$ in any location, time period, or model configuration.

Note, however, that Equation 1.15 takes the form of a sum of a quartic function of P_N and a cubic function of $F_{N,n}^{(R)}$, which introduces the possibility of regression terms of even powers compensating for other terms of even powers, and for coefficients of odd powers similarly compensating for other odd term regression coefficients. The possibility of such compensation

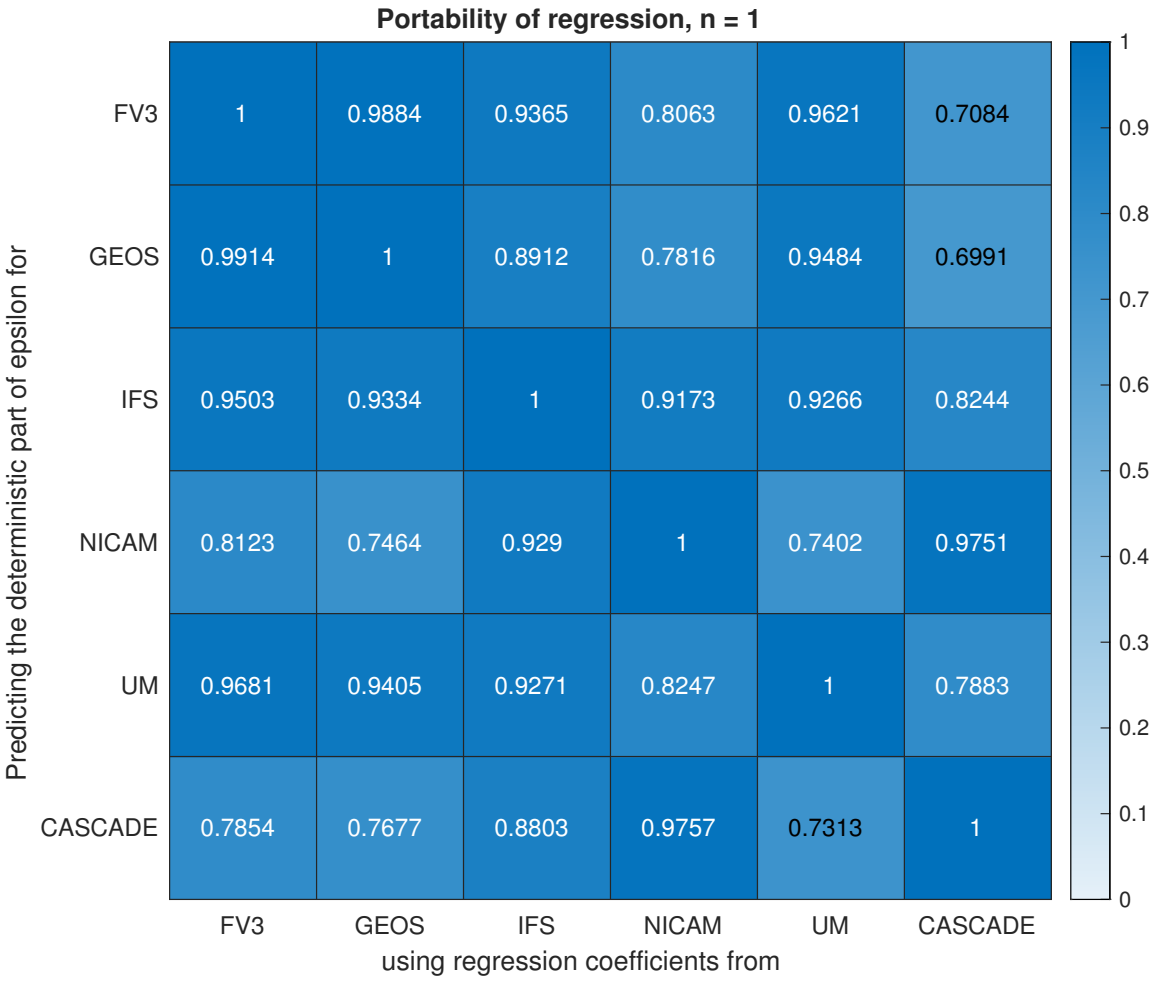

Figure 3.13: Correlation of the deterministic part of the error process for the Indo-Pacific Warm Pool. The regression fit obtained from the model in the horizontall axis is applied to the variables obtained from the model in the vertical axis, and is compared to $\mu_{0.4^\circ,1}$ obtained from the regression and variables of the model in the vertical axis. $N = 0.4^\circ$, $n = 1$.

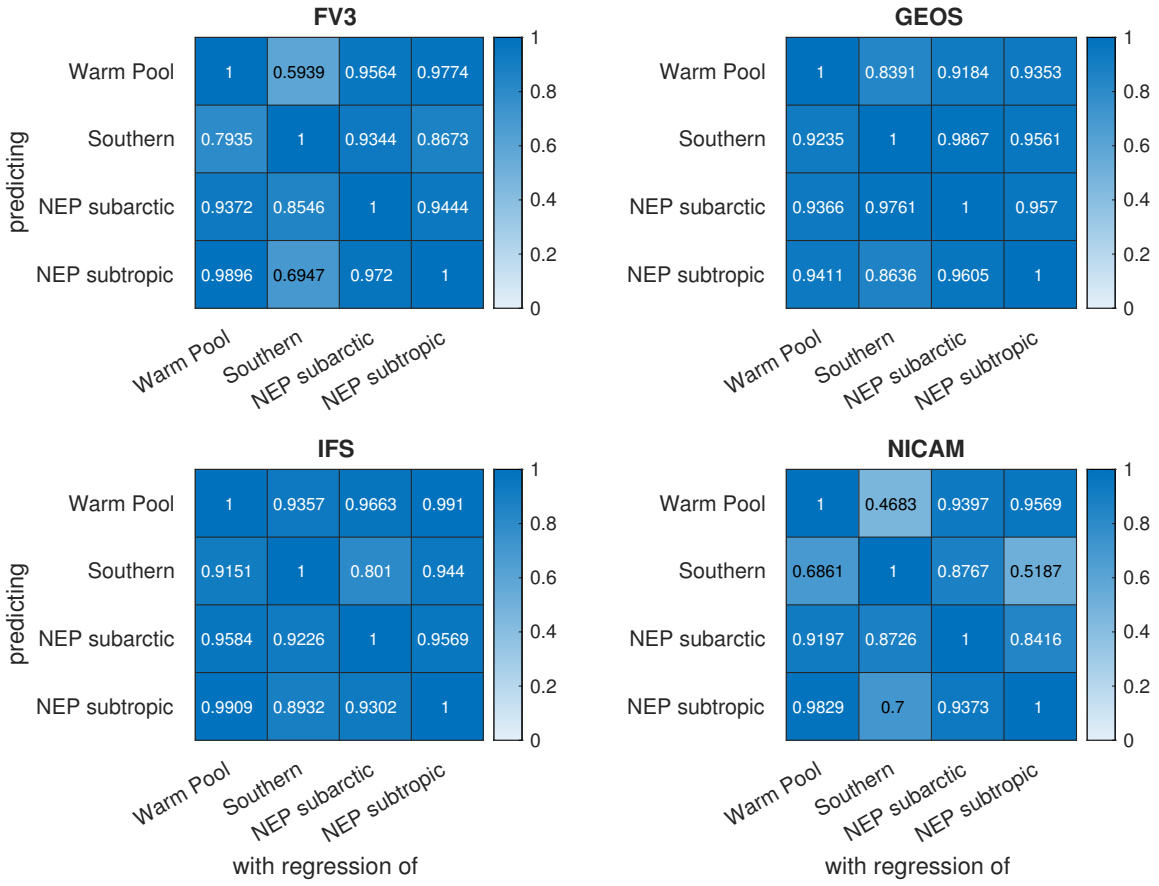

Figure 3.14: Correlation of the deterministic part of the error process for portability across geographical regions, for each global model space.The regression fit obtained from the region in the horizontal axis is applied to the variables obtained from the region in the vertical axis, and is compared to $\mu_{0.4^\circ,1}$ obtained from the regression and variables of the region in the vertical axis. $N = 0.4^\circ$, $n = 1$.

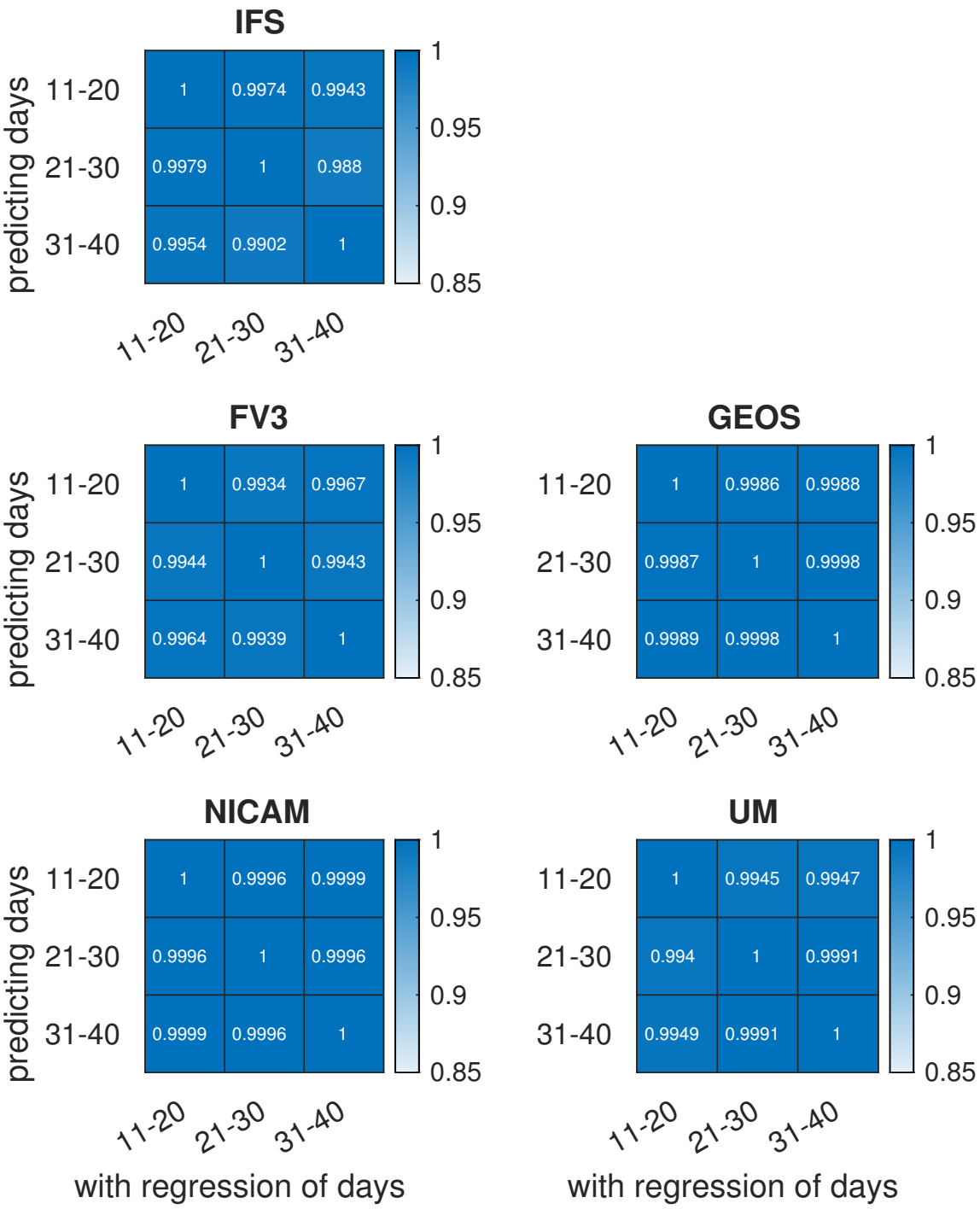

Figure 3.15: Correlation of the deterministic part of the error process for three different ten-day periods, Indo-Pacific Warm Pool. The regression fit obtained from the time period in the horizontal axis is applied to the variables obtained from the time period in the vertical axis, and is compared to $\mu_{0.4^\circ,1}$ obtained from the regression and variables of the time period in the vertical axis. $N = 0.4^\circ$, $n = 1$.

introduces the possibility to generate similar functions with substantially different regression coefficients. As such, it is not particularly meaningful to compare similarities between regression coefficients, but rather more meaningful to compare computed $\mu_{N,n}(F^{(R)}, P)$ values between different regression fits to determine if one regression fit can be used on another set of model variables to retrieve the same resultant values for $\mu_{N,n}$.

Specifically, the portability of the regression model is measured by the correlation coefficient between the deterministic part of the log 10 error process for two different models μ_1, μ_2. The quantity is expressed using the mean and standard deviations (std) of the model output as

$$\mathrm{corr}(\mu_1, \mu_2) = \frac{\mathrm{mean}((\mu_1 - \mathrm{mean}(\mu_1)) \cdot (\mu_2 - \mathrm{mean}(\mu_2)))}{\mathrm{std}(\mu_1)\ \mathrm{std}(\mu_2)} \tag{3.2}$$

where a correlation closer to unity corresponds to a greater degree of portability between the regression models. In Equation 3.2 the correlation is evaluated over all spatial and temporal points in the region. The correlation values between the deterministic part of the log 10 error process computed using output from different models, different geographical regions, and different 10-day sets of model output, are presented as Figures 3.13 to 3.15, and Figures A.121 to A.135.

A number of inferences can be made from inspection of the correlations of the regression fits. Correlations between different models (Figure 3.13) indicate the following:

1. Correlation values range between 0.70 and 0.99, indicating a high degree of portability between models, albeit imperfect and dependent on model combinations. Although the comparison to the Cascade output also involves different time periods, Figure 3.15 indicate that the sensitivity to a ten-day period is small.

2. FV3 and GEOS have the highest mutual correlations, in the 0.99 range. These models share the same dynamical core, and the same PBL parameterization. It is not surprising to find that regression fits are portable between different model versions with somewhat different parameterizations but identical dynamics.

3. NICAM and Cascade have the lowest correlation coefficients with other models (between 0.70 and 0.82, save for one exception) although their mutual correlation values are rather large (in the 0.98 range). The two share nothing substantial in common except for their lack of cumulus parameterization.

Correlations between regression models' fits over different geographical locations are reported in Figure 3.14. The majority of correlation values are relatively high, with none of the values being lower than 0.80 in two of the models (viz. IFS and GEOS) and the other two models (FV3 and NICAM) having no more than three combinations of regions with correlation values lower than 0.70. These correlations indicate a relatively high degree of portability.

Figure 3.15 presents the correlation coefficients for different time periods (August 11–20, 21–30, and August 31 – September 9). All correlation values are in the 0.99 range, indicating excellent portability, and indicate that any ten days' worth of hourly model output is sufficient to produce a regression fit for the Warm Pool domain. While correlation values are somewhat smaller for other domains, the majority exceed 0.9.

The aforementioned results combined indicates that in general the regression model of Bessac et al. (2019) is reasonably portable across different numerical models, geographic regions, and ten day temporal periods.

3.4 Covariance structures

The stochastic part of the log 10 error process $\psi_{N,n}$ is not expected to be uncorrelated white noise in space and time, but rather is expected to have structure (Bessac et al. 2019). The spatial correlation function for $\psi_{N,n}$ is expressed (for temporal domain $\mathcal{T}$ of length M)

$$\begin{aligned}&\mathrm{corr}(x, y, x', y') = \\ &\frac{1}{M}\int_{\mathcal{T}} \frac{(\psi(x,y,t) - \frac{1}{M}\int_{\mathcal{T}}\psi(x,y,t)dt)\cdot(\psi(x+x',y+y',t) - \frac{1}{M}\int_{\mathcal{T}}\psi(x+x',y+y',t)dt)}{\mathrm{std}(\psi(x,y,t))\cdot\mathrm{std}(\psi(x+x',y+y',t))}dt \\ &\qquad\qquad t\in\mathcal{T},\ x,y\in\mathcal{D},\ x+x',y+y'\in\mathcal{D}' \quad (3.3)\end{aligned}$$

for continuum x, y in domain $\mathcal{D}$, displacements x', y', and displaced domain $\mathcal{D}'$. For gridded numerical model output the expression takes the form

$$\text{corr}(x, y, p, q) = \frac{1}{M} \sum_t \frac{(\psi(x, y, t) - \frac{1}{M} \sum_t \psi(x, y, t)) \cdot (\psi(x + p, y + q, t) - \frac{1}{M} \sum_t \psi(x + p, y + q, t))}{\text{std}(\psi(x, y, t)) \cdot \text{std}(\psi(x + p, y + q, t))}$$

$$p, q \in \mathbb{Z} \quad (3.4)$$

for zonal and meridional displacements p, q (in integer units of resolved grid boxes), for the set of M time steps considered. Points (x, y) are contained within the region studied but excludes points that constitute the edge of the domain. The expression is further modified both for computational reasons and to summarize results for a domain, such that

$$\text{corr}(p, q) = \frac{1}{J} \sum_{x,y,t} \frac{(\psi(x, y, t) - \frac{1}{J} \sum_{x,y,t} \psi(x, y, t)) \cdot (\psi(x + p, y + q, t) - \frac{1}{J} \sum_{x,y,t} \psi(x + p, y + q, t))}{\text{std}(\psi(x, y, t)) \cdot \text{std}(\psi(x + p, y + q, t))}$$

$$p, q \in \mathbb{Z} \quad (3.5)$$

for a domain with J points in (x, y, t) coordinates. Note that the standard deviation in Equation 3.5 is computed over all (x, y, t) in the domain whereas in Equation 3.4 the standard deviation is computed for some (x, y) for the choice of temporal domain.

Results for the FV3, GEOS, IFS, and NICAM models, using the Warm Pool region, are presented in Figure 3.16 (n.b. correlations are averaged over all base points in the region). The spatial autocorrelation shows a zonal elongation,which means that any spatial point is correlated more to a point located to the east or west of the point, when compared with the $\psi_{N,n}$ at a point that is located the same distance north or south of the reference point. This feature is present in all geographical regions studied, although the Southern Ocean correlation plots did display noticeably larger decay scales (Figure 3.17, as well as Figures A.65 to A.84). Another notable observation is the spatial correlations for $n = 2$ consistently have larger correlation scales. This result is consistent with what is reported by Bessac et al. (2019). Another result reported by Bessac et al. (2019), viz. the increase in

decay scale with larger coarsening scale, could not be identified from the analysis of the 0.4°, 0.76° coarsening scales. This result is possibly due to the proximity of the two coarsening scales considered here, relative to the larger range 0.25°, 1°, and 2° in Bessac et al. (2019). Notwithstanding modest quantitative differences, general profiles of decay are similar across models. Furthermore, it is interesting to note that decay profiles exhibit very little zonal elongation in the extratropics when measured in physical distance rather than degrees of latitude and longitude (Figures A.85 and A.86).

The temporal autocorrelation function of the ψ field is the correlation between $\psi_{N,n}$ at some given time t and $\psi_{N,n}$ at some lag time m, and is the temporal equivalent of Equation 3.4 computed (for M elements in the time series), without assuming the statistics are stationary, via the `xcov` function in MatLab, viz.

$$\text{acf}(x, y, m) = \sum_{t=0}^{M-m-1} \left(\psi(x, y, t+m) - \frac{1}{M} \sum_{i=0}^{M-1} \psi(x, y, i) \right) \left(\psi(x, y, t) - \frac{1}{M} \sum_{i=0}^{M-1} \psi(x, y, i) \right) \quad (3.6)$$

normalized such that the acf at zero lag is unity. The results (which consider the distribution of pointwise statistics over a regional domain) presented as Figures 3.18 and A.87 to A.96 show the correlation between $\psi_{N,n}$ at some reference time and at some later time decreasing towards zero, with an evident diurnal cycle in the Warm Pool domain but absent in all other regions. No substantial differences can be observed between different N, n or among different models. The decay scale is on the order of several hours. There is no other major substantial difference between temporal autocorrelation functions for different geographical regions, other than the Southern Ocean displaying a narrower spread across different locations within the domain. This fact means that spatial points in the Southern Ocean domain experience less spatial variability in temporal autocorrelation and as such all spatial points experience similar decay in correlation between $\psi_{N,n}$ at some point in time and at some later point in time.

Both the spatial and temporal correlation functions decrease on average with spatial and temporal distance: furthermore, this feature appears across geographical domains and

across different models. Such result motivates the use of a covariance model that captures the three-dimensional decay in the correlation function. Note however that the diurnal cycle that appears in the Warm Pool region is excluded from the covariance model as the cycle only occurs in the Warm Pool region.

A Gaussian process fit is used to model the structure of the ψ field. In particular,

$$k(x, x', y, y', t, t') = \sigma \exp\left(-d(x, x', y, y', t, t')^{\gamma}\right) \tag{3.7}$$

with

$$d(x, x', y, y', t, t') = \sqrt{\left(\frac{x - x'}{\theta_x}\right)^2 + \left(\frac{y - y'}{\theta_y}\right)^2 + \left(\frac{t - t'}{\theta_t}\right)^2} \tag{3.8}$$

is used as the covariance model that defines characteristic lengths θ_x, θ_y, and θ_t, as well as variance parameter σ and shape (roughness) parameter $\gamma \in]0, 2]$. To compute these parameters, assumed to be positive and real, the `fitrgp` function in MATLAB is applied to the $\psi_{N,n}$ field subdivided into 4° blocks. Note that the nugget parameter δ included in Bessac et al. (2019) has been omitted, as was done in Bessac et al. (2021), due to the small contributions made by the term. First guess values for the Gaussian process regression theta coefficients used the zonal distance, meridional distance, and temporal lag where the correlation at the distance or lag is equal to e^{-1}. Gamma and sigma coefficients were initialized with constants 1 and 0.3 respectively. Estimates of θ_x, θ_y, and θ_t, and γ for the Warm Pool region are presented as Figure 3.19, and indicates similar values across space for the characteristic lengths of $\psi_{N,n}$ attenuation for majority of the points contained within the domain.

Despite the general similarity of values across the domain, clearly from Figure 3.19 the estimated Gaussian regression fit parameters display spatial variability. The covariance parameters may exhibit apparent spatial non-stationarity as a consequence of sampling variability even when the true fields are spatially stationary, or because of true underlying spatial heterogeneity. By computing the correlation between the Gaussian process fit parameters obtained from different numerical models, it is possible to investigate if any true spatial heterogeneity in the statistics is present, since sampling variability should not be correlated across fits for different numerical models. Conversely, the existence of correlation between

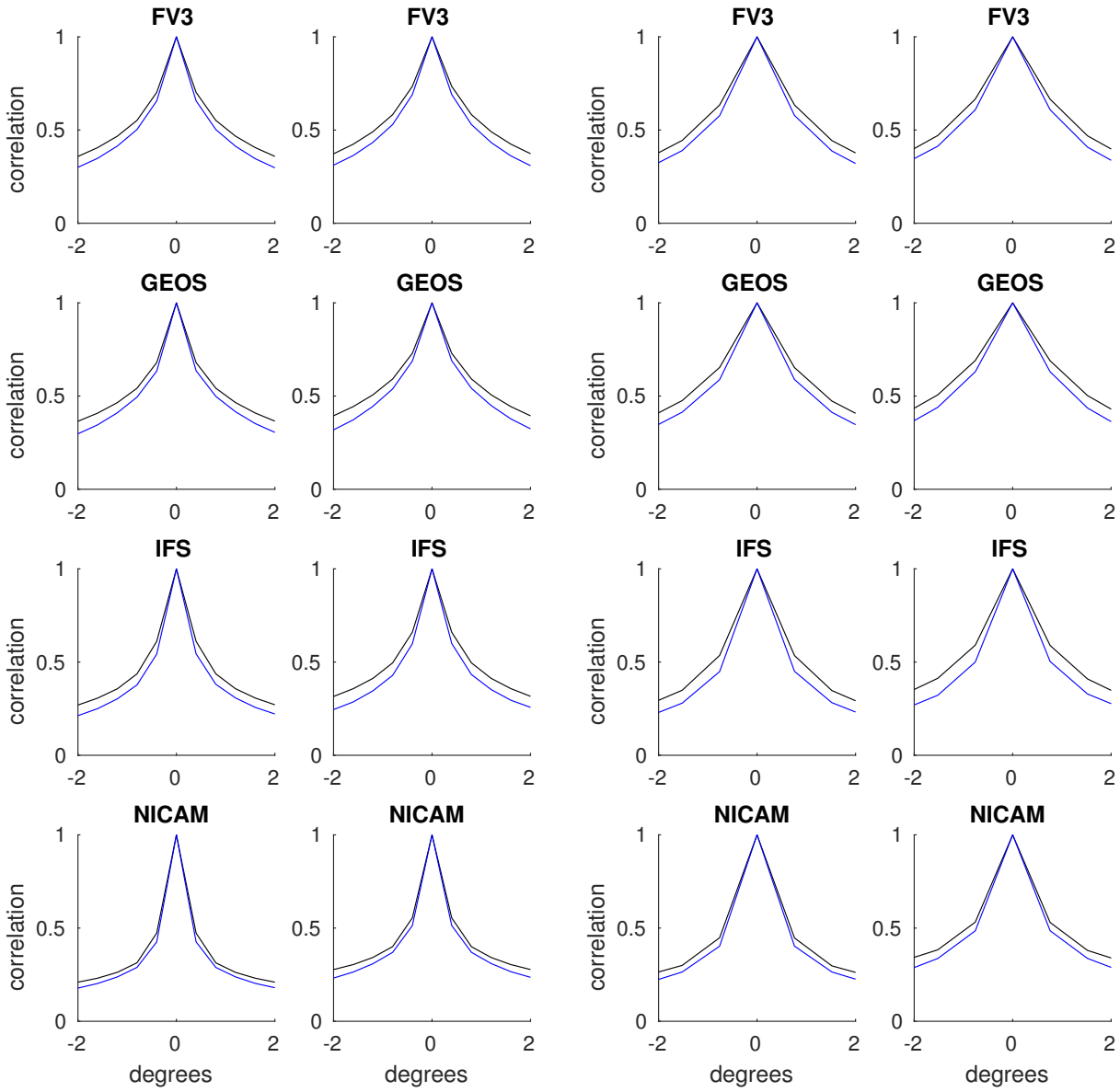

(a) $N = 0.4°$, $n = 1$ (left) and $n = 2$ (right). (b) $N = 0.76°$, $n = 1$ (left) and $n = 2$ (right).

Figure 3.16: Correlations (as per Equation 3.5 averaged over x, y, t and with fixed $p = 0$ or $q = 0$ for the meridional and zonal transects, respectively) in the zonal (black) and meridional (blue) directions for ψ fields in the Indo-Pacific Warm Pool. Corresponding plots for other models and regions included as Figures A.65 to A.84.

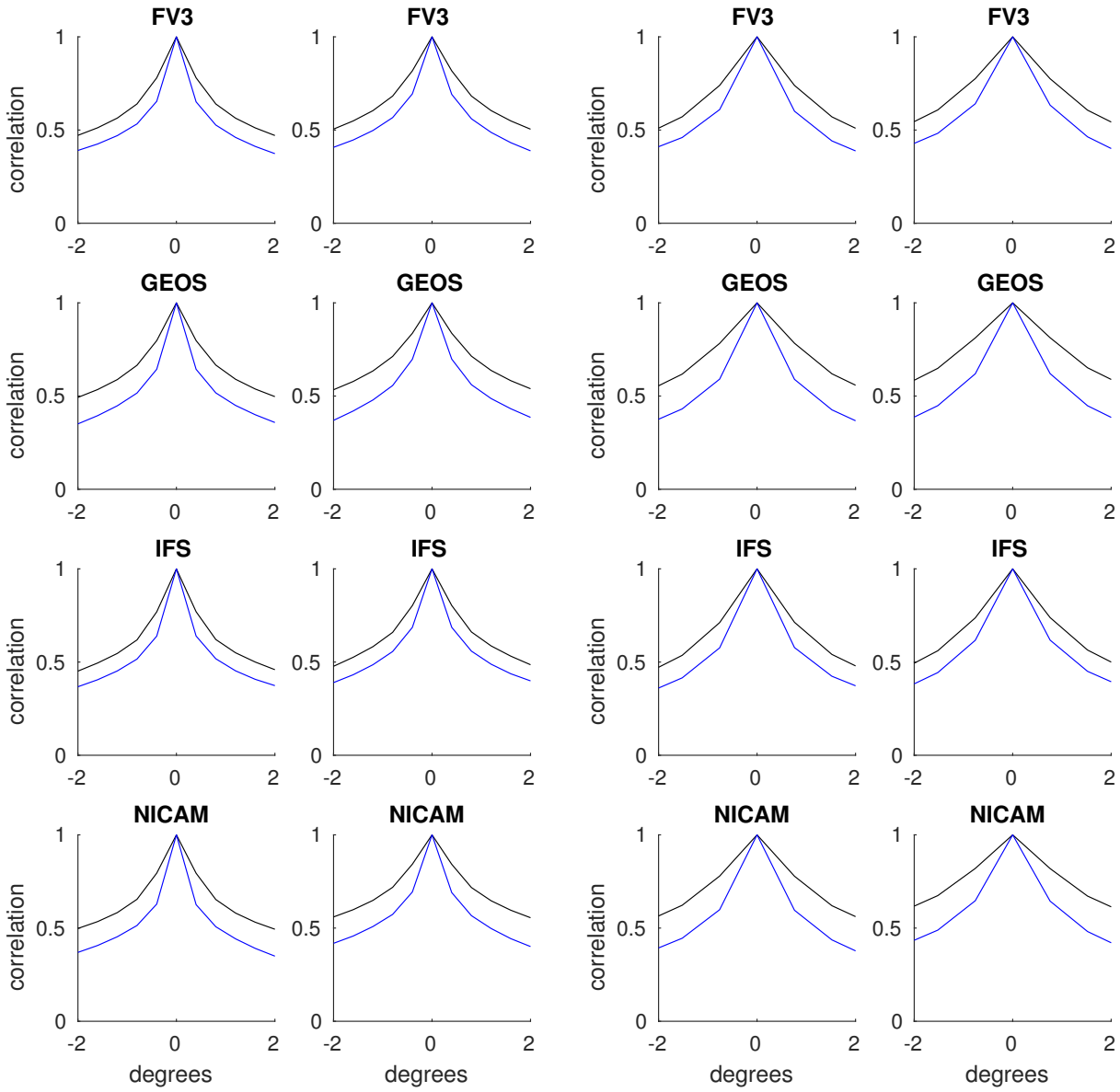

(a) $N = 0.4°$, $n = 1$ (left) and $n = 2$ (right). (b) $N = 0.76°$, $n = 1$ (left) and $n = 2$ (right).

Figure 3.17: Correlations (as per Equation 3.5 averaged over x, y, t and with fixed $p = 0$ or $q = 0$ for the meridional and zonal transects, respectively) in the zonal (black) and meridional (blue) directions for ψ fields in the Southern Ocean region. Correlation scales are larger than those observed in other geographical regions, reported as Figures A.65 to A.84.

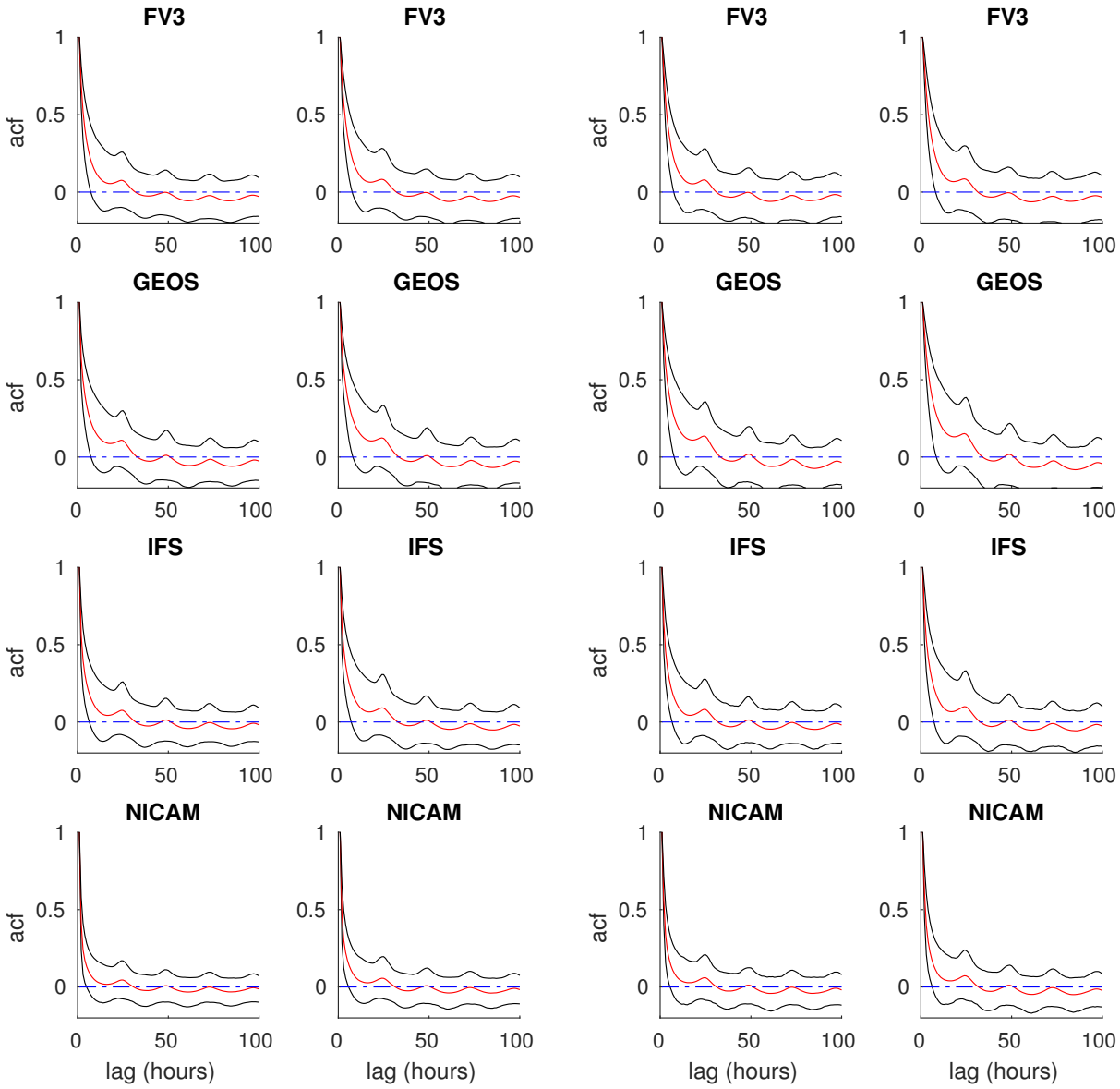

(a) $N = 0.4°$, $n = 1$ (left) and $n = 2$ (right). (b) $N = 0.76°$, $n = 1$ (left) and $n = 2$ (right).

Figure 3.18: Autocorrelation functions for some ψ fields in the Indo-Pacific Warm Pool. Corresponding plots for other models and regions included as Figures A.87 to A.96. Red indicates the median, while the black lines indicate the interdecile range (10 and 90 percentiles) for points across the domain.

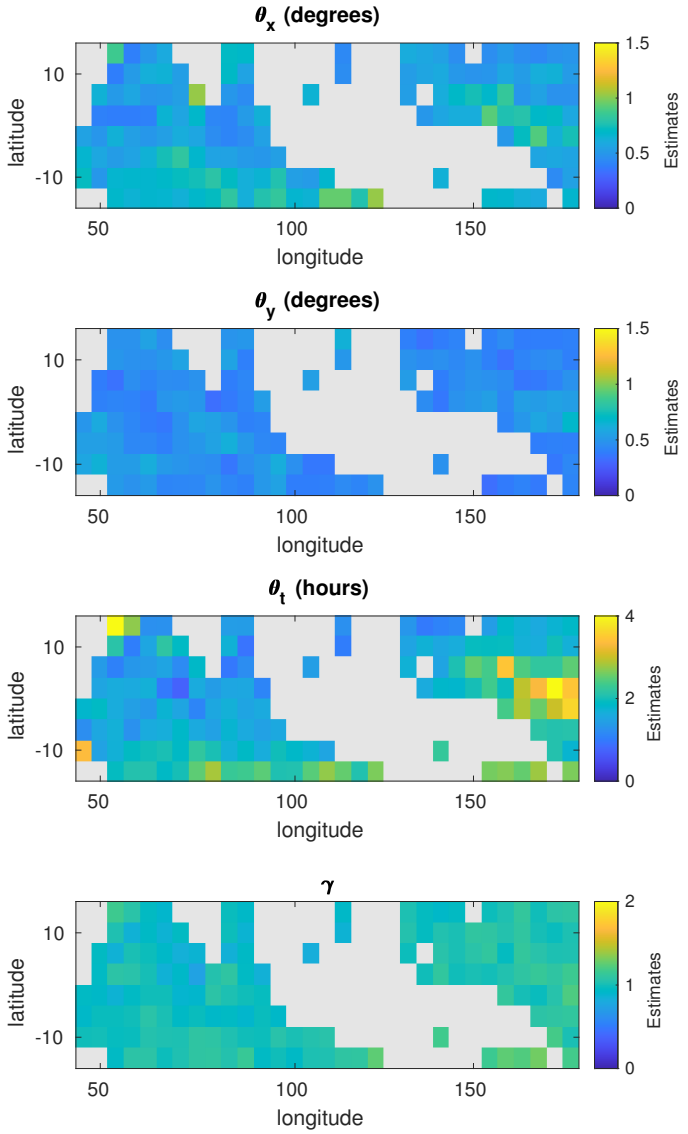

Figure 3.19: Summary fields for IFS Gaussian process regression length scales in the Indo-Pacific Warm Pool. Other models and regions presented as Figures A.97 to A.116. Vertical axis denotes latitude, whereas the horizontal axis denotes longitude. $N = 0.4°$, $n = 2$, for August 11–20.

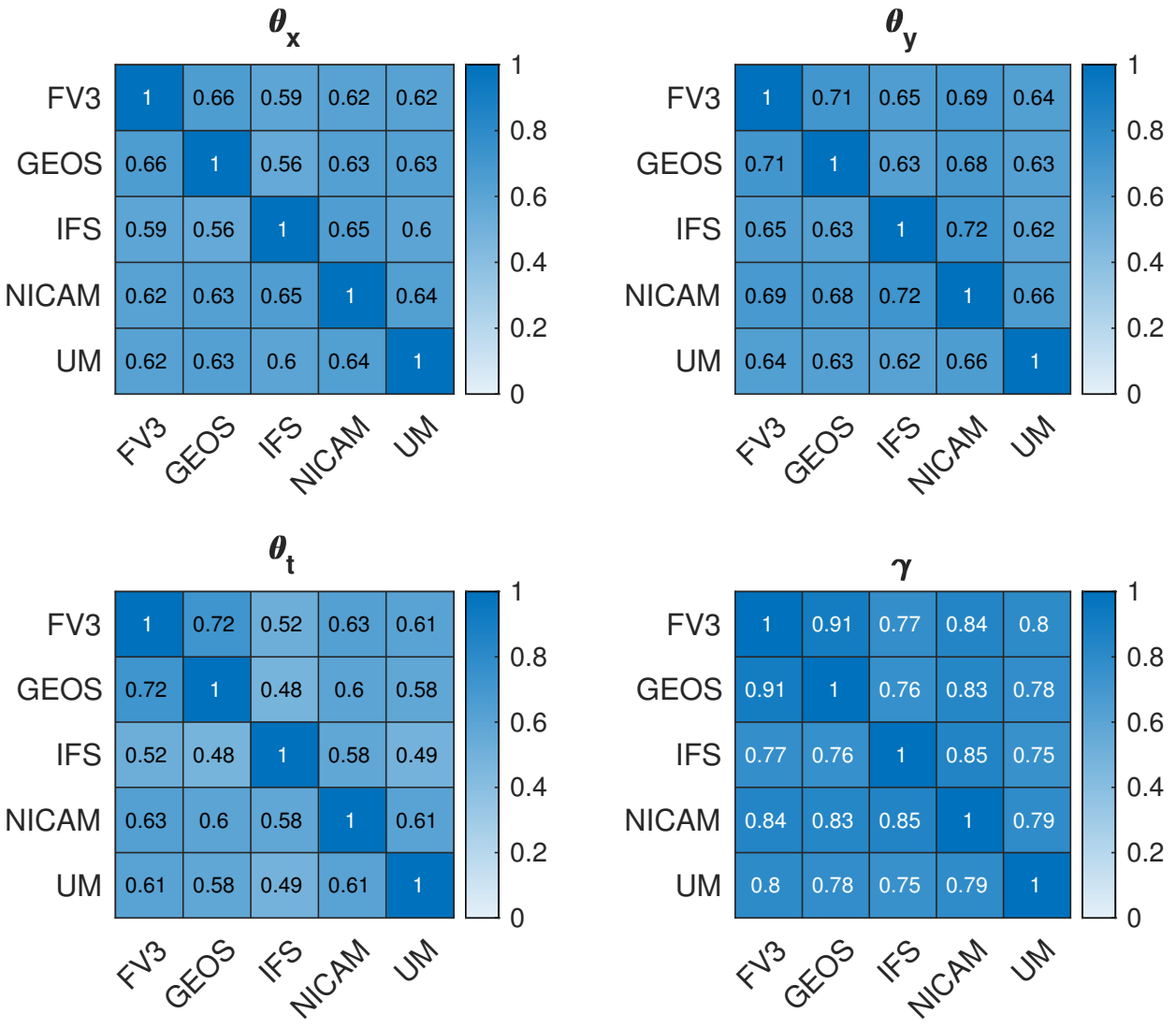

Figure 3.20: Correlations between different models for the computed Gaussian process regression variables. Results for the Indo-pacific Warm Pool are presented: other regions presented as Figures A.117 to A.120.

different models provides evidence of systematic heterogeneity that affects the Gaussian process fits independent of the model used for analysis. Results are presented as Figures 3.20 and A.117 to A.120, and indeed shows that some spatial heterogeneity of statistics is present in the Indo-pacific Warm Pool and the subarctic Northeast Pacific, but is absent in the subtropical Northeast Pacific and the Southern Ocean. Furthermore, it is interesting to note that the roughness parameter has stronger spatial heterogeneity than the decay length scales.

Chapter 4

Discussion

The implications for operational stochastic parameterizations of the results presented in the previous chapter will now be discussed. In particular:

1. The distribution of log 10 error process $\varepsilon_{N,n}$ conditioned on resolved flux $F_{N,n}^{(R)}$ and precipitation P_N is, for a given region, broadly similar across models;

2. The dependencies between resolved flux, precipitation, and the error process exhibit little sensitivity to change in 10 day time periods;

3. Although the regression model of Equation 1.15 is mostly robust across models, domains, and time, the geographical heterogeneity for the Gaussian process fits for $\psi_{N,n}$ suggest a missing predictor that should be used in order to ensure $\psi_{N,n}$ is independent of the resolved state; and

4. The regression model (Equation 1.15) is found to be least portable between models dissimilar in both physics and dynamics.

Implications of these results, as well as possible directions for future research in stochastic parameterization of surface flux enhancements, will be discussed before summarizing the methods, results, and discussion in a concluding section.

4.1 Implications

This study considered a regression analysis which used resolved flux and precipitation to represent the deterministic part of the log 10 error process $\varepsilon_{N,n}$ measuring the difference between true and resolved sea surface fluxes before studying the covariance structure of the stochastic residual $\psi_{N,n}$. A Gaussian process was then fit to $\psi_{N,n}$, in order to model the spatial and temporal correlation structures present in the $\psi_{N,n}$ field. The results obtained from a set of different atmospheric models and geographical regions have several important implications.

First, the statistical dependence between resolved flux and precipitation is comparable both between different models and between different regions. Notwithstanding modest differences between different models in dependence structure and large differences in marginal distributions, the general relationship between the mutual information densities of different regimes of resolved flux and precipitation remains comparable, and similarly modest differences between geographical regions do not substantially change this conclusion. The lack of linear dependence between resolved flux and precipitation, presented in the mutual information densities of Figures A.27 to A.32 supports the form of the regression fit Equation 1.15 using resolved flux and precipitation as separate predictors. The consistency of this relationship is noteworthy, especially because the marginal densities of both resolved flux and precipitation deviate substantially from each other as a consequence of model differences (dynamical core and parameterizations), background climatology (for geographical regions) and internal variability (from specific weather realizations in each numerical model).

Evidence of the portability of the regression model is further provided by the study of correlation between the deterministic parts of the log 10 error process $\mu_{N,n}$, for different models, regions, and time periods. It was found that, with few exceptions, regression coefficients from one set of model output can be used to reliably compute $\mu_{N,n}$ in a different set of model output. This result again supports the portability of the regression fit, and consequently points to a relatively straightforward implementation of the sea surface flux enhancement scheme for operational numerical models.

The random spatiotemporal field $\psi_{N,n}$ has similar but not identical statistical features across different models and regions, to wit: the spatial correlation structure for $\psi_{N,n}$ is similar across models and regions such that the zonal correlation is longer than the meridional correlation, but the decay scale varies somewhat across models and regions; and similarly for temporal autocorrelation all models and regions attenuate with comparable time scales but only the Warm Pool region displays a diurnal cycle (suggestive of a missing predictor for the regression model).

If the random spatiotemporal field $\psi_{N,n}$ truly has spatially homogeneous statistics, the spatial variations in the obtained Gaussian process fits will be due to sampling variability. However, it was determined that in the Indo-Pacific Warm Pool and the subarctic Northeast Pacific, spatial variations in Gaussian process fits between different models were correlated and thus, there exists some spatial structure not caused by sampling variability. This fact may indicate the need for another predictor unaccounted for by the current regression fit, or the need for an alternative form of the regression fit. Investigation of a potential predictor is necessary to ensure the deterministic part of the parameterization captures all of the dependence of $\varepsilon_{N,n}$ on resolved variables. Such change to the regression, be it by the addition of a predictor or the use of a different parametric form of the regression fit, will change the spatial and temporal structure of the residual field $\psi_{N,n}$.

Despite the highest portability being present between two models that share dynamical cores, different models with different dynamical cores appeared to have high correlation coefficients as well. Conversely, the exception to the high degree of portability was NICAM, which differs the most from the other models by virtue of not parameterizing several processes parameterized in the other numerical models. Furthermore, the correlation coefficients between NICAM and Cascade, another experiment that forced most of its cumulus convection to be explicit, was notably high. As such, the degree of parameterization of cumulus convection may be a contributing factor to model sensitivity of the regression fit. This interpretation is consistent with the fact that the statistical fit utilizes precipitation as an input

variable, and this quantity is expected to be influenced by the cumulus parameterization of a given numerical model.

4.2 Future extensions

This study investigated the robustness of the statistical model of Bessac et al. (2019) to find the missing part of wind dependent sea surface flux, however various questions have emerged and remain unanswered. It is thus productive to consider what questions must be prioritized in future research to practically introduce stochastic sea surface flux enhancements into operational weather and climate models.

The use of a combination of polynomial fits may not be the best statistical model for capturing the dependence of $\varepsilon_{N,n}$ on $F_{N,n}^{(R)}$ and P_N space. As such, the investigation of different forms of the statistical model, as well as investigation into other predictors for the regression fit, may improve the statistical model. The use of DYAMOND output may be beneficial for this purpose, due to the large number of variables reported by participating models.

Controlled experiments may also be beneficial to identifying better statistical fits and advancing our understanding of the sea surface flux enhancement as a process. Use of a finer scale model can determine at which point unresolved flow cease to contribute meaningfully to the surface fluxes. Use of a single-column model may allow for controlled experiments to identify factors that influence the sea surface flux enhancement and as such must be accounted for in the general form of parameterization. An improved form of parameterization is anticipated to benefit representations of the sea surface flux enhancements.

A major limitation of the approach considered in this study is the need to specify a parametric form of the regression fit. One possibility to avoid the need for a specified parametric form of the regression fit would be the use of machine learning techniques to effectively and efficiently capture features that may be beneficial to the parameterization of the sea surface flux enhancement. Generative adversarial networks (GANs), for example, may be utilized in

this direction (Gagne et al. 2020). In particular, the ability to draw realizations from high dimensional distributions without explicit expressions for the probability distribution should allow for investigation of a better functional form of the regression fit, without the need to specify its form explicitly.

Finally, it is important to note that surface flux parameterization is not an issue only for the sea surface. As such, an equivalent study should be conducted on the land surface as well. The number of additional parameters that may be involved in such parameterization, however, can be expected to make such study nontrivial due to additional factors such as topography.

4.3 Conclusion

The present study utilized high-resolution global atmospheric model output from the DYAMOND initiative to investigate the stochastic nature of sea surface flux underestimation due to sub-grid scale wind variations, expanding on the works by Bessac et al. (2019, 2021). In particular, the high resolution vector wind field was coarsened to obtain a wind vector field approximating that in a operational global atmospheric model, and the difference between the sea-surface wind dependent part of the sea surface flux in high resolution and coarse resolution wind fields were studied to determine how the 'true' flux from the higher resolution model field can be represented using the 'resolved' coarse scale field.

The resolved surface flux and the resolved scale precipitation were used as variables for a polynomial fit to compute the deterministic part of the flux enhancement. Evaluation of the conditional probability densities of the flux enhancement, or the error process, revealed that there was a broadly similar and consistent behaviour of the log 10 error process in all models and all regions studied, suggesting the existence of common deterministic and stochastic parts of the enhancement, despite the minor quantitative differences in the statistics of the random spatiotemporal field observed between different models and regions. A Gaussian process fit of this stochastic remnant was also found to be comparable across models and

regions, providing evidence of the robustness of the form of both the regression fit and the Gaussian process fit, suggesting for the application of the methods in a robust manner across all oceans on the globe without major region specific or model specific features. A robust spatial heterogeneity in the statistics of the Gaussian process fit was found to be present in the Indo-Pacific Warm Pool and the subarctic Northeast Pacific. This fact suggests potential improvement of the regression fit by the use of additional predictors or by use of a different form of statistical model.

Bibliography

Alexander, M., & Dunkerton, T. (1999). A spectral parameterization of mean-flow forcing due to breaking gravity waves. *Journal of the Atmospheric Sciences*, *56*(24), 4167–4182.

Arakawa, A. (2004). The cumulus parameterization problem: Past, present, and future. *Journal of Climate*, *17*(13), 2493–2525.

Arakawa, A., & Schubert, W. H. (1974). Interaction of a cumulus cloud ensemble with the large-scale environment, Part I. *Journal of Atmospheric Sciences*, *31*(3), 674–701.

Atamanchuk, D., Koelling, J., Send, U., & Wallace, D. (2020). Rapid transfer of oxygen to the deep ocean mediated by bubbles. *Nature Geoscience*, *13*(3), 232–237.

Bacmeister, J., Suarez, M. J., & Robertson, F. R. (2006). Rain reevaporation, boundary layer–convection interactions, and Pacific rainfall patterns in an AGCM. *Journal of the Atmospheric Sciences*, *63*(12), 3383–3403.

Becktold, P. (2019). *Atmospheric moist convection*. European Centre for Medium-Range Weather Forecasts.

Beljaars, A. C. (1995). The parametrization of surface fluxes in large-scale models under free convection. *Quarterly Journal of the Royal Meteorological Society*, *121*(522), 255–270.

Berner, J., Achatz, U., Batté, L., Bengtsson, L., de la Cámara, A., Christensen, H. M., Colangeli, M., Coleman, D. R., Crommelin, D., Dolaptchiev, S. I., Franzke, C. L. E., Friederichs, P., Imkeller, P., Järvinen, H., Juricke, S., Kitsios, V., Lott, F., Lucarini, V., Mahajan, S., … Yano, J.-I. (2017). Stochastic parameterization: Toward a new

view of weather and climate models. *Bulletin of the American Meteorological Society*, *98*(3), 565–588.

Bessac, J., Christensen, H. M., Endo, K., Monahan, A. H., & Weitzel, N. (2021). Scale-aware space-time stochastic parameterization of subgrid-scale velocity enhancement of sea surface fluxes. *Journal of Advances in Modeling Earth Systems*, *13*(4), e2020MS002367.

Bessac, J., Monahan, A. H., Christensen, H. M., & Weitzel, N. (2019). Stochastic parameterization of subgrid-scale velocity enhancement of sea surface fluxes. *Monthly Weather Review*, *147*(5), 1447–1469.

Blein, S., Roehrig, R., Voldoire, A., & Faure, G. (2020). Meso-scale contribution to air–sea turbulent fluxes at GCM scale. *Quarterly Journal of the Royal Meteorological Society*, *146*(730), 2466–2495.

Bushell, A. C., Butchart, N., Derbyshire, S. H., Jackson, D. R., Shutts, G. J., Vosper, S. B., & Webster, S. (2015). Parameterized gravity wave momentum fluxes from sources related to convection and large-scale precipitation processes in a global atmosphere model. *Journal of the Atmospheric Sciences*, *72*(11), 4349–4371.

Centre of Excellence in Simulation of Weather and Climate in Europe. (n.d.). *FV3 – ESiWACE*. Deutsches Klimarechenzentrum GmbH. https://www.esiwace.eu/services/dyamond-initiative/dyamond-specific-pages-and-material/fv3

Charlton-Perez, A. J., Baldwin, M. P., Birner, T., Black, R. X., Butler, A. H., Calvo, N., Davis, N. A., Gerber, E. P., Gillett, N., Hardiman, S., Kim, J., Krüger, K., Lee, Y.-Y., Manzini, E., McDaniel, B. A., Polvani, L., Reichler, T., Shaw, T. A., Sigmond, M., ... Watanabe, S. (2013). On the lack of stratospheric dynamical variability in low-top versions of the CMIP5 models. *Journal of Geophysical Research: Atmospheres*, *118*(6), 2494–2505.

Chen, J., & Stein, M. L. (2021). Linear-cost covariance functions for Gaussian random fields. *Journal of the American Statistical Association*, 1–18.

Chen, T., Rossow, W. B., & Zhang, Y. (2000). Radiative effects of cloud-type variations. *Journal of Climate*, *13*(1), 264–286.

Chikira, M., & Sugiyama, M. (2010). A cumulus parameterization with state-dependent entrainment rate. Part I: Description and sensitivity to temperature and humidity profiles. *Journal of Atmospheric Sciences*, *67*(7), 2171–2193.

de Grandpré, J., Tanguay, M., Qaddouri, A., Zerroukat, M., & McLinden, C. A. (2016). Semi-Lagrangian advection of stratospheric ozone on a Yin–Yang grid system. *Monthly Weather Review*, *144*(3), 1035–1050.

Deardorff, D. W. (1970). Preliminary results from numerical integrations of the unstable planetary boundary layer. *Journal of the Atmospheric Sciences*, *27*(8), 1209–1211.

European Centre for Medium-Range Weather Forecasts. (2020a). *IFS Documentation CY47R1 Part III: Dynamics and numerical procedures*. European Centre for Medium-Range Weather Forecasts. Reading, England.

European Centre for Medium-Range Weather Forecasts. (2020b). *IFS Documentation CY47R1 Part IV: Physical processes*. European Centre for Medium-Range Weather Forecasts. Reading, England.

Fagan, K. E., & Mackenzie, F. T. (2007). Air–sea CO2 exchange in a subtropical estuarine-coral reef system, Kaneohe Bay, Oahu, Hawaii. *Marine Chemistry*, *106*(1-2), 174–191.

Franco, A. C., Ianson, D., Ross, T., Hamme, R. C., Monahan, A. H., Christian, J. R., Davelaar, M., Johnson, W. K., Miller, L. A., Robert, M., & Tortell, P. D. (2021). Anthropogenic and climatic contributions to observed carbon system trends in the Northeast Pacific. *Global Biogeochemical Cycles*, *35*(7), e2020GB006829.

Fritts, D., & Alexander, M. (2003). Gravity wave dynamics and effects in the middle atmosphere. *Reviews of Geophysics*, *41*(1).

Fritts, D., & VanZandt, T. E. (1993). Spectral estimates of gravity wave energy and momentum fluxes. Part I: Energy dissipation, acceleration, and constraints. *Journal of Atmospheric Sciences*, *50*(22), 3685–3694.

Gagne, D. J., Christensen, H. M., Subramanian, A. C., & Monahan, A. H. (2020). Machine learning for stochastic parameterization: Generative adversarial networks in the Lorenz '96 model. *Journal of Advances in Modeling Earth Systems*, *12*(3), e2019MS001896.

Garcia, R. R., & Boville, B. A. (1994). "Downward control" of the mean meridional circulation and temperature distribution of the polar winter stratosphere. *Journal of Atmospheric Sciences*, *51*(15), 2238–2245.

Garner, S. T. (2005). A topographic drag closure built on an analytical base flux. *Journal of Atmospheric Sciences*, *62*(7), 2302–2315.

Goddijn-Murphy, L., Woolf, D. K., & Callaghan, A. H. (2011). Parameterizations and algorithms for oceanic whitecap coverage. *Journal of Physical Oceanography*, *41*(4), 742–756.

Godfrey, J., & Beljaars, A. (1991). On the turbulent fluxes of buoyancy, heat and moisture at the air-sea interface at low wind speeds. *Journal of Geophysical Research: Oceans*, *96*(C12), 22043–22048.

Grabowski, W. W. (1998). Toward cloud resolving modeling of large-scale tropical circulations: A simple cloud microphysics parameterization. *Journal of the Atmospheric Sciences*, *55*(21), 3283–3298.

Guichard, F., & Couvreux, F. (2017). A short review of numerical cloud-resolving models. *Tellus A: Dynamic Meteorology and Oceanography*, *69*(1), 1373578.

Harris, L., Chen, X., Zhou, L., & Chen, J.-H. (2020). *The nonhydrostatic solver of the GFDL Finite-Volume Cubed-Sphere dynamical core*. National Oceanic and Atmospheric Administration, Geophysical Fluids Dynamics Laboratory.

Heymsfield, A. J., & Miloshevich, L. M. (1991). Limit to greenhouse warming? *Nature*, *351*(6321), 14–15.

Holloway, C., Woolnough, S., & Lister, G. (2012). Precipitation distributions for explicit versus parametrized convection in a large-domain high-resolution tropical case study. *Quarterly Journal of the Royal Meteorological Society*, *138*(668), 1692–1708.

Jabouille, P., Redelsperger, J., & Lafore, J. (1996). Modification of surface fluxes by atmospheric convection in the TOGA COARE region. *Monthly Weather Review*, *124*(5), 816–837.

Jensen, E., Kinne, S., & Toon, O. (1994). Tropical cirrus cloud radiative forcing: Sensitivity studies. *Geophysical Research Letters*, *21*(18), 2023–2026.

Jones, P. W. (1998). *A user's guide for SCRIP: A Spherical Coordinate Remapping and Interpolation Package*. Los Alamos National Laboratory. Los Alamos, NM.

Jones, P. W. (1999). First-and second-order conservative remapping schemes for grids in spherical coordinates. *Monthly Weather Review*, *127*(9), 2204–2210.

Kihm, C., & Körtzinger, A. (2010). Air-sea gas transfer velocity for oxygen derived from float data. *Journal of Geophysical Research: Oceans*, *115*(C12).

Lean, H. W., Clark, P. A., Dixon, M., Roberts, N. M., Fitch, A., Forbes, R., & Halliwell, C. (2008). Characteristics of high-resolution versions of the Met Office Unified Model for forecasting convection over the United Kingdom. *Monthly Weather Review*, *136*(9), 3408–3424.

Lin, S.-J. (2004). A "vertically Lagrangian" finite-volume dynamical core for global models. *Monthly Weather Review*, *132*(10), 2293–2307.

Lin, S.-J., & Rood, R. B. (1996). Multidimensional flux-form semi-Lagrangian transport schemes. *Monthly Weather Review*, *124*(9), 2046–2070.

Lin, S.-J., & Rood, R. B. (1997). An explicit flux-form semi-Lagrangian shallow-water model on the sphere. *Quarterly Journal of the Royal Meteorological Society*, *123*(544), 2477–2498.

Lindzen, R. S. (1981). Turbulence and stress owing to gravity wave and tidal breakdown. *Journal of Geophysical Research: Oceans*, *86*(C10), 9707–9714.

Lister, G., & Woolnough, S. (2008). *Cascade - Scale interactions in the tropical atmosphere model runs. NCAS British Atmospheric Data Centre*. https://catalogue.ceda.ac.uk/uuid/20981e3052a66ca71c2ba92b94760150

Lock, A., Brown, A., Bush, M., Martin, G., & Smith, R. (2000). A new boundary layer mixing scheme. Part I: Scheme description and single-column model tests. *Monthly Weather Review*, *128*(9), 3187–3199.

Lott, F., & Miller, M. J. (1997). A new subgrid-scale orographic drag parametrization: Its formulation and testing. *Quarterly Journal of the Royal Meteorological Society*, *123*(537), 101–127.

Love, B. S., Matthews, A. J., & Lister, G. M. (2011). The diurnal cycle of precipitation over the maritime continent in a high-resolution atmospheric model. *Quarterly Journal of the Royal Meteorological Society*, *137*(657), 934–947.

Mahrt, L., Belušić, D., & Acevedo, O. (2021). Small-scale spatial variation of the nocturnal wind field. *Boundary-Layer Meteorology*, *180*(2), 225–245.

Mahrt, L., & Sun, J. (1995). The subgrid velocity scale in the bulk aerodynamic relationship for spatially averaged scalar fluxes. *Monthly Weather Review*, *123*(10), 3032–3041.

Malardel, S., Wedi, N., Deconinck, W., Diamantakis, M., Kühnlein, C., Mozdzynski, G., Hamrud, M., & Smolarkiewicz, P. (2016). A new grid for the IFS. *ECMWF Newsletter*, *146*(321), 23–28.

Martin, G., Ringer, M., Pope, V., Jones, A., Dearden, C., & Hinton, T. (2006). The physical properties of the atmosphere in the new Hadley Centre Global Environmental Model (HadGEM1). Part I: Model description and global climatology. *Journal of Climate*, *19*(7), 1274–1301.

McFarlane, N. (1987). The effect of orographically excited gravity wave drag on the general circulation of the lower stratosphere and troposphere. *Journal of Atmospheric Sciences*, *44*(14), 1775–1800.

Miller, M. J., Beljaars, A. C. M., & Palmer, T. N. (1992). The sensitivity of the ECMWF model to the parameterization of evaporation from the tropical oceans. *Journal of Climate*, *5*(5), 418–434.

Mo, R., Brugman, M. M., Milbrandt, J. A., Goosen, J., Geng, Q., Emond, C., Bau, J., & Erfani, A. (2019). Impacts of hydrometeor drift on orographic precipitation: Two case

studies of landfalling atmospheric rivers in British Columbia, Canada. *Weather and Forecasting*, *34*(5), 1211–1237.

Molod, A. (2012). Constraints on the profiles of total water PDF in AGCMs from AIRS and a high-resolution model. *Journal of Climate*, *25*(23), 8341–8352.

Molod, A., Takacs, L., Suarez, M., & Bacmeister, J. (2015). Development of the GEOS-5 atmospheric general circulation model: Evolution from MERRA to MERRA2. *Geoscientific Model Development*, *8*(5), 1339–1356.

Monahan, E. C., & Muircheartaigh, I. (1980). Optimal power-law description of oceanic whitecap coverage dependence on wind speed. *Journal of Physical Oceanography*, *10*(12), 2094–2099.

Moorthi, S., & Suarez, M. J. (1992). Relaxed Arakawa-Schubert. A parameterization of moist convection for general circulation models. *Monthly Weather Review*, *120*(6), 978–1002.

Müller, S. K., Manzini, E., Giorgetta, M., Sato, K., & Nasuno, T. (2018). Convectively generated gravity waves in high resolution models of tropical dynamics. *Journal of Advances in Modeling Earth Systems*, *10*(10), 2564–2588.

Nasuno, T. (2021). Impacts of cloud microphysics modifications on diurnal convection and the ISO over the Maritime Continent: A case study of YMC-Sumatra 2017. *SOLA*, *17*, 16–23.

Noda, A. T., Satoh, M., Yamada, Y., Kodama, C., Miyakawa, T., & Seiki, T. (2015). Cold and warm rain simulated using a global nonhydrostatic model without cumulus parameterization, and their responses to global warming. *Journal of the Meteorological Society of Japan. Ser. II*, *93*(2), 181–197.

Palmer, T. N., Buizza, R., Doblas-Reyes, F., Jung, T., Leutbecher, M., Shutts, G. J., Steinheimer, M., & Weisheimer, A. (2009). *Stochastic parametrization and model uncertainty*. European Centre for Medium-Range Weather Forecasts. Reading, England.

Pruppacher, H. R., & Klett, J. D. (2010). *Microphysics of clouds and precipitation*. Springer Science + Business Media.

Putman, W. M., & Lin, S.-J. (2007). Finite-volume transport on various cubed-sphere grids. *Journal of Computational Physics*, *227*(1), 55–78.

Putman, W. M., & Suarez, M. (2011). Cloud-system resolving simulations with the NASA Goddard Earth Observing System global atmospheric model (GEOS-5). *Geophysical Research Letters*, *38*(16), L16809.

Räisänen, P., Barker, H. W., Khairoutdinov, M. F., Li, J., & Randall, D. A. (2004). Stochastic generation of subgrid-scale cloudy columns for large-scale models. *Quarterly Journal of the Royal Meteorological Society*, *130*(601), 2047–2067.

Randall, D., Khairoutdinov, M., Arakawa, A., & Grabowski, W. (2003). Breaking the cloud parameterization deadlock. *Bulletin of the American Meteorological Society*, *84*(11), 1547–1564.

Rasmussen, C. E., & Williams, C. K. I. (2006). *Gaussian processes for machine learning*. MIT Press.

Redelsperger, J.-L., Guichard, F., & Mondon, S. (2000). A parameterization of mesoscale enhancement of surface fluxes for large-scale models. *Journal of Climate*, *13*(2), 402–421.

Rees, A. P., Owens, N. J. P., & Upstill-Goddard, R. C. (1997). Nitrous oxide in the Bellingshausen Sea and Drake Passage. *Journal of Geophysical Research: Oceans*, *102*(C2), 3383–3391.

Rosenthal, S. L. (1978). Numerical simulation of tropical cyclone development with latent heat release by the resolvable scales I: Model description and preliminary results. *Journal of Atmospheric Sciences*, *35*(2), 258–271.

Rotstayn, L. D., Ryan, B. F., & Katzfey, J. J. (2000). A scheme for calculation of the liquid fraction in mixed-phase stratiform clouds in large-scale models. *Monthly Weather Review*, *128*(4), 1070–1088.

Sadourny, R. (1972). Conservative finite-difference approximations of the primitive equations on quasi-uniform spherical grids. *Monthly Weather Review*, *100*(2), 136–144.

Satoh, M., Matsuno, T., Tomita, H., Miura, H., Nasuno, T., & Iga, S.-i. (2008). Nonhydrostatic icosahedral atmospheric model (NICAM) for global cloud resolving simulations. *Journal of Computational Physics*, *227*(7), 3486–3514.

Satoh, M., Noda, A. T., Seiki, T., Chen, Y.-W., Kodama, C., Yamada, Y., Kuba, N., & Sato, Y. (2018). Toward reduction of the uncertainties in climate sensitivity due to cloud processes using a global non-hydrostatic atmospheric model. *Progress in Earth and Planetary Science*, *5*(67).

Satoh, M., Stevens, B., Judt, F., Khairoutdinov, M., Lin, S.-J., Putman, W. M., & Düben, P. (2019). Global cloud-resolving models. *Current Climate Change Reports*, *5*(3), 172–184.

Satoh, M., Tomita, H., Yashiro, H., Miura, H., Kodama, C., Seiki, T., Noda, A. T., Yamada, Y., Goto, D., Sawada, M., Miyoshi, T., Niwa, Y., Hara, M., Ohno, T., Iga, S.-i., Arakawa, T., Inoue, T., & Kubokawa, H. (2014). The Non-hydrostatic ICosahedral Atmospheric Model: Description and development. *Progress in Earth and Planetary Science*, *1*(18).

Scaife, A., Butchart, N., Warner, C., & Swinbank, R. (2002). Impact of a spectral gravity wave parameterization on the stratosphere in the Met Office Unified Model. *Journal of the Atmospheric Sciences*, *59*(9), 1473–1489.

Schulzweida, U. (2020). *CDO user guide*. Max Planck Institute for Meteorology.

Scinocca, J. F. (2003). An accurate spectral nonorographic gravity wave drag parameterization for general circulation models. *Journal of the Atmospheric Sciences*, *60*(4), 667–682.

Seifert, A., & Beheng, K. D. (2006). A two-moment cloud microphysics parameterization for mixed-phase clouds. Part 1: Model description. *Meteorology and Atmospheric Physics*, *92*, 45–66.

Seiki, T., & Nakajima, T. (2014). Aerosol effects of the condensation process on a convective cloud simulation. *Journal of Atmospheric Sciences*, *71*(2), 833–853.

Smith, R. (1990). A scheme for predicting layer clouds and their water content in a general circulation model. *Quarterly Journal of the Royal Meteorological Society*, *116*(492), 435–460.

Staniforth, A., & Côté, J. (1991). Semi-Lagrangian integration schemes for atmospheric models—A review. *Monthly Weather Review*, *119*(9), 2206–2223.

Stephan, C. C., Strube, C., Klocke, D., Ern, M., Hoffmann, L., Preusse, P., & Schmidt, H. (2019a). Gravity waves in global high-resolution simulations with explicit and parameterized convection. *Journal of Geophysical Research: Atmospheres*, *124*(8), 4446–4459.

Stephan, C. C., Strube, C., Klocke, D., Ern, M., Hoffmann, L., Preusse, P., & Schmidt, H. (2019b). Intercomparison of gravity waves in global convection-permitting models. *Journal of the Atmospheric Sciences*, *76*(9), 2739–2759.

Stevens, B., Satoh, M., Auger, L., Biercamp, J., Bretherton, C. S., Chen, X., Düben, P., Judt, F., Khairoutdinov, M., Klocke, D., Kodama, C., Kornblueh, L., Lin, S.-J., Neumann, P., Putman, W. M., Röber, N., Shibuya, R., Vanniere, B., Vidale, P. L., ... Zhou, L. (2019). DYAMOND: The DYnamics of the Atmospheric general circulation Modeled On Non-hydrostatic Domains. *Progress in Earth and Planetary Science*, *6*(61).

Sundqvist, H. (1978). A parameterization scheme for non-convective condensation including prediction of cloud water content. *Quarterly Journal of the Royal Meteorological Society*, *104*(441), 677–690.

Tiedke, M. (1993). Representation of clouds in large-scale models. *Monthly Weather Review*, *121*(11), 3040–3061.

Tomita, H., & Satoh, M. (2004). A new dynamical framework of nonhydrostatic global model using the icosahedral grid. *Fluid Dynamics Research*, *34*(6), 357.

Tsyrulnikov, M., & Gayfulin, D. (2017). A limited-area spatio-temporal stochastic pattern generator for simulation of uncertainties in ensemble applications. *Meteorologische Zeitschrift*, *26*(5), 549–566.

Vidale, P. L., Hodges, K., Vannière, B., Davini, P., Roberts, M. J., Strommen, K., Weisheimer, A., Plesca, E., & Corti, S. (2021). Impact of stochastic physics and model resolution on the simulation of tropical cyclones in climate GCMs. *Journal of Climate*, *34*(11), 4315–4341.

Vosper, S. (2015). Mountain waves and wakes generated by South Georgia: Implications for drag parametrization. *Quarterly Journal of the Royal Meteorological Society*, *141*(692), 2813–2827.

Walters, D., Baran, A. J., Boutle, I., Brooks, M., Earnshaw, P., Edwards, J., Furtado, K., Hill, P., Lock, A., Manners, J., Morcrette, C., Mulcahy, J., Sanchez, C., Smith, C., Stratton, R., Tennant, W., Tomassini, L., VanWeverberg, K., Vosper, S., ... Zerroukat, M. (2019). The Met Office Unified Model Global Atmosphere 7.0/7.1 and JULES Global Land 7.0 configurations. *Geoscientific Model Development*, *12*(5), 1909–1963.

Walters, D., Boutle, I., Brooks, M., Melvin, T., Stratton, R., Vosper, S., Wells, H., Williams, K., Wood, N., Allen, T., Bushell, A., Copsey, D., Earnshaw, P., Edwards, J., Gross, M., Hardiman, S., Harris, C., Heming, J., Klingaman, N., ... Xavier, P. (2017). The Met Office Unified Model Global Atmosphere 6.0/6.1 and JULES Global Land 6.0/6.1 configurations. *Geoscientific Model Development*, *10*(4), 1487–1520.

Wanninkhof, R. (2014). Relationship between wind speed and gas exchange over the ocean revisited. *Limnology and Oceanography: Methods*, *12*(6), 351–362.

Warner, C., & McIntyre, M. (1996). On the propagation and dissipation of gravity wave spectra through a realistic middle atmosphere. *Journal of Atmospheric Sciences*, *53*(22), 3213–3235.

Warner, C., & McIntyre, M. (1999). Toward an ultra-simple spectral gravity wave parameterization for general circulation models. *Earth, Planets and Space*, *51*(7-8), 475–484.

Warren, S. G., Eastman, R. M., & Hahn, C. J. (2007). A survey of changes in cloud cover and cloud types over land from surface observations, 1971–96. *Journal of Climate*, *20*(4), 717–738.

Wedi, N. P. (2014). Increasing horizontal resolution in numerical weather prediction and climate simulations: Illusion or panacea? *Philosophical Transactions of the Royal Society A: Mathematical, Physical and Engineering Sciences*, *372*(2018), 20130289.

Williams, P. D. (2012). Climatic impacts of stochastic fluctuations in air–sea fluxes. *Geophysical Research Letters*, *39*(10), L10705.

Williamson, D. L. (2007). The evolution of dynamical cores for global atmospheric models. *Journal of the Meteorological Society of Japan. Ser. II*, *85*, 241–269.

Wilson, D. R., & Ballard, S. P. (1999). A microphysically based precipitation scheme for the UK Meteorological Office Unified Model. *Quarterly Journal of the Royal Meteorological Society*, *125*(557), 1607–1636.

Wilson, D. R., Bushell, A. C., Kerr-Munslow, A. M., Price, J. D., & Morcrette, C. J. (2008). PC2: A prognostic cloud fraction and condensation scheme. I: Scheme description. *Quarterly Journal of the Royal Meteorological Society*, *134*(637), 2093–2107.

Wood, N., Staniforth, A., White, A., Allen, T., Diamantakis, M., Gross, M., Melvin, T., Smith, C., Vosper, S., Zerroukat, M., & Thuburn, J. (2014). An inherently mass-conserving semi-implicit semi-Lagrangian discretization of the deep-atmosphere global non-hydrostatic equations. *Quarterly Journal of the Royal Meteorological Society*, *140*(682), 1505–1520.

Xu, K.-M., & Krueger, S. K. (1991). Evaluation of cloudiness parameterizations using a cumulus ensemble model. *Monthly Weather Review*, *119*(2), 342–367.

Yamasaki, M. (1977). A preliminary experiment of the tropical cyclone without parameterizing the effects of cumulus convection. *Journal of the Meteorological Society of Japan. Ser. II*, *55*(1), 11–31.

Yamasaki, M. (1983). A further study of the tropical cyclone without parameterizing the effects of cumulus convection. *Papers in Meteorology and Geophysics*, *34*(4), 221–260.

Yano, J.-I., & Plant, R. (2012). Interactions between shallow and deep convection under a finite departure from convective quasi equilibrium. *Journal of the Atmospheric Sciences*, *69*(12), 3463–3470.

Zadra, A., Roch, M., Laroche, S., & Charron, M. (2003). The subgrid-scale orographic blocking parametrization of the GEM model. *Atmosphere-Ocean*, *41*(2), 155–170.

Zadra, A., Williams, K., Frassoni, A., Rixen, M., Adames, Á. F., Berner, J., Bouyssel, F., Casati, B., Christensen, H., Ek, M. B., Flato, G., Huang, Y., Judt, F., Lin, H., Maloney, E., Merryfield, W., Van Niekerk, A., Rackow, T., Saito, K., ... Yadav, P. (2018). Systematic errors in weather and climate models: Nature, origins, and ways forward. *Bulletin of the American Meteorological Society*, *99*(4), ES67–ES70.

Zeng, X., Zhang, Q., Johnson, D., & Tao, W. (2002). Parameterization of wind gustiness for the computation of ocean surface fluxes at different spatial scales. *Monthly Weather Review*, *130*(8), 2125–2133.

Zeng, X., Zhao, M., & Dickinson, R. E. (1998). Intercomparison of bulk aerodynamic algorithms for the computation of sea surface fluxes using TOGA COARE and TAO data. *Journal of Climate*, *11*(10), 2628–2644.

Zhang, K., Zhao, C., Wan, H., Qian, Y., Easter, R. C., Ghan, S. J., Sakaguchi, K., & Liu, X. (2016). Quantifying the impact of sub-grid surface wind variability on sea salt and dust emissions in CAM5. *Geoscientific Model Development*, *9*(2), 607–632.

Zhang, M., Lin, W., Klein, S., Bacmeister, J., Bony, S., Cederwall, R., Del Genio, A., Hack, J., Loeb, N., Lohmann, U., Minnis, P., Musat, I., Pincus, R., Stier, P., Suarez, M. J., Webb, M. J., Wu, J. B., Xie, S. C., Yao, M.-S., & Zhang, J. H. (2005). Comparing clouds and their seasonal variations in 10 atmospheric general circulation models with satellite measurements. *Journal of Geophysical Research: Atmospheres*, *110*(D15).

Zhao, M., Golaz, J.-C., Held, I., Guo, H., Balaji, V., Benson, R., Chen, J.-H., Chen, X., Donner, L. J., Dunne, J. P., Dunne, K., Durachta, J., Fan, S.-M., Freidenreich, S., Garner, S., Ginoux, P., Harris, L., Horowitz, L., Krasting, J., ... Xiang, B. (2018). The GFDL global atmosphere and land model AM4.0/LM4.0: 2. Model description,

sensitivity studies, and tuning strategies. *Journal of Advances in Modeling Earth Systems*, *10*(3), 735–769.

Zhou, B., Simon, J. S., & Chow, F. K. (2014). The convective boundary layer in the terra incognita. *Journal of the Atmospheric Sciences*, *71*(7), 2545–2563.

Zhou, L., Lin, S.-J., Chen, J.-H., Harris, L. M., Chen, X., & Rees, S. L. (2019). Toward convective-scale prediction within the next generation global prediction system. *Bulletin of the American Meteorological Society*, *100*(7), 1225–1243.

Appendix A

Supplementary figures

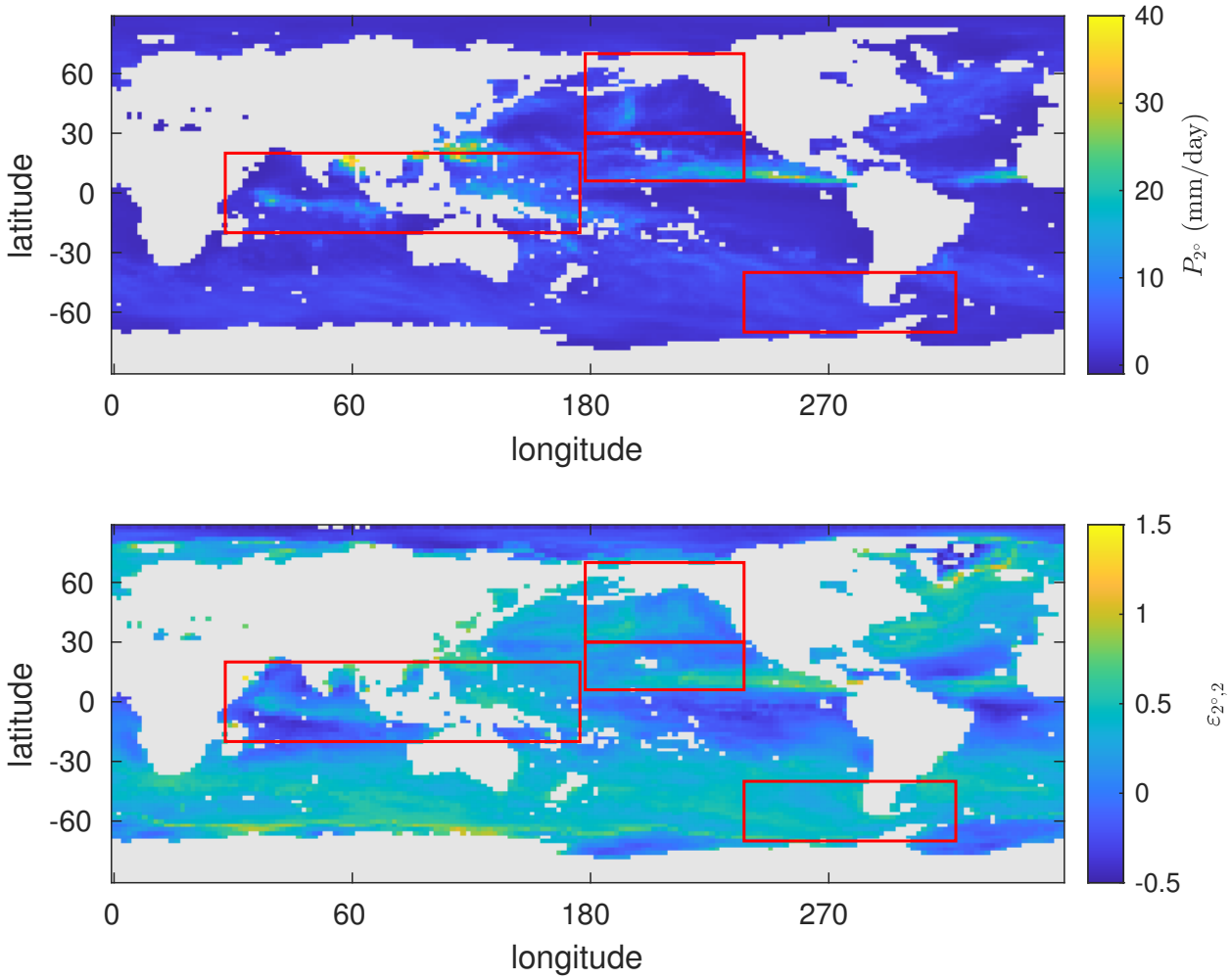

Figure A.1: Global P_{2° (top) and $\varepsilon_{2^\circ,2}$ (bottom) time means for the FV3 model, with land mask. The regions considered in this study are outlined in red. Vertical axis denotes latitude, whereas the horizontal axis denotes longitude.

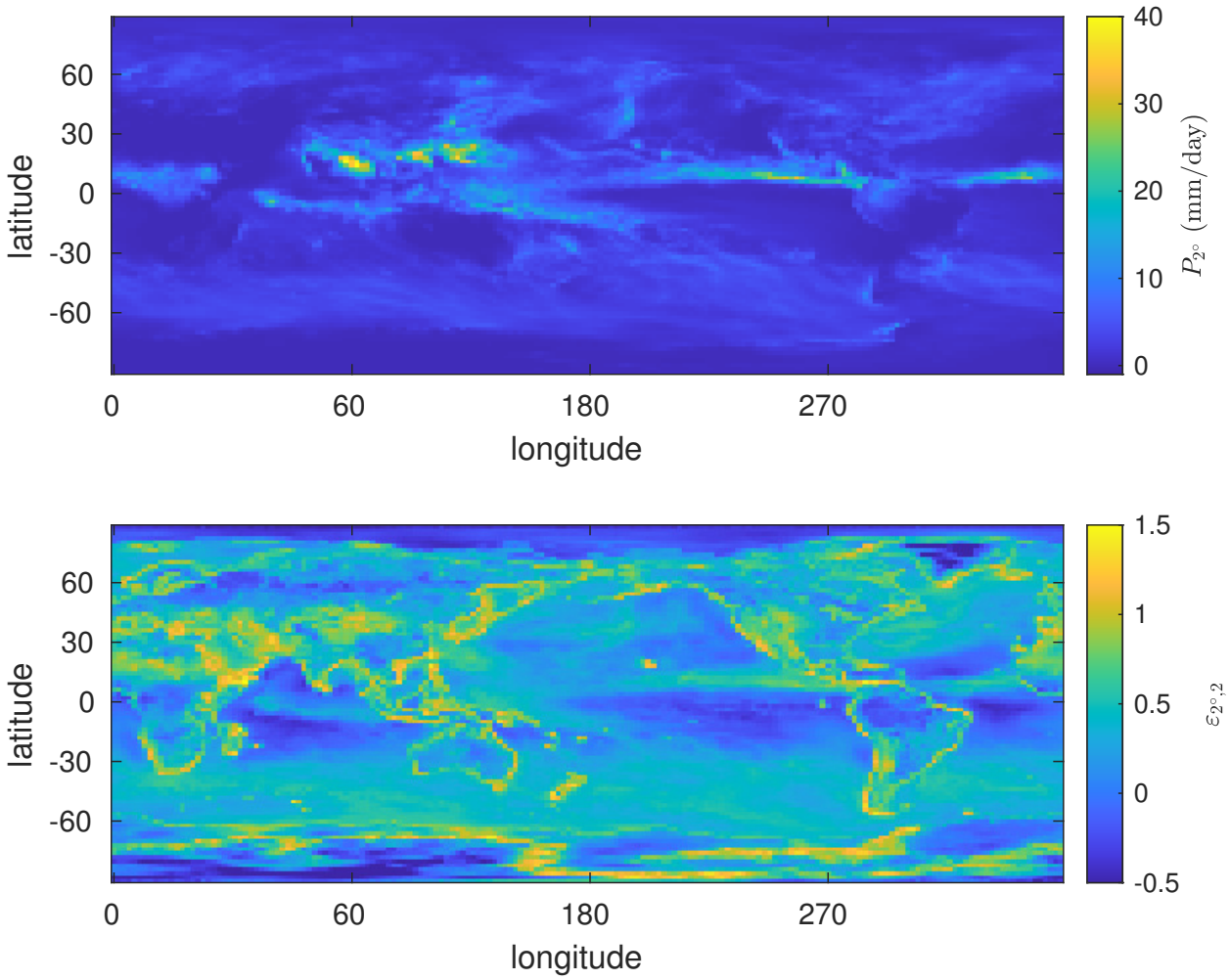

Figure A.2: Global P_{2° (top) and $\varepsilon_{2^\circ,2}$ (bottom) time means for the FV3 model. Vertical axis denotes latitude, whereas the horizontal axis denotes longitude.

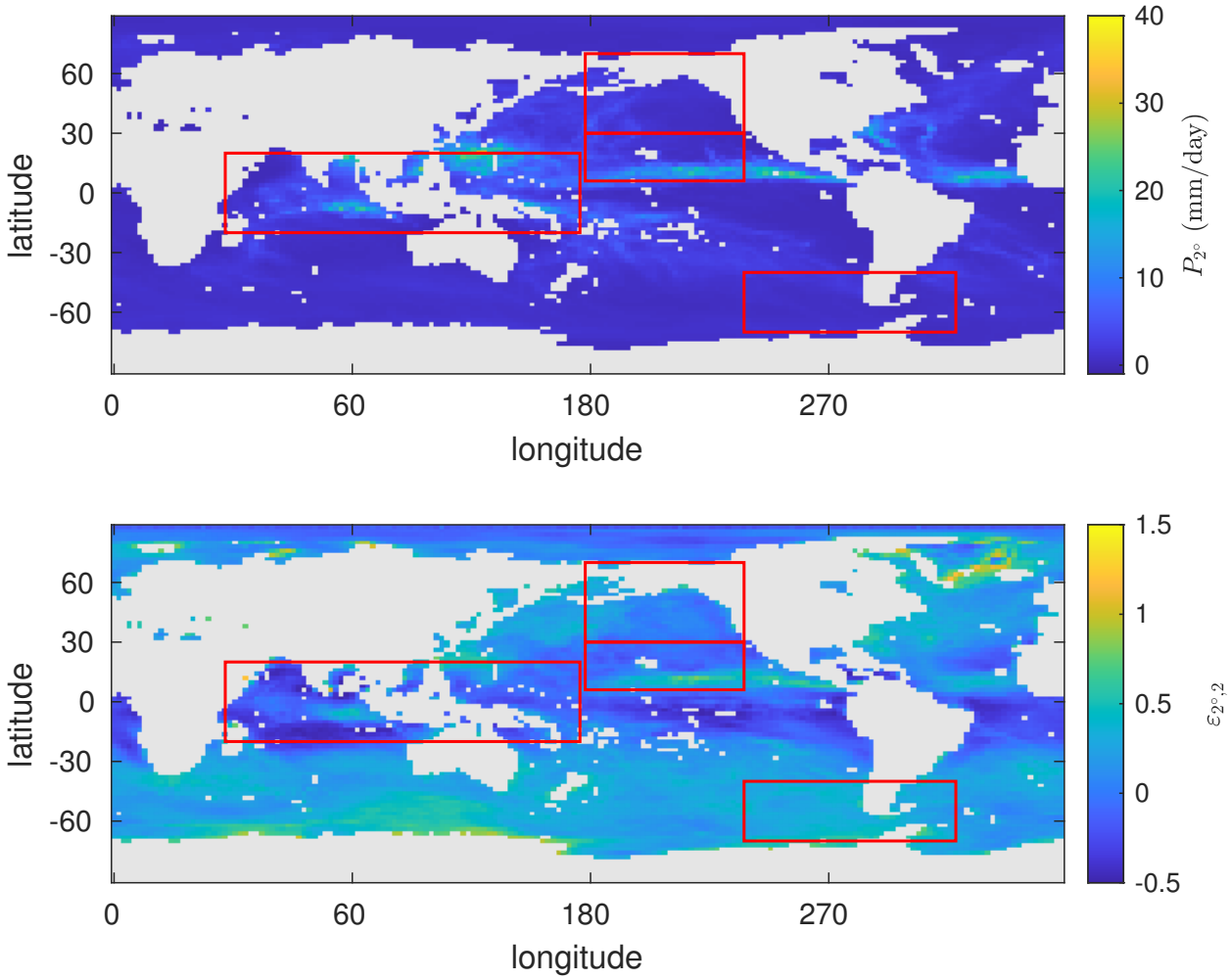

Figure A.3: Global P_{2° (top) and $\varepsilon_{2^\circ,2}$ (bottom) time means for the GEOS model, with land mask. The regions considered in this study are outlined in red. Vertical axis denotes latitude, whereas the horizontal axis denotes longitude.

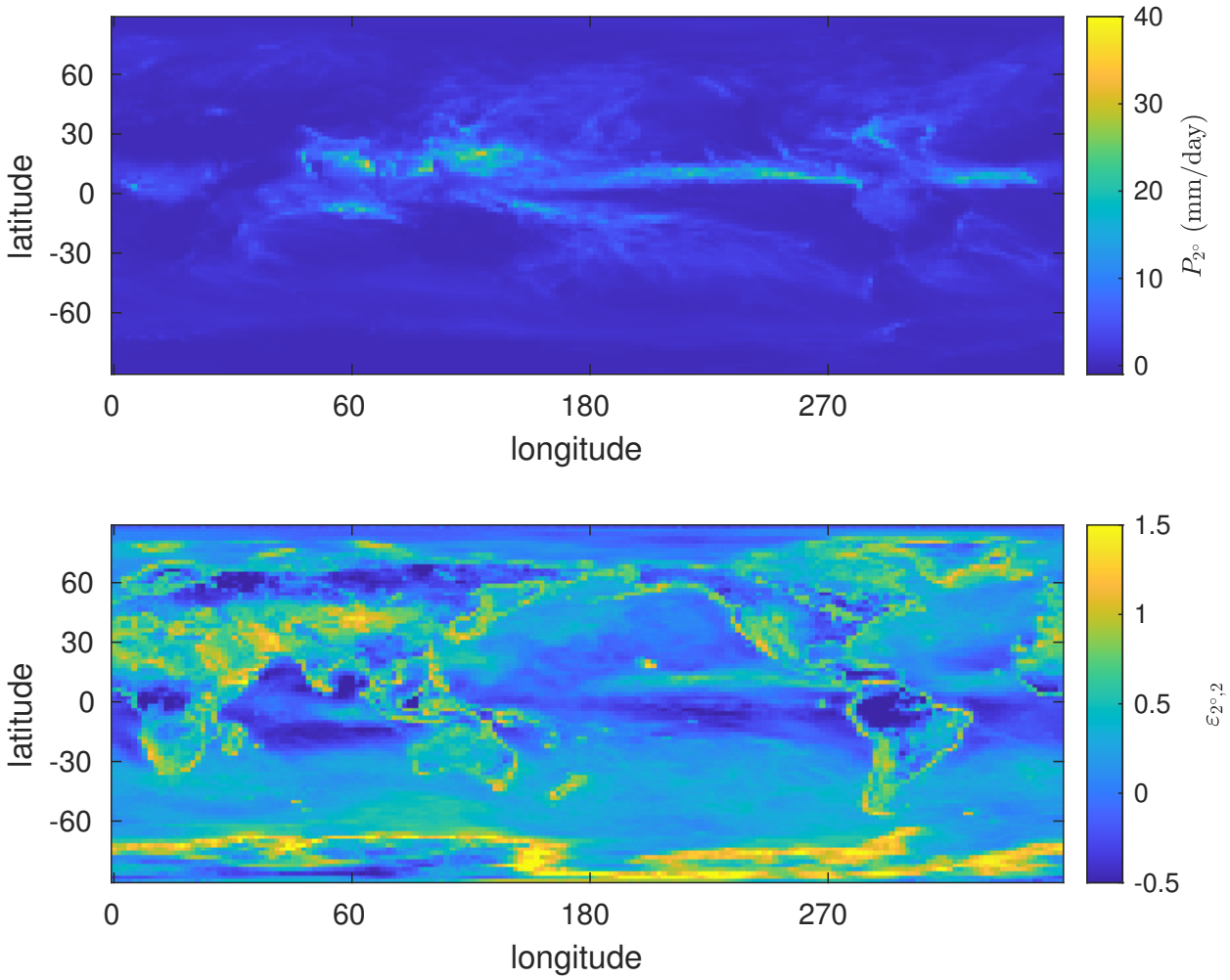

Figure A.4: Global P_{2° (top) and $\varepsilon_{2^\circ,2}$ (bottom) time means for the GEOS model. Vertical axis denotes latitude, whereas the horizontal axis denotes longitude.

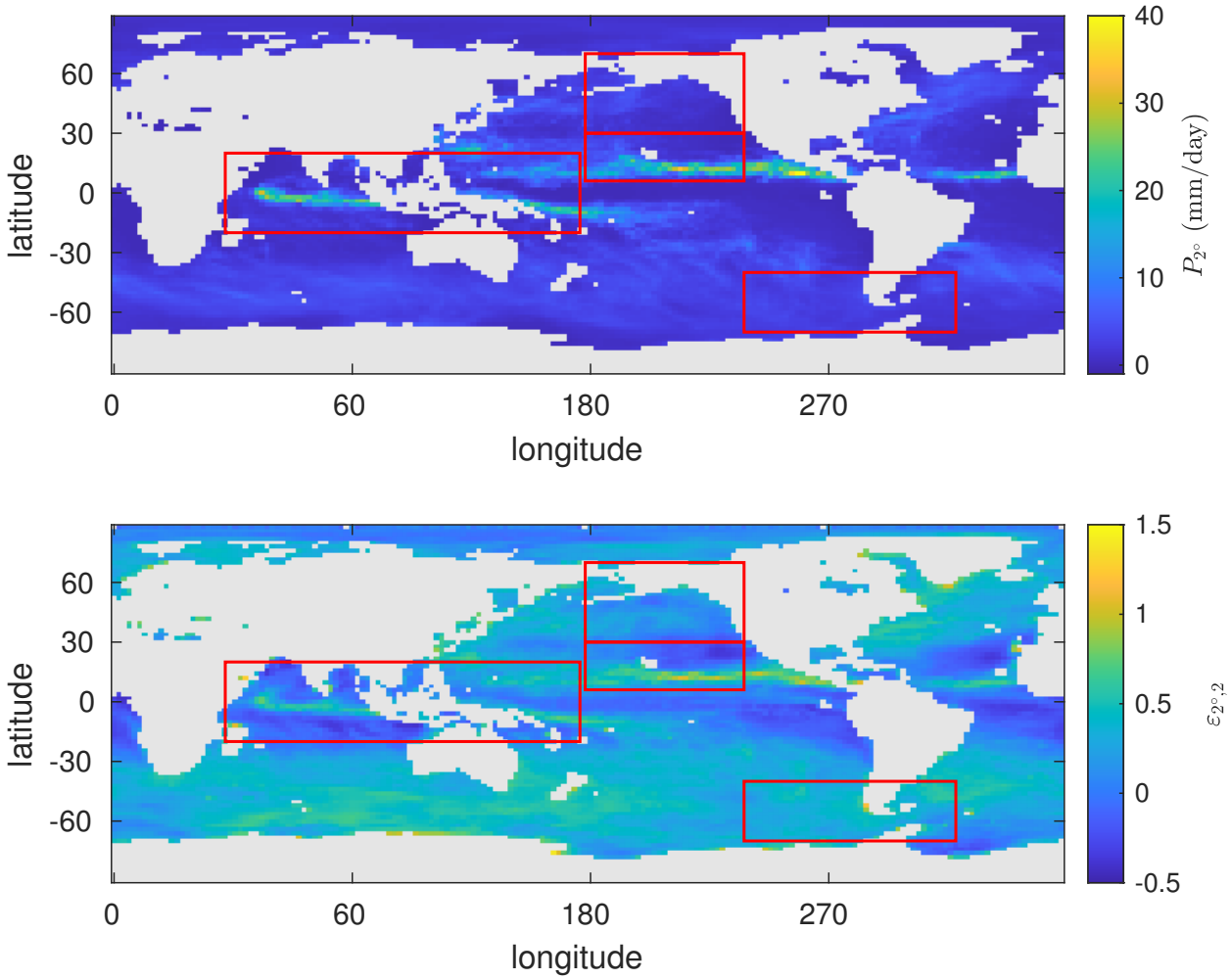

Figure A.5: Global P_{2° (top) and $\varepsilon_{2^\circ,2}$ (bottom) time means for the IFS model, with land mask. The regions considered in this study are outlined in red. Vertical axis denotes latitude, whereas the horizontal axis denotes longitude.

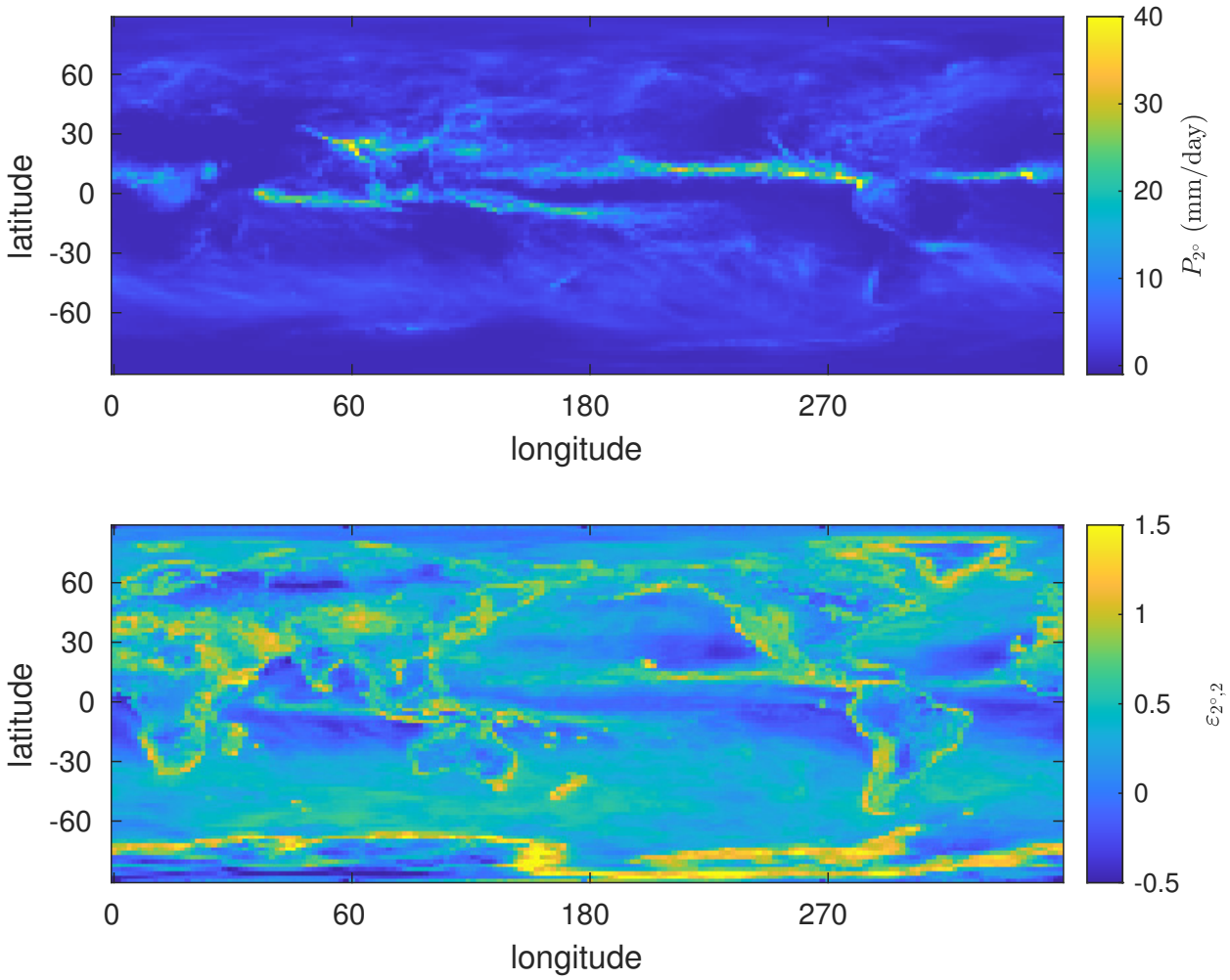

Figure A.6: Global P_{2° (top) and $\varepsilon_{2^\circ,2}$ (bottom) time means for the IFS model. Vertical axis denotes latitude, whereas the horizontal axis denotes longitude.

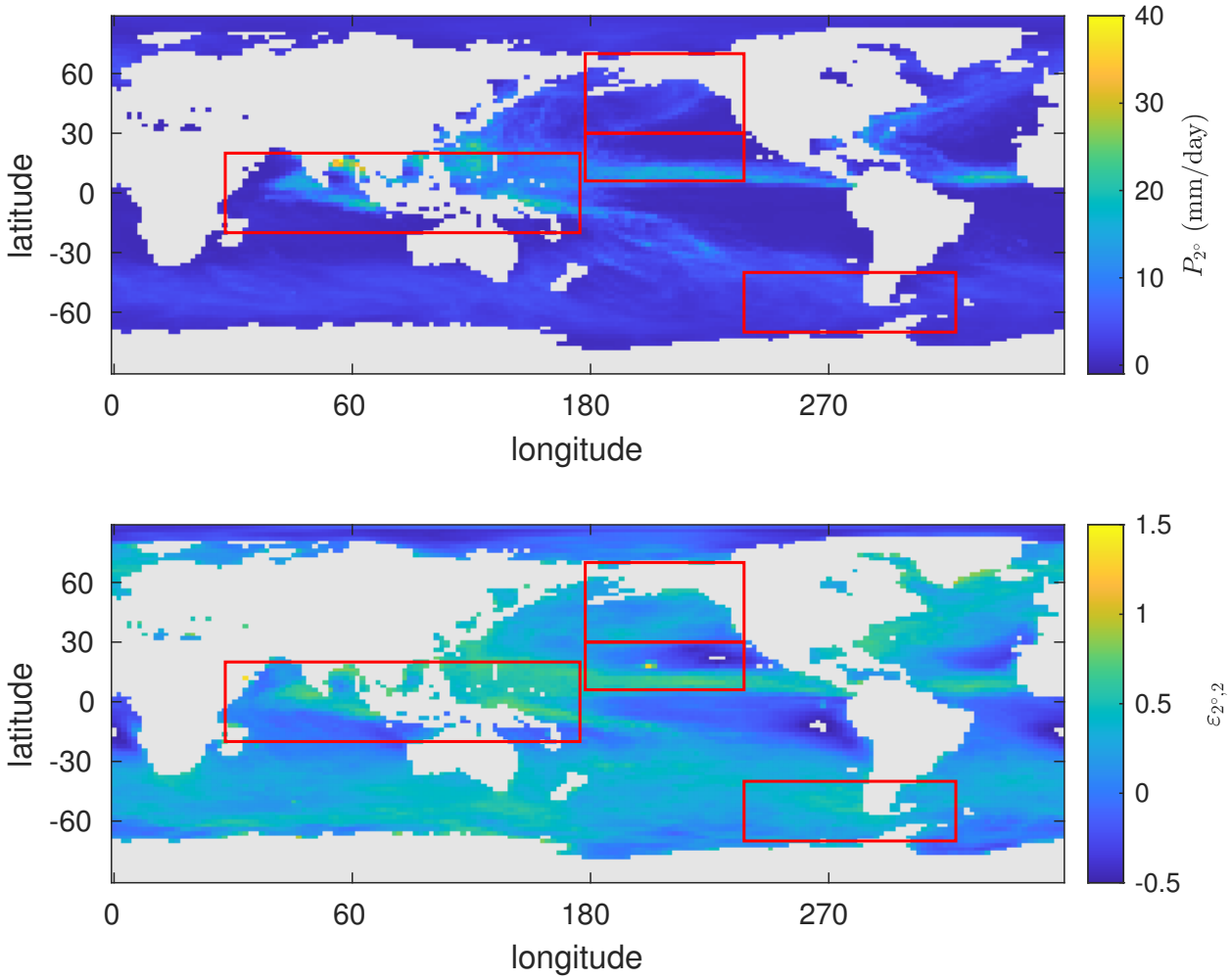

Figure A.7: Global P_{2° (top) and $\varepsilon_{2^\circ,2}$ (bottom) time means for the NICAM model, with land mask. The regions considered in this study are outlined in red. Vertical axis denotes latitude, whereas the horizontal axis denotes longitude.

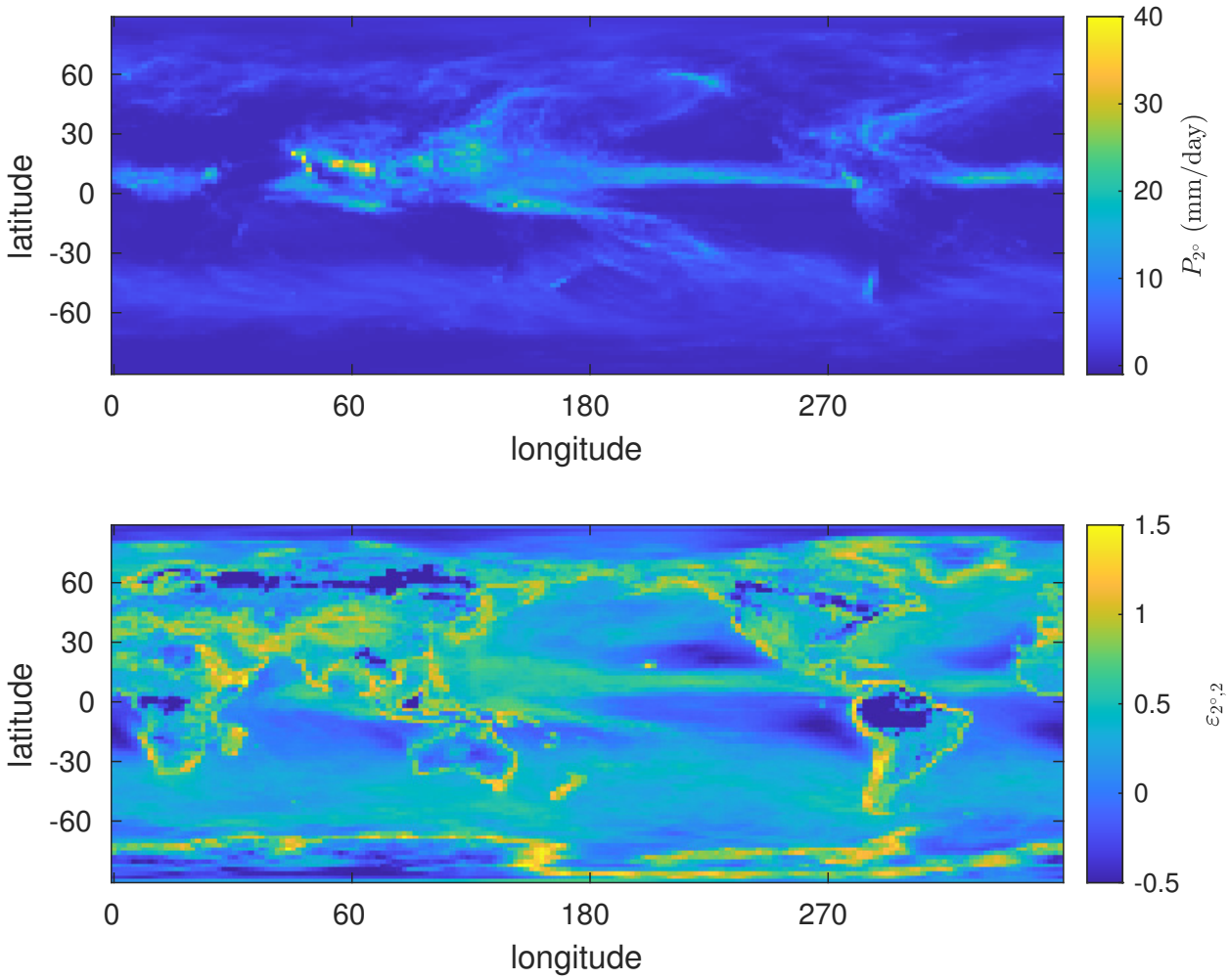

Figure A.8: Global P_{2° (top) and $\varepsilon_{2^\circ,2}$ (bottom) time means for the NICAM model. Vertical axis denotes latitude, whereas the horizontal axis denotes longitude.

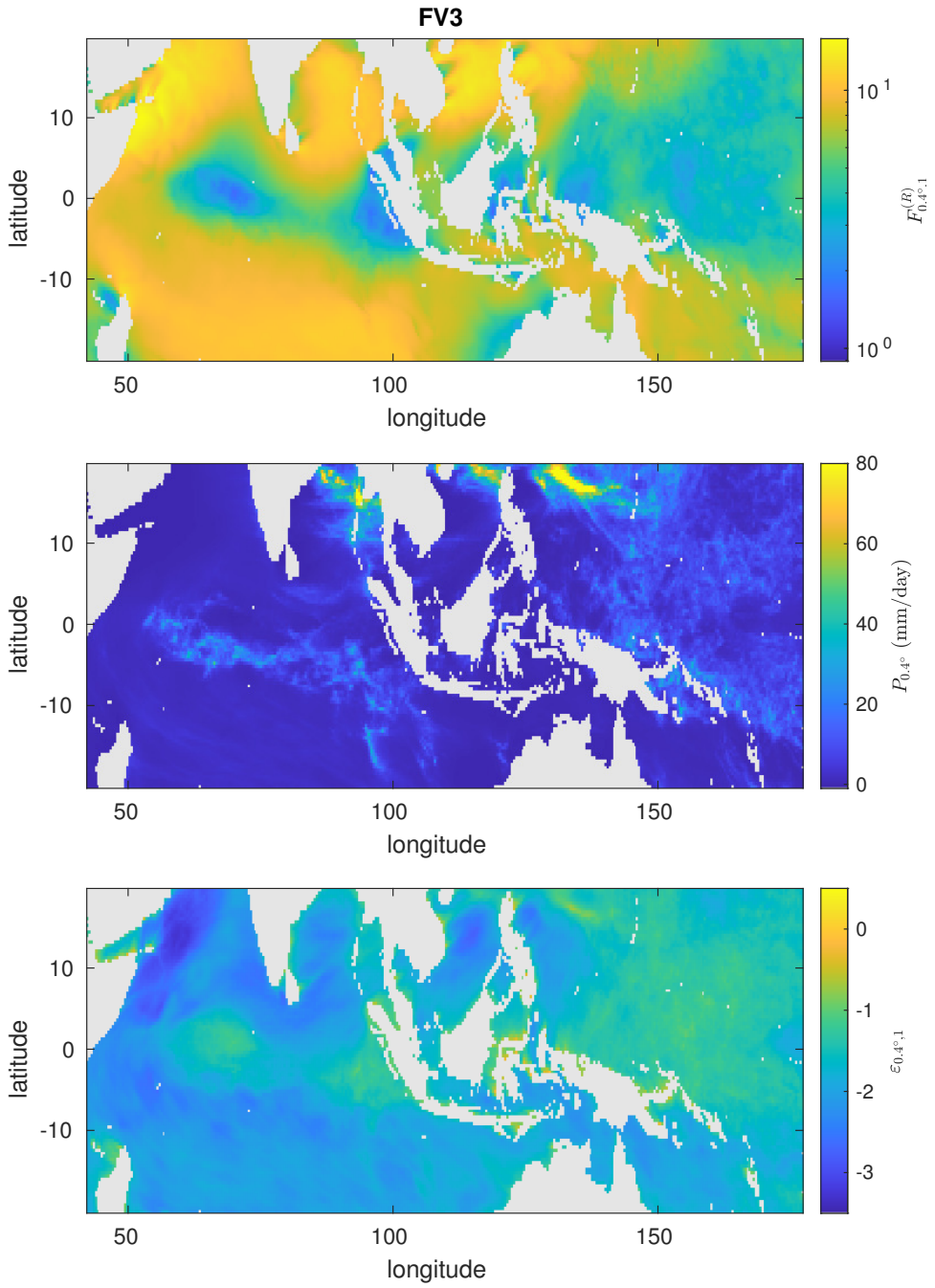

Figure A.9: Time means of $F^{(R)}_{0.4^\circ,1}$, $P_{0.4^\circ}$, $\varepsilon_{0.4^\circ,1}$ in the Warm Pool for the FV3 model. Vertical axis denotes latitude, whereas the horizontal axis denotes longitude.

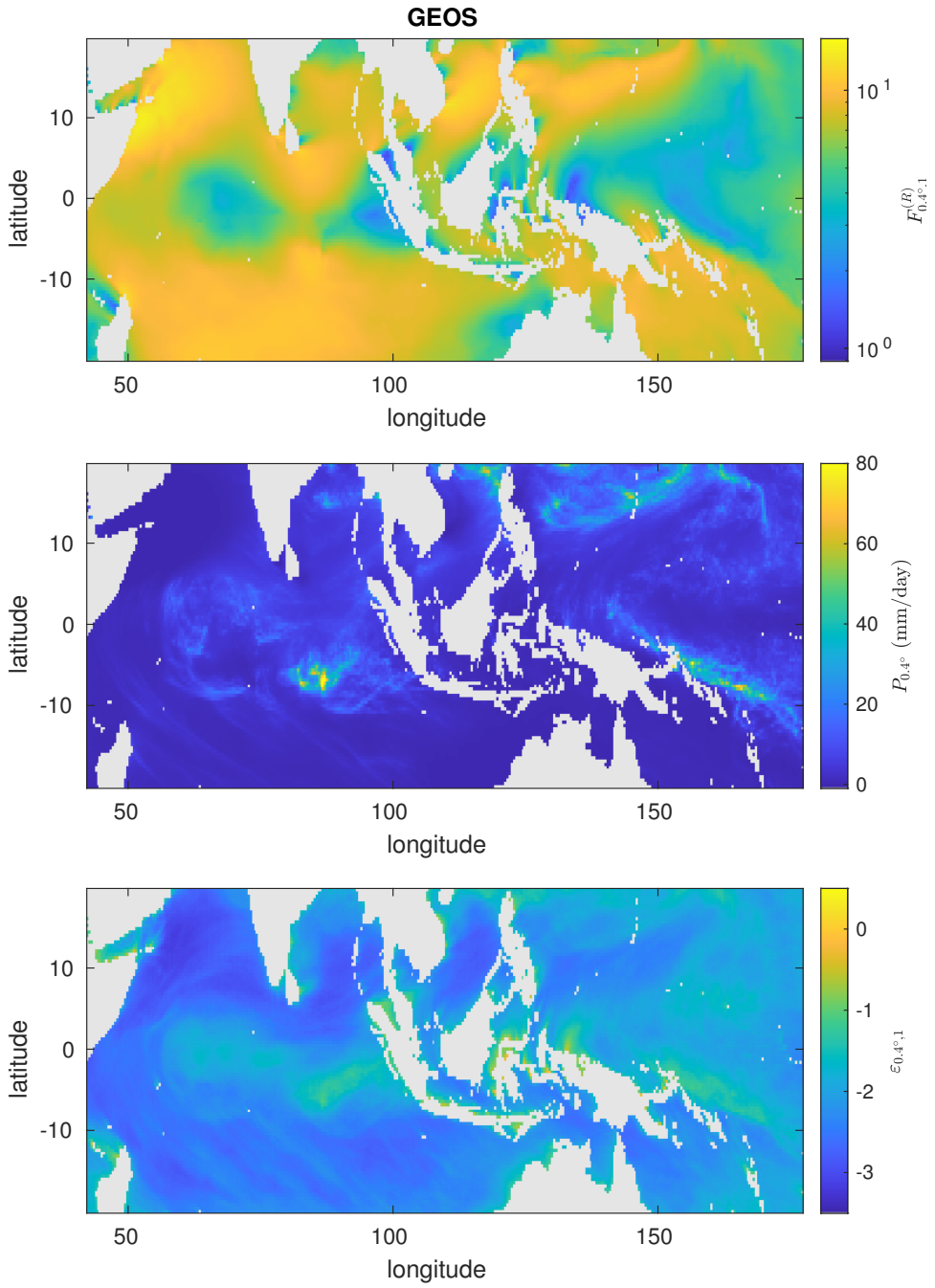

Figure A.10: Time means of $F^{(R)}_{0.4^\circ,1}$, $P_{0.4^\circ}$, $\varepsilon_{0.4^\circ,1}$ in the Warm Pool for the GEOS model. Vertical axis denotes latitude, whereas the horizontal axis denotes longitude.

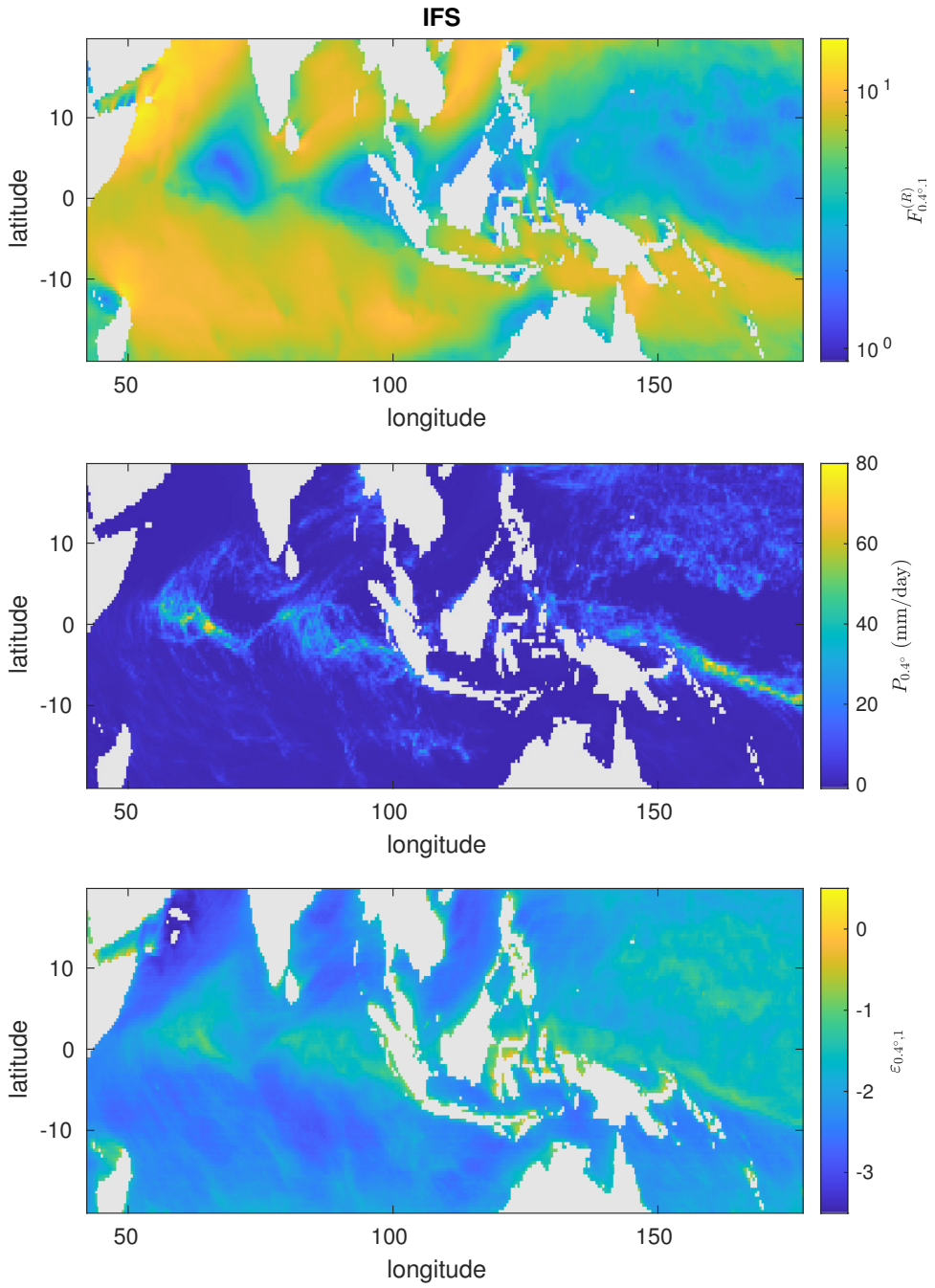

Figure A.11: Time means of $F^{(R)}_{0.4^\circ,1}$, $P_{0.4^\circ}$, $\varepsilon_{0.4^\circ,1}$ in the Warm Pool for the IFS model. Vertical axis denotes latitude, whereas the horizontal axis denotes longitude.

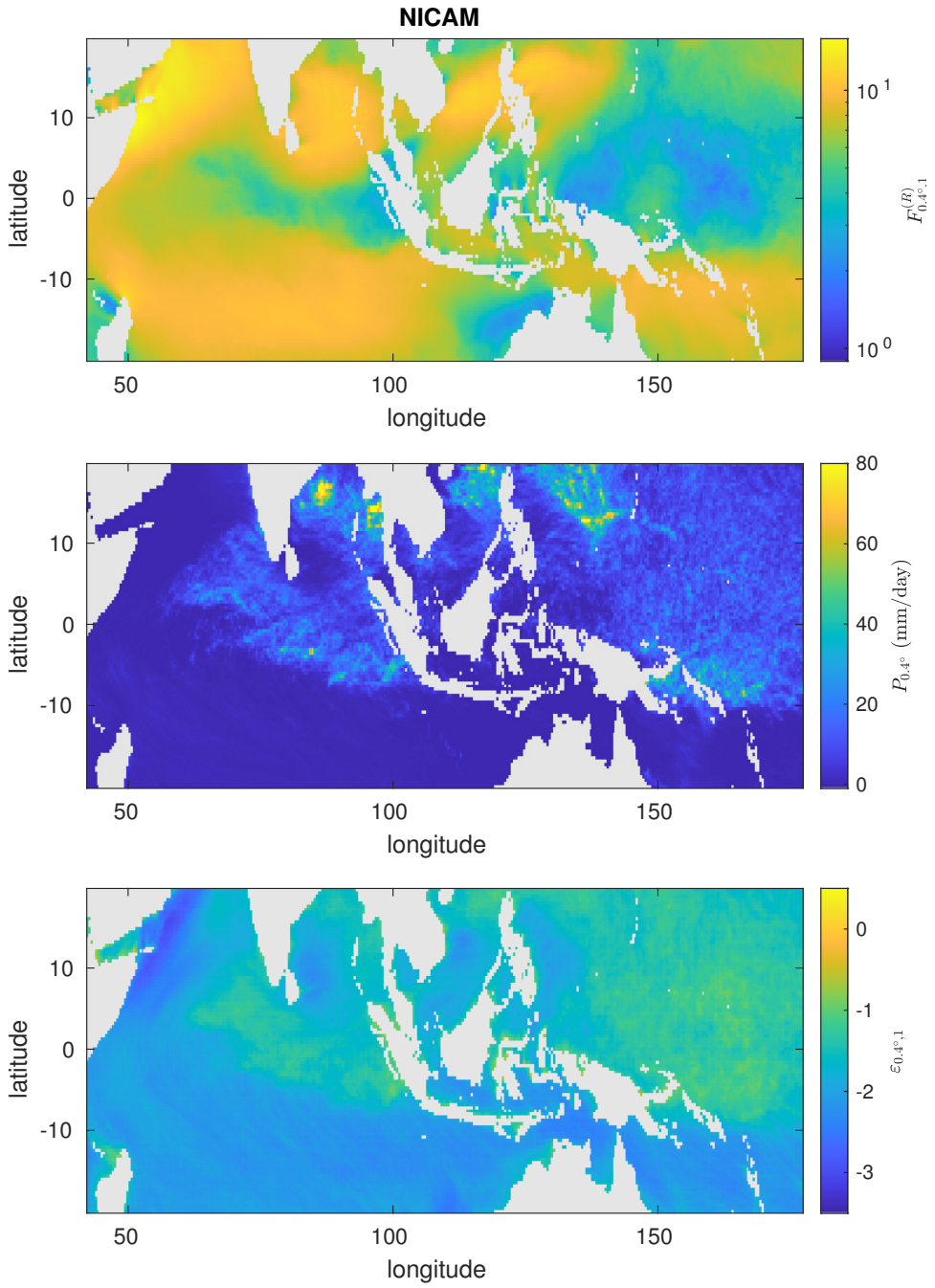

Figure A.12: Time means of $F^{(R)}_{0.4^\circ,1}$, $P_{0.4^\circ}$, $\varepsilon_{0.4^\circ,1}$ in the Warm Pool for the NICAM model. Vertical axis denotes latitude, whereas the horizontal axis denotes longitude.

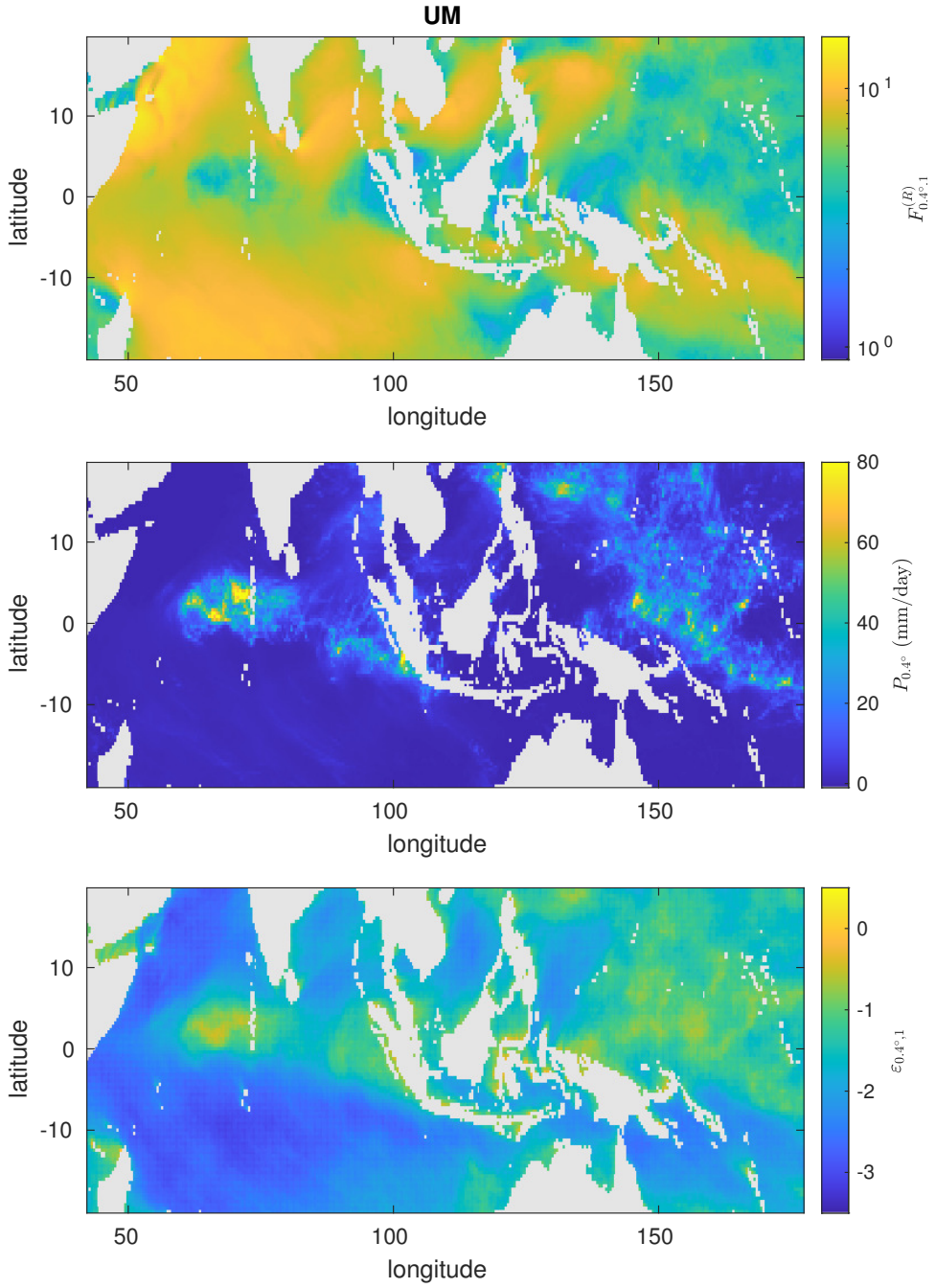

Figure A.13: Time means of $F^{(R)}_{0.4^\circ,1}$, $P_{0.4^\circ}$, $\varepsilon_{0.4^\circ,1}$ in the Warm Pool for the UM model. Vertical axis denotes latitude, whereas the horizontal axis denotes longitude.

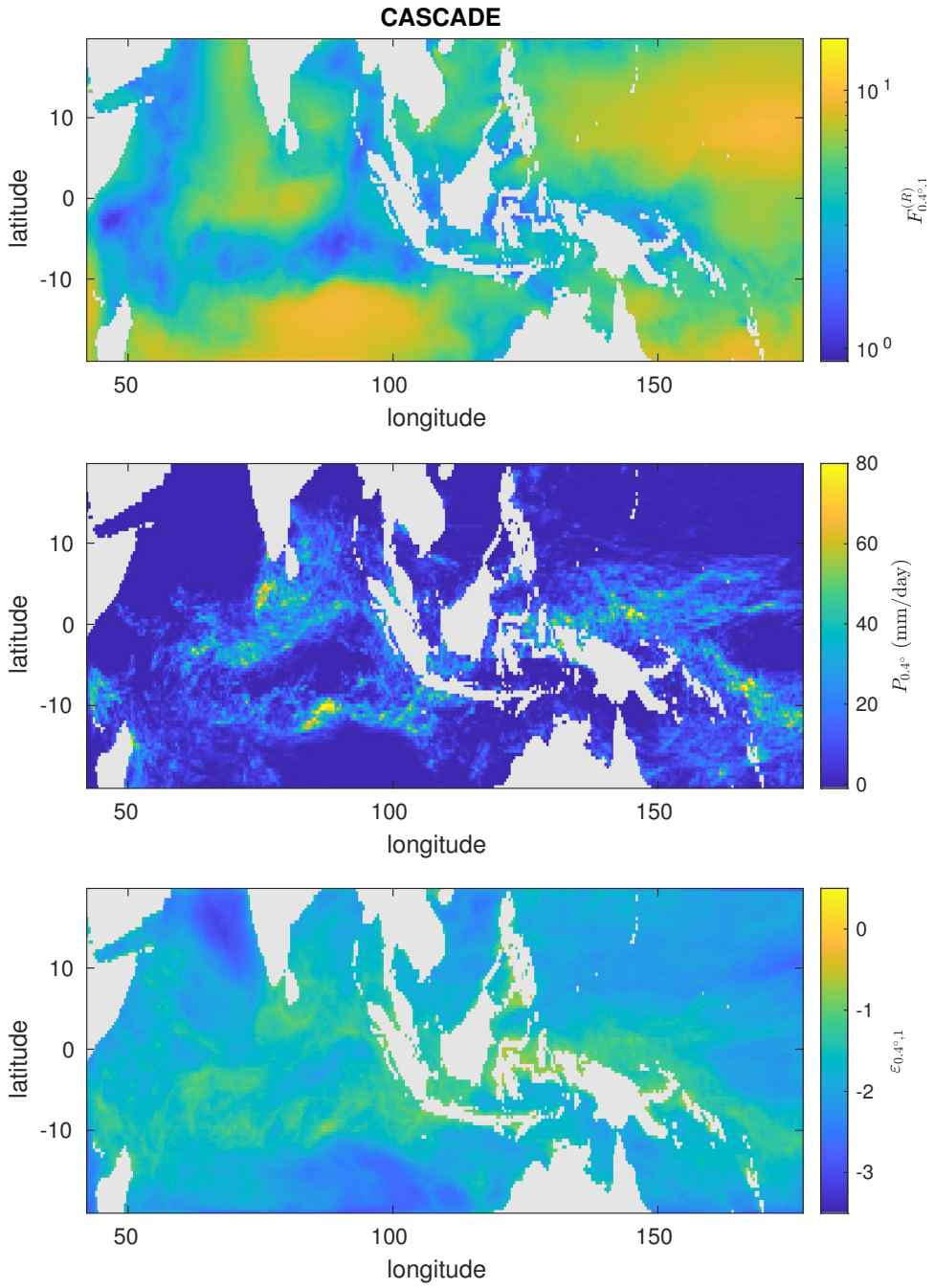

Figure A.14: Time means of $F^{(R)}_{0.4^\circ,1}$, $P_{0.4^\circ}$, $\varepsilon_{0.4^\circ,1}$ in the Warm Pool for the Cascade model run. Vertical axis denotes latitude, whereas the horizontal axis denotes longitude.

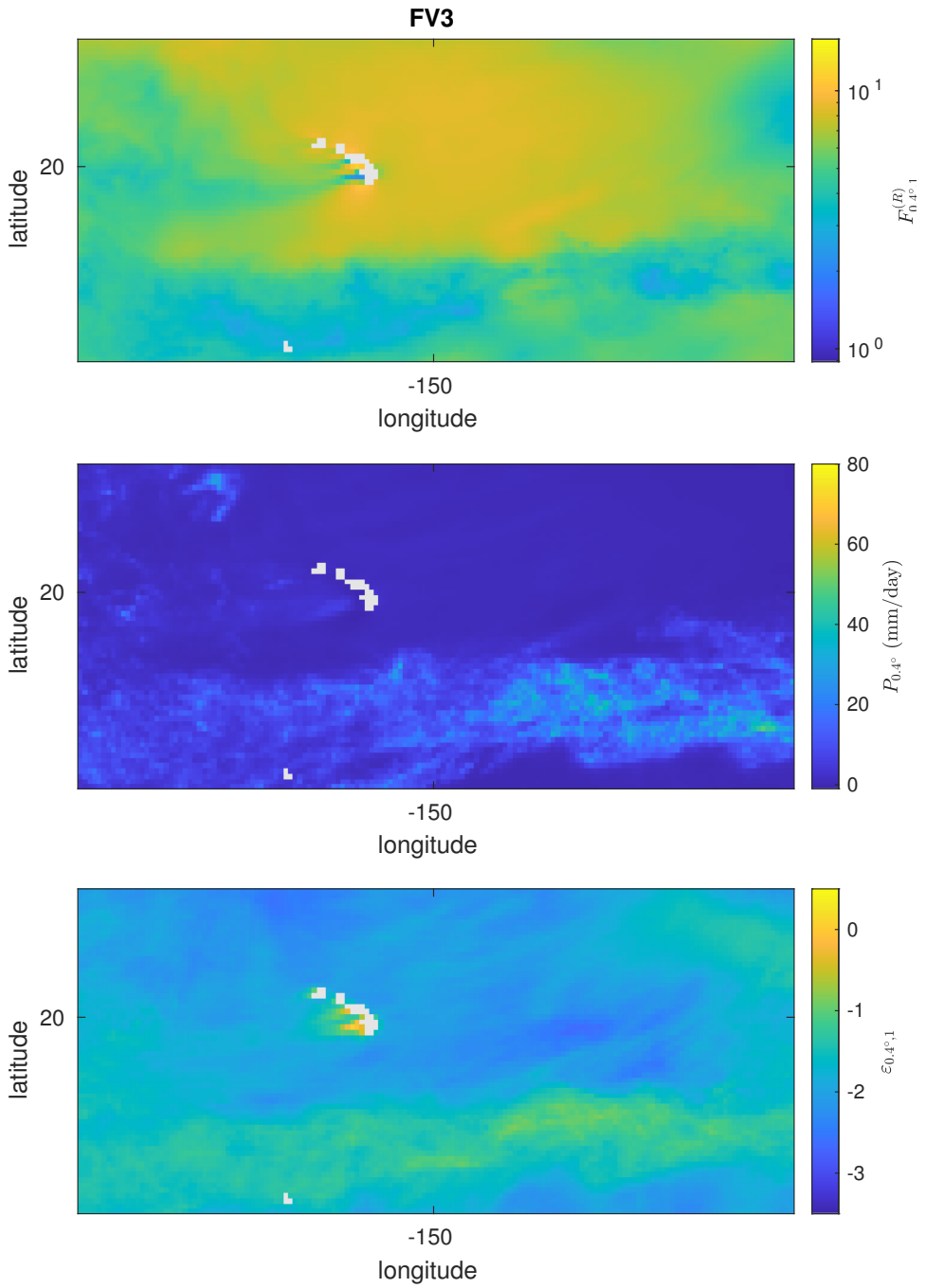

Figure A.15: Time means of $F^{(R)}_{0.4^\circ,1}$, $P_{0.4^\circ}$, $\varepsilon_{0.4^\circ,1}$ in the subtropical Northeast Pacific for the FV3 model. Vertical axis denotes latitude, whereas the horizontal axis denotes longitude.

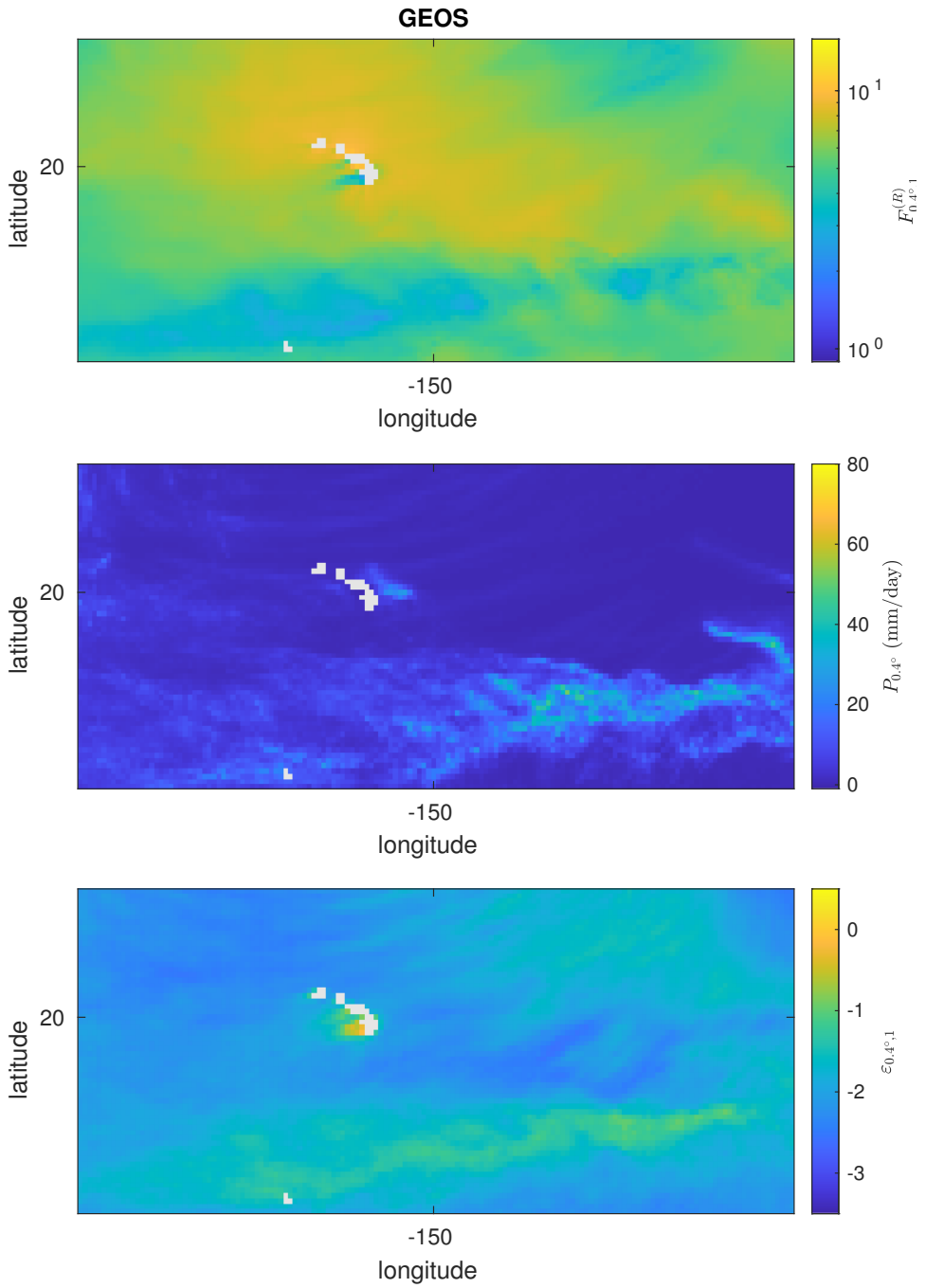

Figure A.16: Time means of $F^{(R)}_{0.4^\circ,1}$, $P_{0.4^\circ}$, $\varepsilon_{0.4^\circ,1}$ in the subtropical Northeast Pacific for the GEOS model. Vertical axis denotes latitude, whereas the horizontal axis denotes longitude.

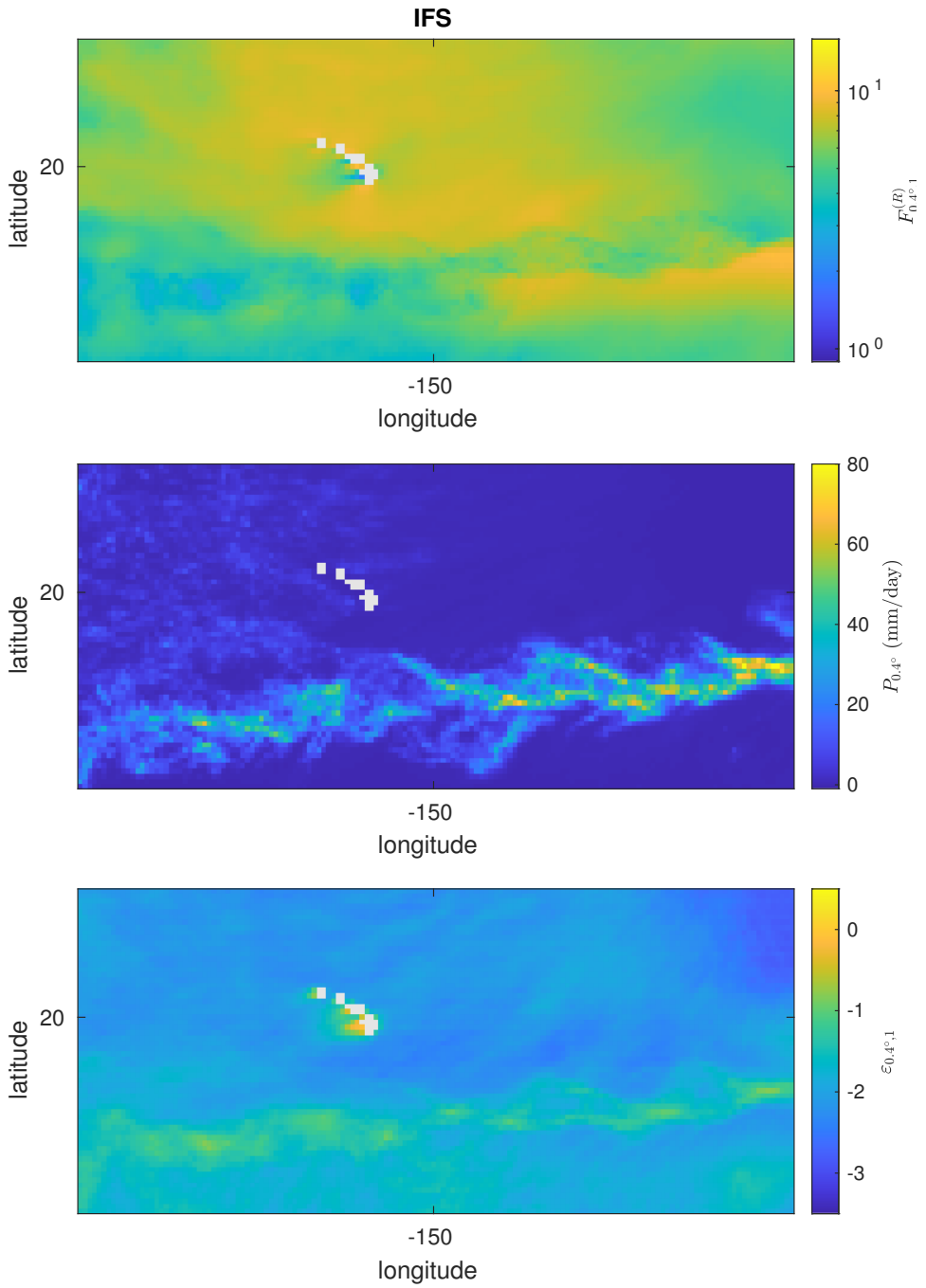

Figure A.17: Time means of $F^{(R)}_{0.4^\circ,1}$, $P_{0.4^\circ}$, $\varepsilon_{0.4^\circ,1}$ in the subtropical Northeast Pacific for the IFS model. Vertical axis denotes latitude, whereas the horizontal axis denotes longitude.

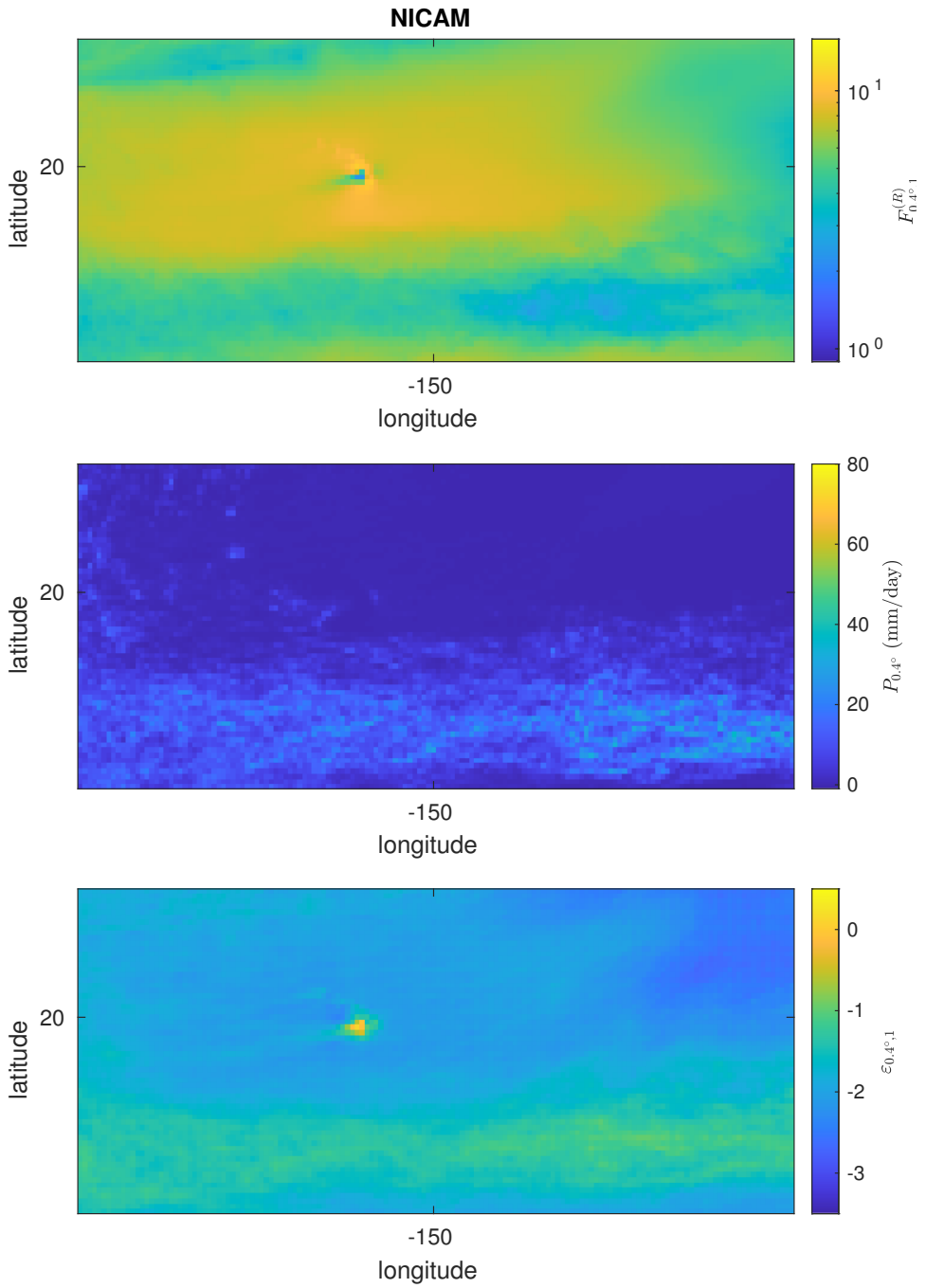

Figure A.18: Time means of $F^{(R)}_{0.4^\circ,1}$, $P_{0.4^\circ}$, $\varepsilon_{0.4^\circ,1}$ in the subtropical Northeast Pacific for the NICAM model. Vertical axis denotes latitude, whereas the horizontal axis denotes longitude.

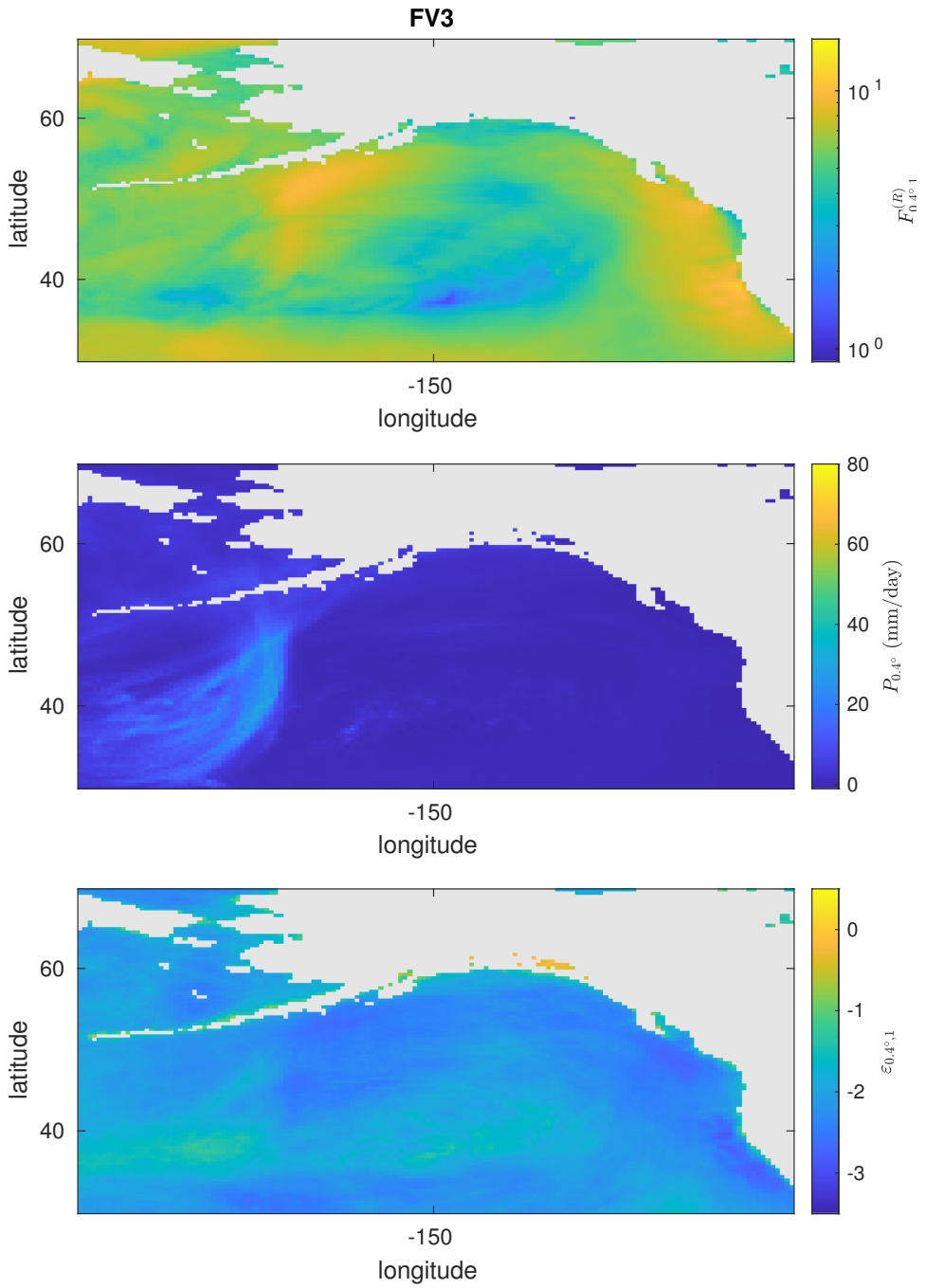

Figure A.19: Time means of $F^{(R)}_{0.4^\circ,1}$, $P_{0.4^\circ}$, $\varepsilon_{0.4^\circ,1}$ in the subarctic Northeast Pacific for the FV3 model. Vertical axis denotes latitude, whereas the horizontal axis denotes longitude.

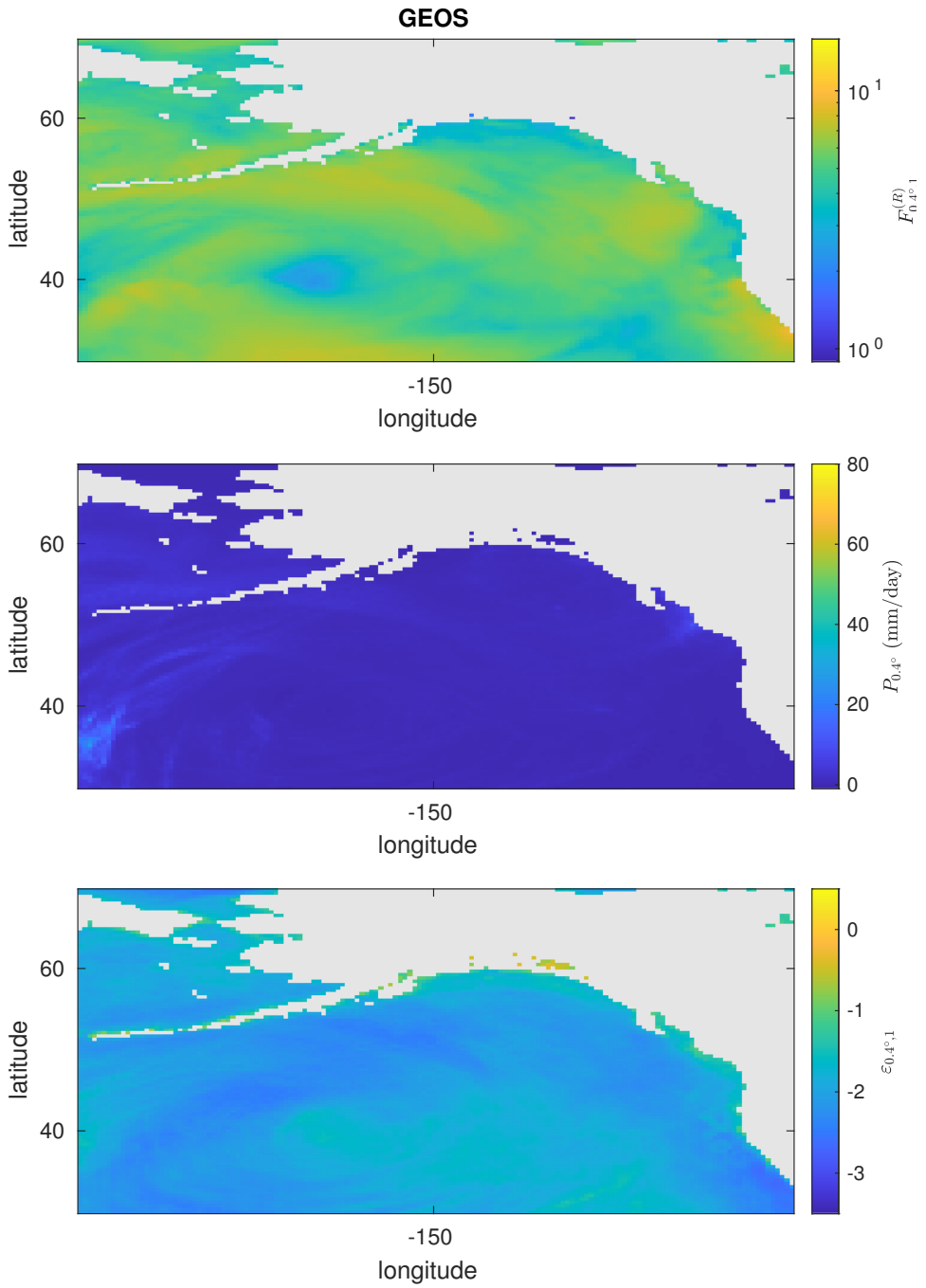

Figure A.20: Time means of $F^{(R)}_{0.4^\circ,1}$, $P_{0.4^\circ}$, $\varepsilon_{0.4^\circ,1}$ in the subarctic Northeast Pacific for the GEOS model. Vertical axis denotes latitude, whereas the horizontal axis denotes longitude.

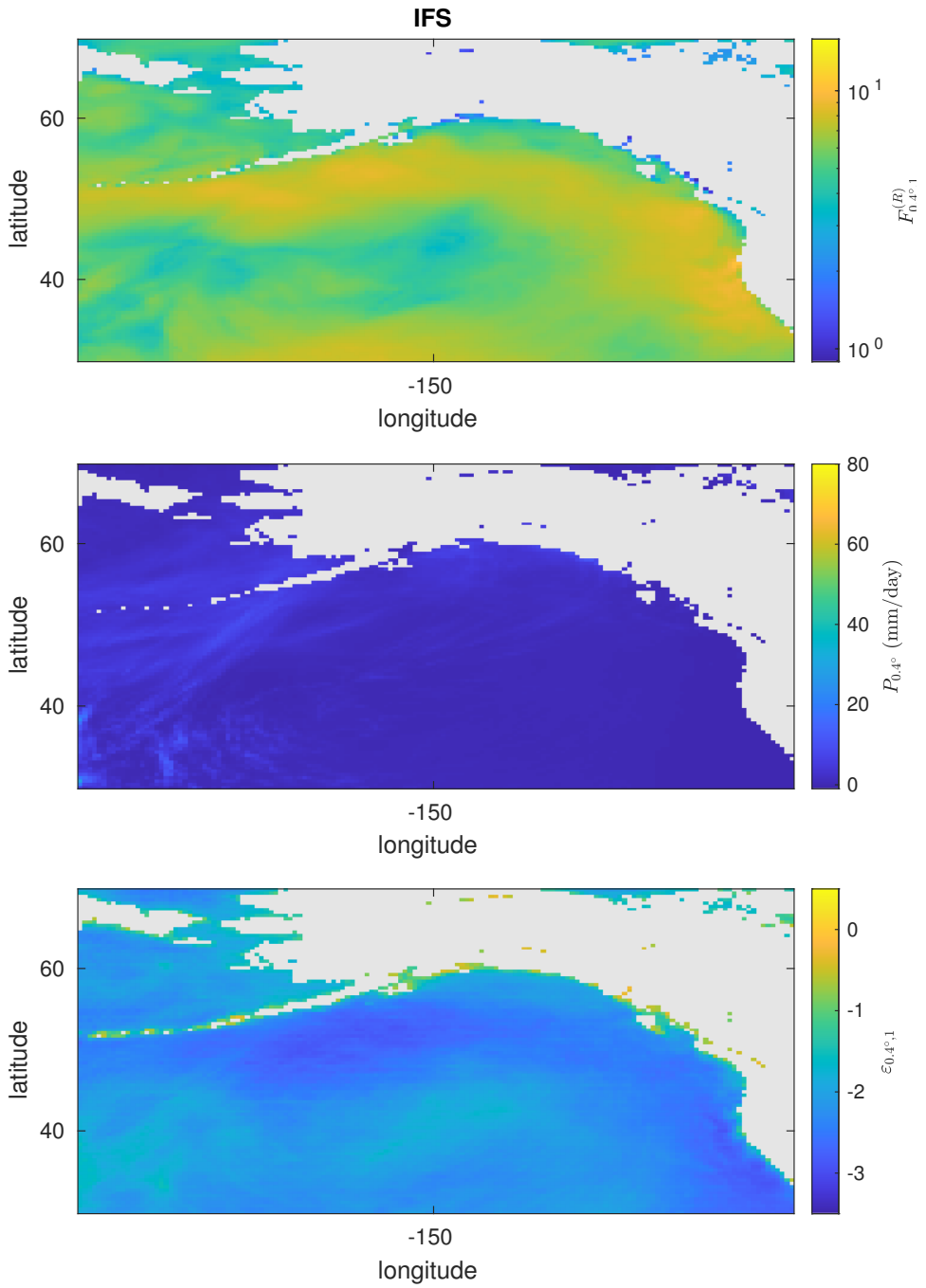

Figure A.21: Time means of $F^{(R)}_{0.4^\circ,1}$, $P_{0.4^\circ}$, $\varepsilon_{0.4^\circ,1}$ in the subarctic Northeast Pacific for the IFS model. Vertical axis denotes latitude, whereas the horizontal axis denotes longitude.

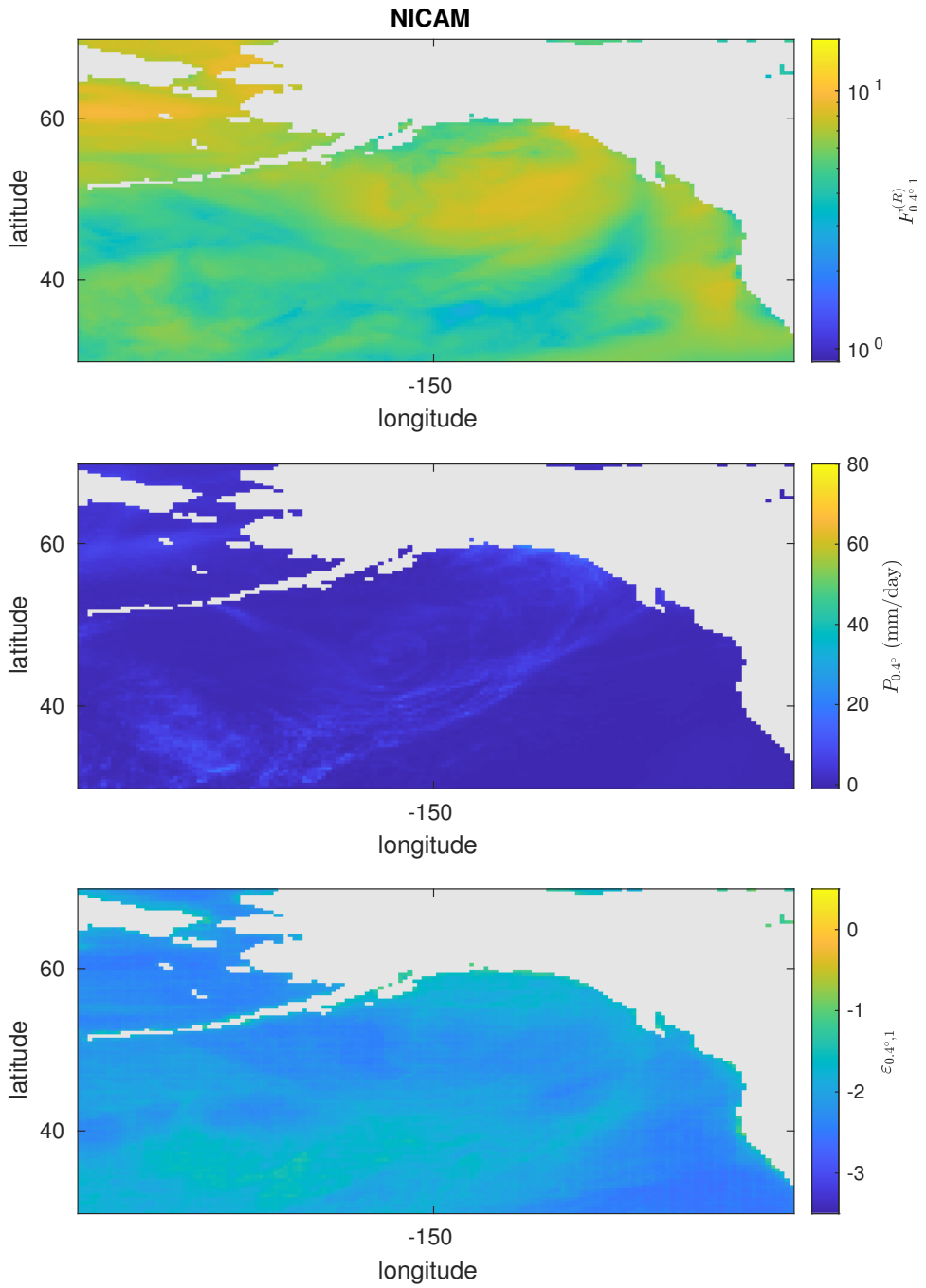

Figure A.22: Time means of $F^{(R)}_{0.4^\circ,1}$, $P_{0.4^\circ}$, $\varepsilon_{0.4^\circ,1}$ in the subarctic Northeast Pacific for the NICAM model. Vertical axis denotes latitude, whereas the horizontal axis denotes longitude.

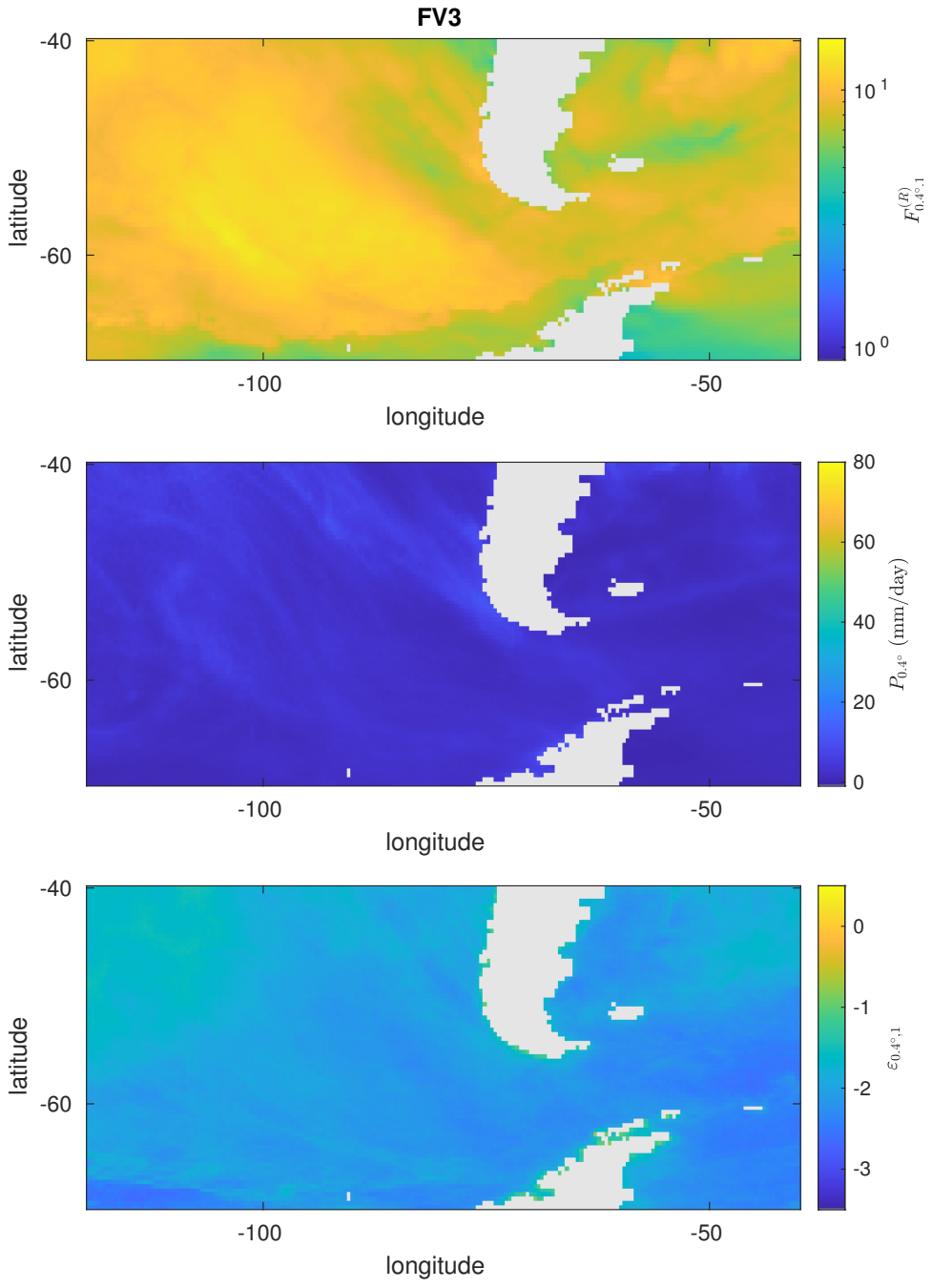

Figure A.23: Time means of $F^{(R)}_{0.4^\circ,1}$, $P_{0.4^\circ}$, $\varepsilon_{0.4^\circ,1}$ in the Southern Ocean for the FV3 model. Vertical axis denotes latitude, whereas the horizontal axis denotes longitude.

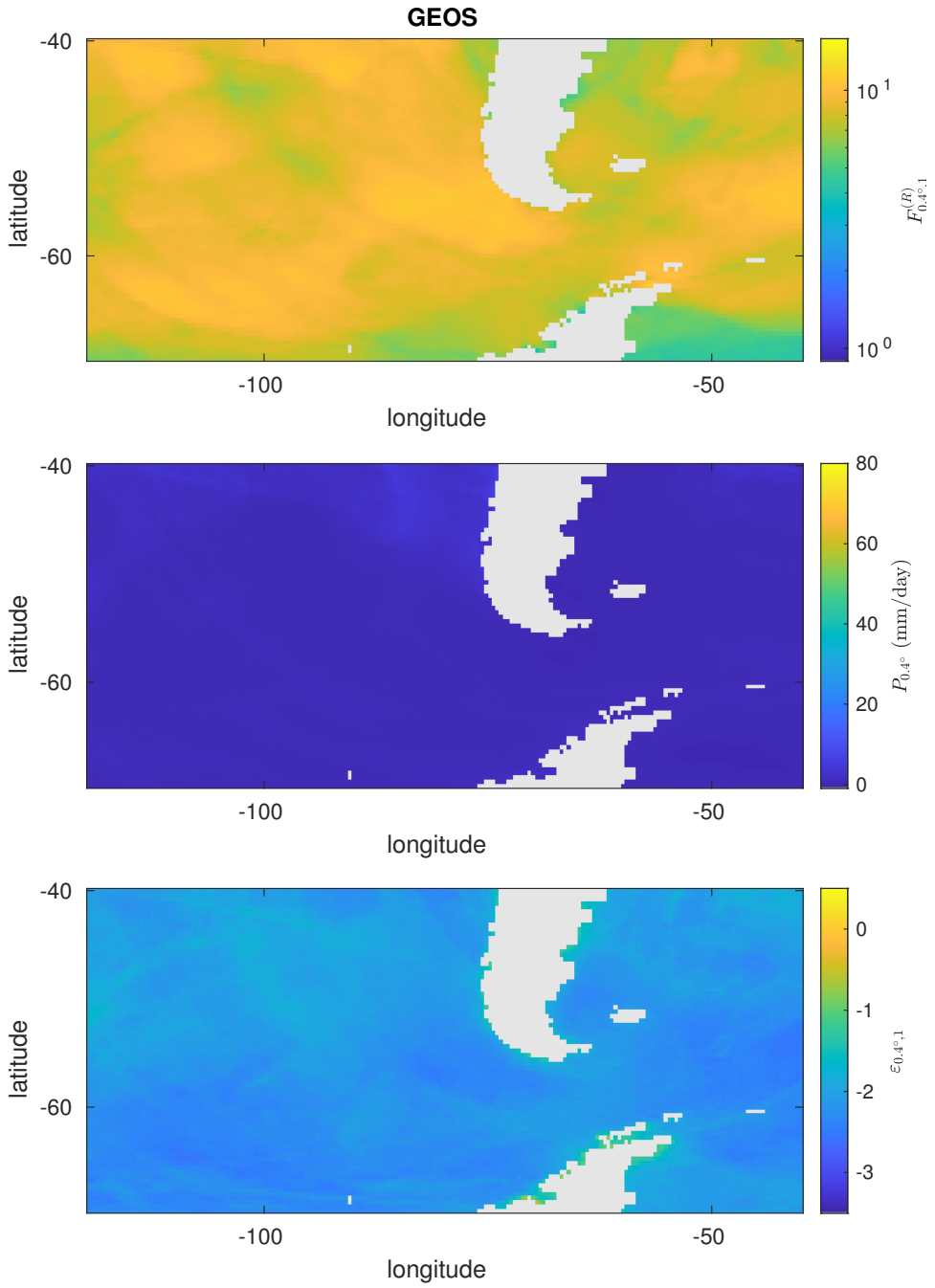

Figure A.24: Time means of $F^{(R)}_{0.4^\circ,1}$, $P_{0.4^\circ}$, $\varepsilon_{0.4^\circ,1}$ in the Southern Ocean for the GEOS model. Vertical axis denotes latitude, whereas the horizontal axis denotes longitude.

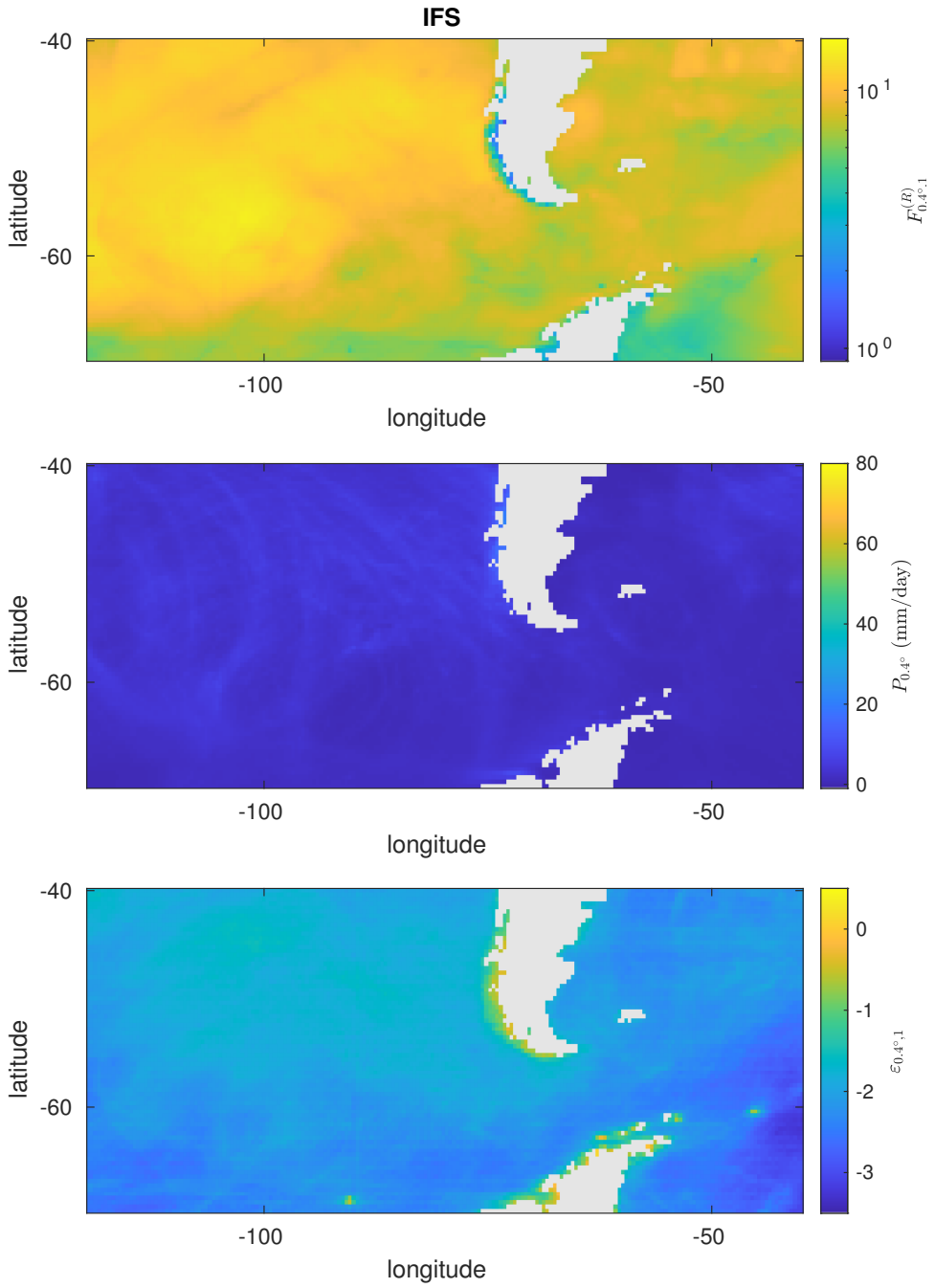

Figure A.25: Time means of $F^{(R)}_{0.4^\circ,1}$, $P_{0.4^\circ}$, $\varepsilon_{0.4^\circ,1}$ in the Southern Ocean for the IFS model. Vertical axis denotes latitude, whereas the horizontal axis denotes longitude.

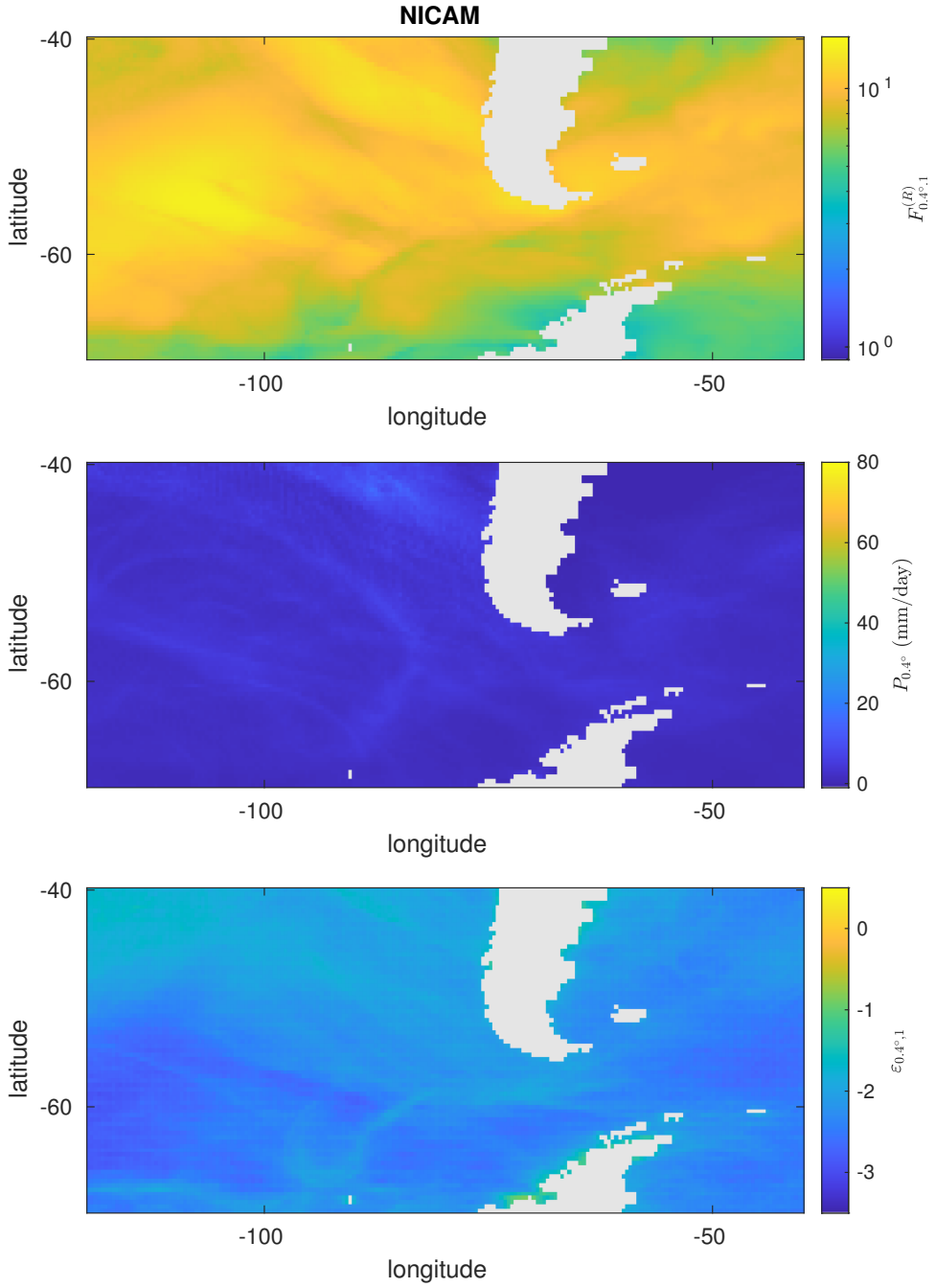

Figure A.26: Time means of $F^{(R)}_{0.4^\circ,1}$, $P_{0.4^\circ}$, $\varepsilon_{0.4^\circ,1}$ in the Southern Ocean for the NICAM model. Vertical axis denotes latitude, whereas the horizontal axis denotes longitude.

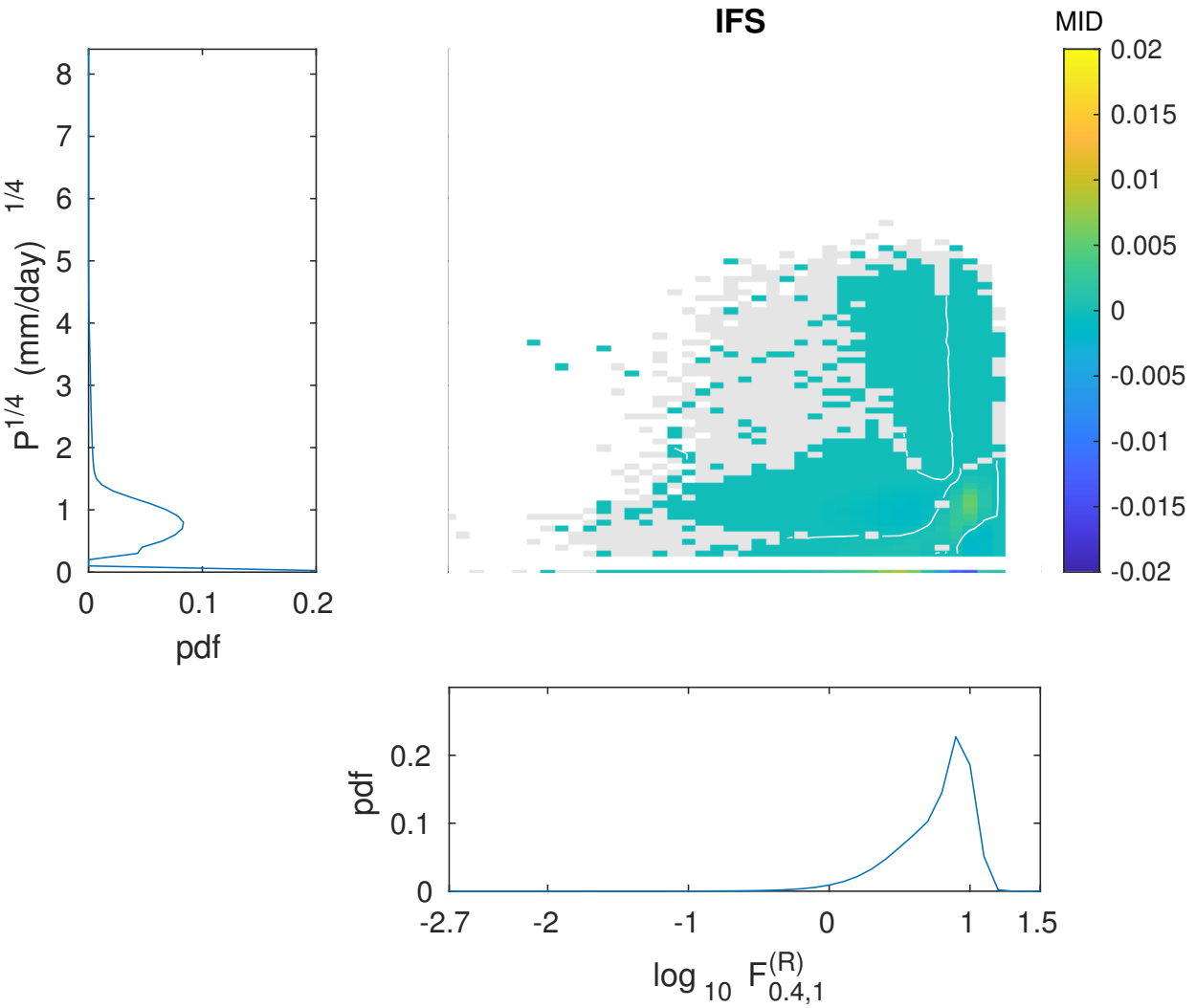

Figure A.27: Marginal distributions and mutual information densities in the Warm Pool, IFS model, $N = 0.4°$, $n = 1$. Colour denotes five percent statistical significance with a two-tail test. White contour denotes a value of zero.

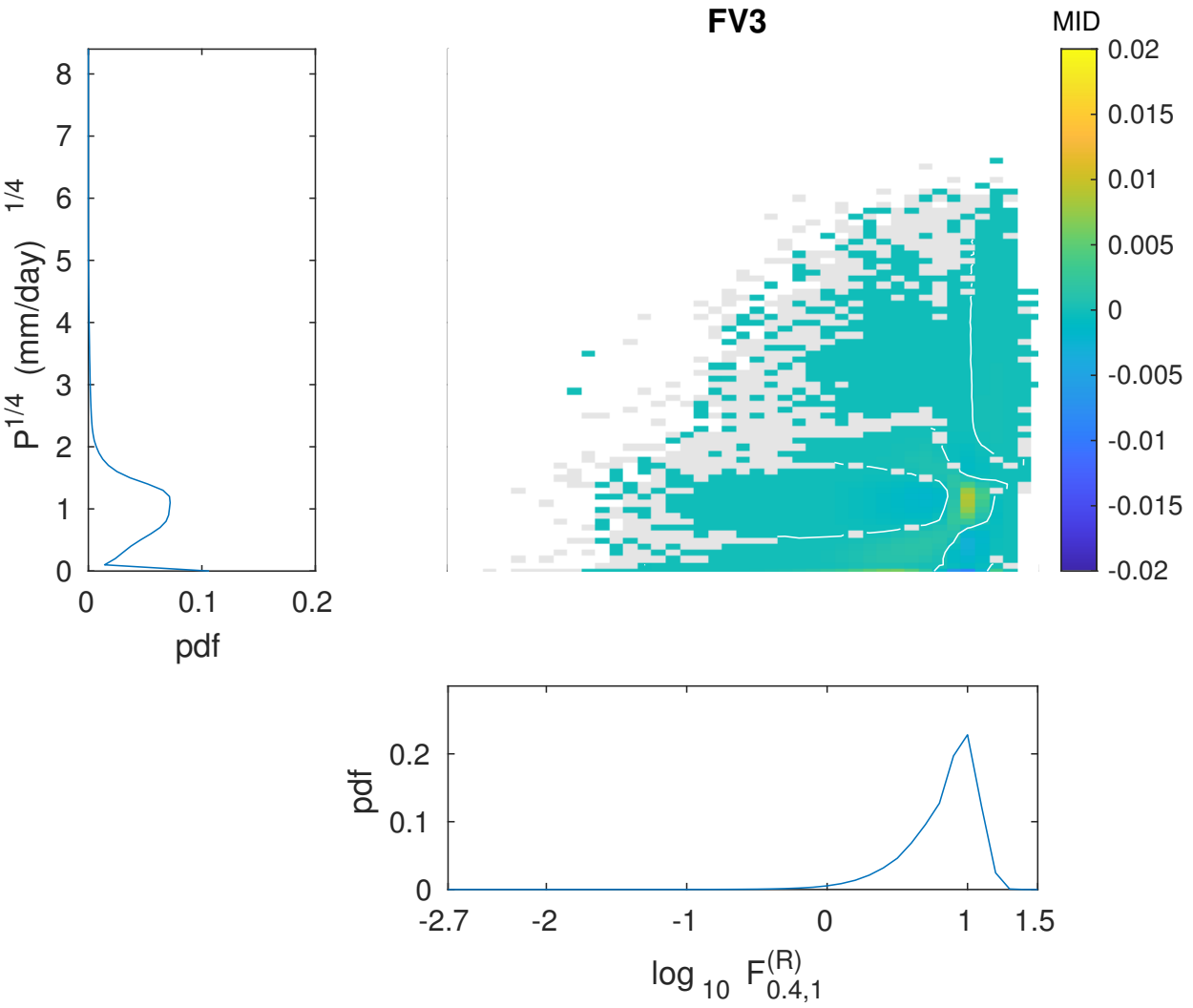

Figure A.28: Marginal distributions and mutual information densities in the Warm Pool, FV3 model, $N = 0.4°$, $n = 1$. Colour denotes five percent statistical significance with a two-tail test. White contour denotes a value of zero.

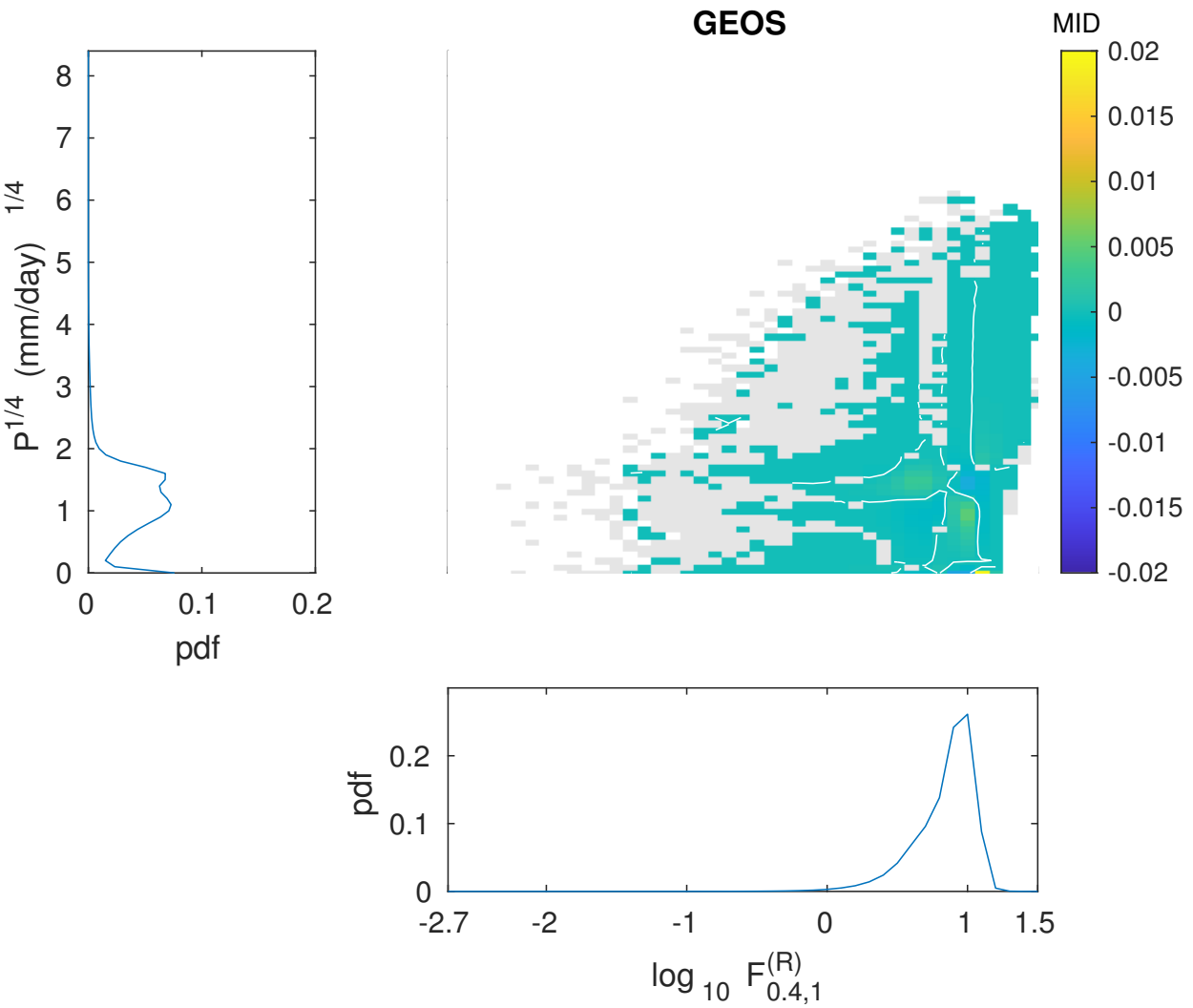

Figure A.29: Marginal distributions and mutual information densities in the Warm Pool, GEOS model, $N = 0.4°$, $n = 1$. Colour denotes five percent statistical significance with a two-tail test. White contour denotes a value of zero.

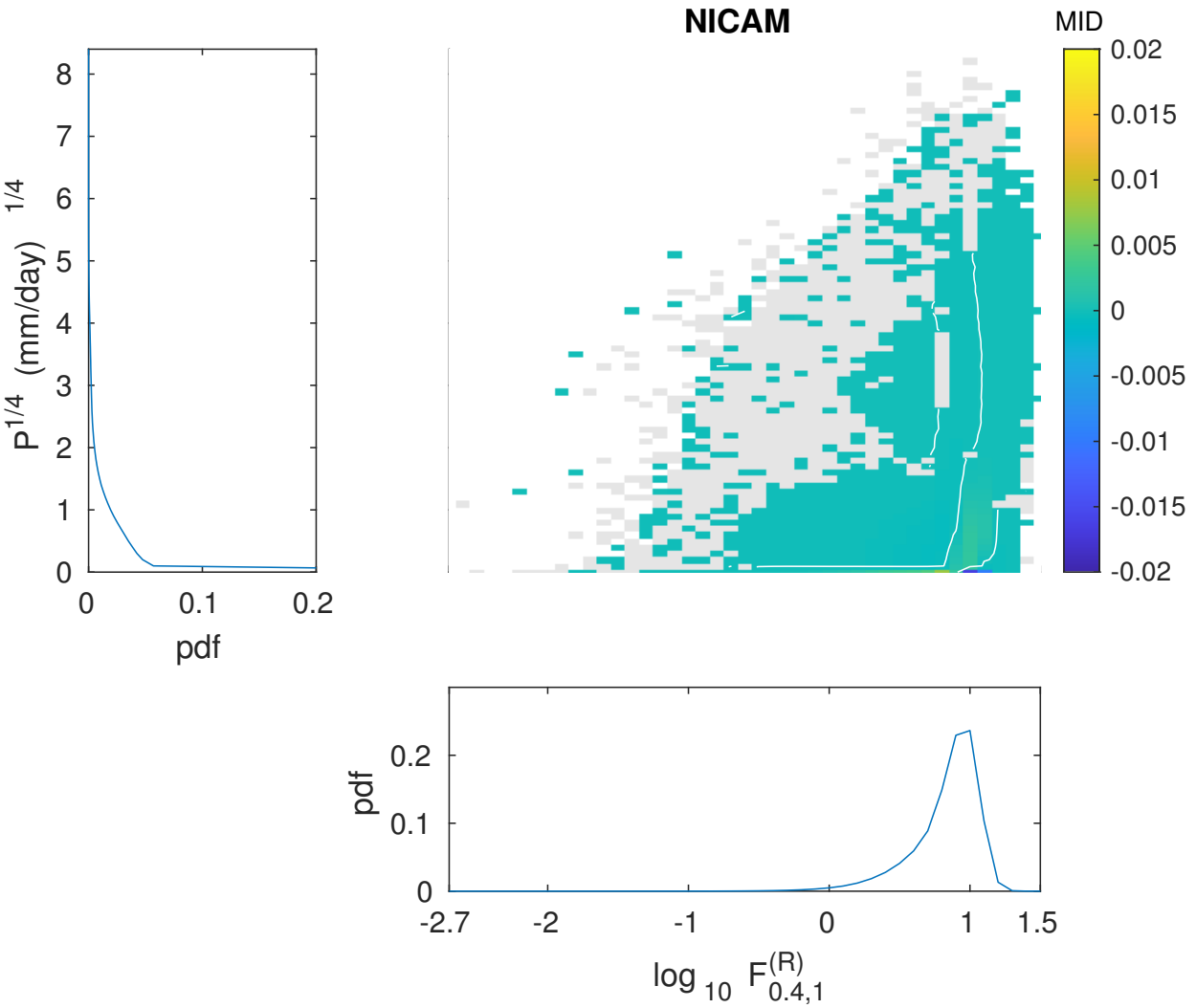

Figure A.30: Marginal distributions and mutual information densities in the Warm Pool, NICAM model, $N = 0.4°$, $n = 1$. Colour denotes five percent statistical significance with a two-tail test. White contour denotes a value of zero.

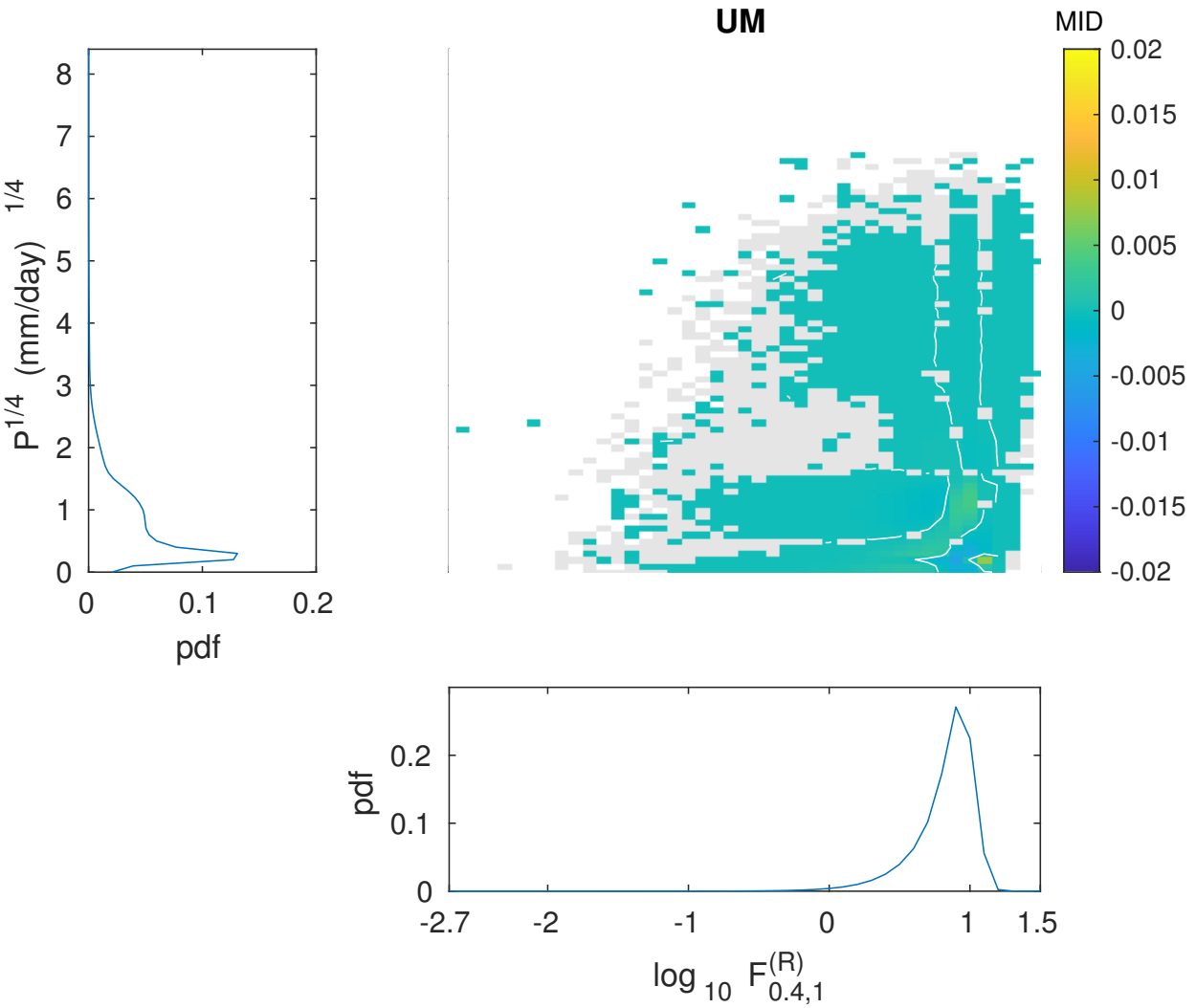

Figure A.31: Marginal distributions and mutual information densities in the Warm Pool, UM model, $N = 0.4°$, $n = 1$. Colour denotes five percent statistical significance with a two-tail test. White contour denotes a value of zero.

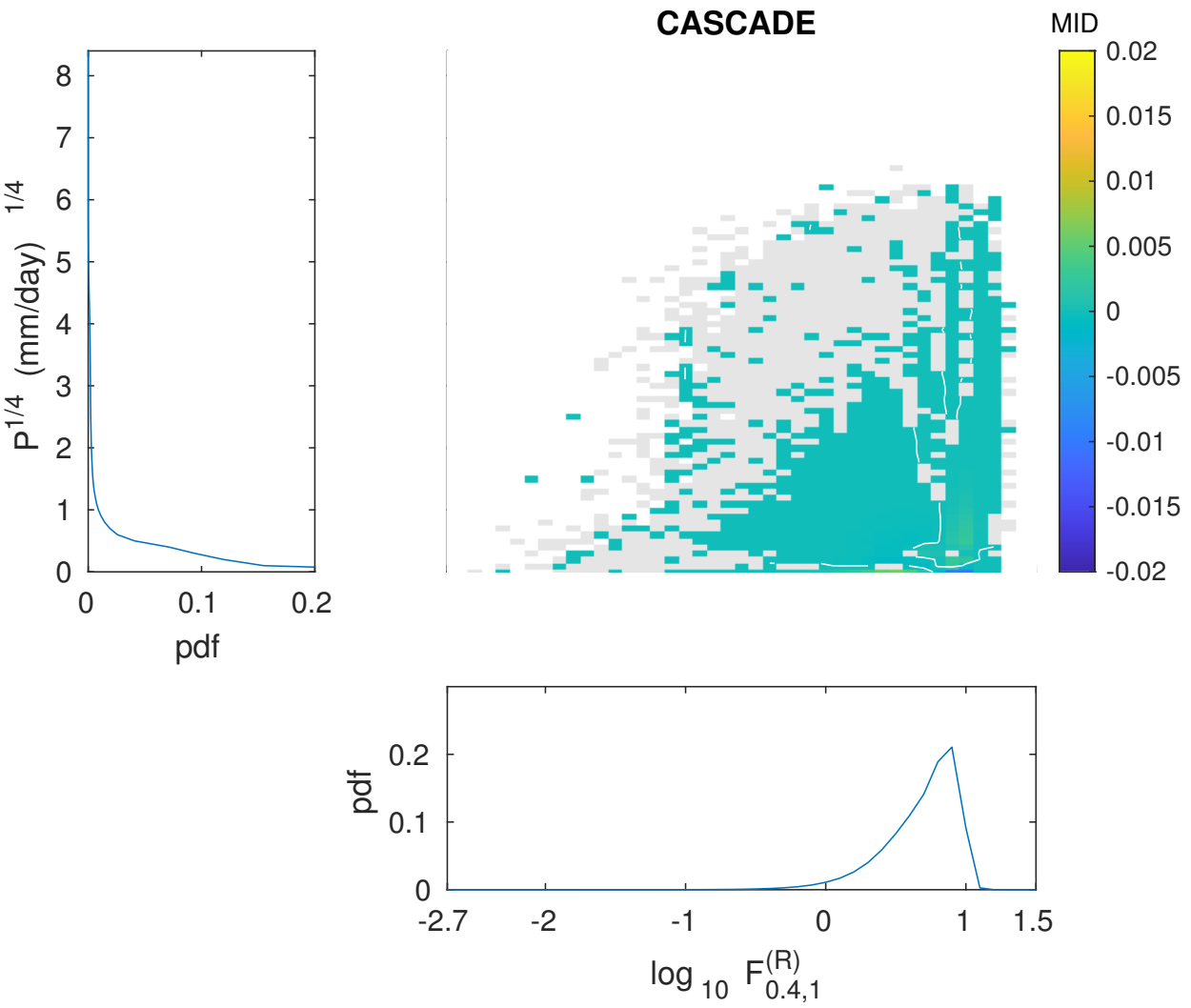

Figure A.32: Marginal distributions and mutual information densities in the Warm Pool, Cascade model run, $N = 0.4°$, $n = 1$. Colour denotes five percent statistical significance with a two-tail test. White contour denotes a value of zero.

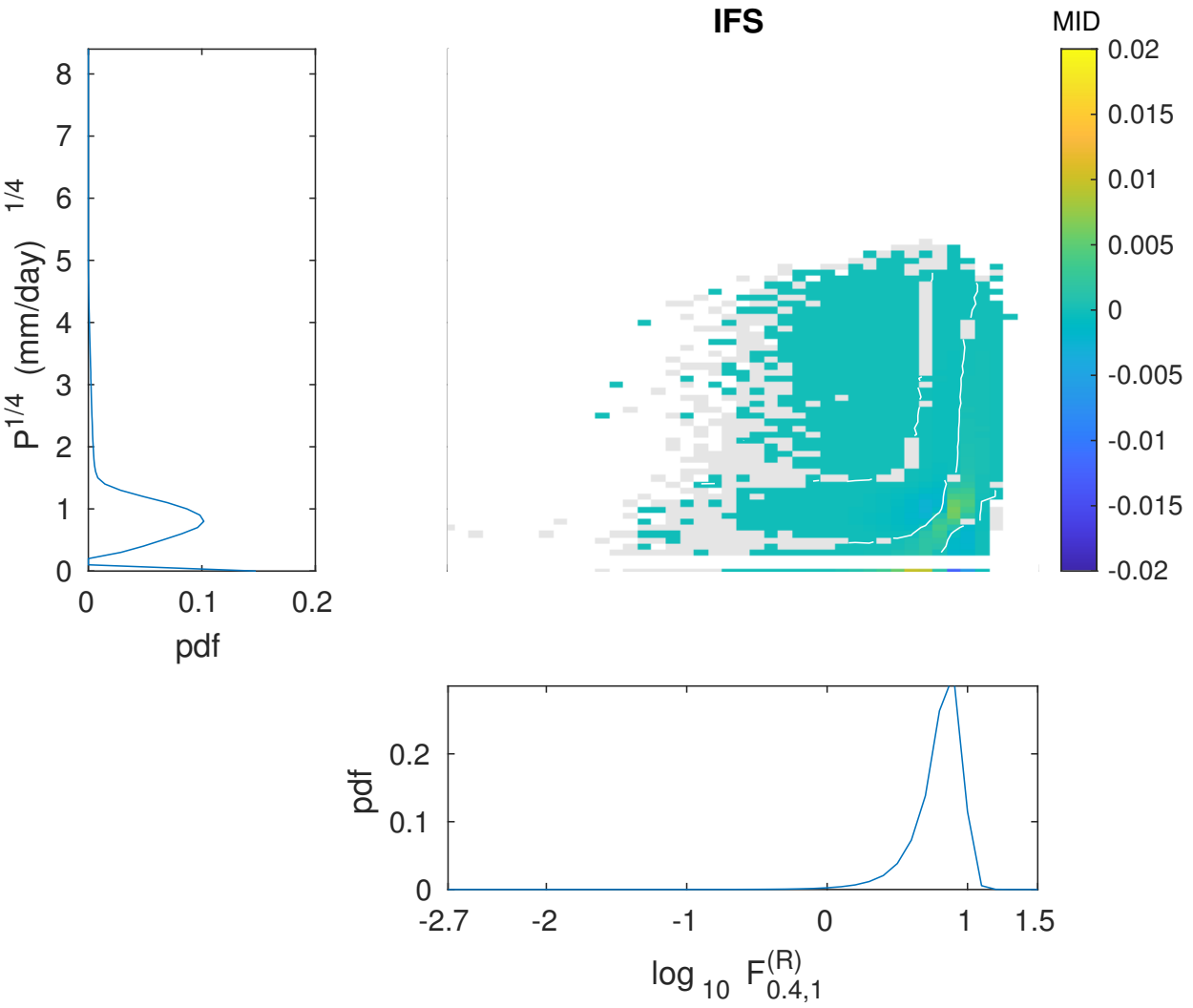

Figure A.33: Marginal distributions and mutual information densities in the subarctic Northeast Pacific, IFS model, $N = 0.4°$, $n = 1$. Colour denotes five percent statistical significance with a two-tail test. White contour denotes a value of zero.

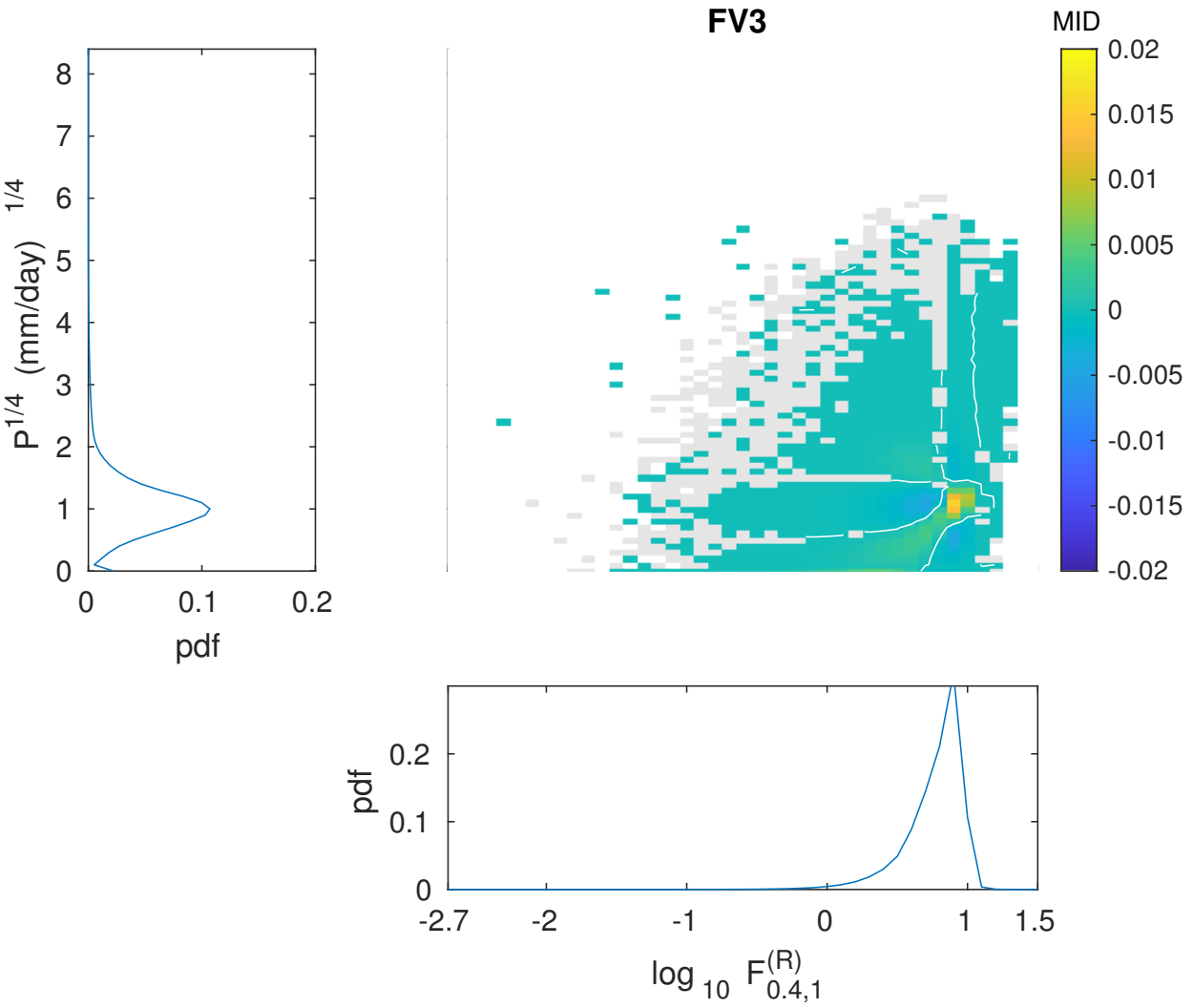

Figure A.34: Marginal distributions and mutual information densities in the subarctic Northeast Pacific, FV3 model, $N = 0.4°$, $n = 1$. Colour denotes five percent statistical significance with a two-tail test. White contour denotes a value of zero.

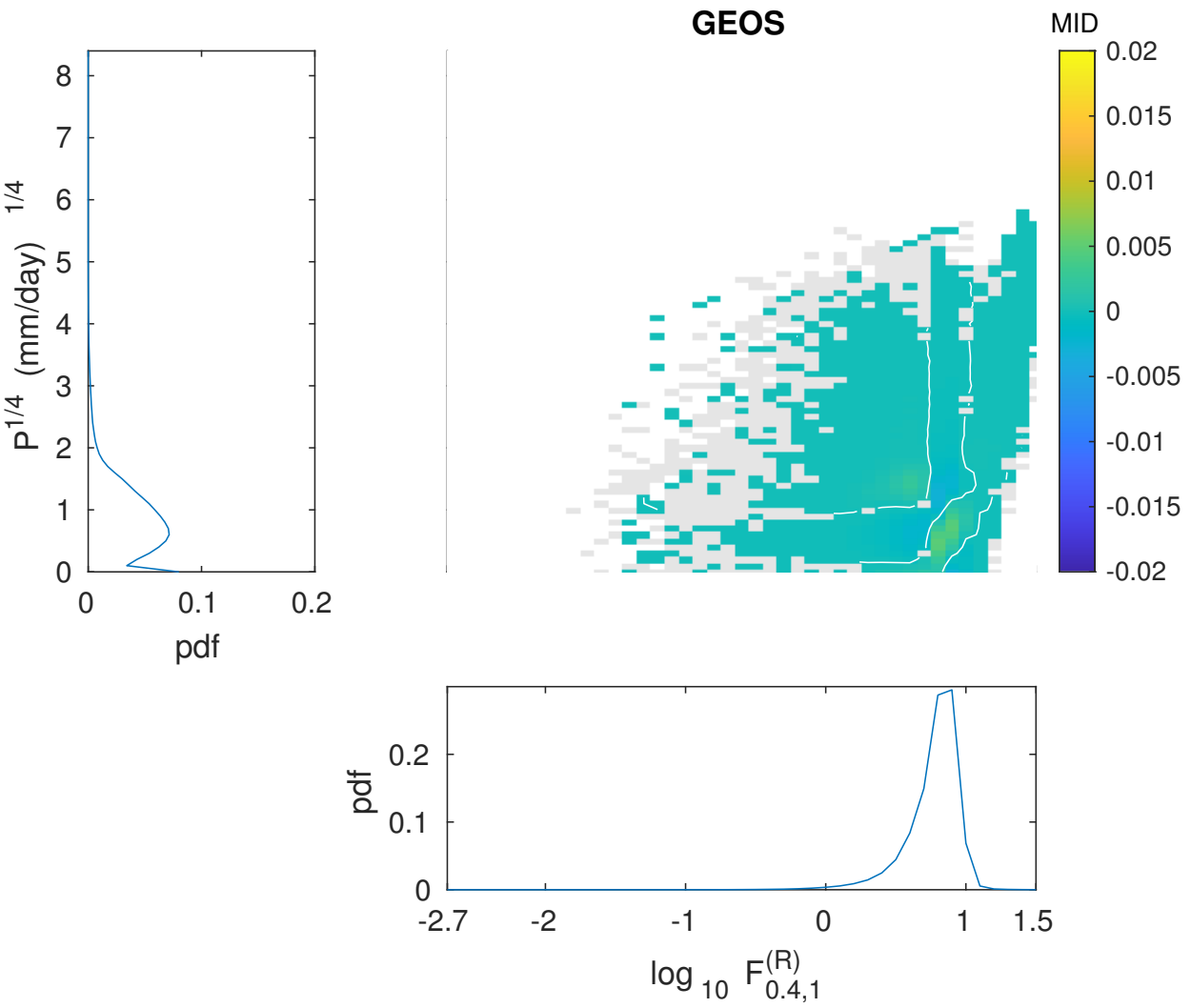

Figure A.35: Marginal distributions and mutual information densities in the subarctic Northeast Pacific, GEOS model, $N = 0.4°$, $n = 1$. Colour denotes five percent statistical significance with a two-tail test. White contour denotes a value of zero.

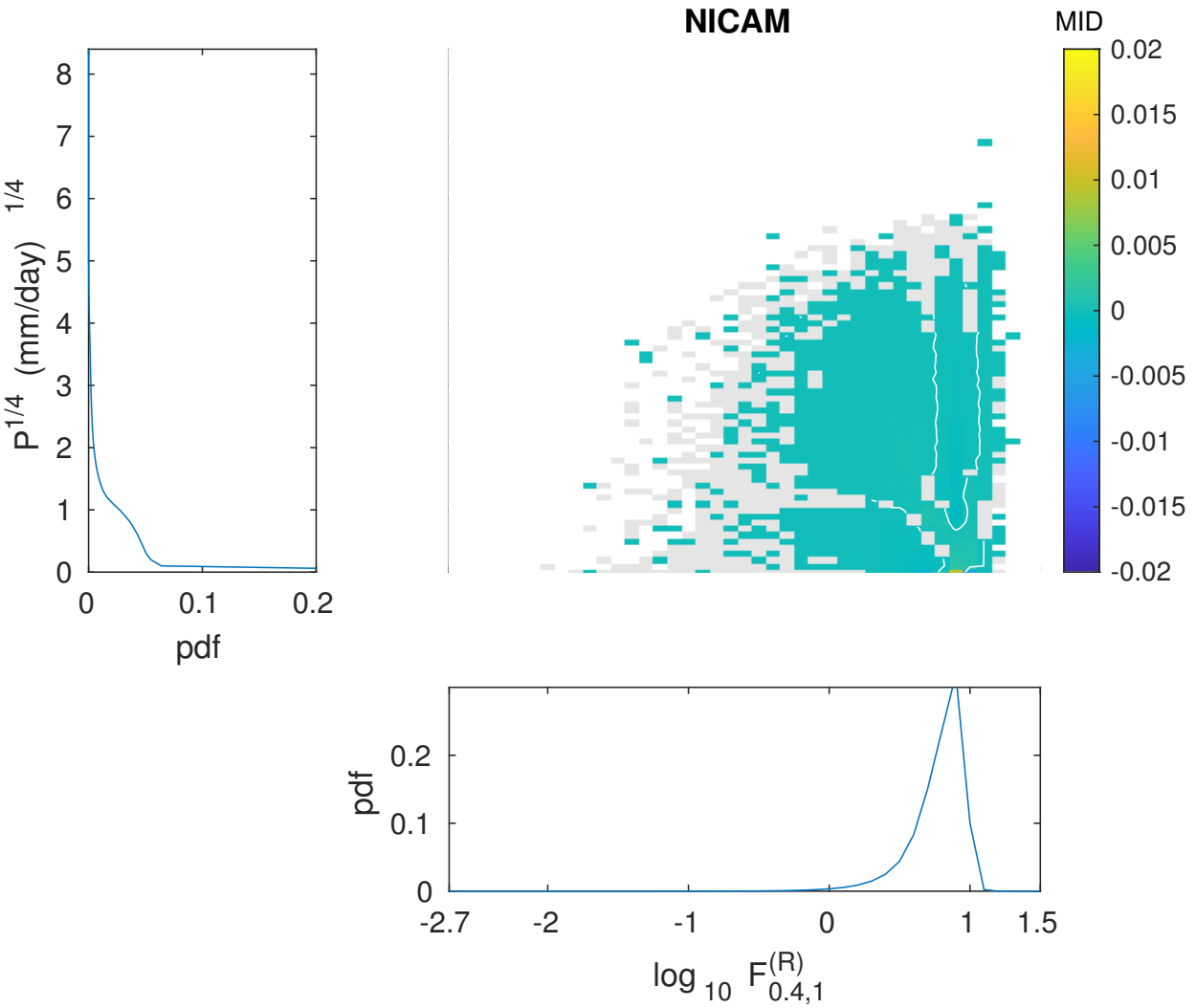

Figure A.36: Marginal distributions and mutual information densities in the subarctic Northeast Pacific, NICAM model, $N = 0.4°$, $n = 1$. Colour denotes five percent statistical significance with a two-tail test. White contour denotes a value of zero.

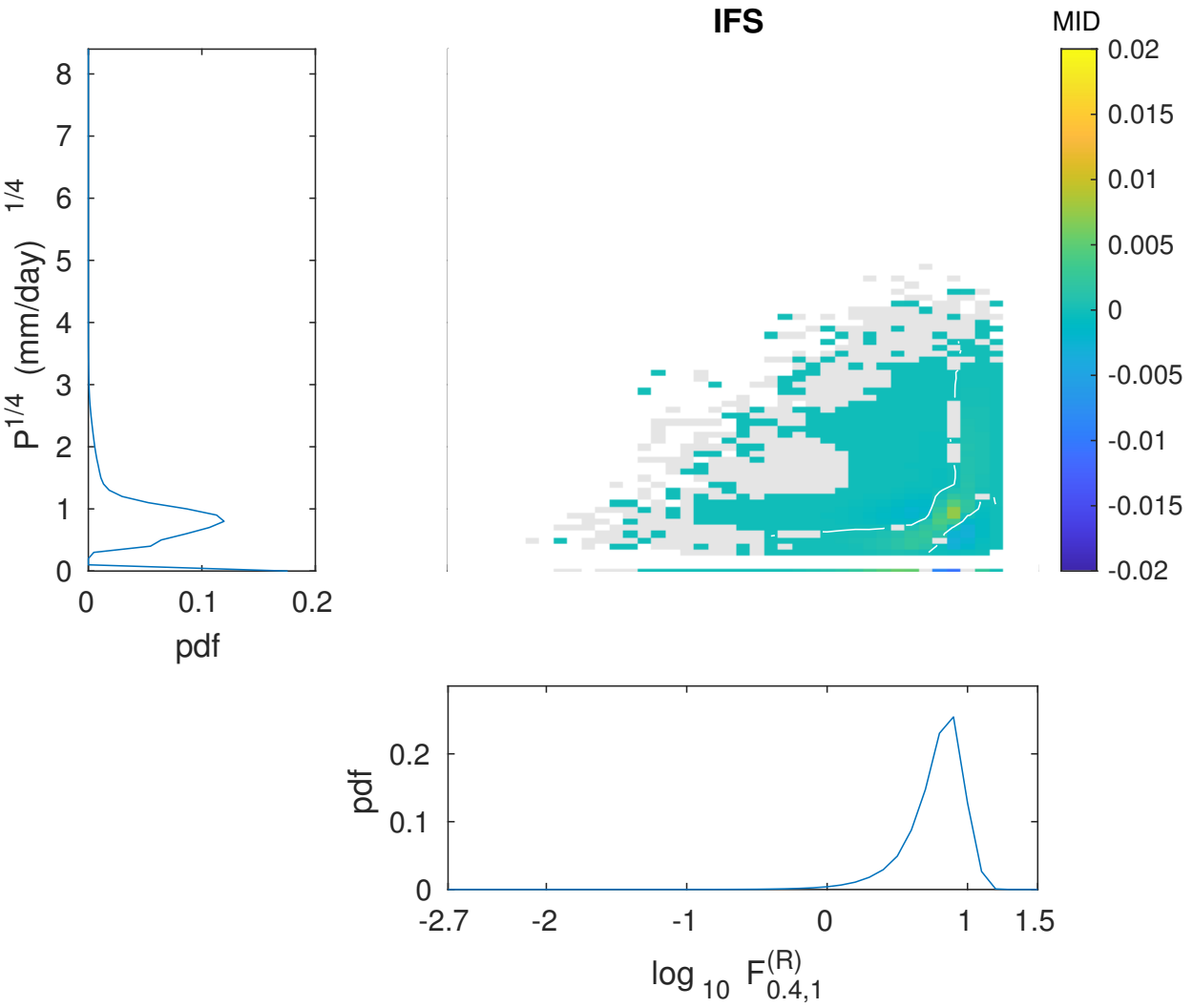

Figure A.37: Marginal distributions and mutual information densities in the subtropical Northeast Pacific, IFS model, $N = 0.4°$, $n = 1$. Colour denotes five percent statistical significance with a two-tail test. White contour denotes a value of zero.

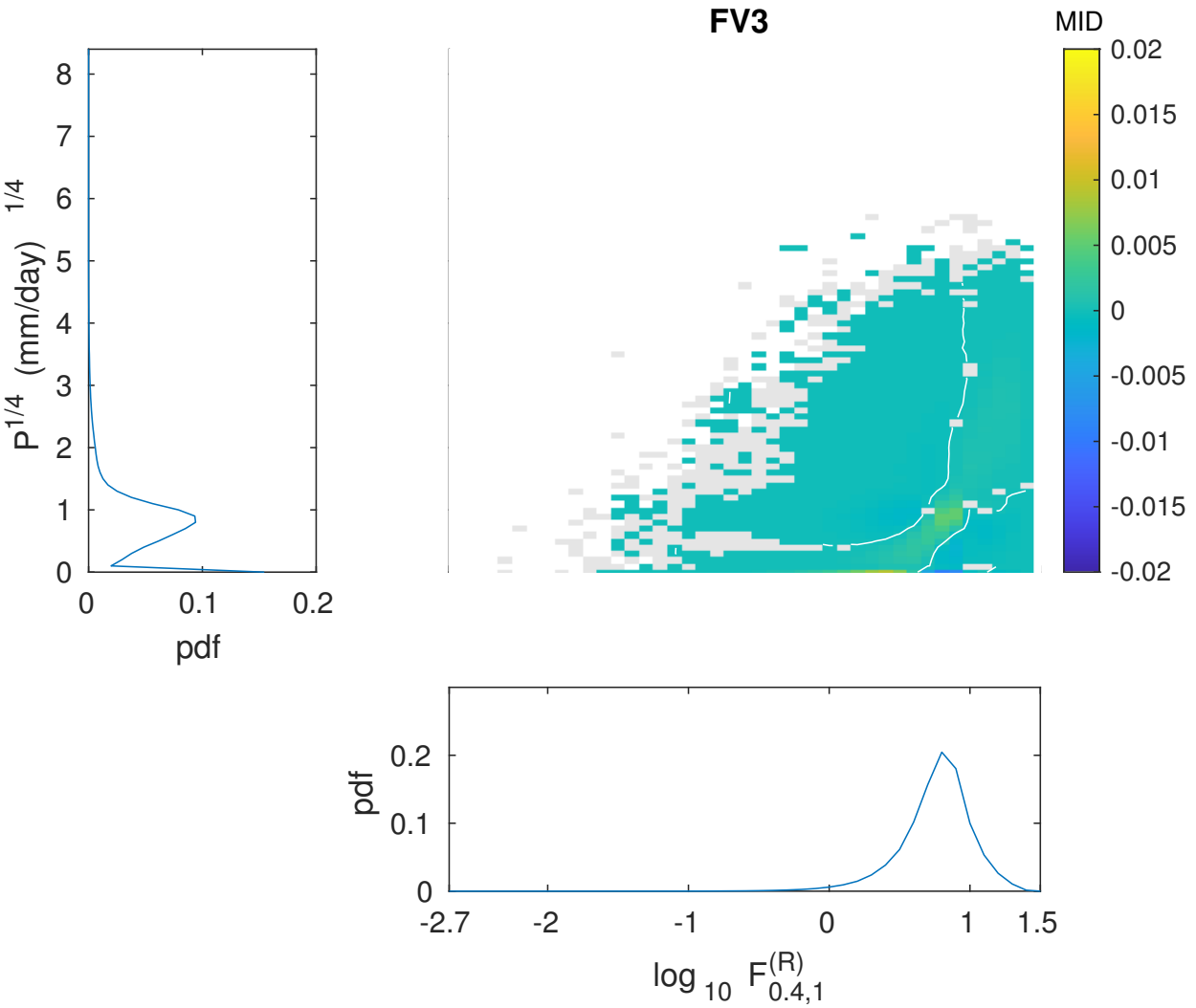

Figure A.38: Marginal distributions and mutual information densities in the subtropical Northeast Pacific, FV3 model, $N = 0.4°$, $n = 1$. Colour denotes five percent statistical significance with a two-tail test. White contour denotes a value of zero.

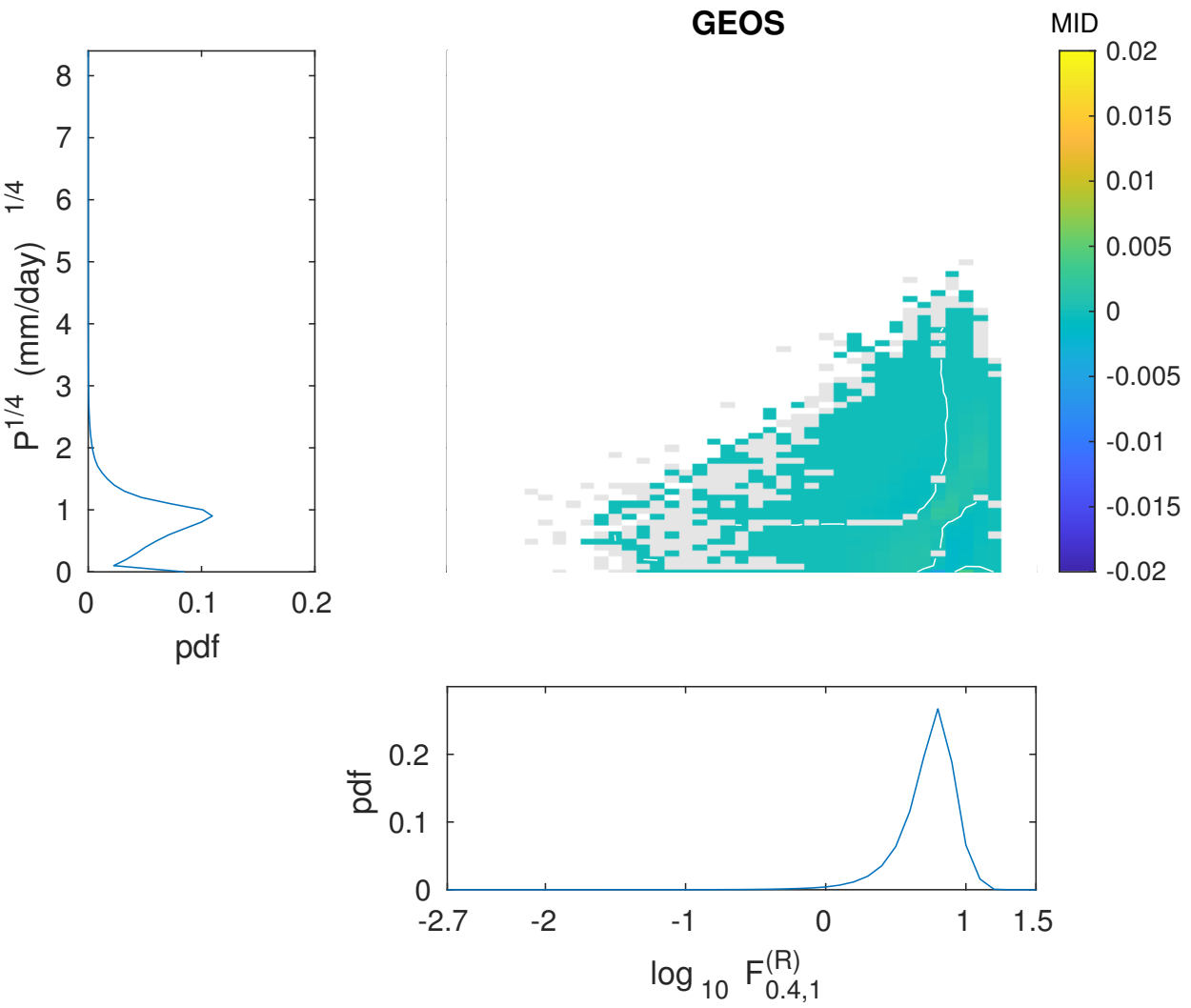

Figure A.39: Marginal distributions and mutual information densities in the subtropical Northeast Pacific, GEOS model, $N = 0.4°$, $n = 1$. Colour denotes five percent statistical significance with a two-tail test. White contour denotes a value of zero.

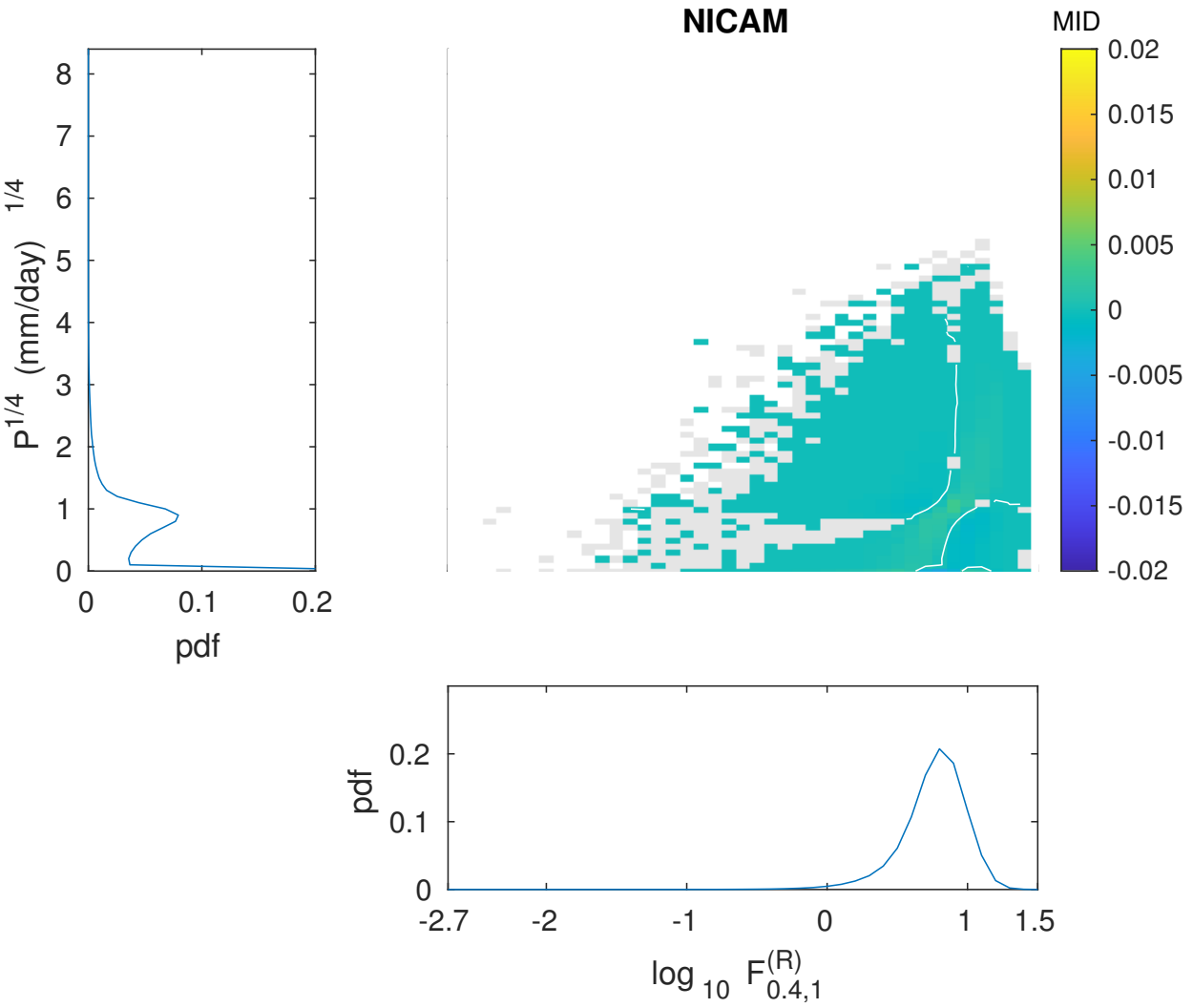

Figure A.40: Marginal distributions and mutual information densities in the subtropical Northeast Pacific, NICAM model, $N = 0.4°$, $n = 1$. Colour denotes five percent statistical significance with a two-tail test. White contour denotes a value of zero.

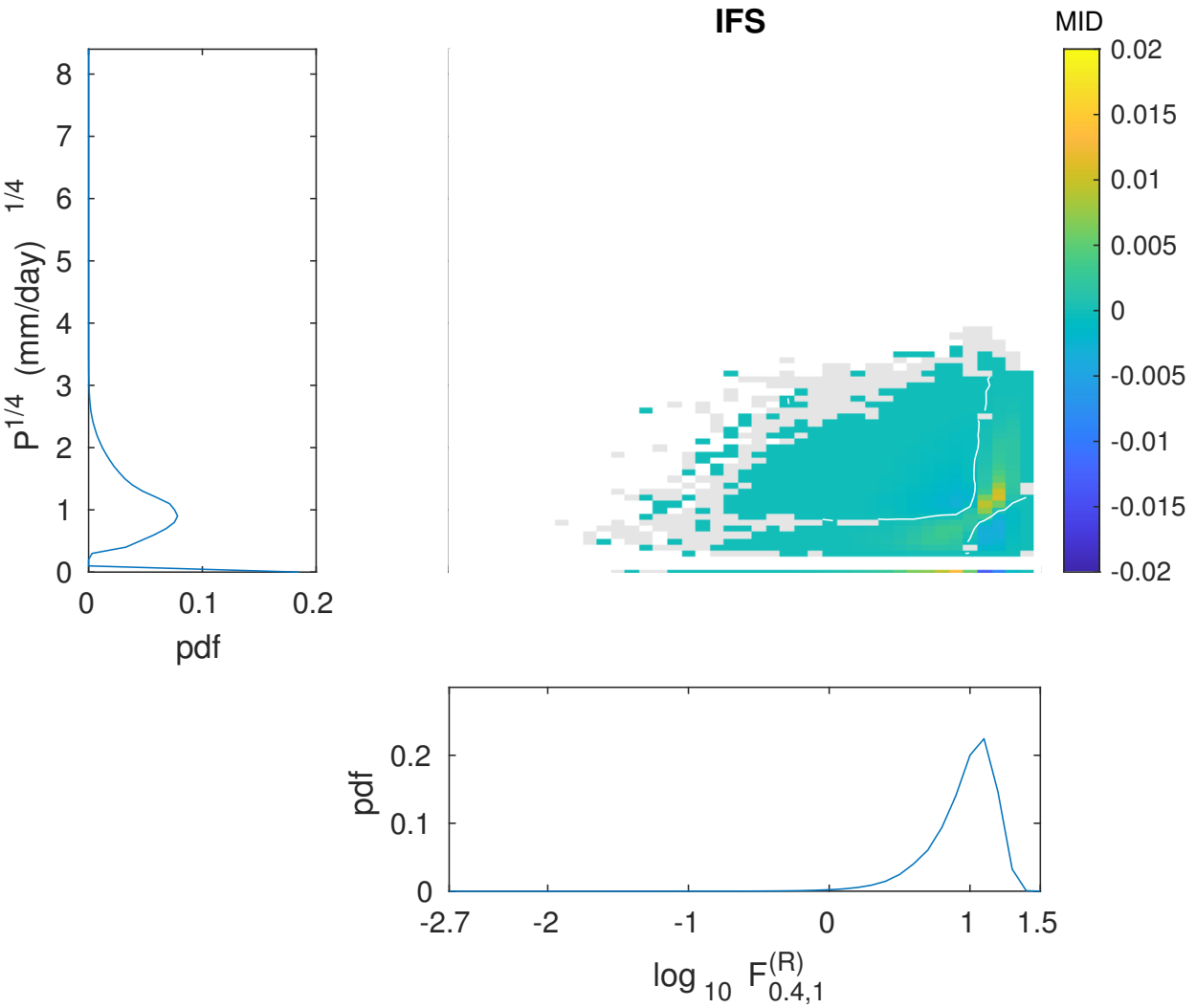

Figure A.41: Marginal distributions and mutual information densities in the Southern Ocean, IFS model, $N = 0.4°$, $n = 1$. Colour denotes five percent statistical significance with a two-tail test. White contour denotes a value of zero.

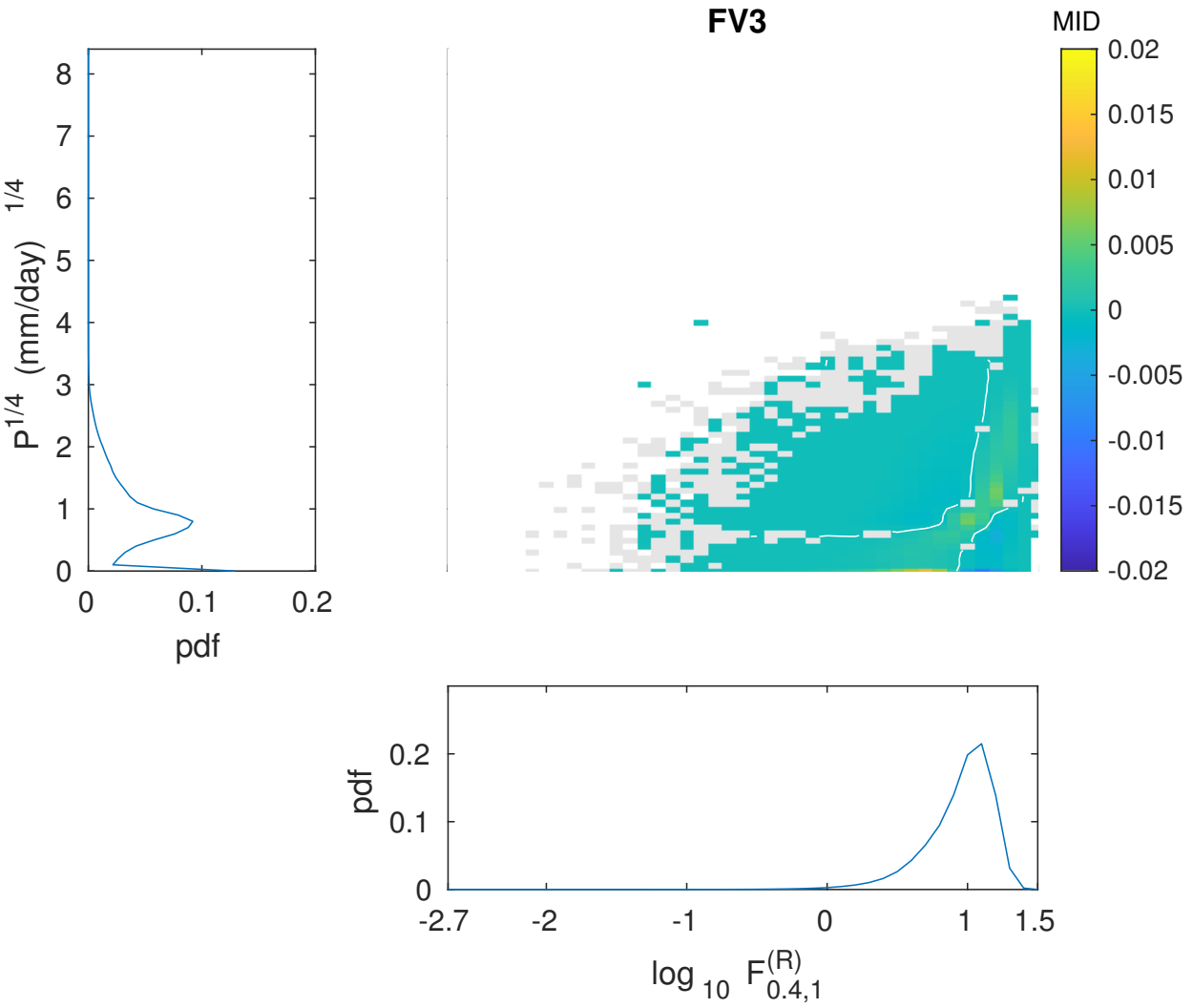

Figure A.42: Marginal distributions and mutual information densities in the Southern Ocean, FV3 model, $N = 0.4°$, $n = 1$. Colour denotes five percent statistical significance with a two-tail test. White contour denotes a value of zero.

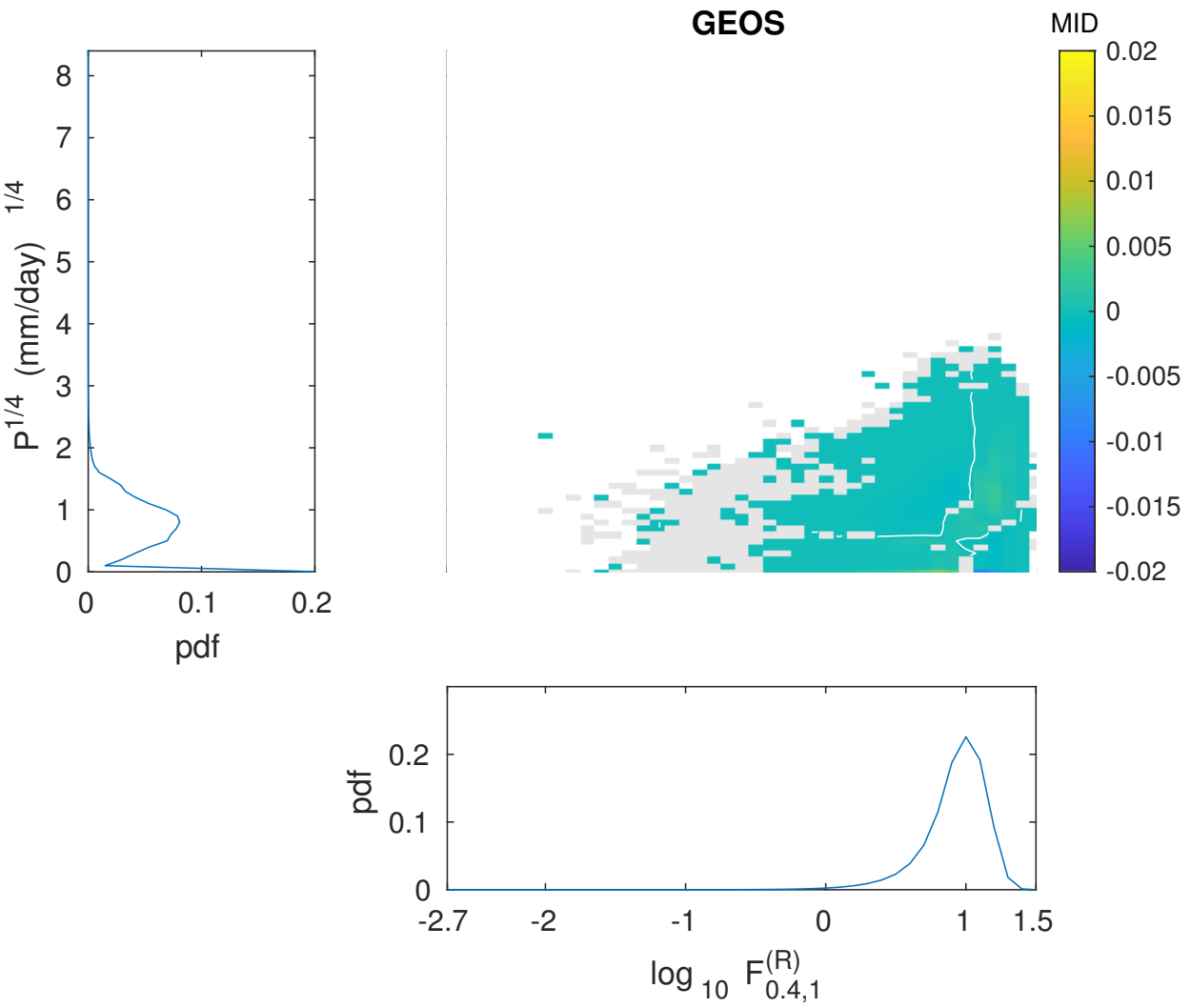

Figure A.43: Marginal distributions and mutual information densities in the Southern Ocean, GEOS model, $N = 0.4°$, $n = 1$. Colour denotes five percent statistical significance with a two-tail test. White contour denotes a value of zero.

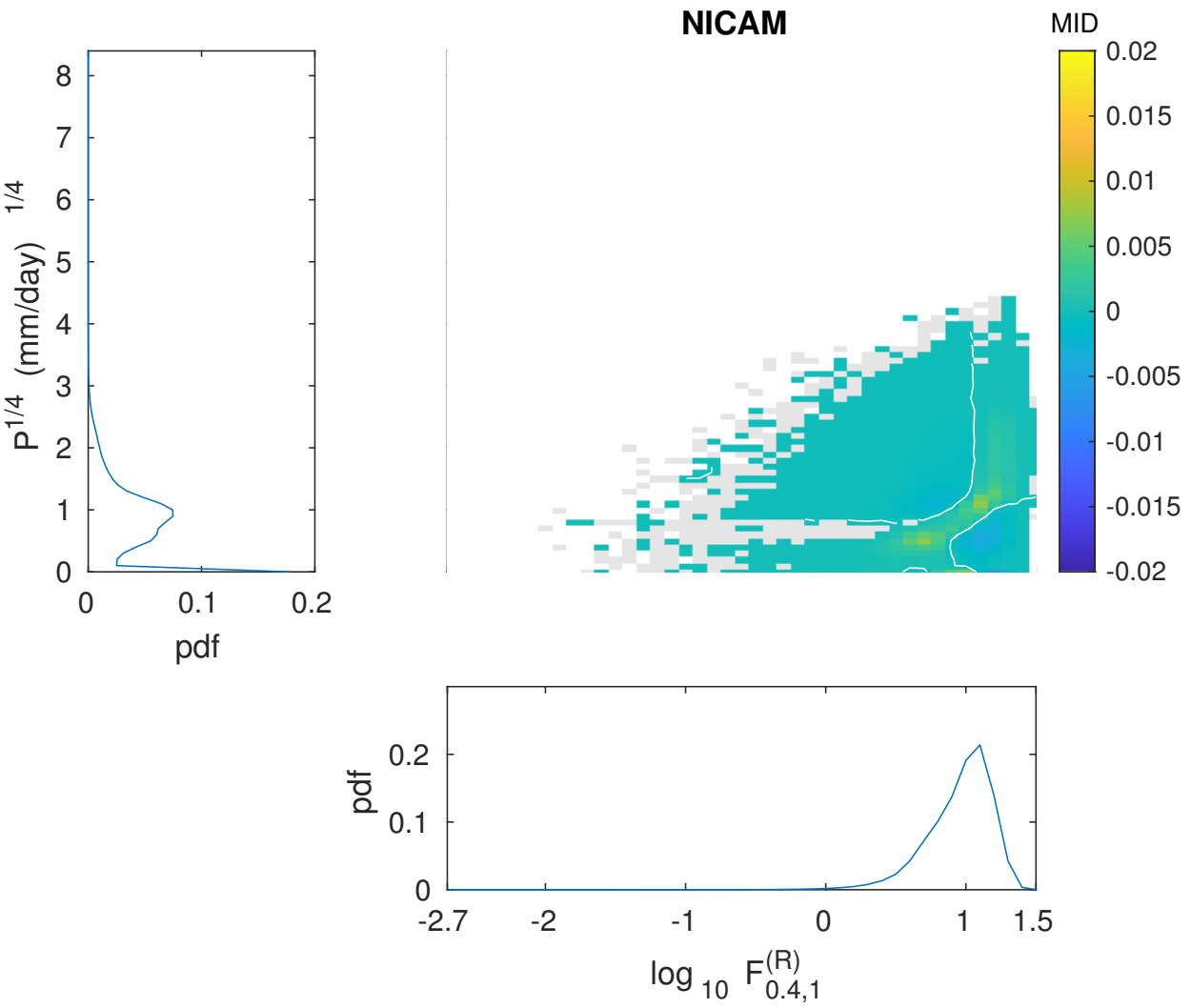

Figure A.44: Marginal distributions and mutual information densities in the Southern Ocean, NICAM model, $N = 0.4°$, $n = 1$. Colour denotes five percent statistical significance with a two-tail test. White contour denotes a value of zero.

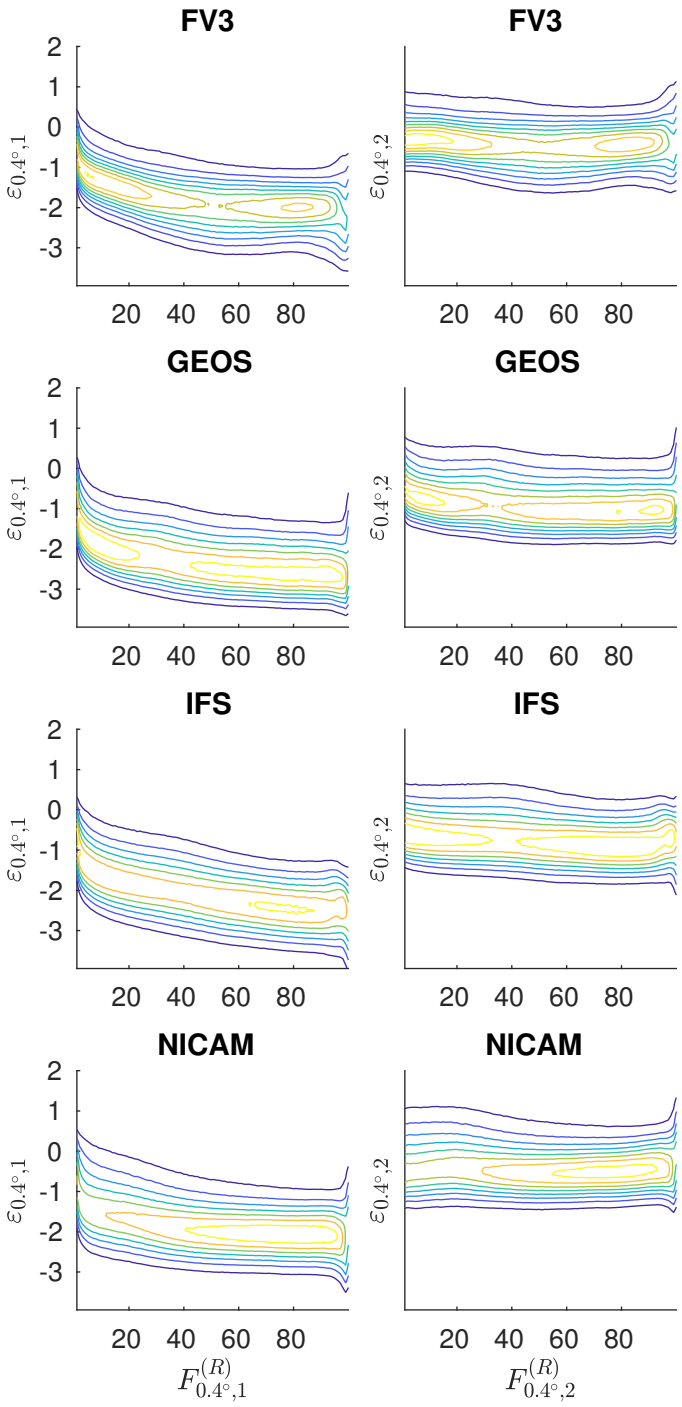

Figure A.45: Probability density function contours of the log 10 error processes conditioned on resolved flux percentiles for the Warm Pool domain. Left: $n = 1$. Right: $n = 2$. $N = 0.4^\circ$.

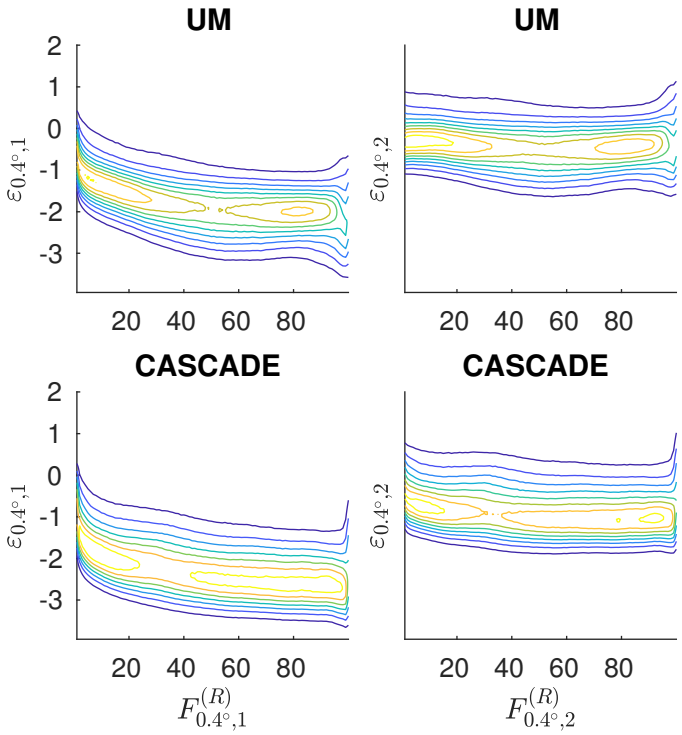

Figure A.46: Probability density function contours of the log 10 error processes conditioned on resolved flux percentiles for the Warm Pool domain. Left: $n = 1$. Right: $n = 2$. $N = 0.4^\circ$.

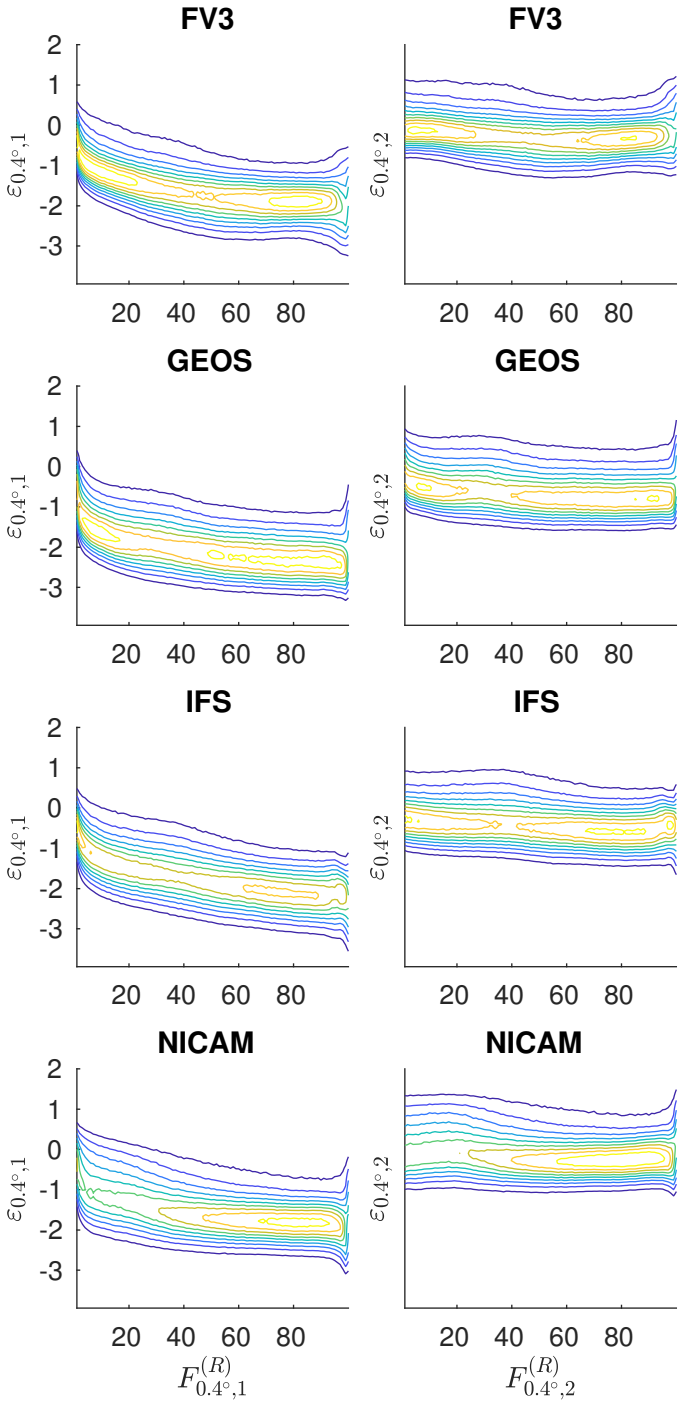

Figure A.47: Probability density function contours of the log 10 error processes conditioned on resolved flux percentiles for the Warm Pool domain. Left: $n = 1$. Right: $n = 2$. $N = 0.76^\circ$.

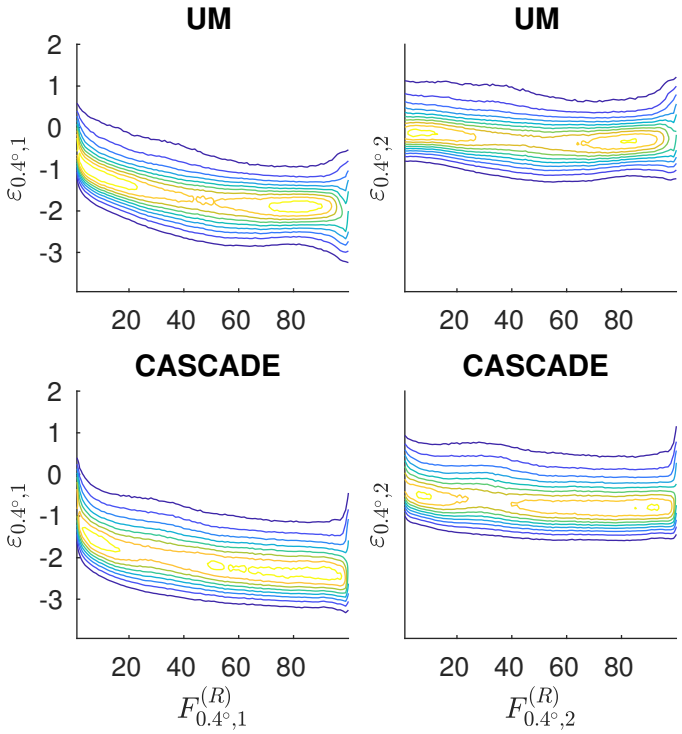

Figure A.48: Probability density function contours of the log 10 error processes conditioned on resolved flux percentiles for the Warm Pool domain. Left: $n = 1$. Right: $n = 2$. $N = 0.76^\circ$.

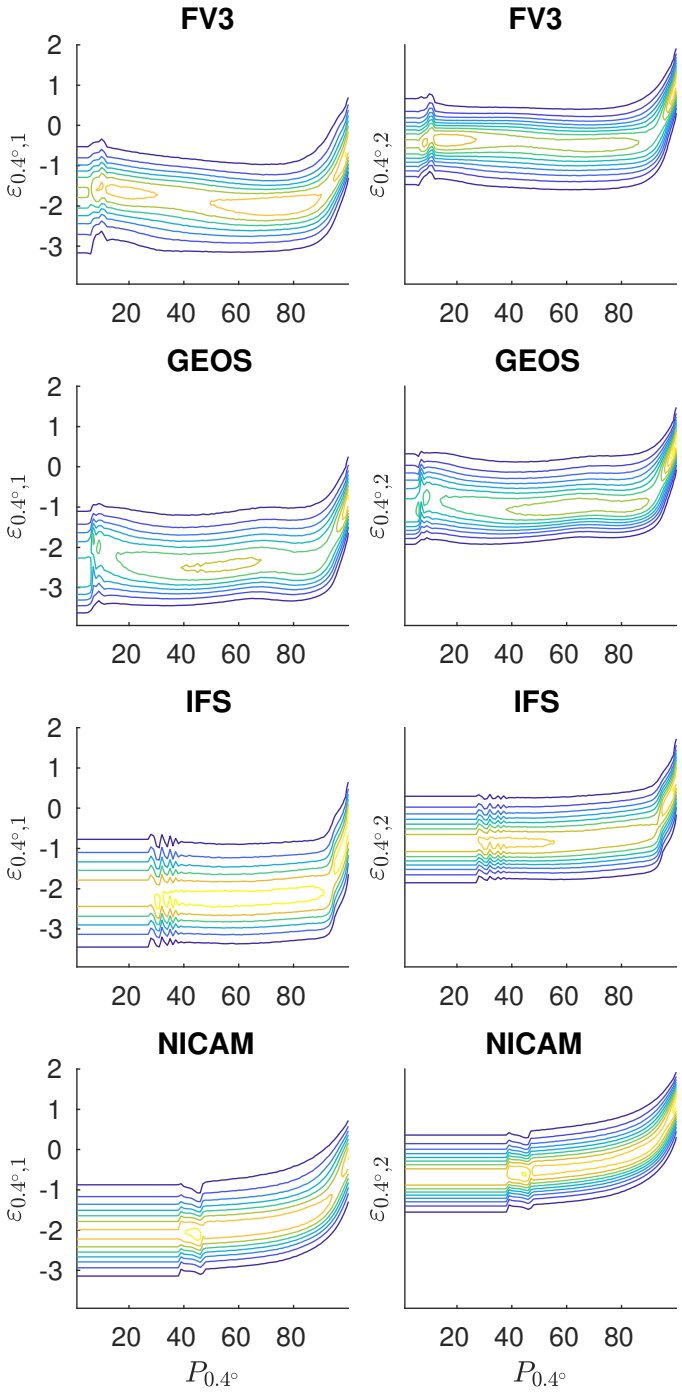

Figure A.49: Probability density function contours of the log 10 error processes conditioned on precipitation percentiles for the Warm Pool domain. Left: $n = 1$. Right: $n = 2$. $N = 0.4^\circ$.

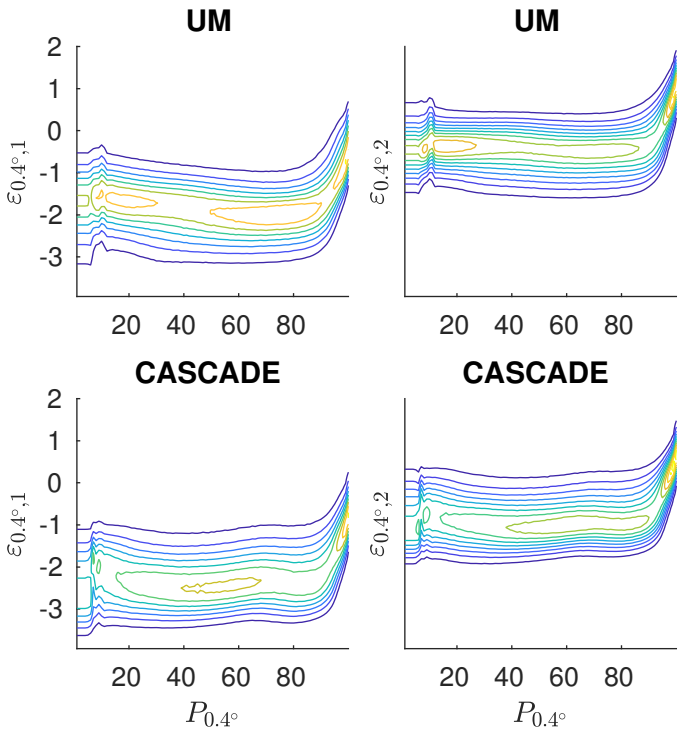

Figure A.50: Probability density function contours of the log 10 error processes conditioned on precipitation percentiles for the Warm Pool domain. Left: $n = 1$. Right: $n = 2$. $N = 0.4^\circ$.

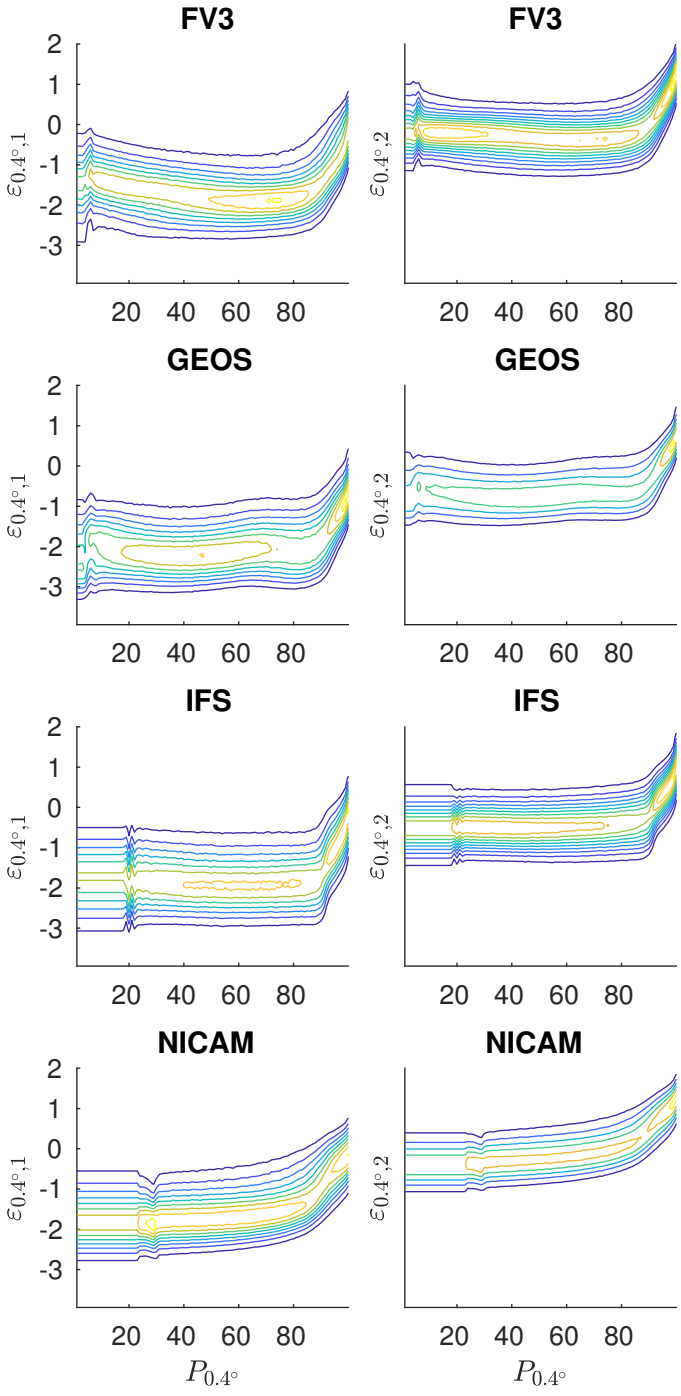

Figure A.51: Probability density function contours of the log 10 error processes conditioned on precipitation percentiles for the Warm Pool domain. Left: $n = 1$. Right: $n = 2$. $N = 0.76^\circ$.

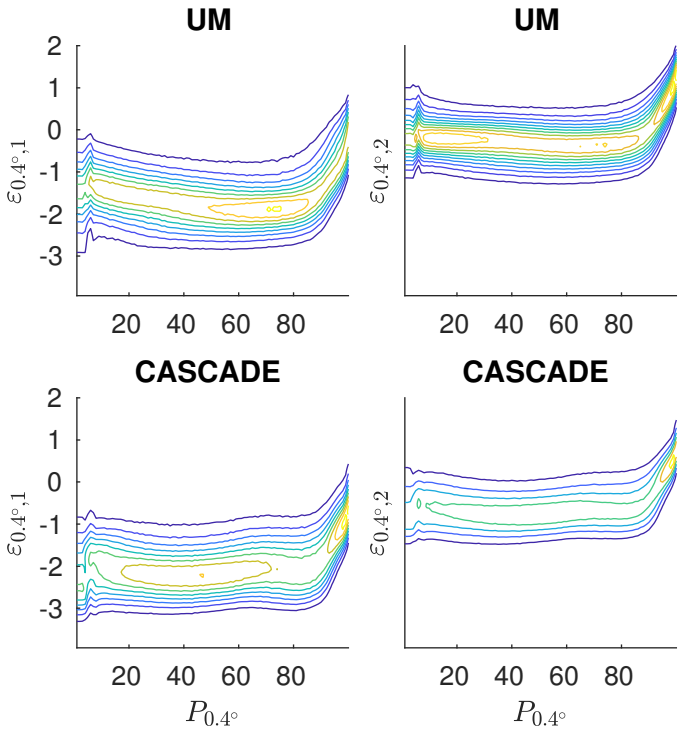

Figure A.52: Probability density function contours of the log 10 error processes conditioned on precipitation percentiles for the Warm Pool domain. Left: $n = 1$. Right: $n = 2$. $N = 0.76^\circ$.

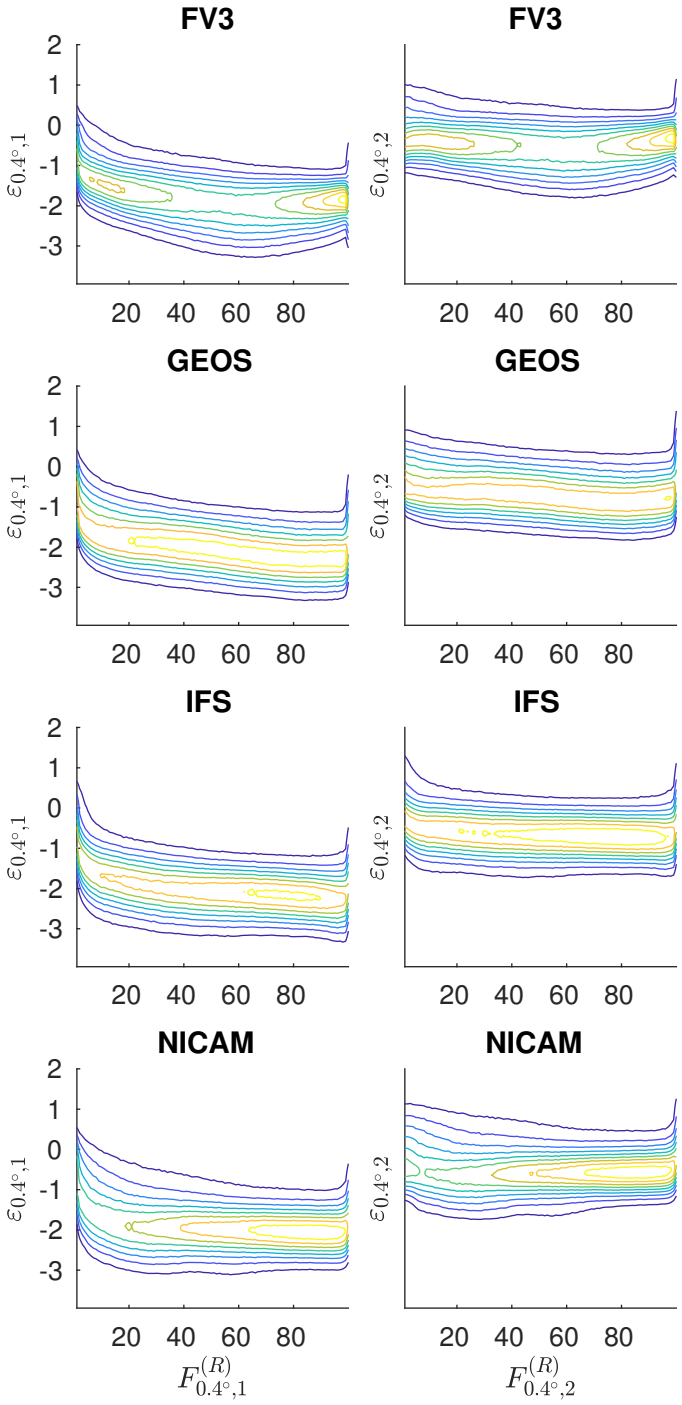

Figure A.53: Probability density function contours of the log 10 error processes conditioned on resolved flux percentiles for the subtropical Northeast Pacific. Left: $n = 1$. Right: $n = 2$. $N = 0.4°$.

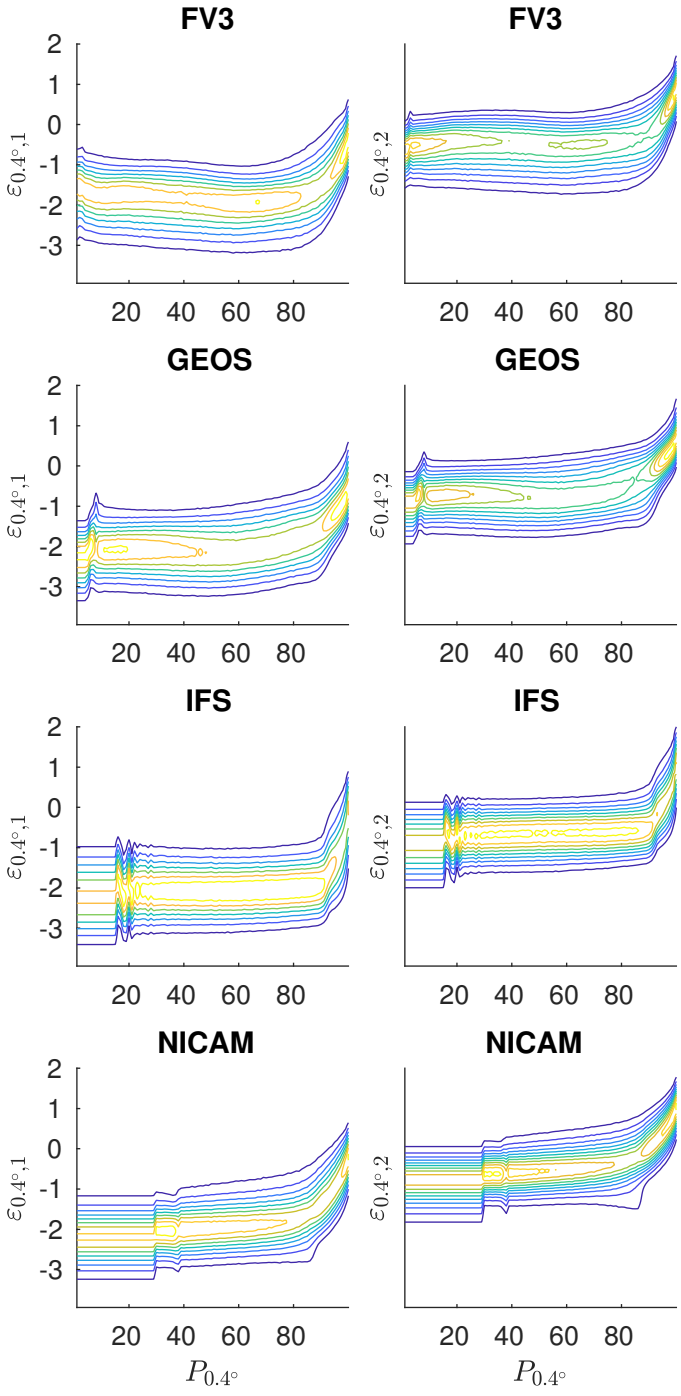

Figure A.54: Probability density function contours of the log 10 error processes conditioned on precipitation percentiles for the subtropical Northeast Pacific. Left: $n = 1$. Right: $n = 2$. $N = 0.4°$.

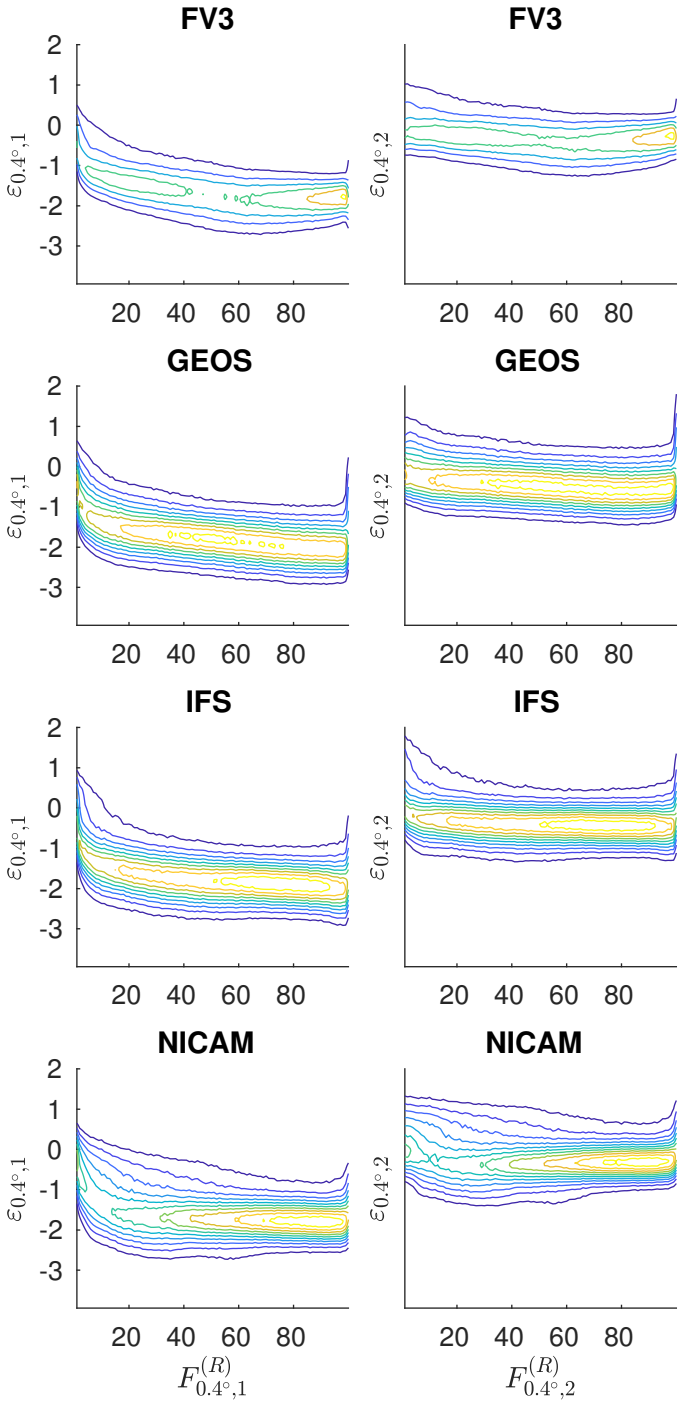

Figure A.55: Probability density function contours of the log 10 error processes conditioned on resolved flux percentiles for the subtropical Northeast Pacific. Left: $n = 1$. Right: $n = 2$. $N = 0.76°$.

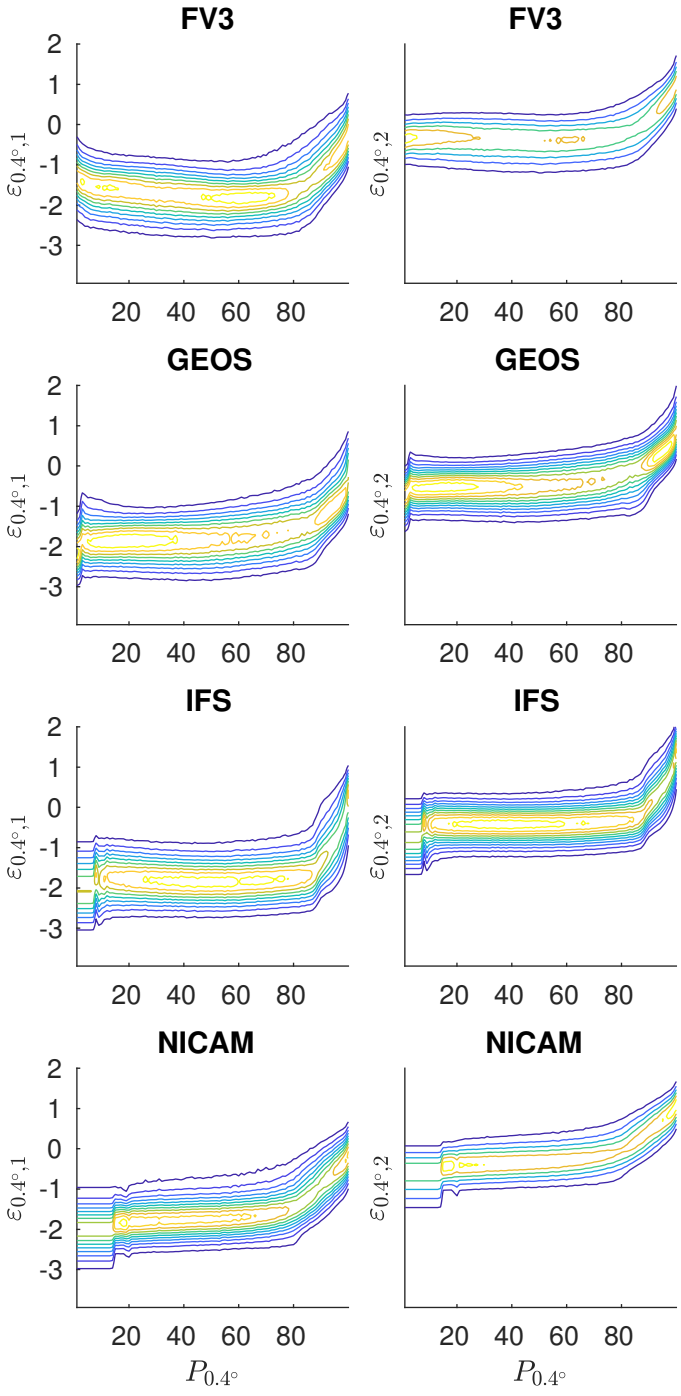

Figure A.56: Probability density function contours of the log 10 error processes conditioned on precipitation percentiles for the subtropical Northeast Pacific. Left: $n = 1$. Right: $n = 2$. $N = 0.76^\circ$.

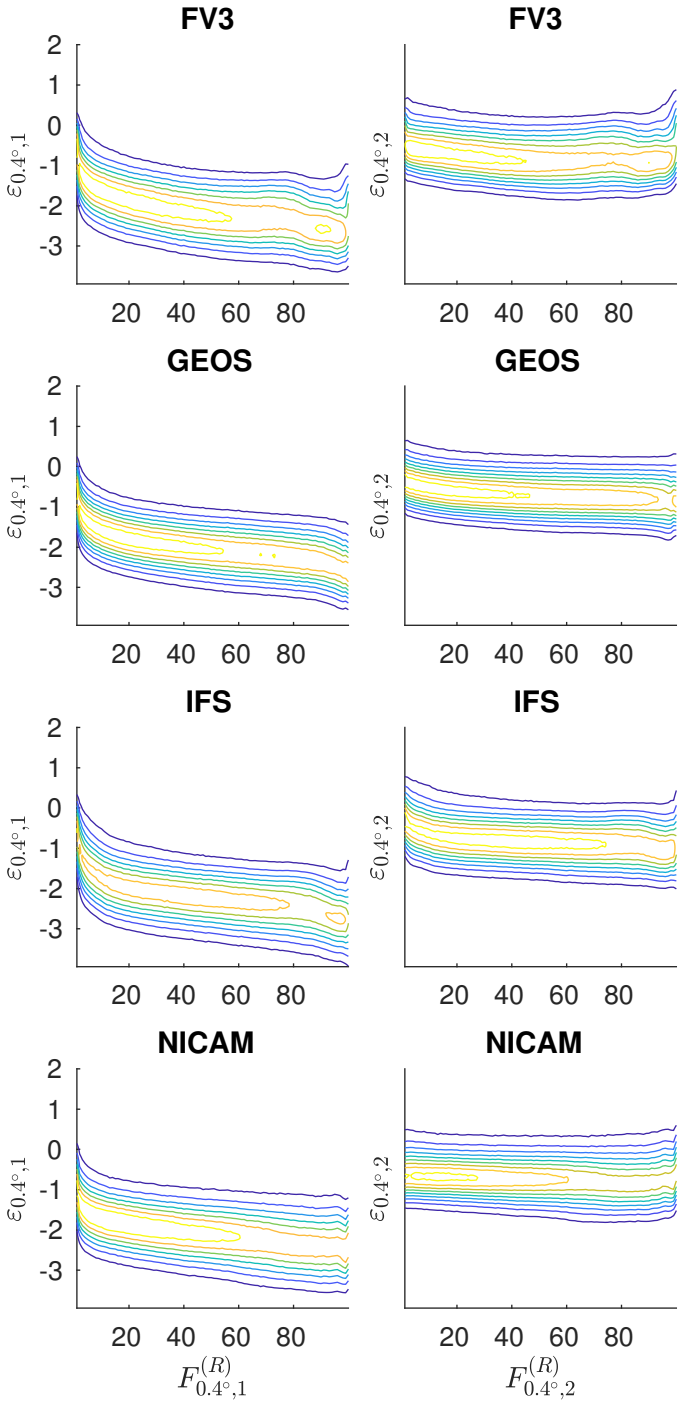

Figure A.57: Probability density function contours of the log 10 error processes conditioned on resolved flux percentiles for the subarctic Northeast Pacific. Left: $n = 1$. Right: $n = 2$. $N = 0.4^\circ$.

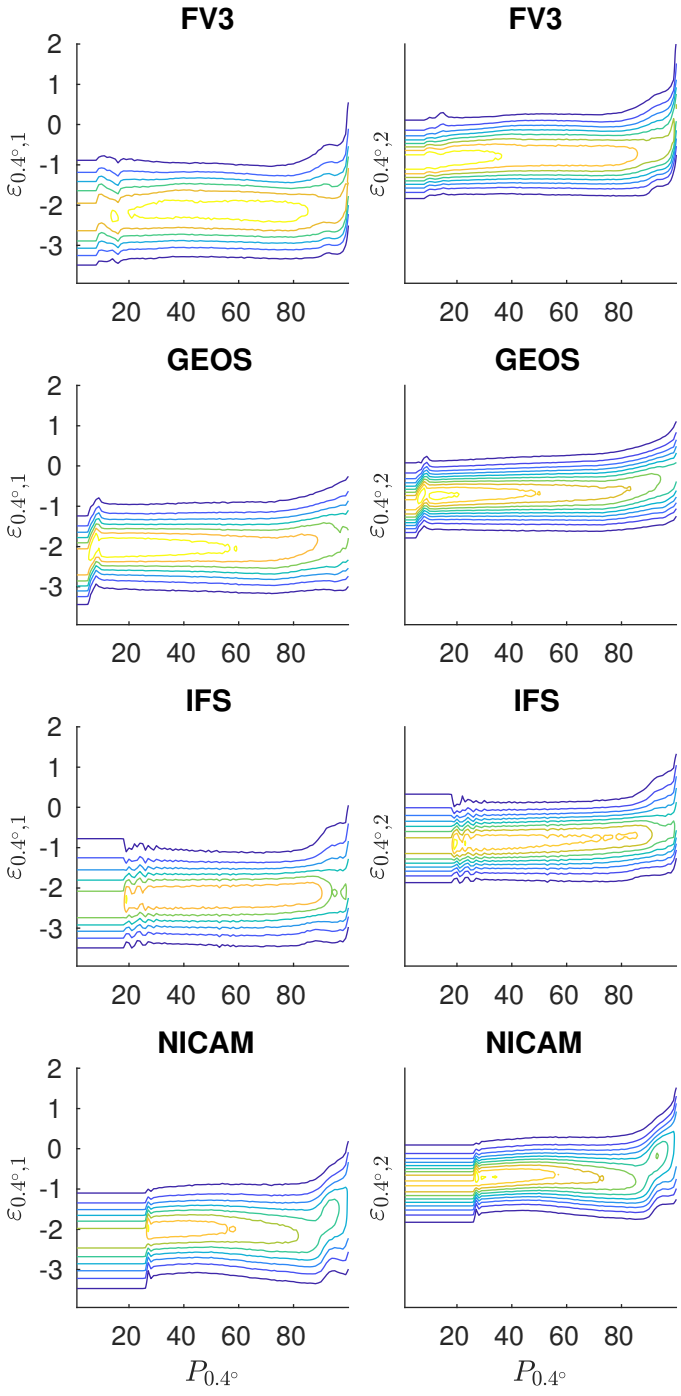

Figure A.58: Probability density function contours of the log 10 error processes conditioned on precipitation percentiles for the subarctic Northeast Pacific. Left: $n = 1$. Right: $n = 2$. $N = 0.4^\circ$.

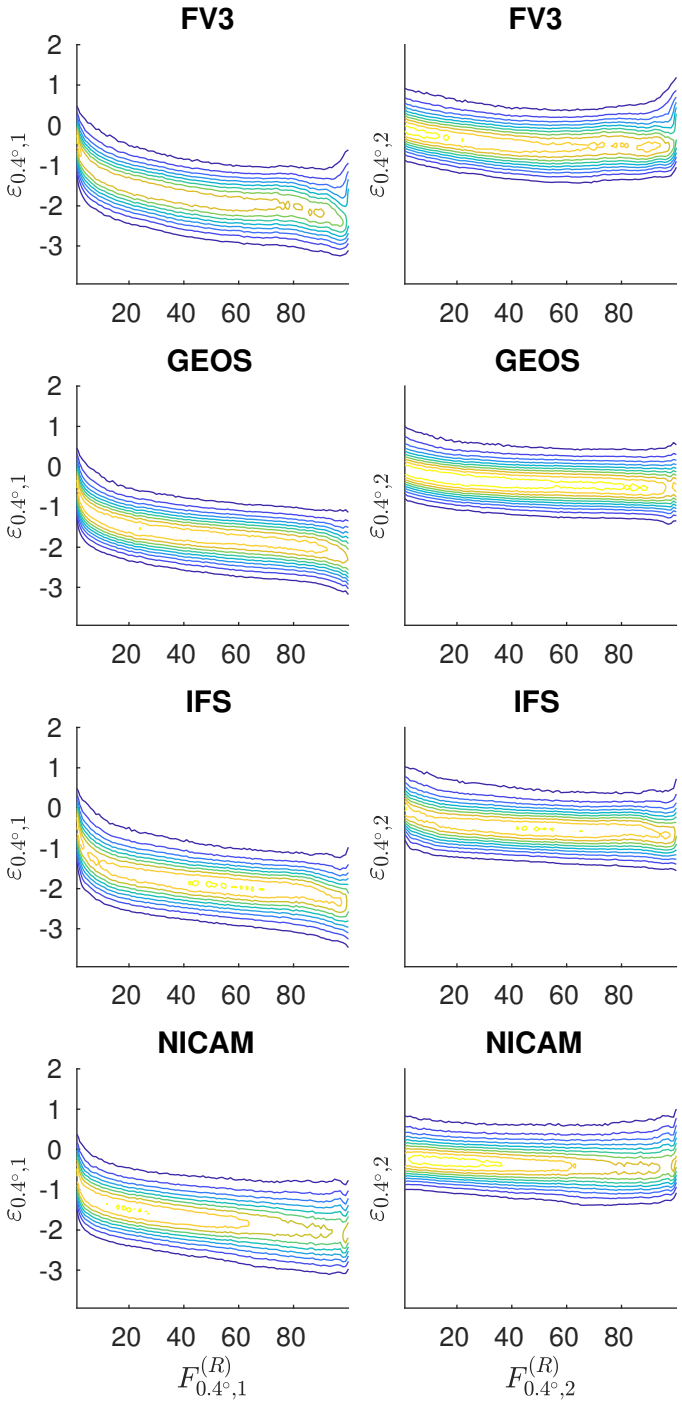

Figure A.59: Probability density function contours of the log 10 error processes conditioned on resolved flux percentiles for the subarctic Northeast Pacific. Left: $n = 1$. Right: $n = 2$. $N = 0.76°$.

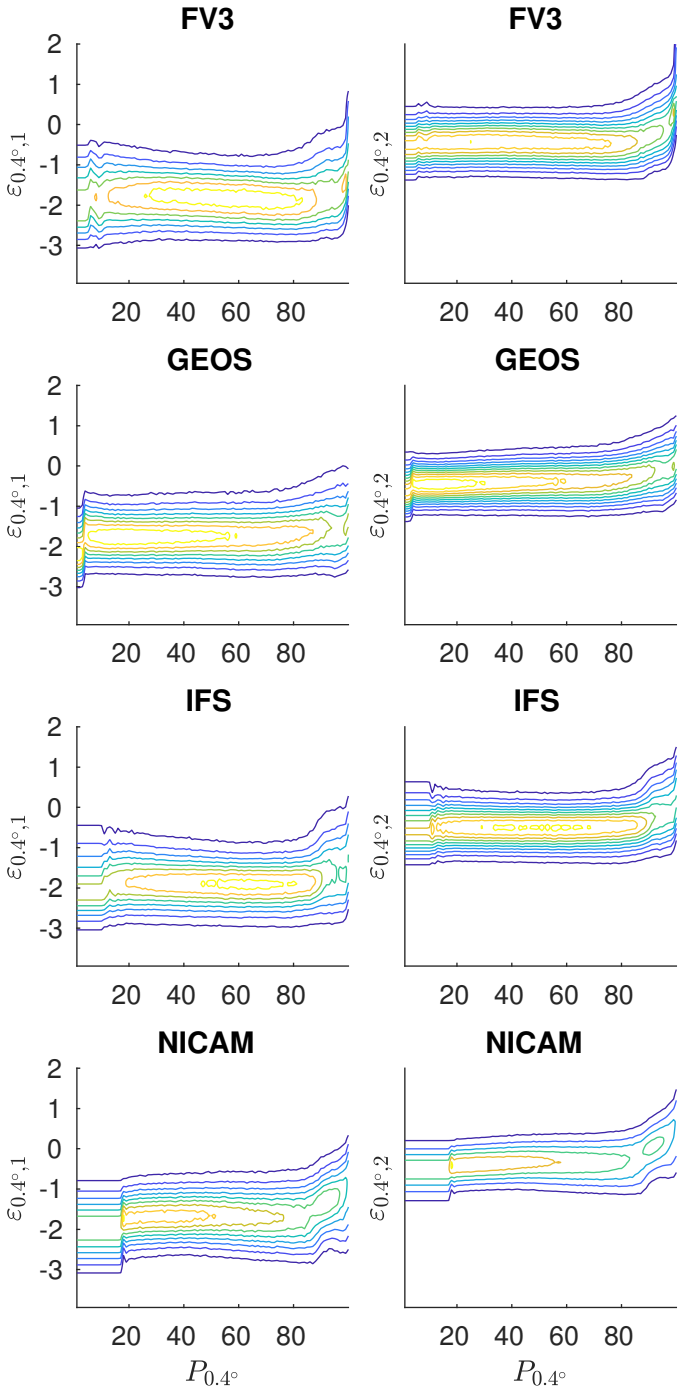

Figure A.60: Probability density function contours of the log 10 error processes conditioned on precipitation percentiles for the subarctic Northeast Pacific. Left: $n = 1$. Right: $n = 2$. $N = 0.76^\circ$.

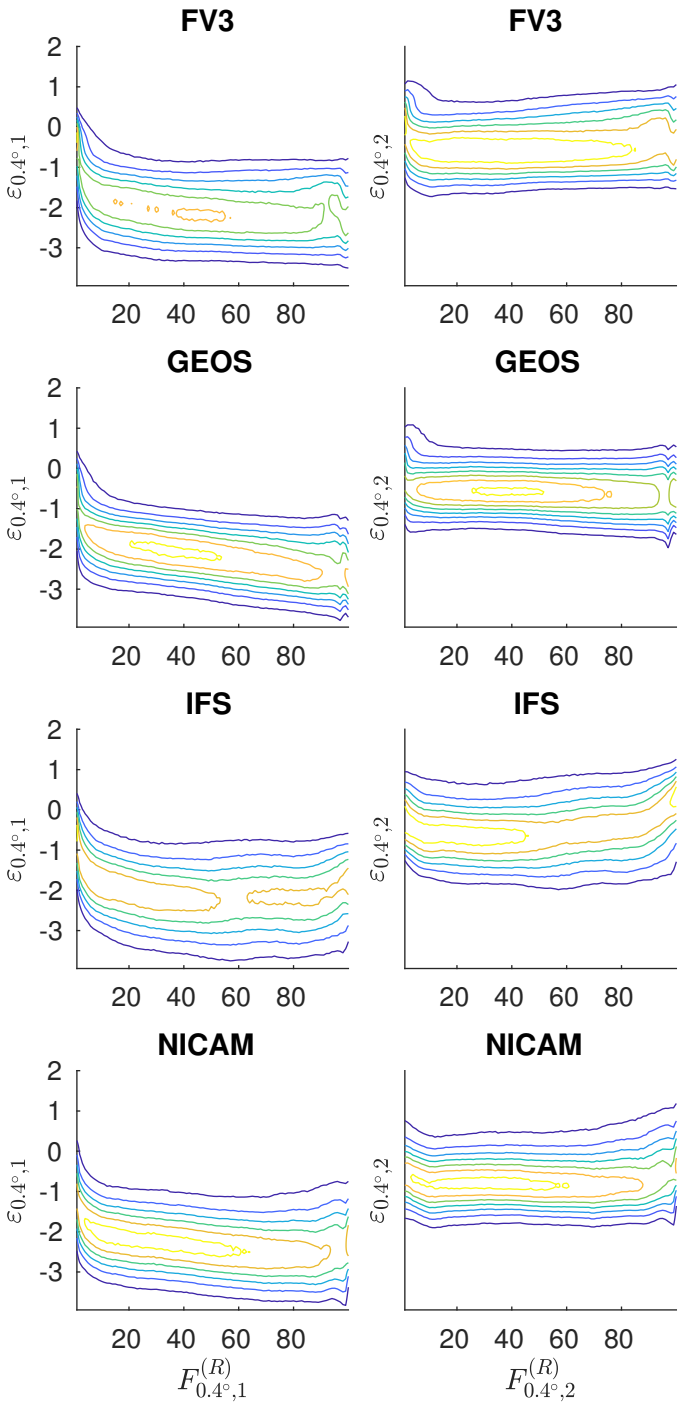

Figure A.61: Probability density function contours of the log 10 error processes conditioned on resolved flux percentiles for the Southern Ocean. Left: $n = 1$. Right: $n = 2$. $N = 0.4°$.

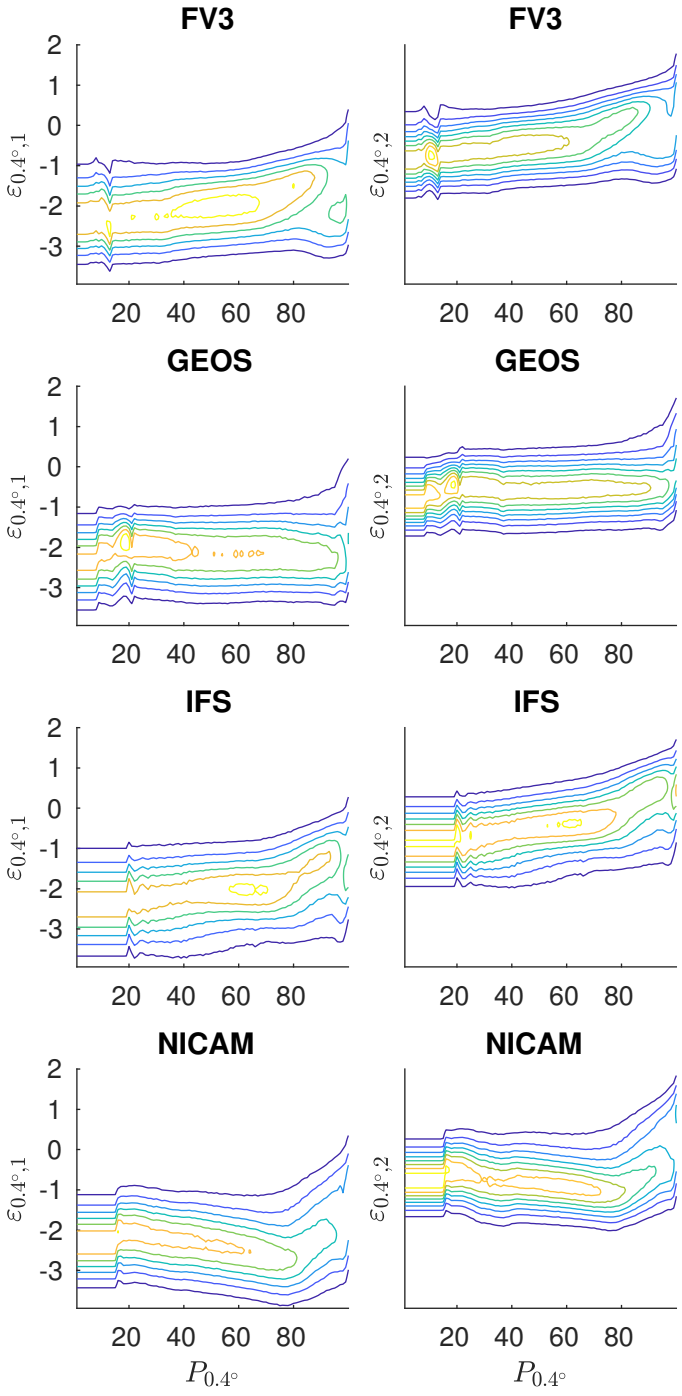

Figure A.62: Probability density function contours of the log 10 error processes conditioned on precipitation percentiles for the Southern Ocean. Left: $n = 1$. Right: $n = 2$. $N = 0.4°$.

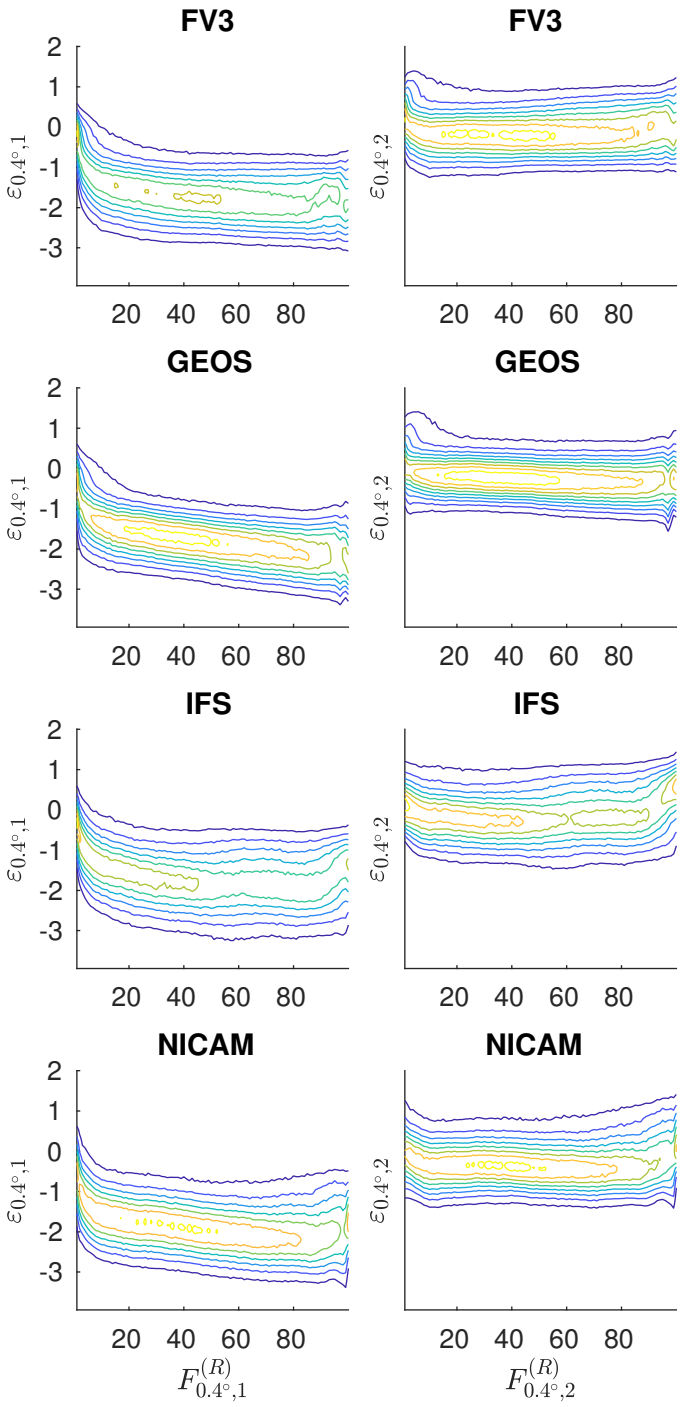

Figure A.63: Probability density function contours of the log 10 error processes conditioned on resolved flux percentiles for the Southern Ocean. Left: $n = 1$. Right: $n = 2$. $N = 0.76°$.

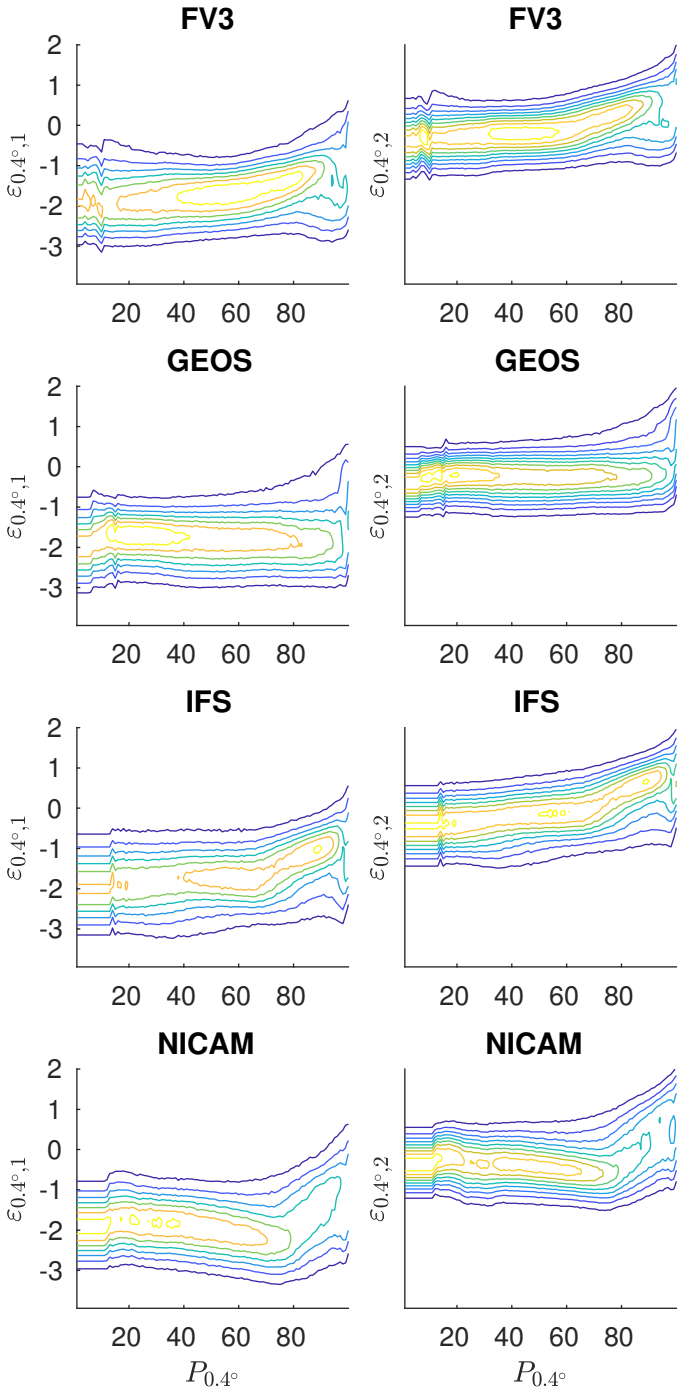

Figure A.64: Probability density function contours of the log 10 error processes conditioned on precipitation percentiles for the Southern Ocean. Left: $n = 1$. Right: $n = 2$. $N = 0.76°$.

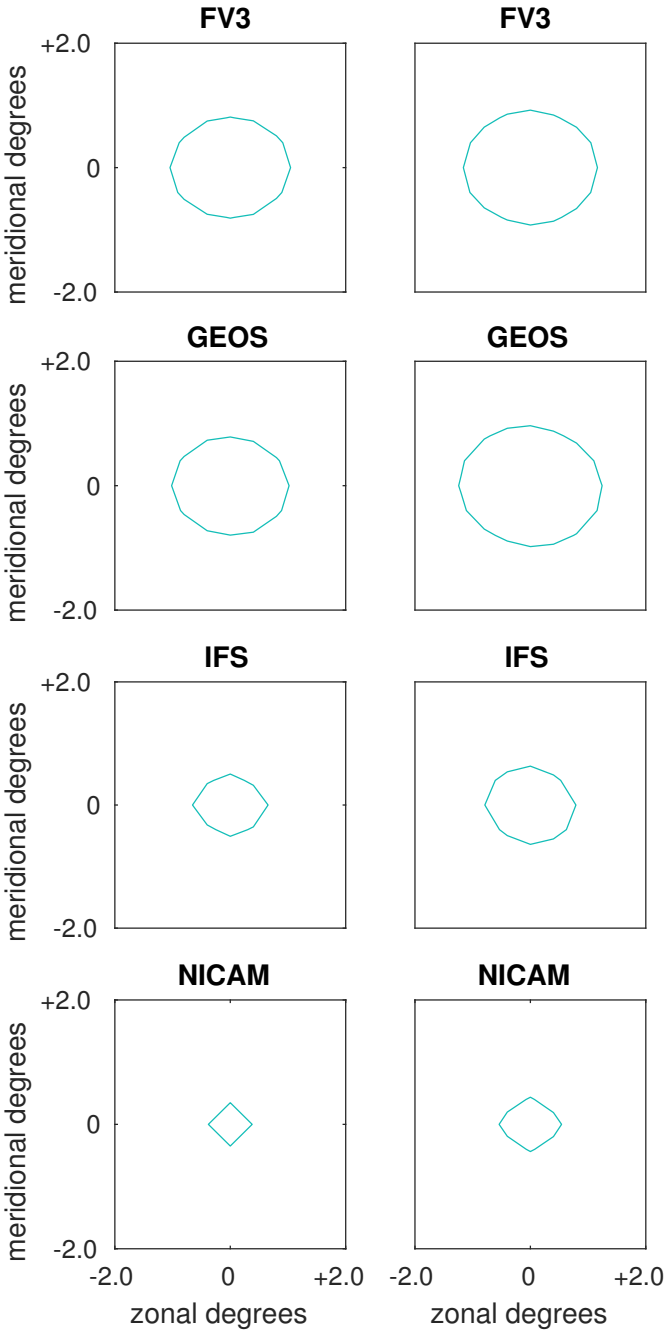

Figure A.65: Spatial correlation contours at the 0.5 level for $\psi_{0.4^\circ,1}$ (left), $\psi_{0.4^\circ,2}$ (right), in the Warm Pool domain.

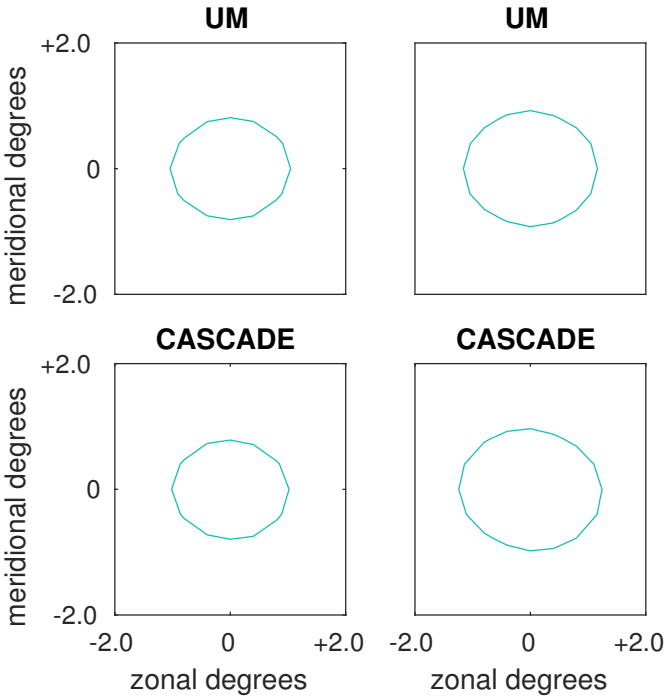

Figure A.66: Spatial correlation contours at the 0.5 level for $\psi_{0.4^\circ,1}$ (left), $\psi_{0.4^\circ,2}$ (right), in the Warm Pool domain.

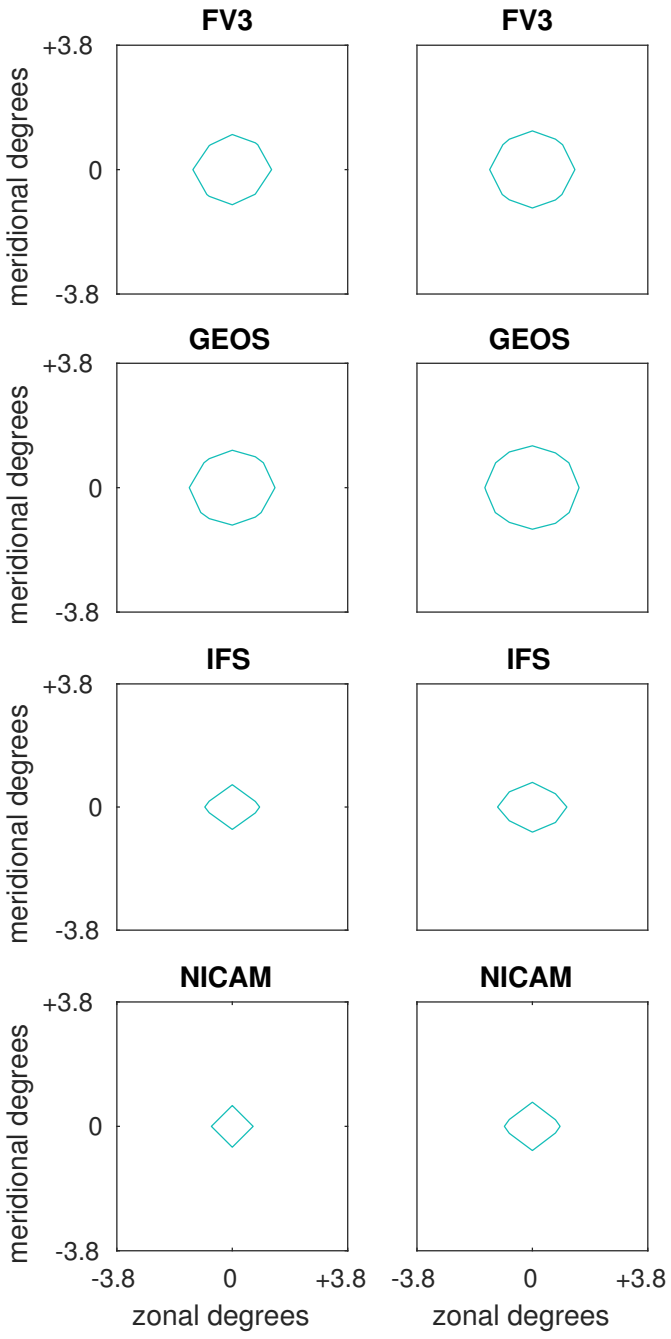

Figure A.67: Spatial correlation contours at the 0.5 level for $\psi_{0.76^\circ,1}$ (left), $\psi_{0.76^\circ,2}$ (right), in the Warm Pool domain.

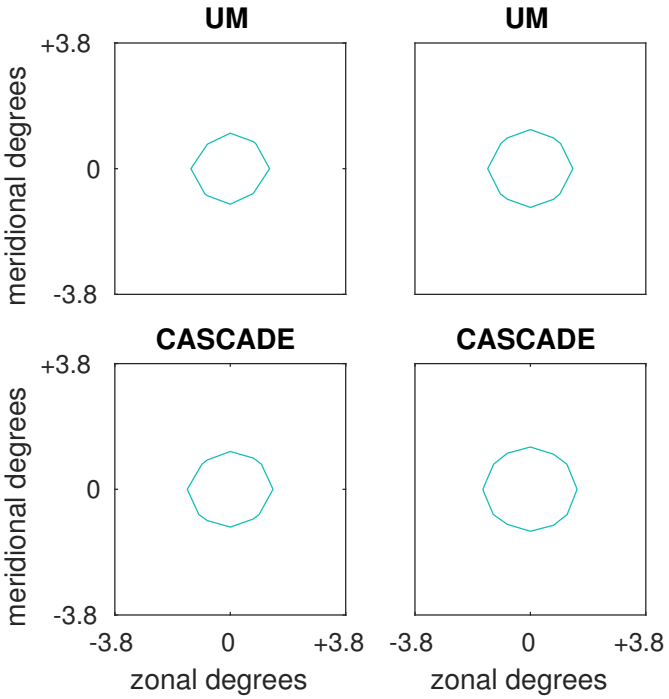

Figure A.68: Spatial correlation contours at the 0.5 level for $\psi_{0.76^\circ,1}$ (left), $\psi_{0.76^\circ,2}$ (right), in the Warm Pool domain.

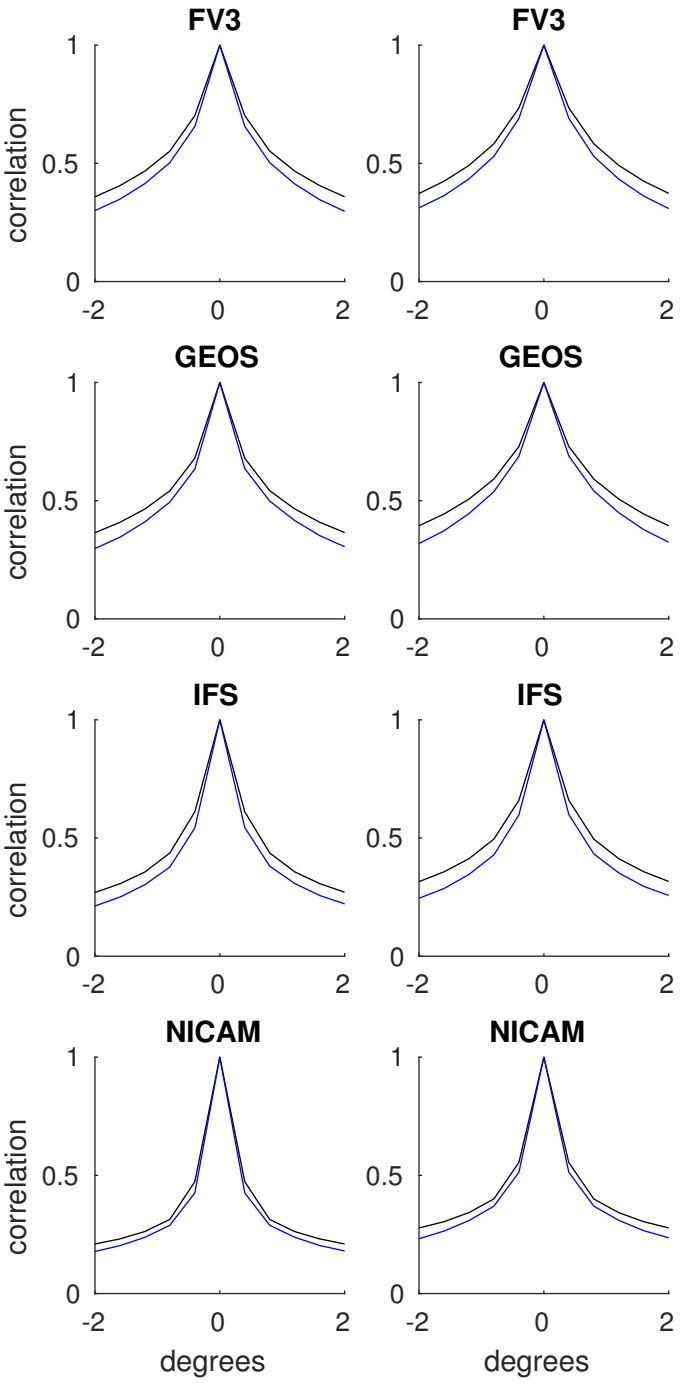

Figure A.69: Spatial correlations (as per Equation 3.5 averaged over x, y, t and with fixed $p = 0$ or $q = 0$ for the meridional and zonal transects, respectively) for $\psi_{0.4^\circ,1}$ (left), $\psi_{0.4^\circ,2}$ (right), in the Warm Pool domain. Black: zonal. Blue: meridional.

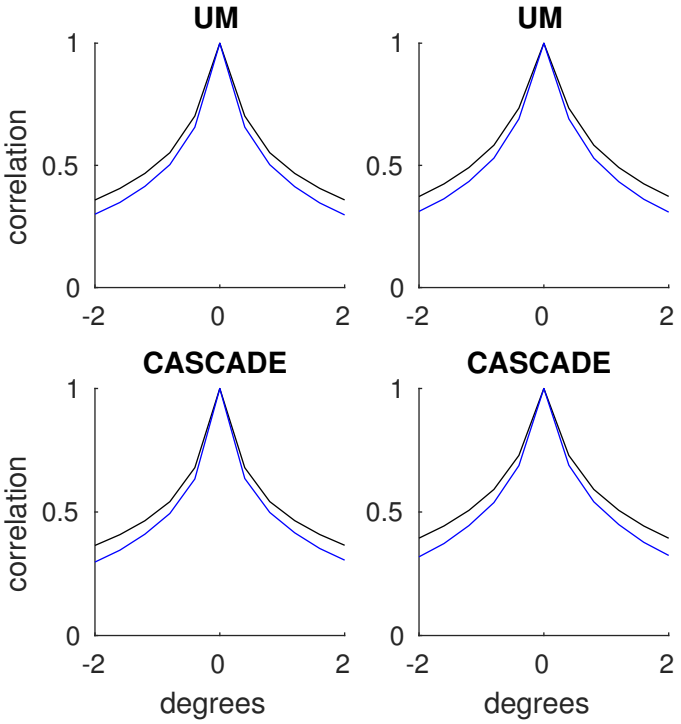

Figure A.70: Spatial correlations (as per Equation 3.5 averaged over x, y, t and with fixed $p = 0$ or $q = 0$ for the meridional and zonal transects, respectively) for $\psi_{0.4^\circ,1}$ (left), $\psi_{0.4^\circ,2}$ (right), in the Warm Pool domain. Black: zonal. Blue: meridional.

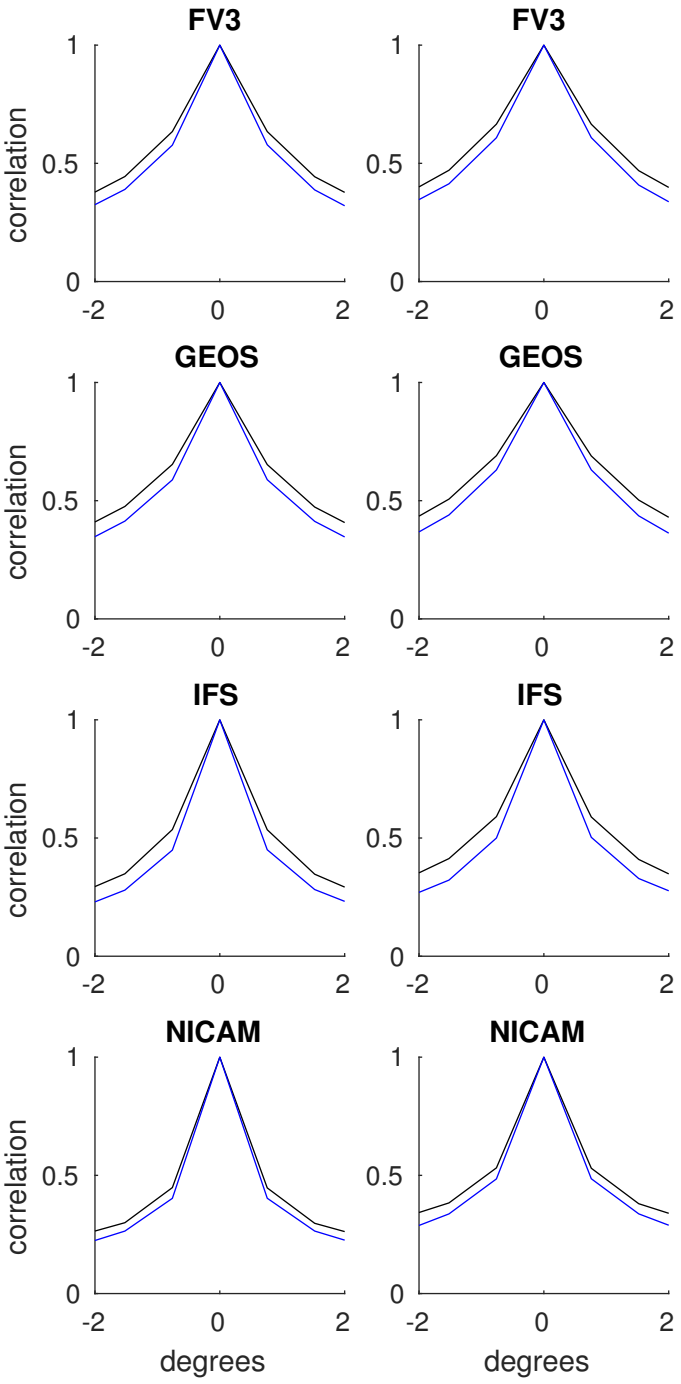

Figure A.71: Spatial correlations (as per Equation 3.5 averaged over x, y, t and with fixed $p = 0$ or $q = 0$ for the meridional and zonal transects, respectively) for $\psi_{0.76^\circ,1}$ (left), $\psi_{0.76^\circ,2}$ (right), in the Warm Pool domain. Black: zonal. Blue: meridional.

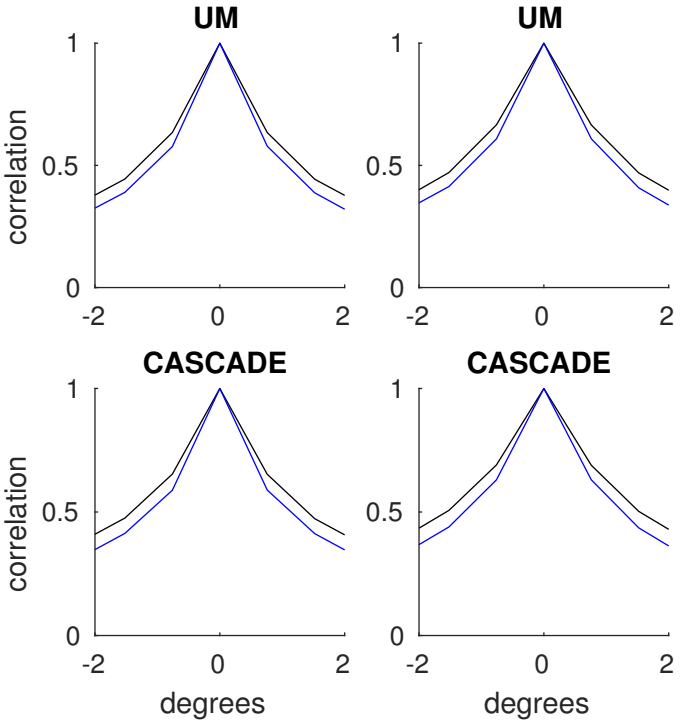

Figure A.72: Spatial correlations (as per Equation 3.5 averaged over x, y, t and with fixed $p = 0$ or $q = 0$ for the meridional and zonal transects, respectively) for $\psi_{0.76^\circ,1}$ (left), $\psi_{0.76^\circ,2}$ (right), in the Warm Pool domain. Black: zonal. Blue: meridional.

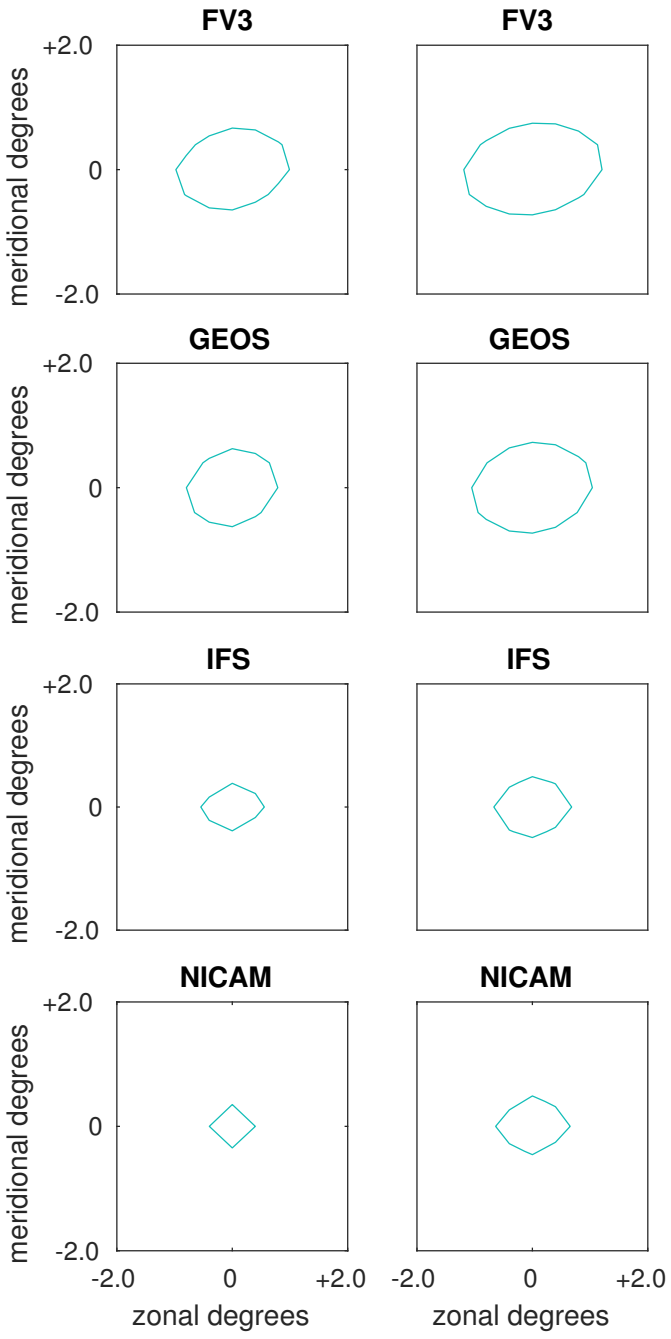

Figure A.73: Spatial correlation contours at the 0.5 level for $\psi_{0.4^\circ,1}$ (left), $\psi_{0.4^\circ,2}$ (right), in the subtropical Northeast Pacific.

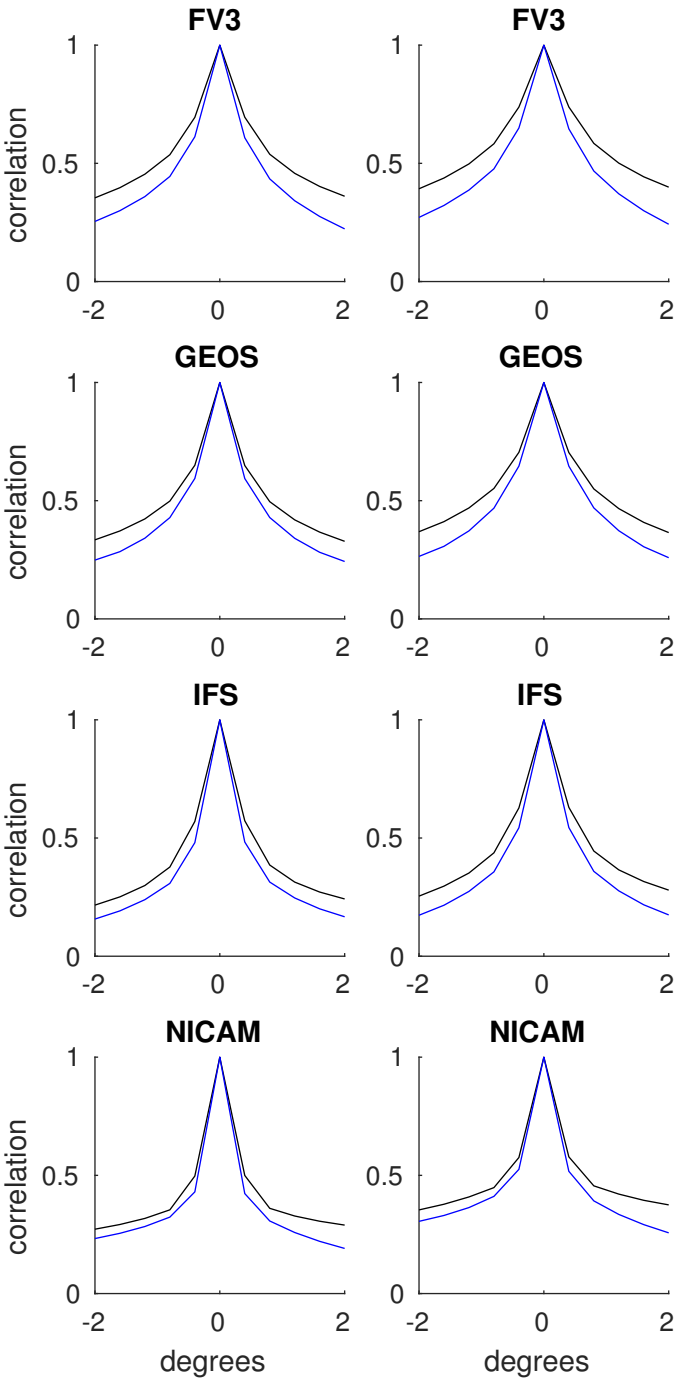

Figure A.74: Spatial correlations (as per Equation 3.5 averaged over x, y, t and with fixed $p = 0$ or $q = 0$ for the meridional and zonal transects, respectively) for $\psi_{0.4^\circ,1}$ (left), $\psi_{0.4^\circ,2}$ (right), in the subtropical Northeast Pacific. Black: zonal. Blue: meridional.

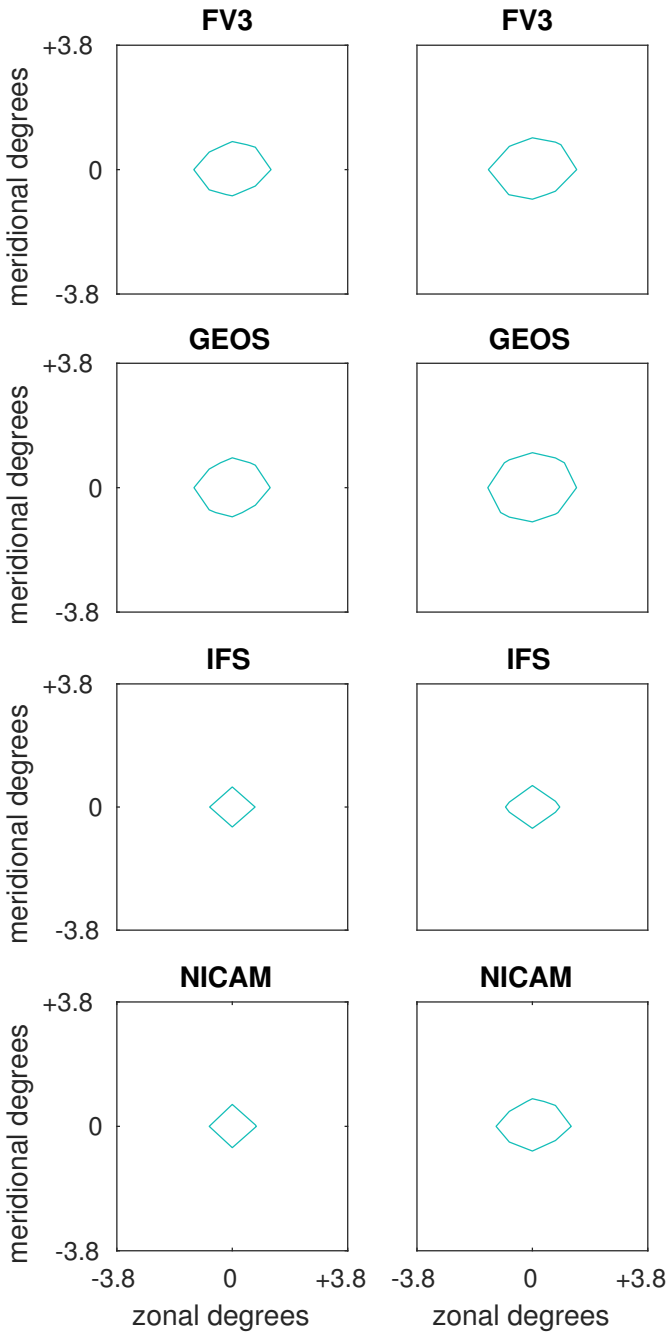

Figure A.75: Spatial correlation contours at the 0.5 level for $\psi_{0.76^\circ,1}$ (left), $\psi_{0.76^\circ,2}$ (right), in the subtropical Northeast Pacific.

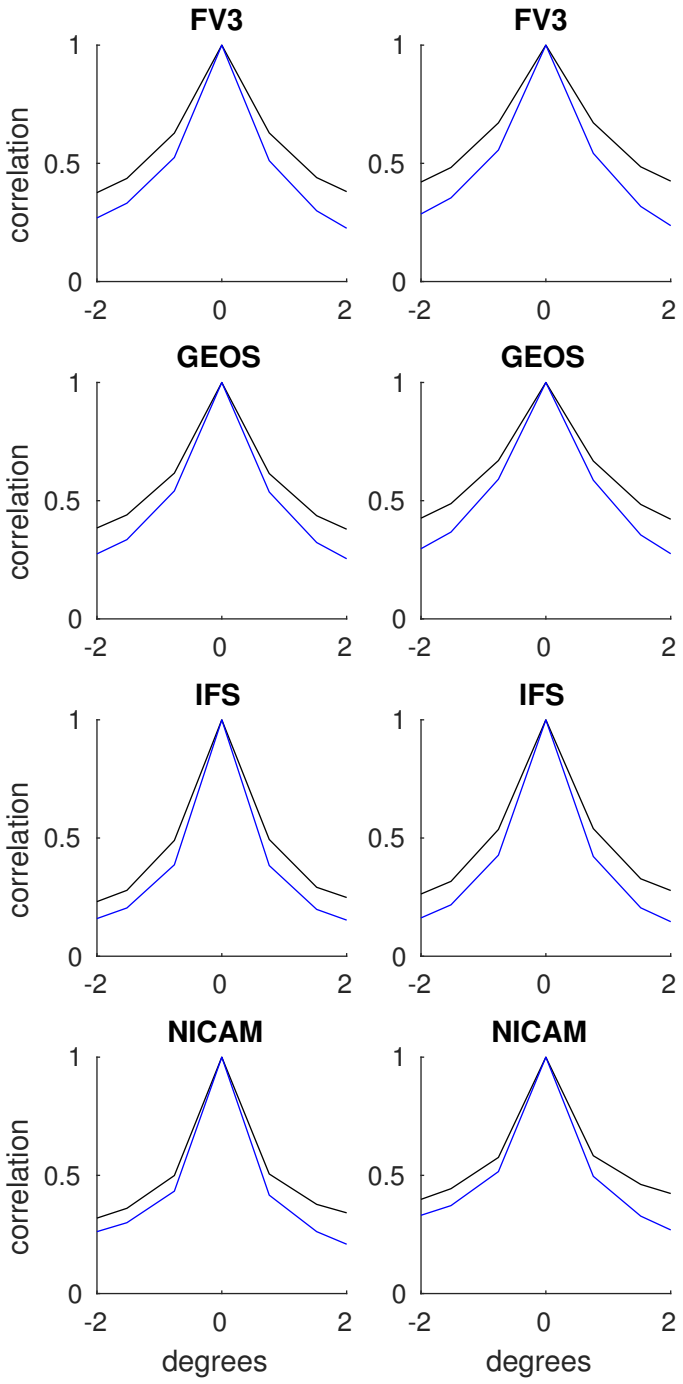

Figure A.76: Spatial correlations (as per Equation 3.5 averaged over x, y, t and with fixed $p = 0$ or $q = 0$ for the meridional and zonal transects, respectively) for $\psi_{0.76^\circ,1}$ (left), $\psi_{0.76^\circ,2}$ (right), in the subtropical Northeast Pacific. Black: zonal. Blue: meridional.

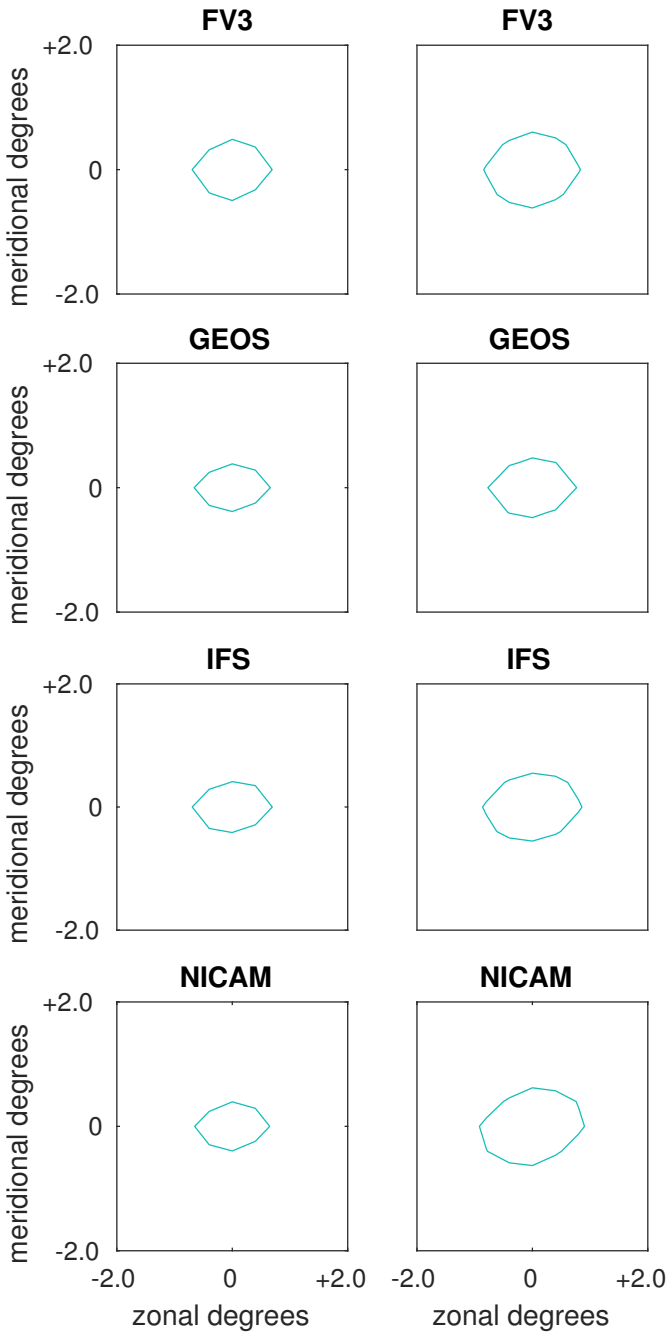

Figure A.77: Spatial correlation contours at the 0.5 level for $\psi_{0.4^\circ,1}$ (left), $\psi_{0.4^\circ,2}$ (right), in the subarctic Northeast Pacific.

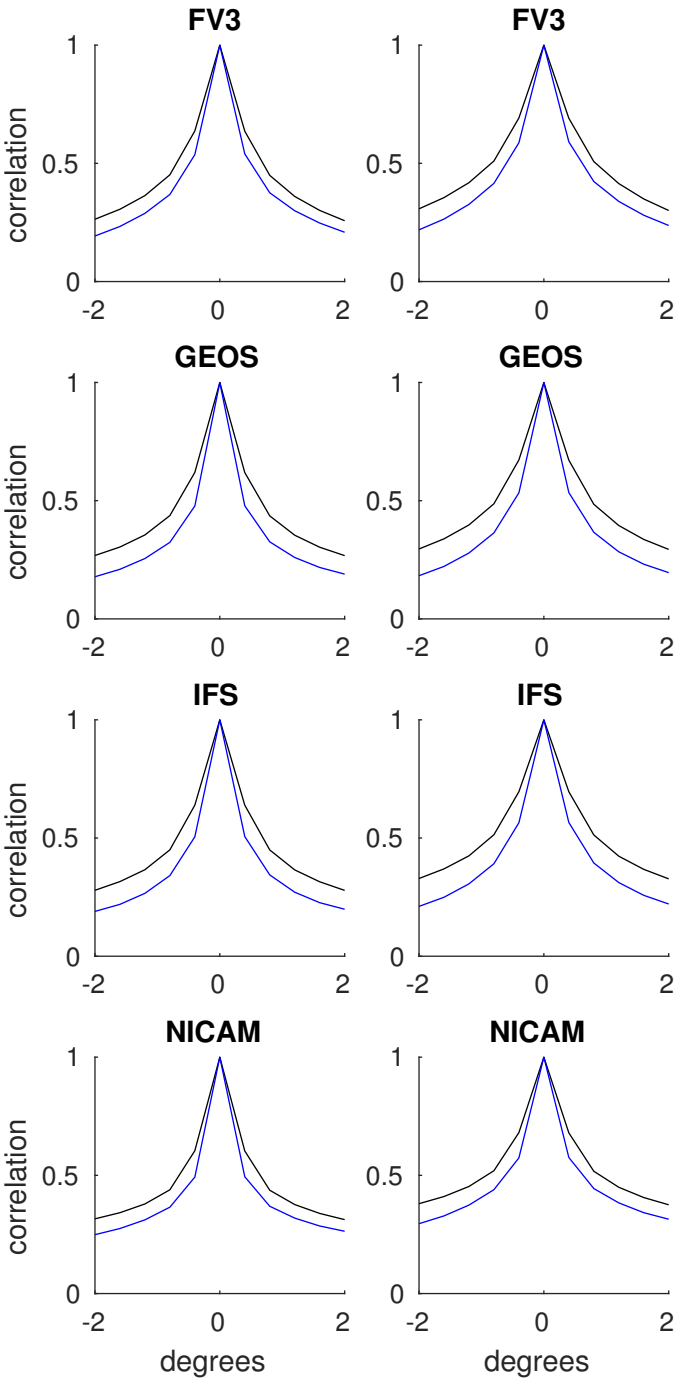

Figure A.78: Spatial correlations (as per Equation 3.5 averaged over x, y, t and with fixed $p = 0$ or $q = 0$ for the meridional and zonal transects, respectively) for $\psi_{0.4^\circ,1}$ (left), $\psi_{0.4^\circ,2}$ (right), in the subarctic Northeast Pacific. Black: zonal. Blue: meridional.

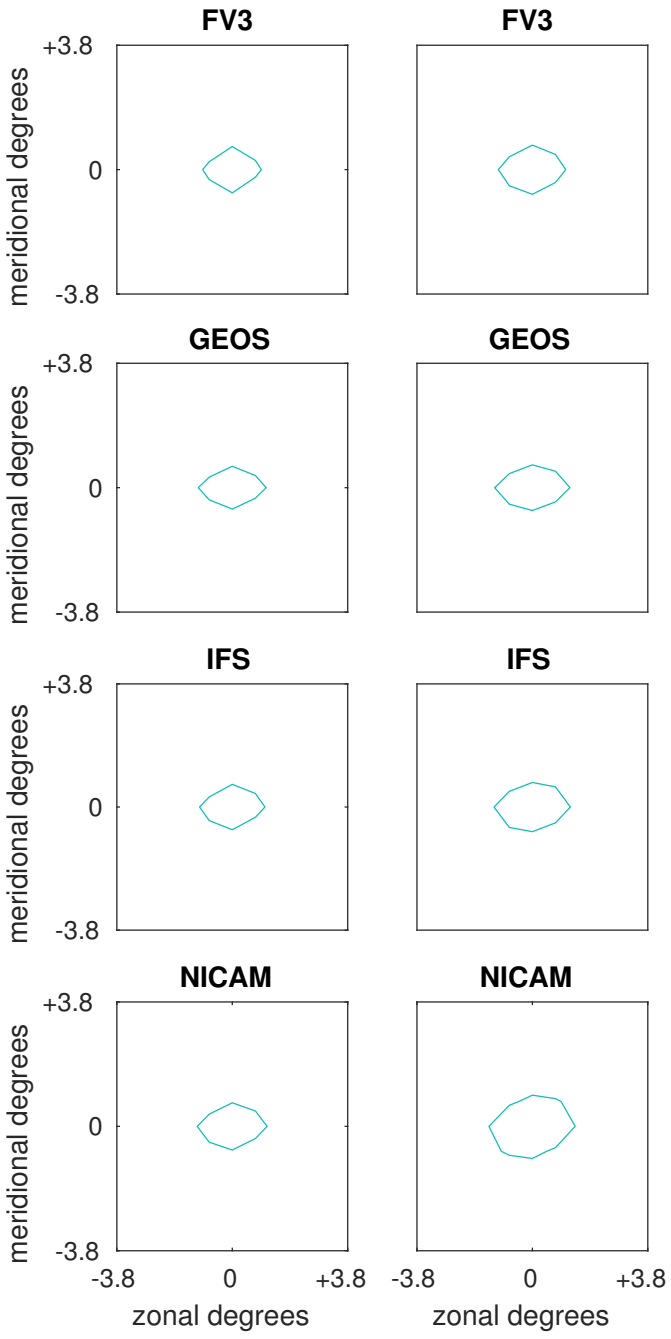

Figure A.79: Spatial correlation contours at the 0.5 level for $\psi_{0.76^\circ,1}$ (left), $\psi_{0.76^\circ,2}$ (right), in the subarctic Northeast Pacific.

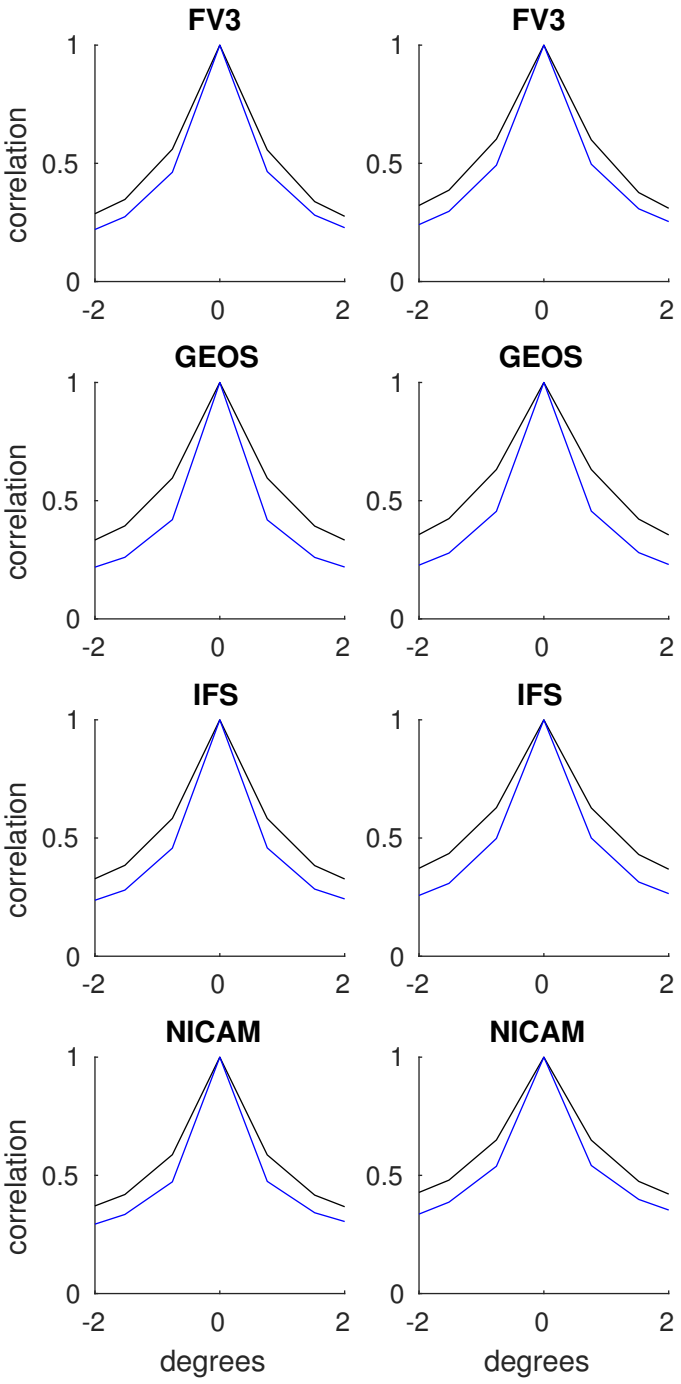

Figure A.80: Spatial correlations (as per Equation 3.5 averaged over x, y, t and with fixed $p = 0$ or $q = 0$ for the meridional and zonal transects, respectively) for $\psi_{0.76^\circ,1}$ (left), $\psi_{0.76^\circ,2}$ (right), in the subarctic Northeast Pacific. Black: zonal. Blue: meridional.

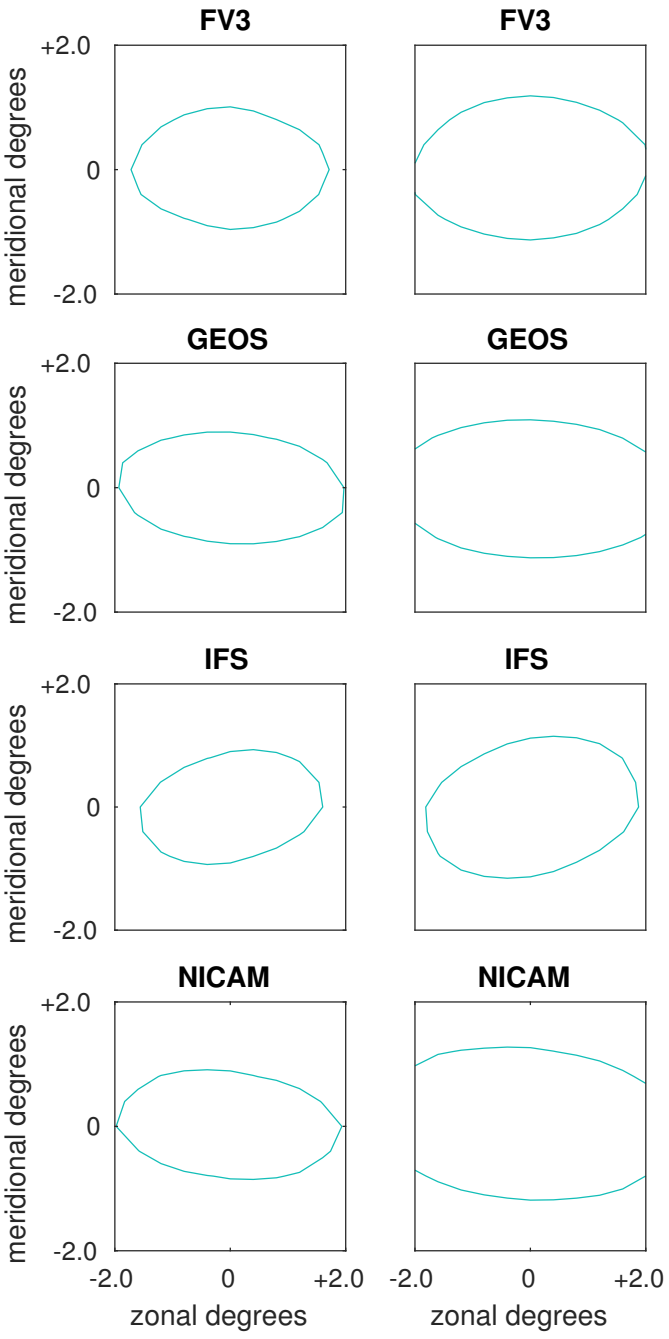

Figure A.81: Spatial correlation contours at the 0.5 level for $\psi_{0.4^\circ,1}$ (left), $\psi_{0.4^\circ,2}$ (right), in the Southern Ocean.

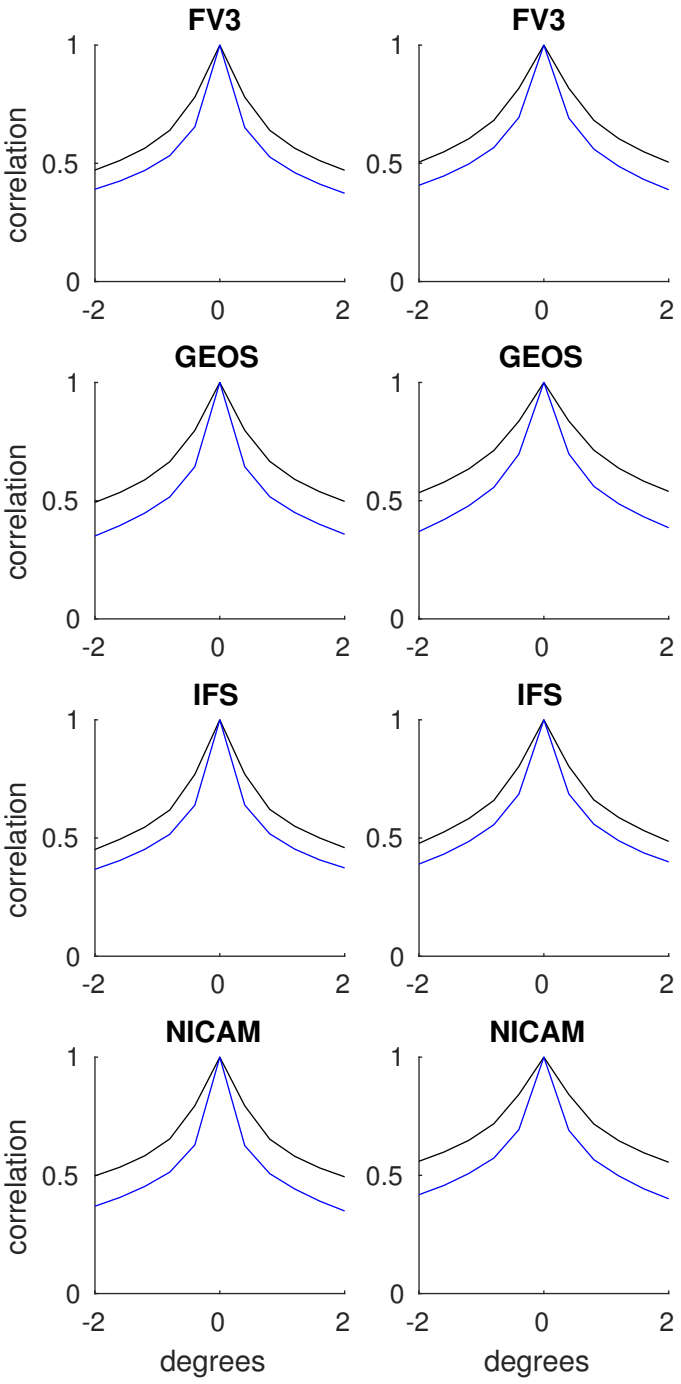

Figure A.82: Spatial correlations (as per Equation 3.5 averaged over x, y, t and with fixed $p = 0$ or $q = 0$ for the meridional and zonal transects, respectively) for $\psi_{0.4^\circ,1}$ (left), $\psi_{0.4^\circ,2}$ (right), in the Southern Ocean. Black: zonal. Blue: meridional.

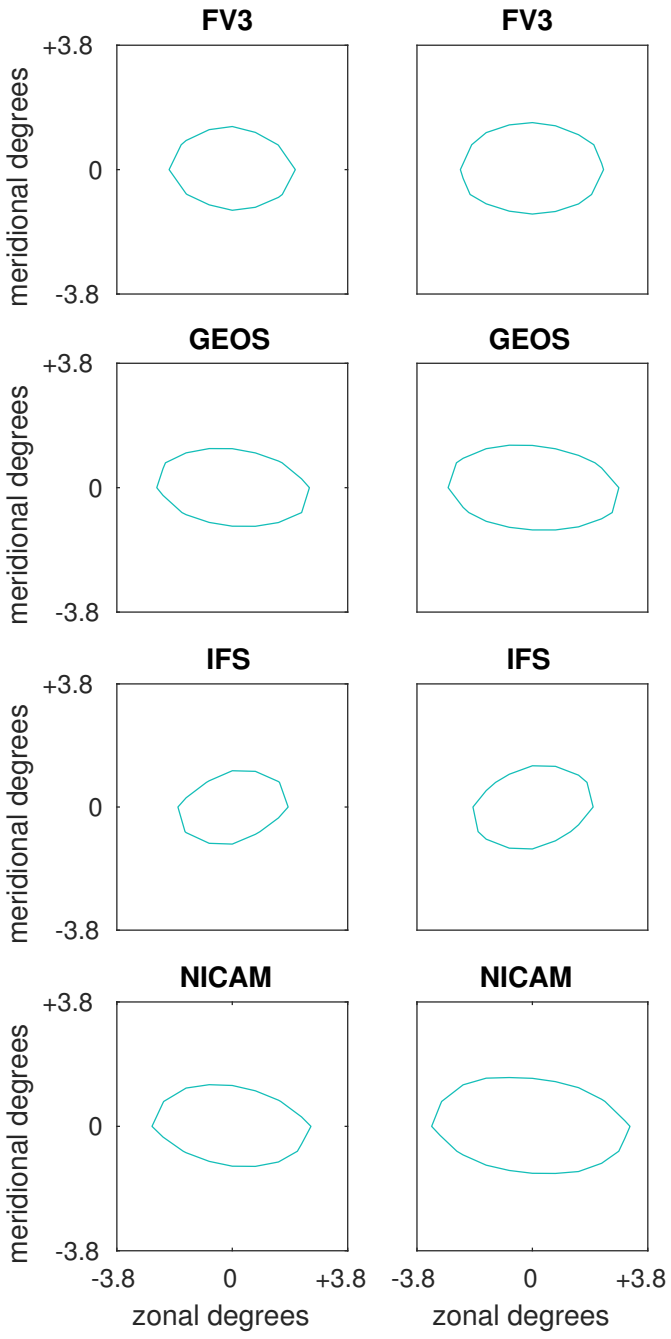

Figure A.83: Spatial correlation contours at the 0.5 level for $\psi_{0.76^\circ,1}$ (left), $\psi_{0.76^\circ,2}$ (right), in the Southern Ocean.

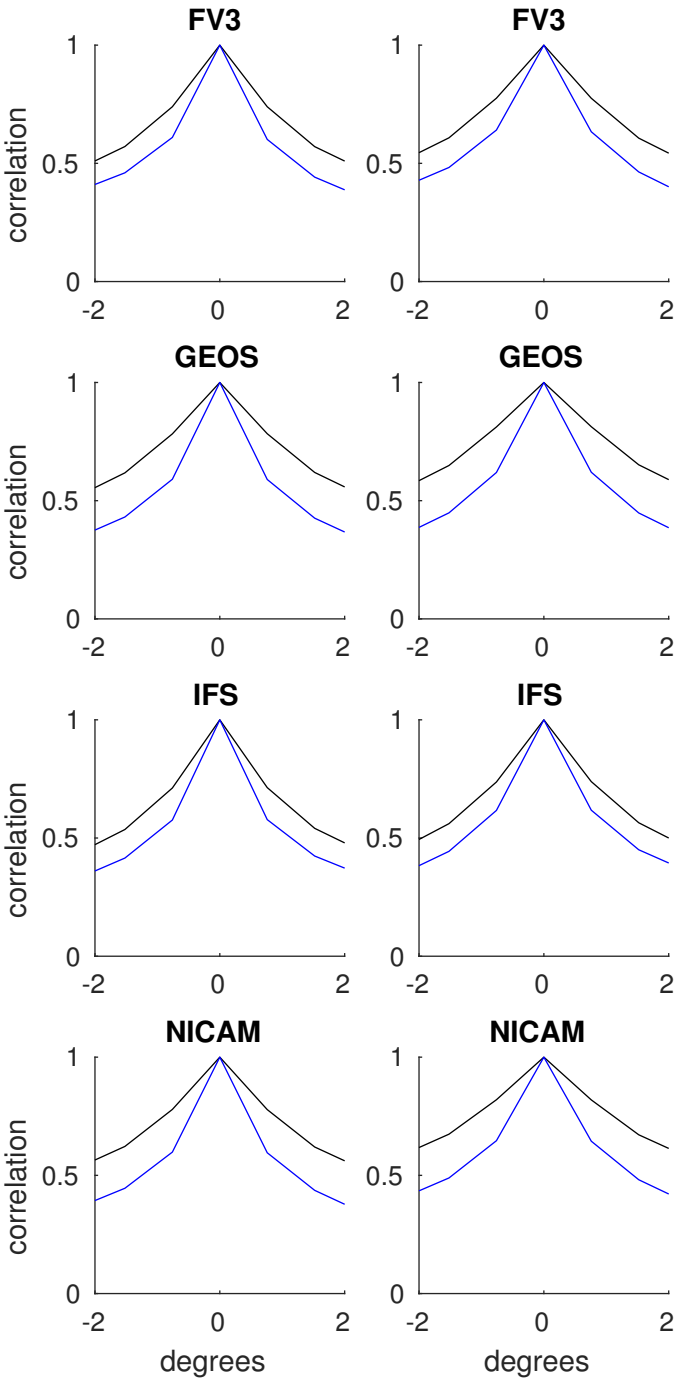

Figure A.84: Spatial correlations (as per Equation 3.5 averaged over x, y, t and with fixed $p = 0$ or $q = 0$ for the meridional and zonal transects, respectively) for $\psi_{0.76^\circ,1}$ (left), $\psi_{0.76^\circ,2}$ (right), in the Southern Ocean. Black: zonal. Blue: meridional.

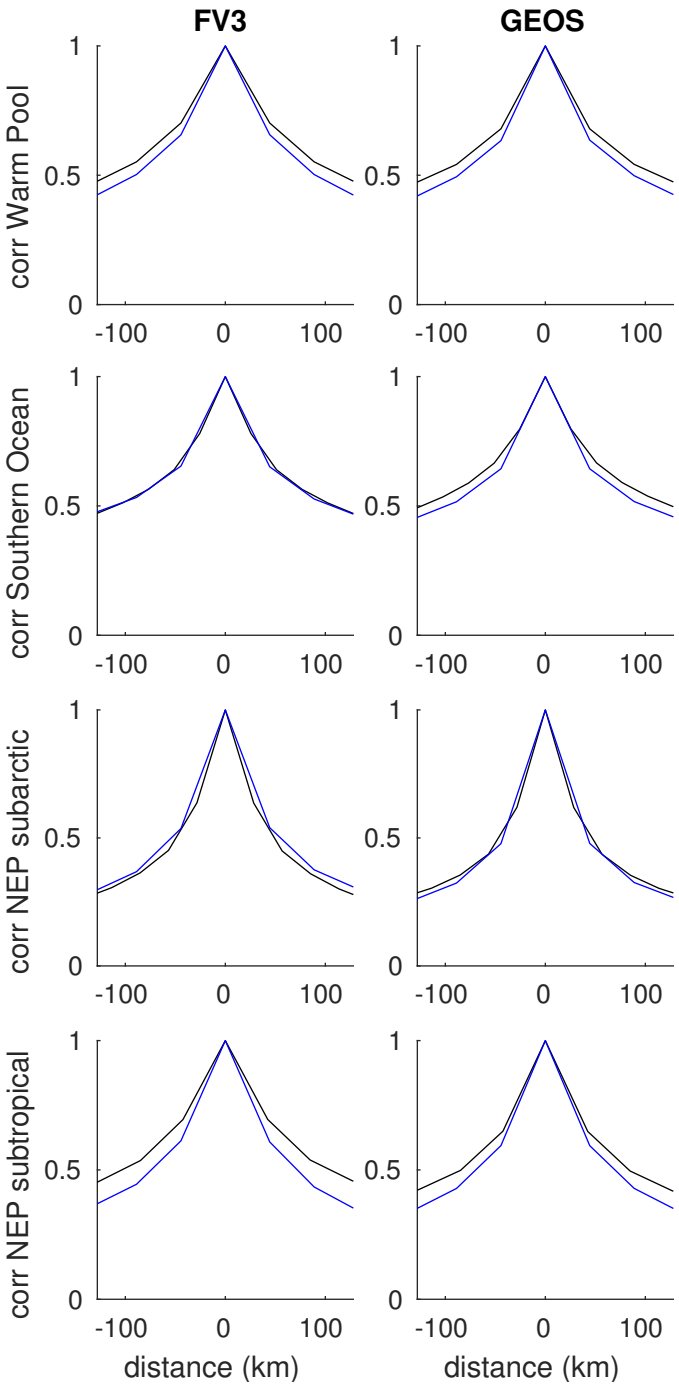

Figure A.85: Spatial correlations (as per Equation 3.5 averaged over x, y, t and with fixed $p = 0$ or $q = 0$ for the meridional and zonal transects, respectively) for FV3 and GEOS, with physical distances. Black: zonal. Blue: meridional.

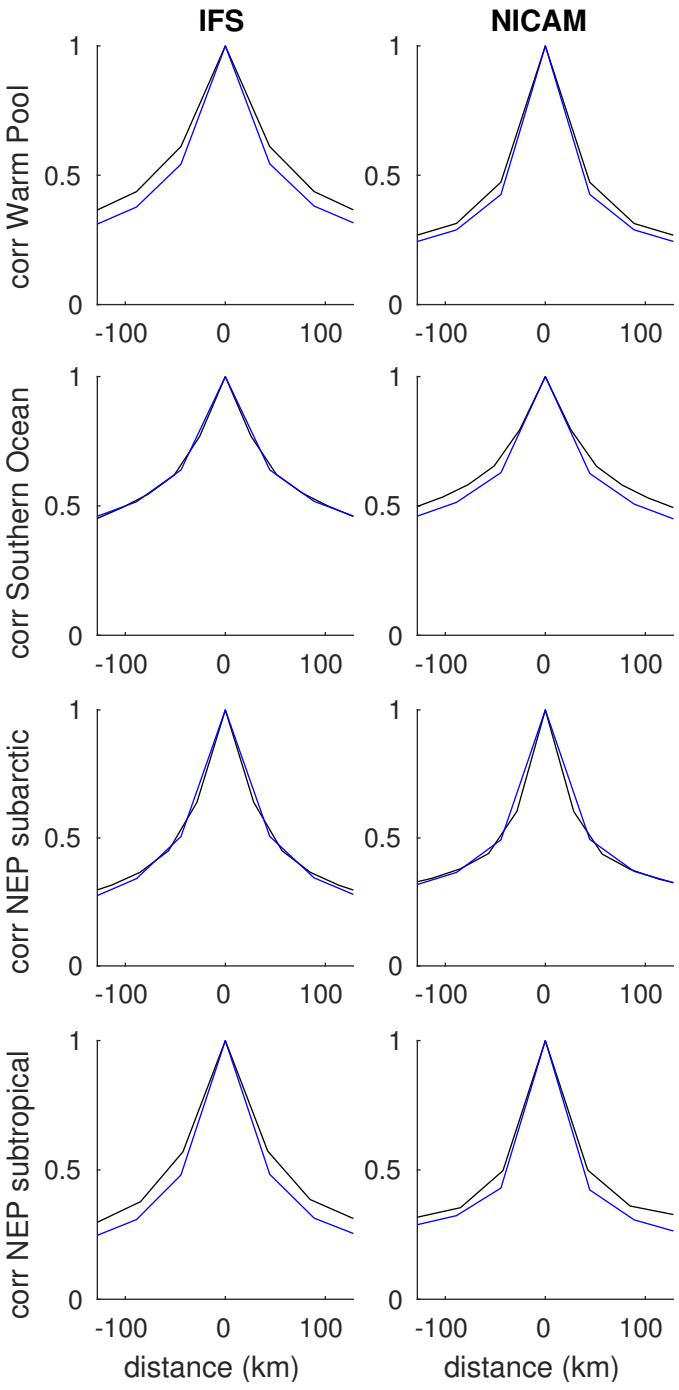

Figure A.86: Spatial correlations (as per Equation 3.5 averaged over x, y, t and with fixed $p = 0$ or $q = 0$ for the meridional and zonal transects, respectively) for IFS and NICAM, with physical distances. Black: zonal. Blue: meridional.

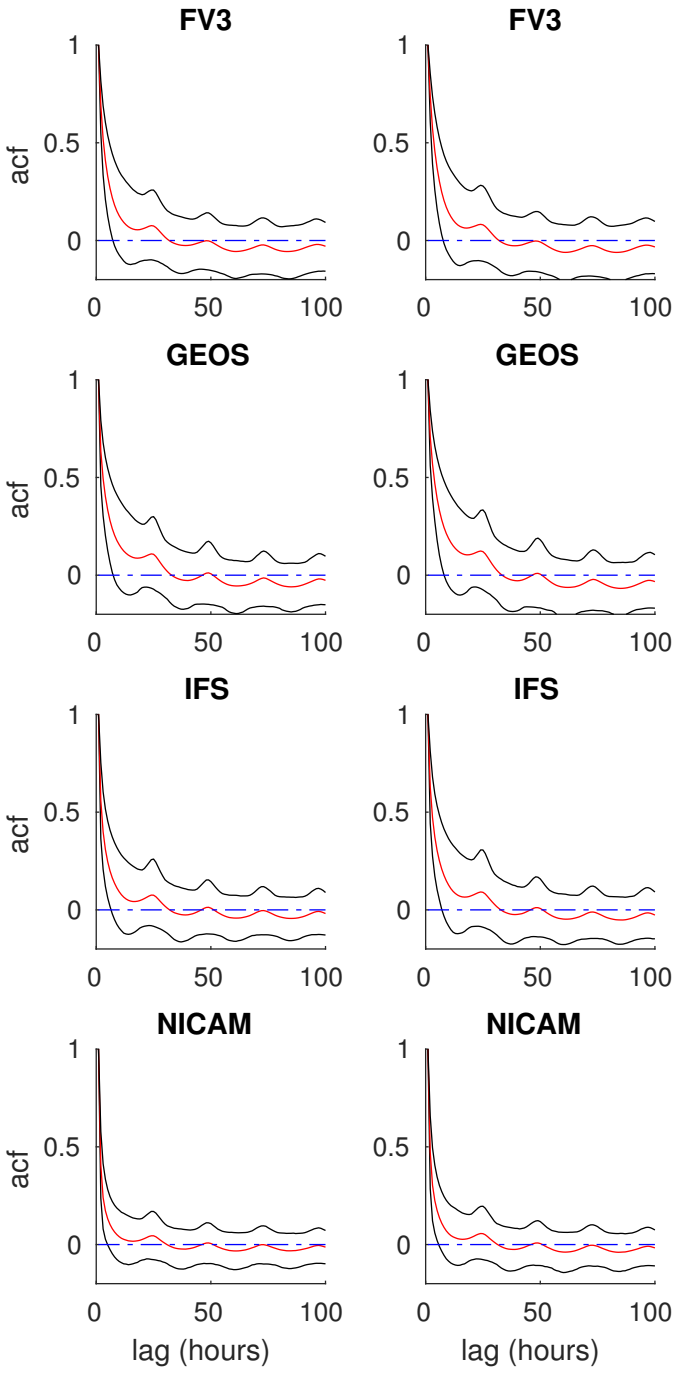

Figure A.87: Temporal autocorrelation functions for $\psi_{0.4^\circ,1}$ (left), $\psi_{0.4^\circ,2}$ (right) in the Warm Pool. Red: median. Black: interdecile range, both for points across the domain.

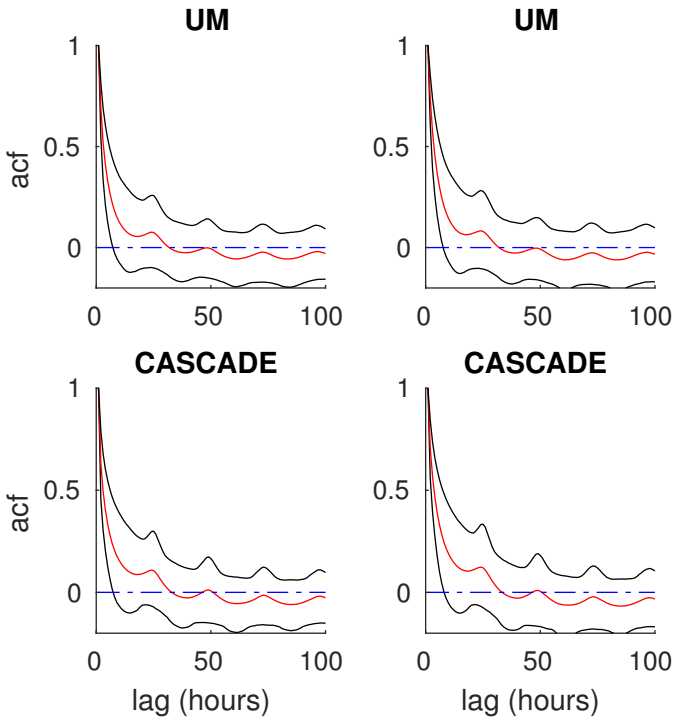

Figure A.88: Temporal autocorrelation functions for $\psi_{0.4^\circ,1}$ (left), $\psi_{0.4^\circ,2}$ (right) in the Warm Pool. Red: median. Black: interdecile range, both for points across the domain.

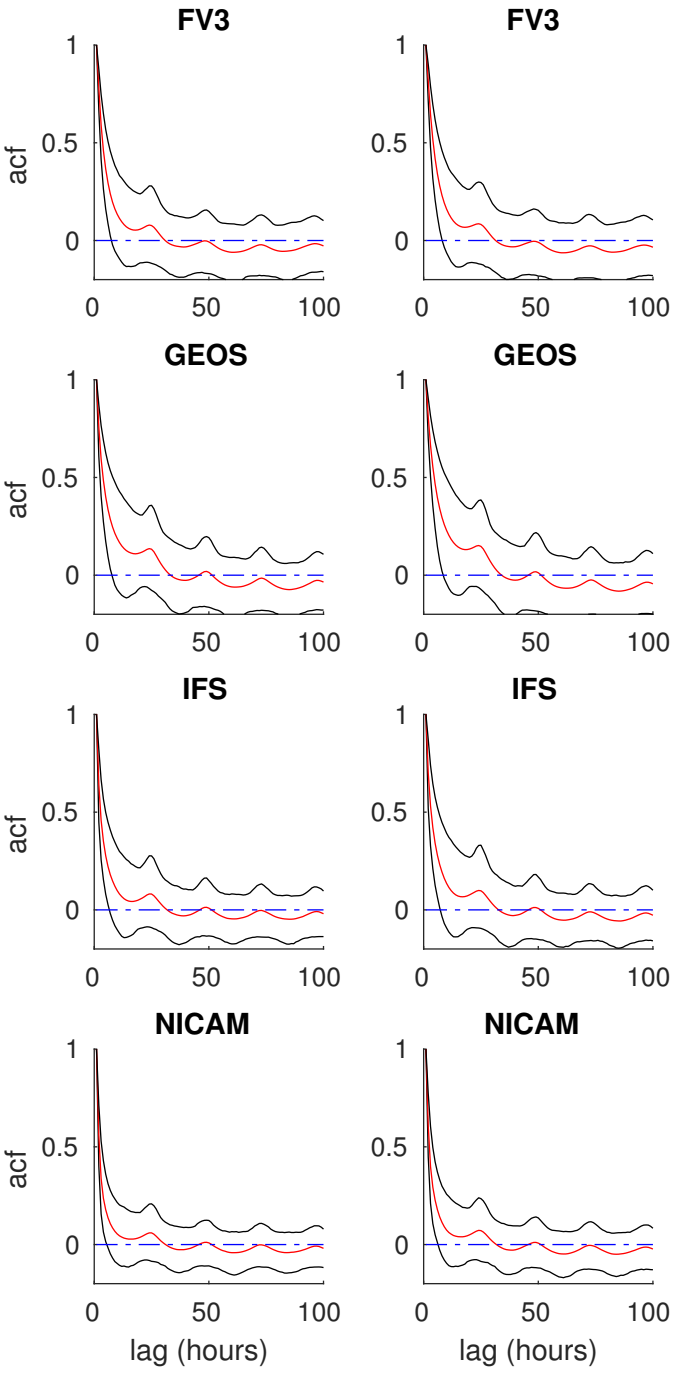

Figure A.89: Temporal autocorrelation functions for $\psi_{0.76^\circ,1}$ (left), $\psi_{0.76^\circ,2}$ (right) in the Warm Pool. Red: median. Black: interdecile range, both for points across the domain.

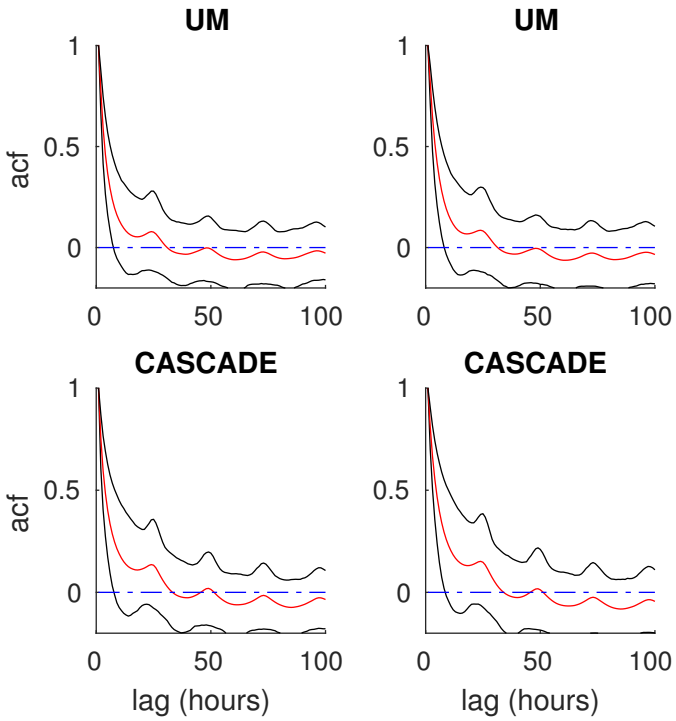

Figure A.90: Temporal autocorrelation functions for $\psi_{0.76^\circ,1}$ (left), $\psi_{0.76^\circ,2}$ (right) in the Warm Pool. Red: median. Black: interdecile range, both for points across the domain.

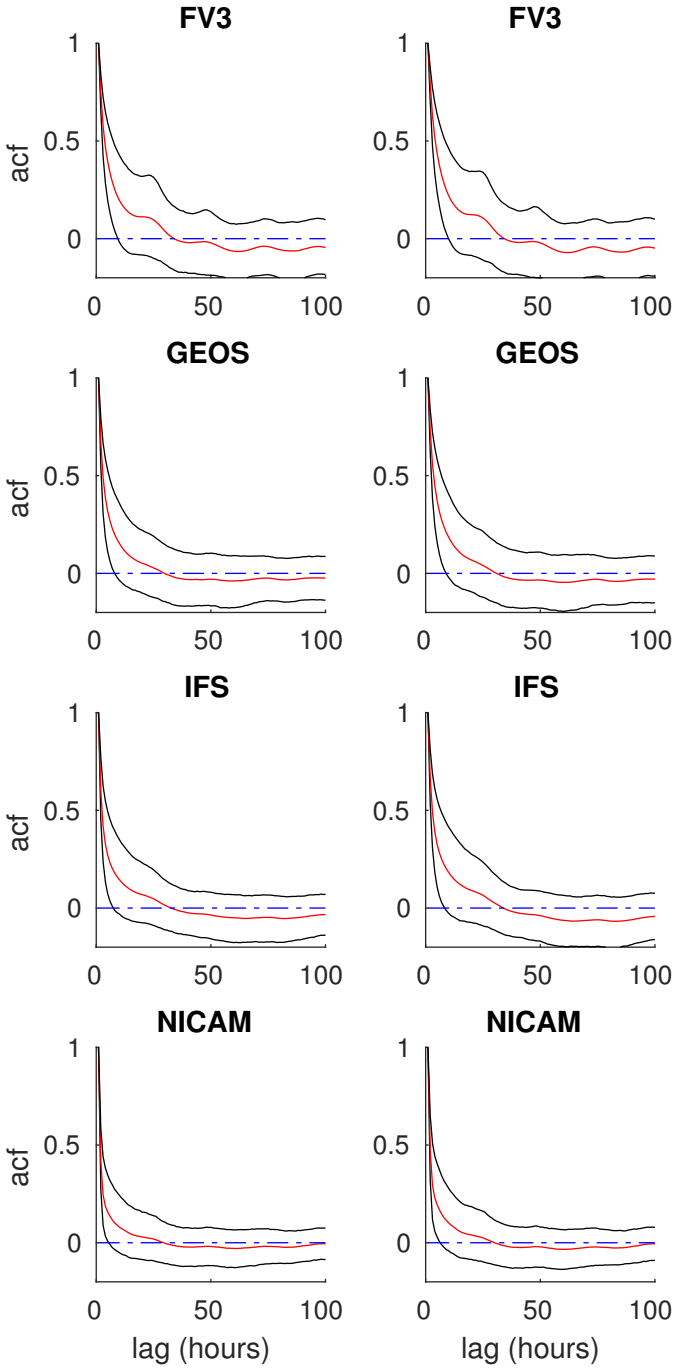

Figure A.91: Temporal autocorrelation functions for $\psi_{0.4^\circ,1}$ (left), $\psi_{0.4^\circ,2}$ (right) in the subtropical Northeast Pacific. Red: median. Black: interdecile range, both for points across the domain.

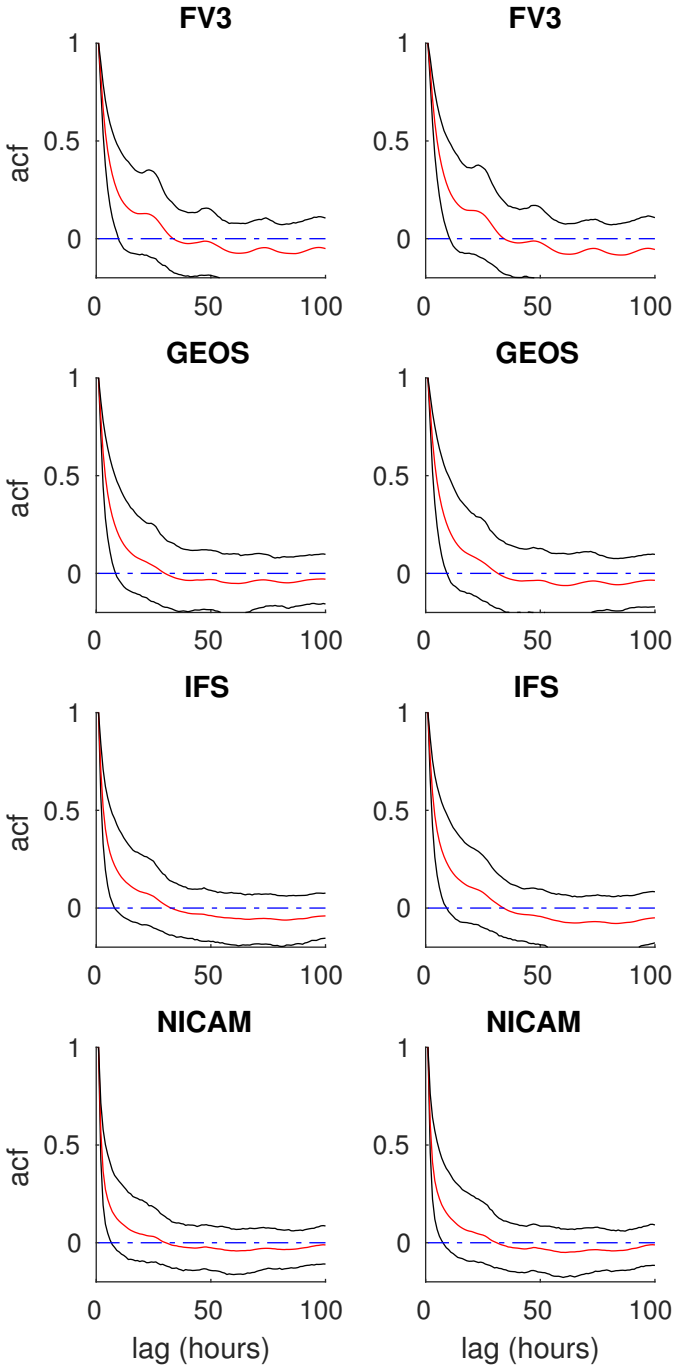

Figure A.92: Temporal autocorrelation functions for $\psi_{0.76^\circ,1}$ (left), $\psi_{0.76^\circ,2}$ (right) in the subtropical Northeast Pacific. Red: median. Black: interdecile range, both for points across the domain.

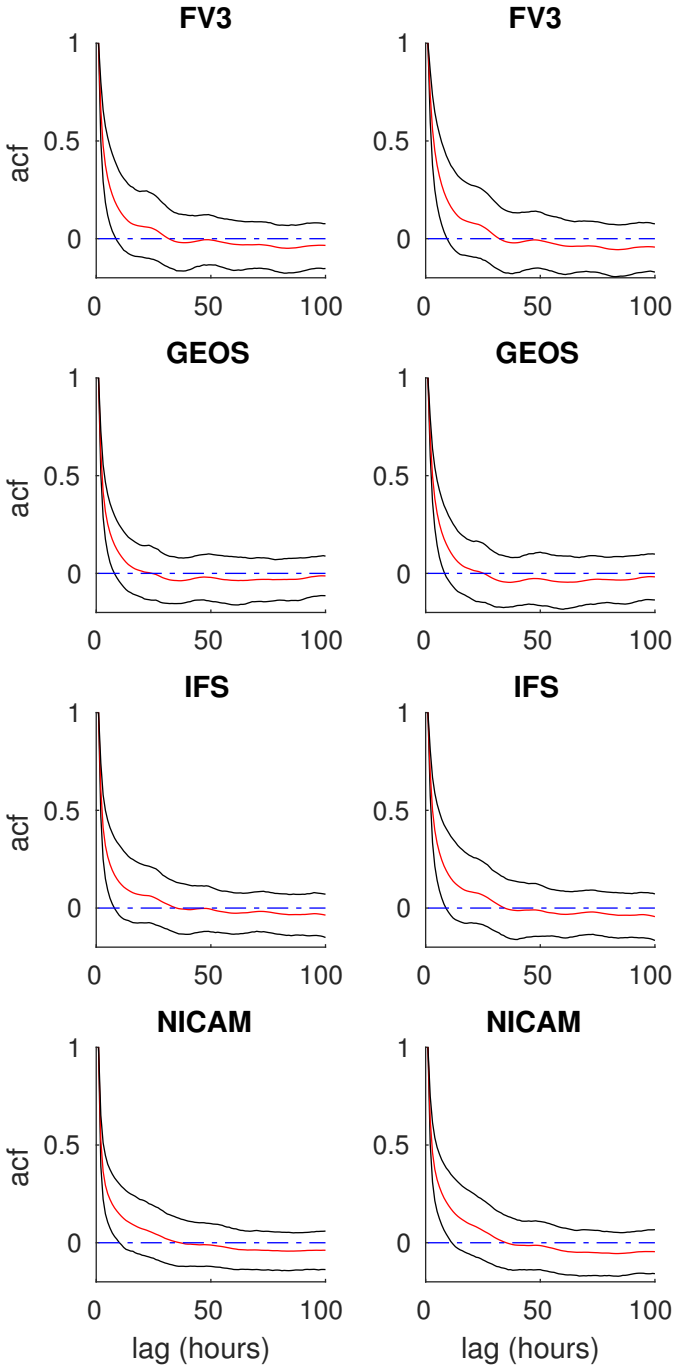

Figure A.93: Temporal autocorrelation functions for $\psi_{0.4^\circ,1}$ (left), $\psi_{0.4^\circ,2}$ (right) in the subarctic Northeast Pacific. Red: median. Black: interdecile range, both for points across the domain.

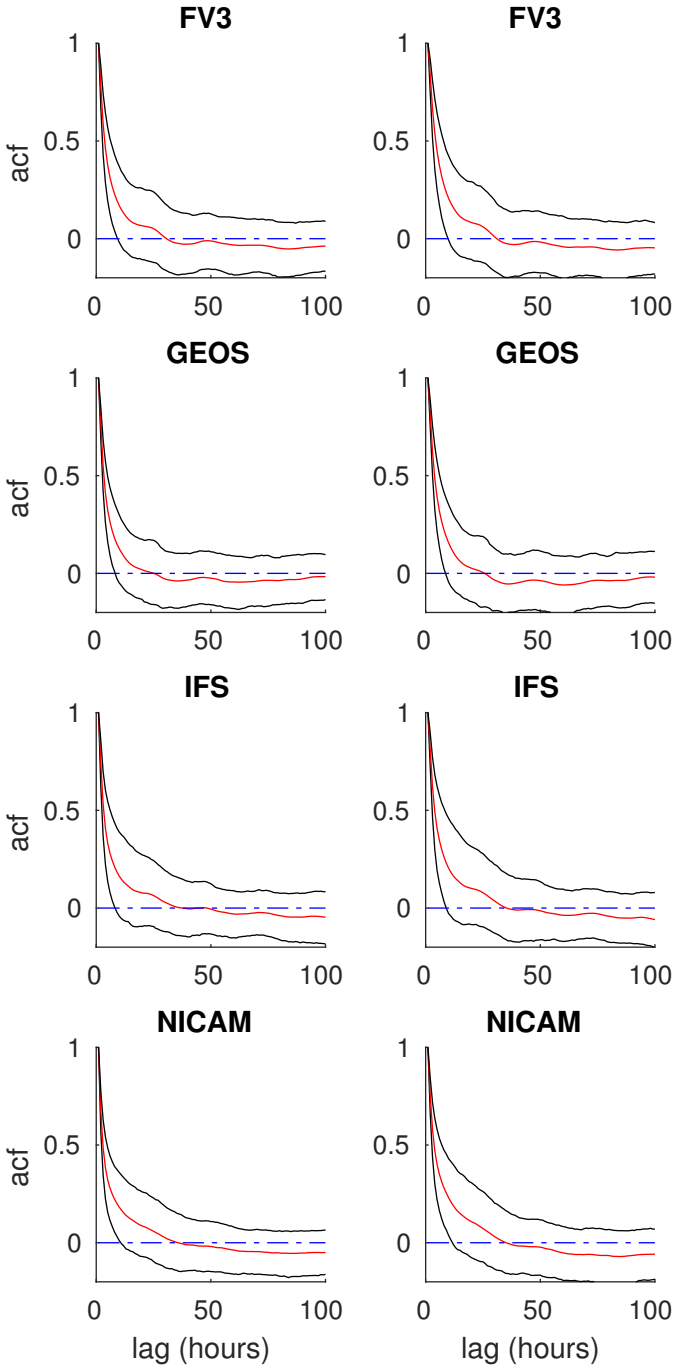

Figure A.94: Temporal autocorrelation functions for $\psi_{0.76^\circ,1}$ (left), $\psi_{0.76^\circ,2}$ (right) in the subarctic Northeast Pacific. Red: median. Black: interdecile range, both for points across the domain.

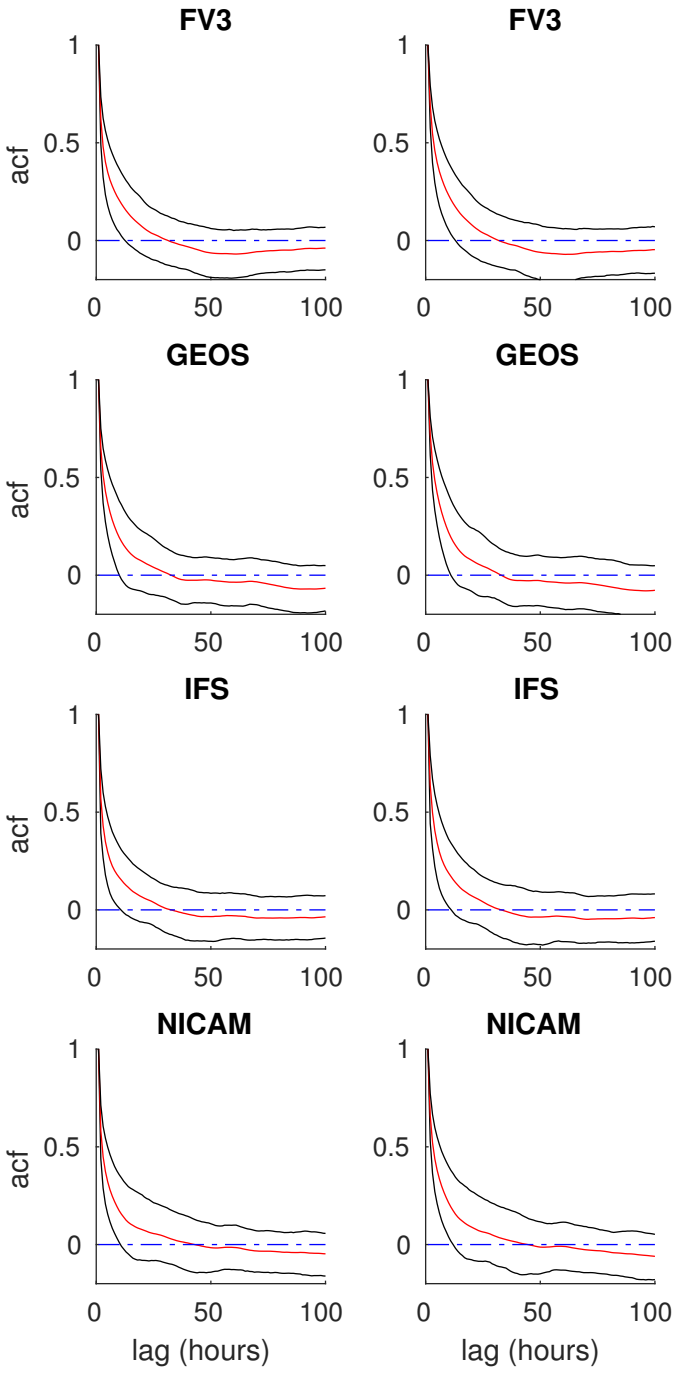

Figure A.95: Temporal autocorrelation functions for $\psi_{0.4^\circ,1}$ (left), $\psi_{0.4^\circ,2}$ (right) in the Southern Ocean. Red: median. Black: interdecile range, both for points across the domain.

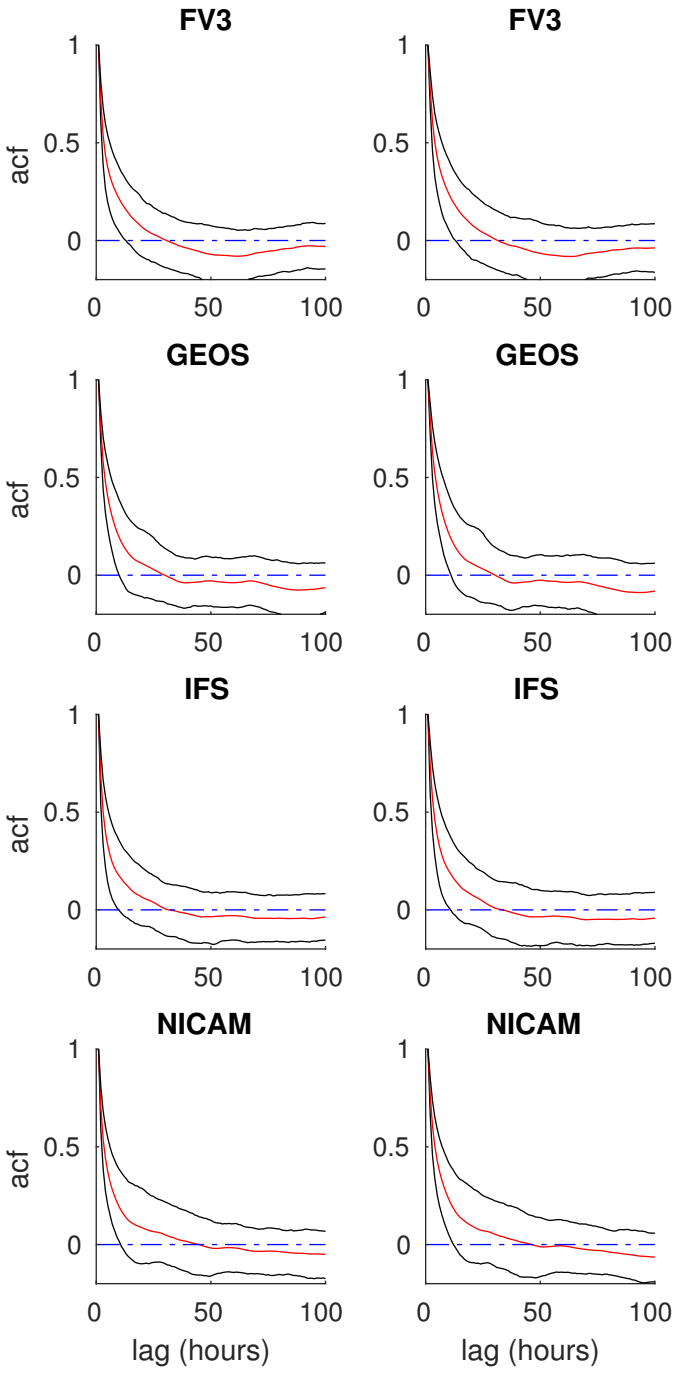

Figure A.96: Temporal autocorrelation functions for $\psi_{0.76^\circ,1}$ (left), $\psi_{0.76^\circ,2}$ (right) in the Southern Ocean. Red: median. Black: interdecile range, both for points across the domain.

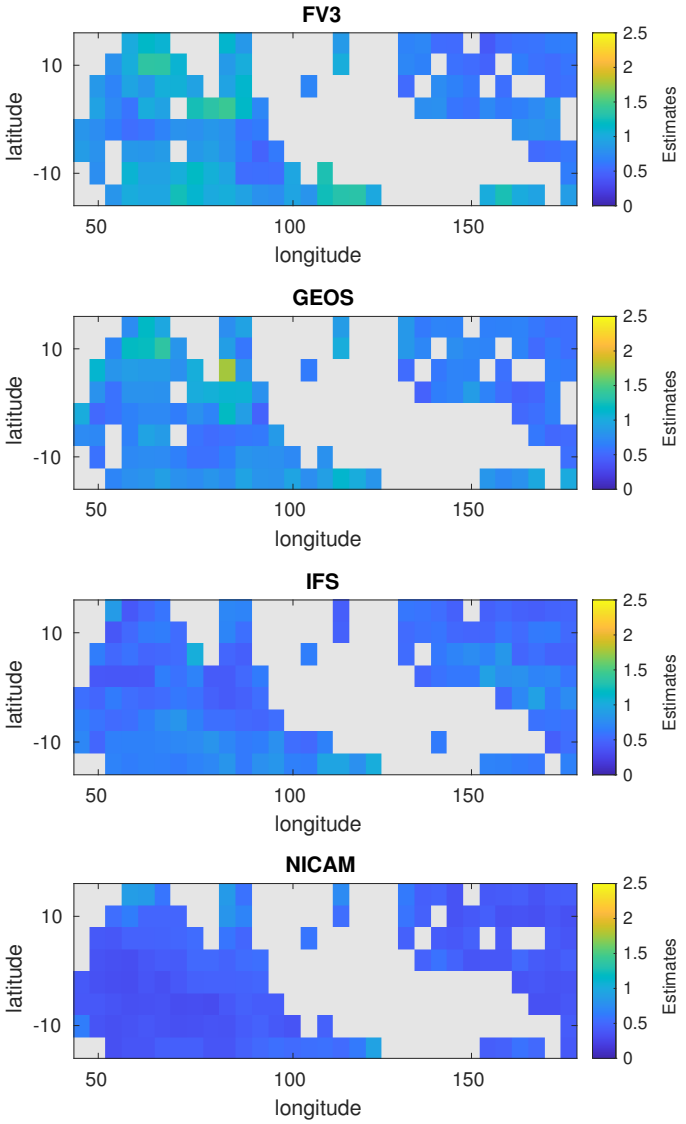

Figure A.97: Gaussian process fits for θ_x in the Warm Pool. Vertical axis denotes latitude, whereas the horizontal axis denotes longitude. $N = 0.4°$, $n = 2$, for August 11–20.

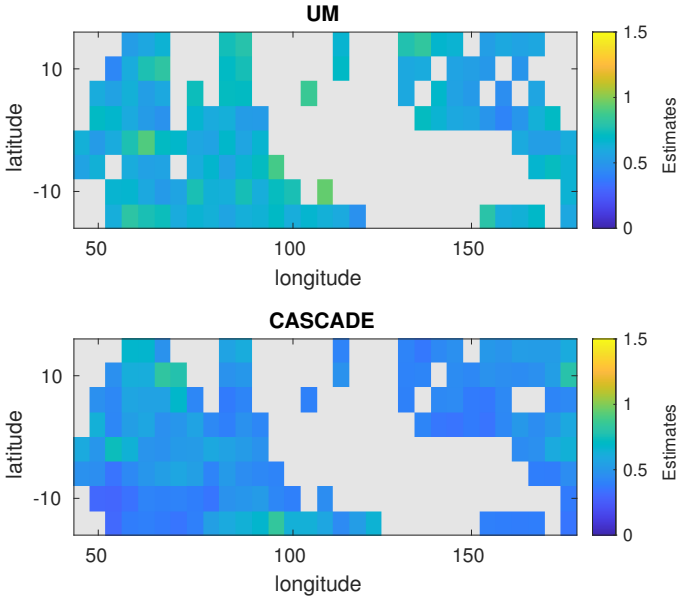

Figure A.98: Gaussian process fits for θ_x in the Warm Pool. Vertical axis denotes latitude, whereas the horizontal axis denotes longitude. $N = 0.4°$, $n = 2$, for August 11–20.

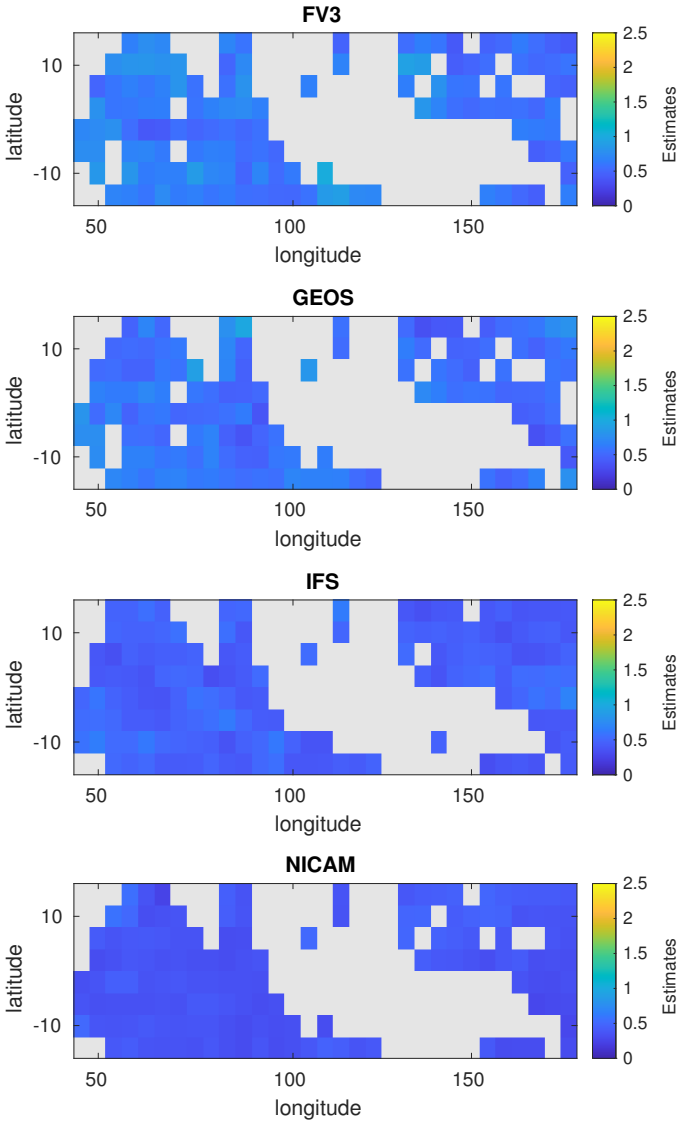

Figure A.99: Gaussian process fits for θ_y in the Warm Pool. Vertical axis denotes latitude, whereas the horizontal axis denotes longitude. $N = 0.4°$, $n = 2$, for August 11–20.

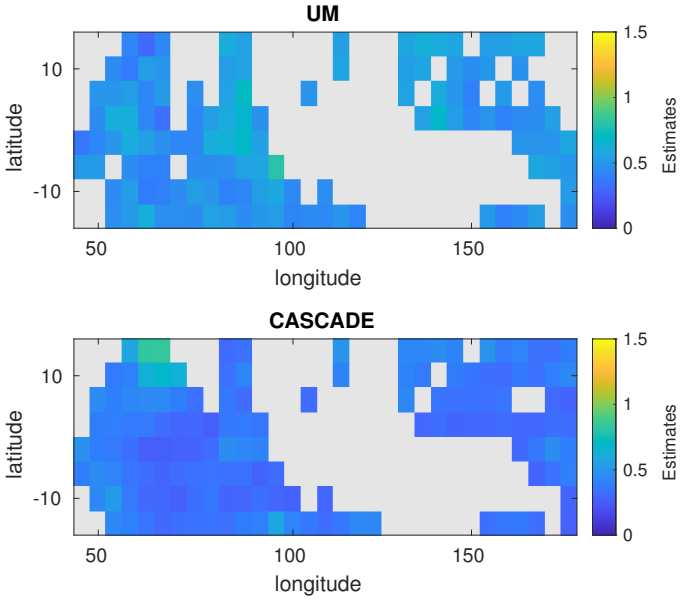

Figure A.100: Gaussian process fits for θ_y in the Warm Pool. Vertical axis denotes latitude, whereas the horizontal axis denotes longitude. $N = 0.4°$, $n = 2$, for August 11–20.

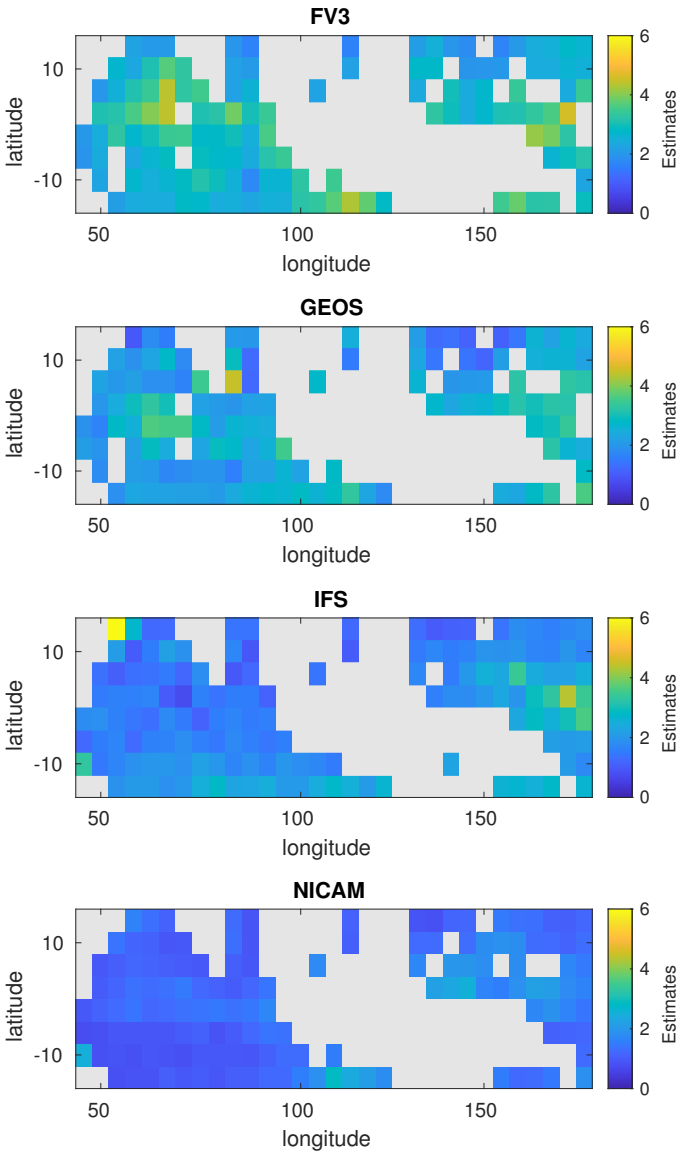

Figure A.101: Gaussian process fits for θ_t in the Warm Pool. Vertical axis denotes latitude, whereas the horizontal axis denotes longitude. $N = 0.4°$, $n = 2$, for August 11–20.

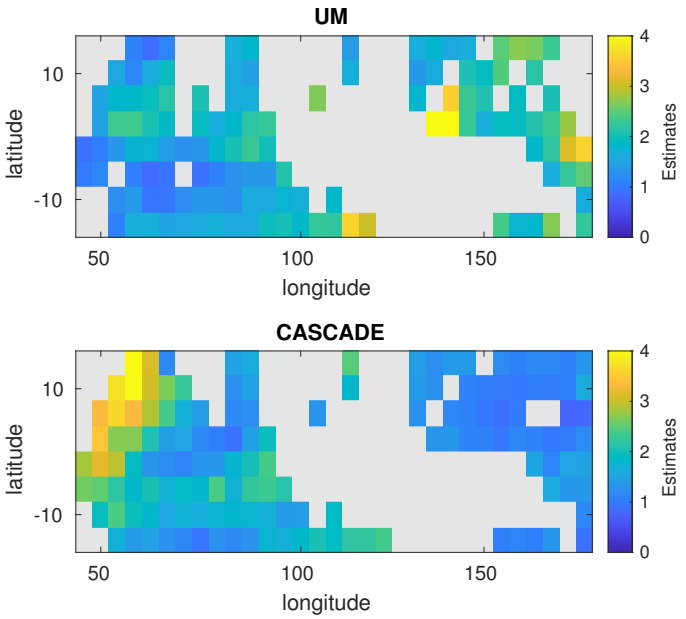

Figure A.102: Gaussian process fits for θ_t in the Warm Pool. Vertical axis denotes latitude, whereas the horizontal axis denotes longitude. $N = 0.4°$, $n = 2$, for August 11–20.

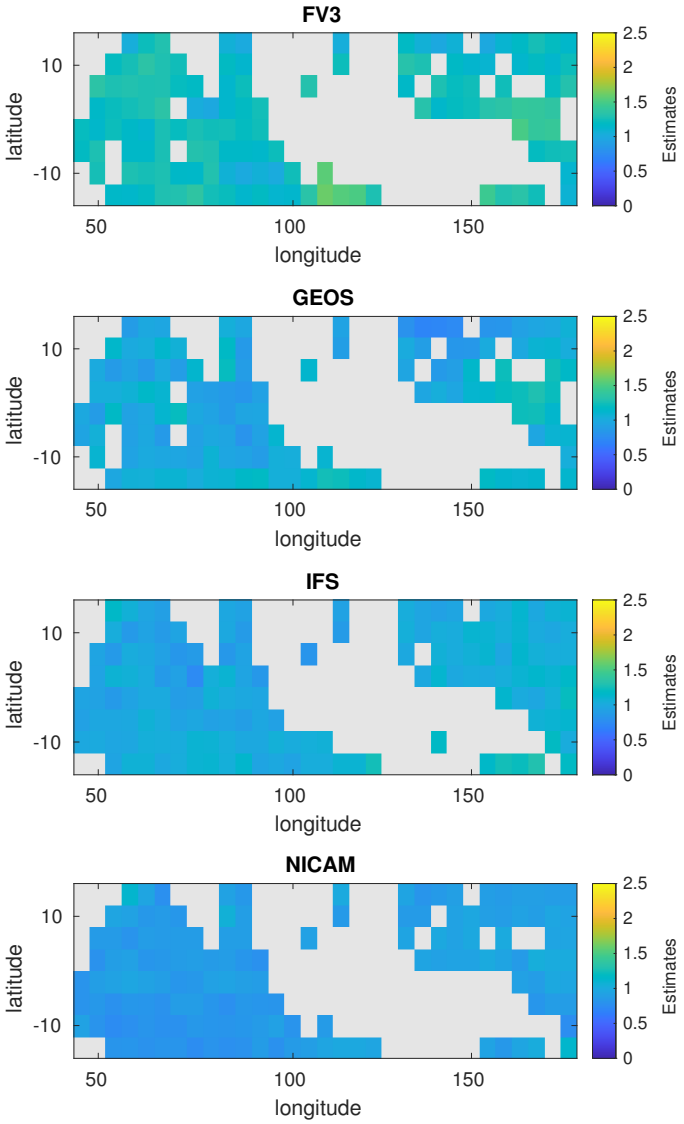

Figure A.103: Gaussian process fits for γ in the Warm Pool. Vertical axis denotes latitude, whereas the horizontal axis denotes longitude. $N = 0.4°$, $n = 2$, for August 11–20.

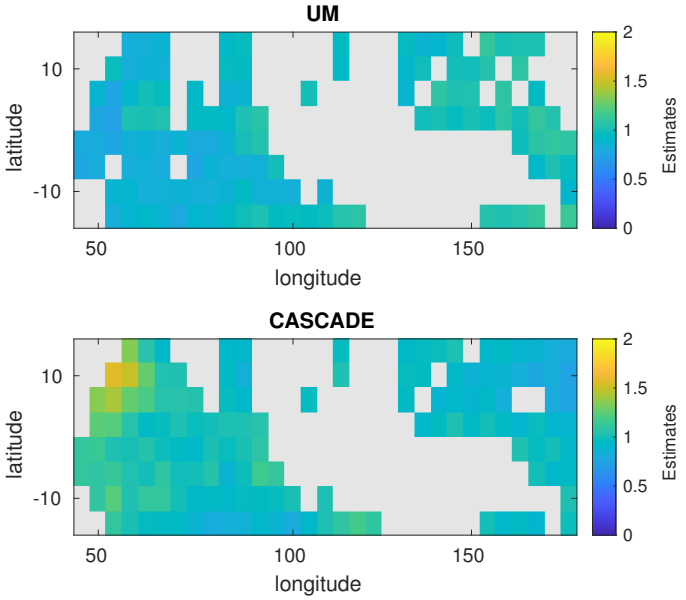

Figure A.104: Gaussian process fits for γ in the Warm Pool. Vertical axis denotes latitude, whereas the horizontal axis denotes longitude. $N = 0.4°$, $n = 2$, for August 11–20.

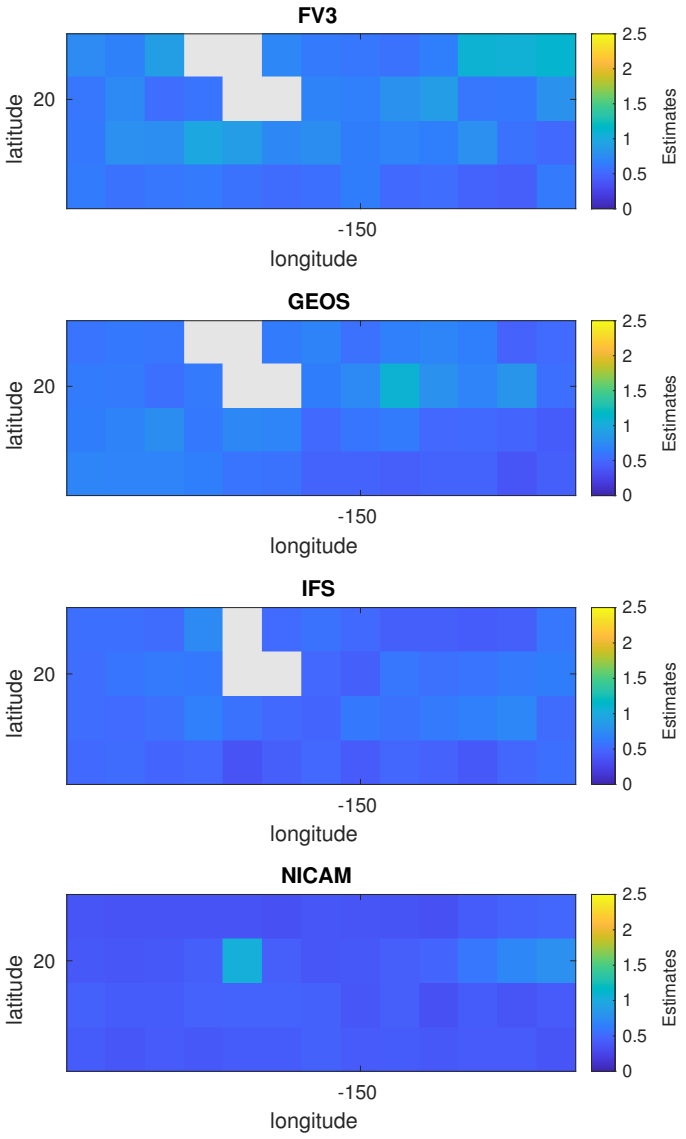

Figure A.105: Gaussian process fits for θ_x in the subtropical Northeast Pacific. Vertical axis denotes latitude, whereas the horizontal axis denotes longitude. $N = 0.4°$, $n = 2$, for August 11–20.

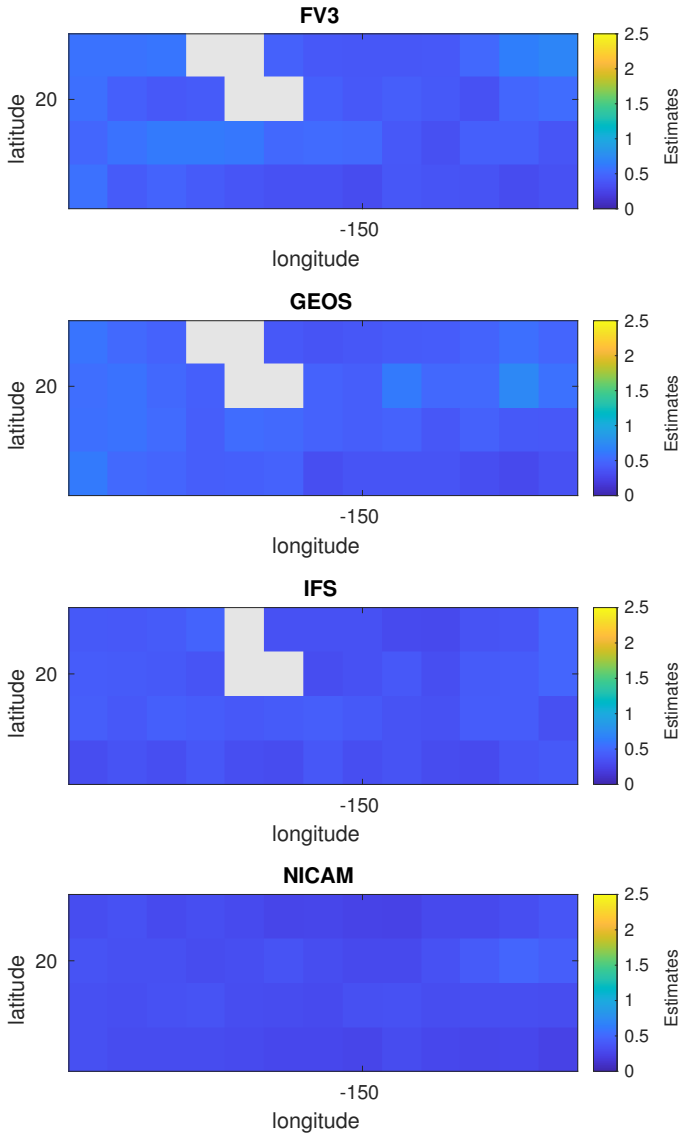

Figure A.106: Gaussian process fits for θ_y in the subtropical Northeast Pacific. Vertical axis denotes latitude, whereas the horizontal axis denotes longitude. $N = 0.4°$, $n = 2$, for August 11–20.

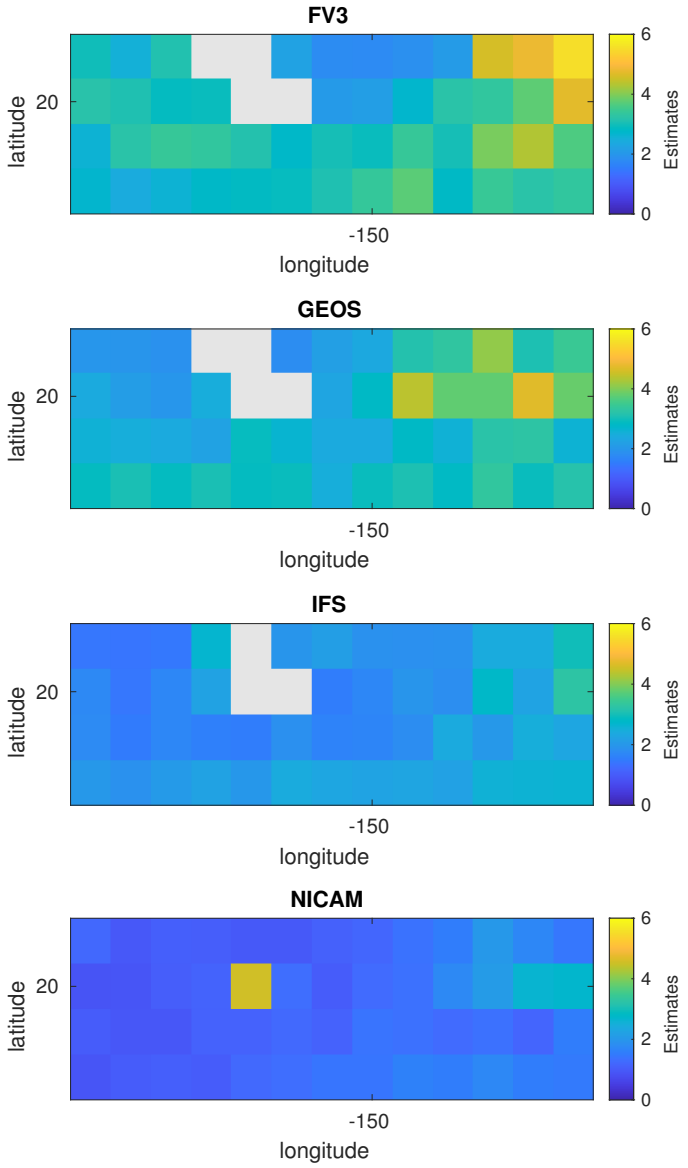

Figure A.107: Gaussian process fits for θ_t in the subtropical Northeast Pacific. Vertical axis denotes latitude, whereas the horizontal axis denotes longitude. $N = 0.4°$, $n = 2$, for August 11–20.

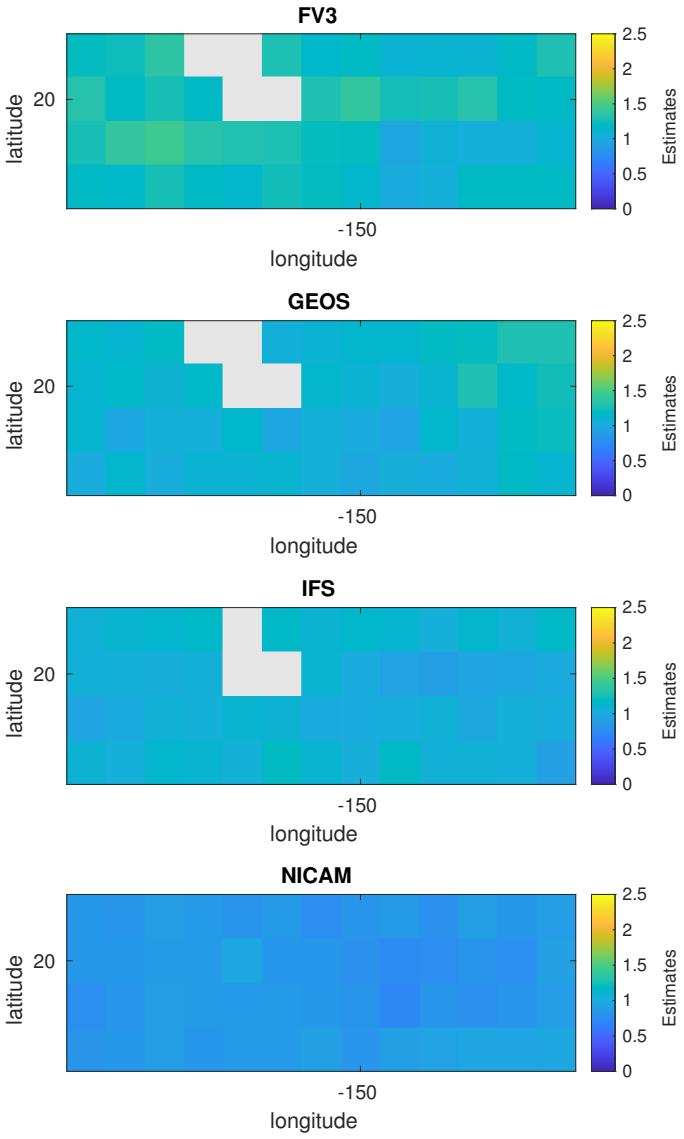

Figure A.108: Gaussian process fits for γ in the subtropical Northeast Pacific. Vertical axis denotes latitude, whereas the horizontal axis denotes longitude. $N = 0.4°$, $n = 2$, for August 11–20.

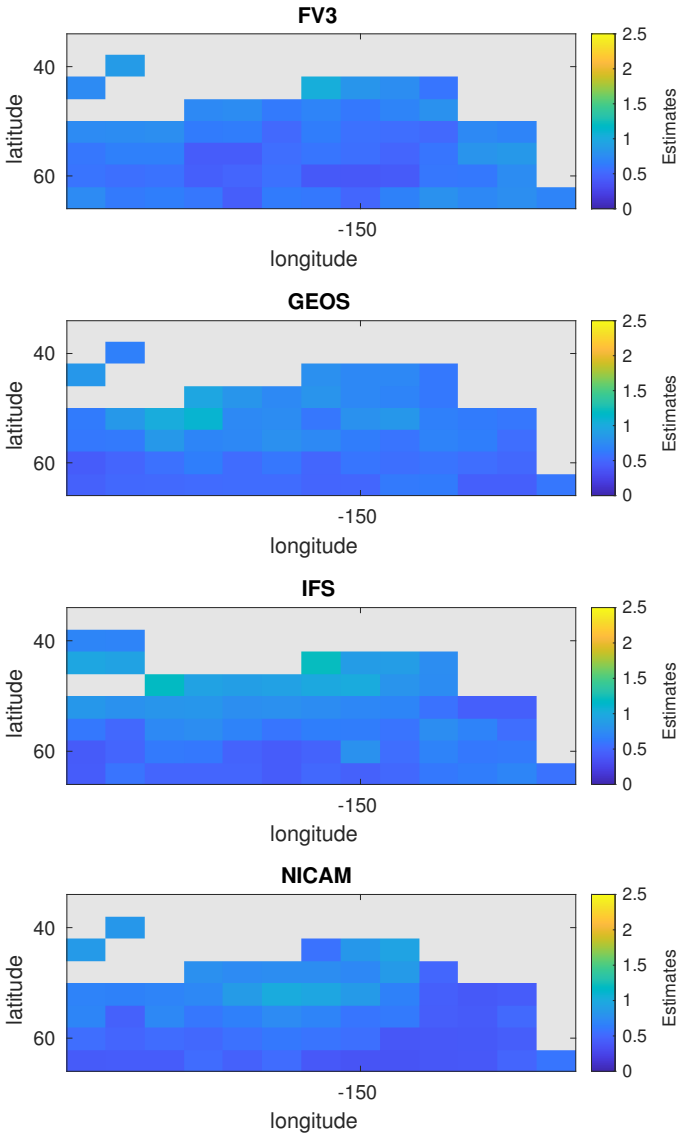

Figure A.109: Gaussian process fits for θ_x in the subarctic Northeast Pacific. Vertical axis denotes latitude, whereas the horizontal axis denotes longitude. $N = 0.4°$, $n = 2$, for August 11–20.

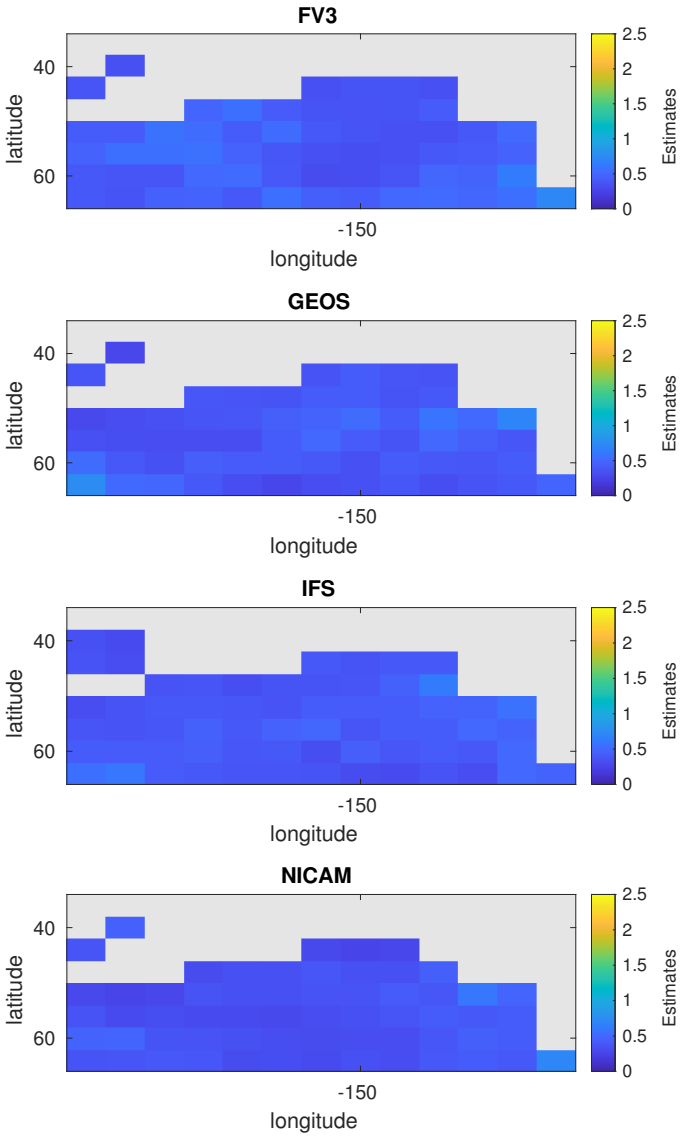

Figure A.110: Gaussian process fits for θ_y in the subarctic Northeast Pacific. Vertical axis denotes latitude, whereas the horizontal axis denotes longitude. $N = 0.4°$, $n = 2$, for August 11–20.

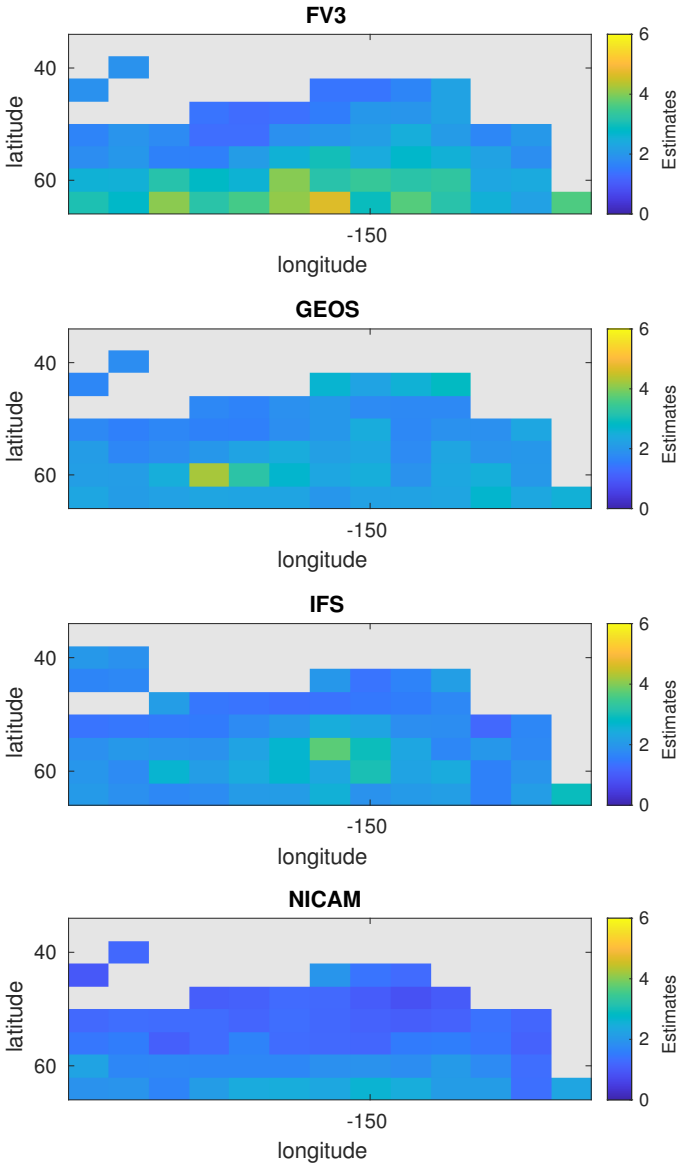

Figure A.111: Gaussian process fits for θ_t in the subarctic Northeast Pacific. Vertical axis denotes latitude, whereas the horizontal axis denotes longitude. $N = 0.4°$, $n = 2$, for August 11–20.

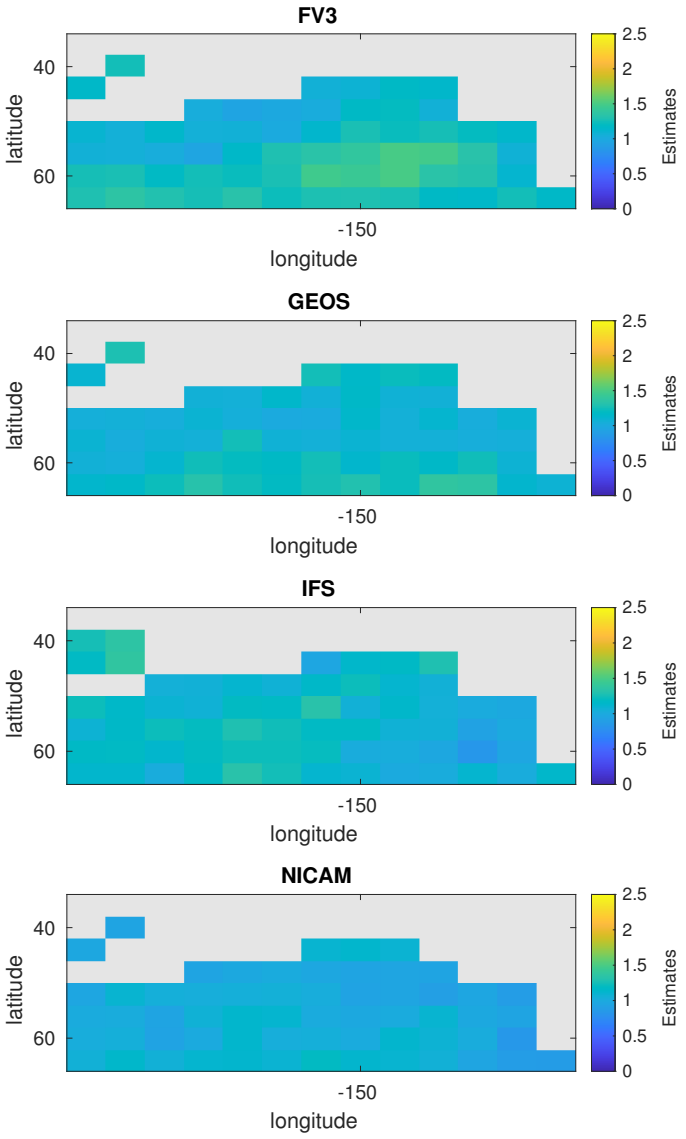

Figure A.112: Gaussian process fits for γ in the subarctic Northeast Pacific. Vertical axis denotes latitude, whereas the horizontal axis denotes longitude. $N = 0.4°$, $n = 2$, for August 11–20.

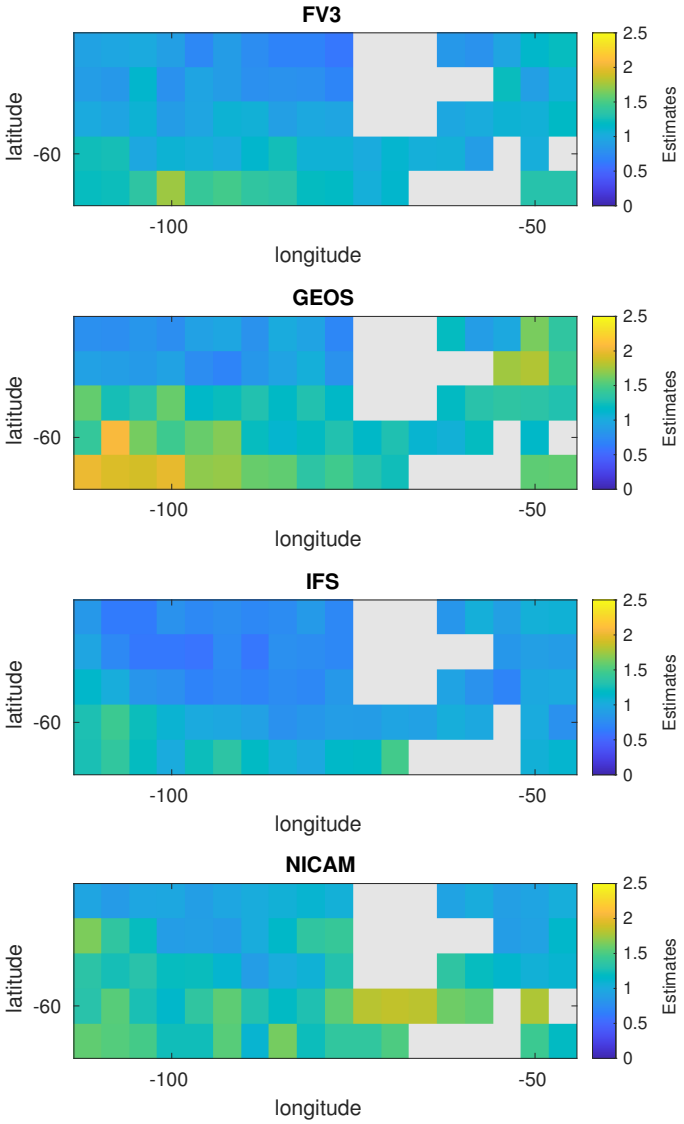

Figure A.113: Gaussian process fits for θ_x in the Southern Ocean. Vertical axis denotes latitude, whereas the horizontal axis denotes longitude. $N = 0.4°$, $n = 2$, for August 11–20.

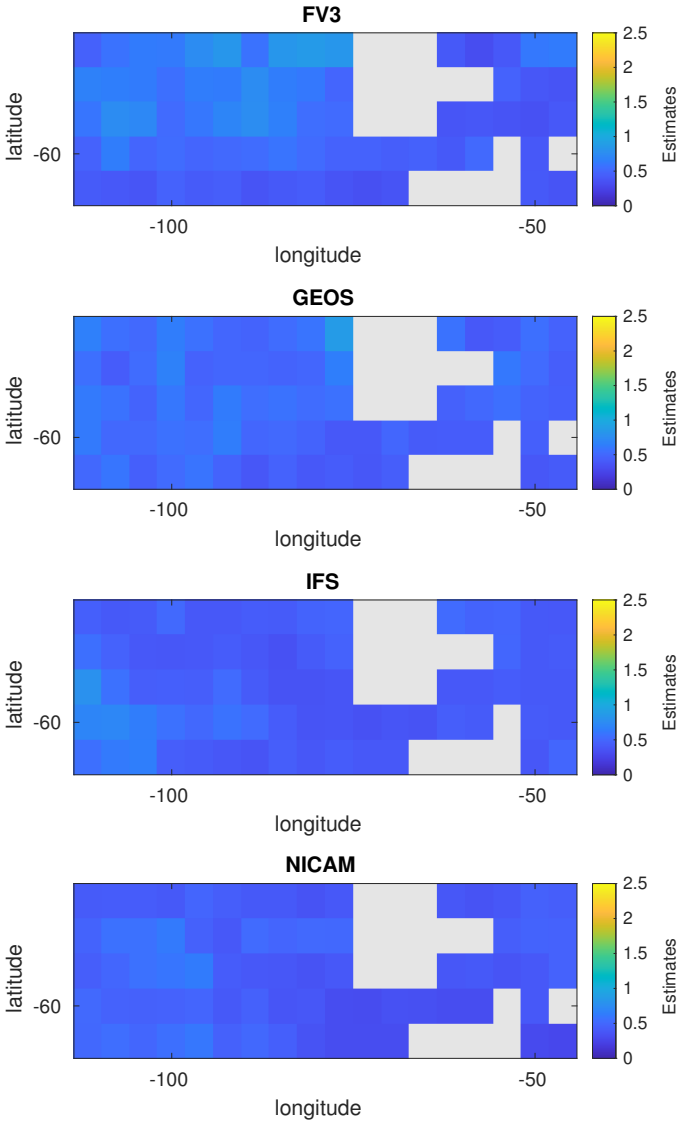

Figure A.114: Gaussian process fits for θ_y in the Southern Ocean. Vertical axis denotes latitude, whereas the horizontal axis denotes longitude. $N = 0.4°$, $n = 2$, for August 11–20.

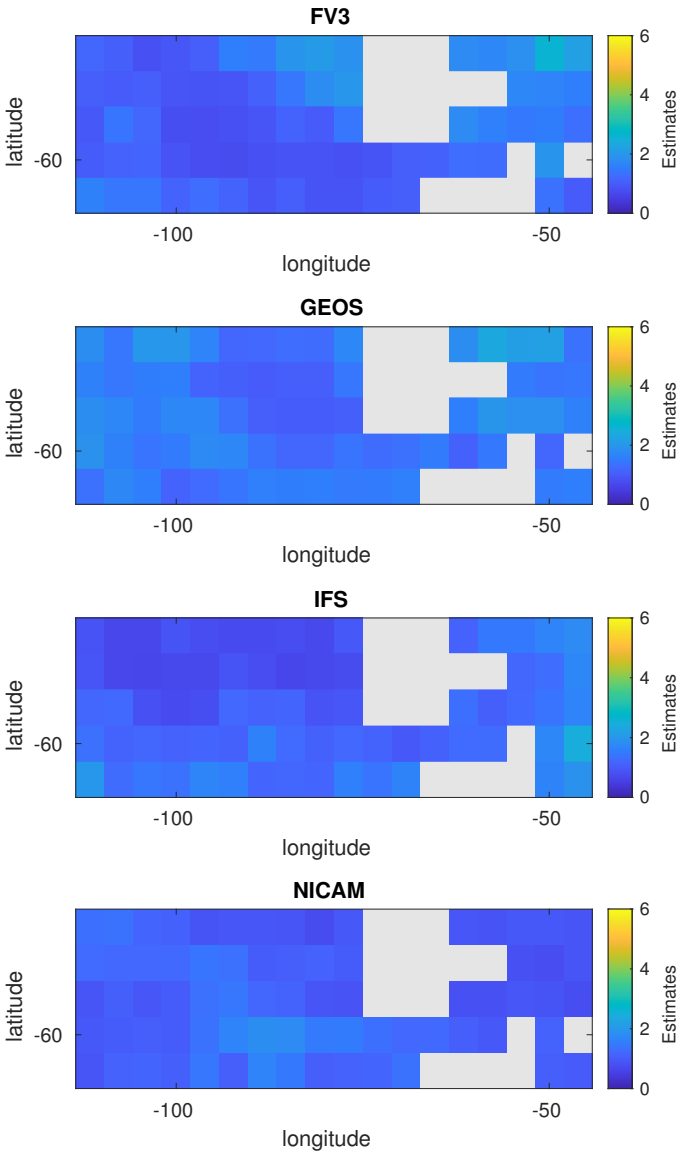

Figure A.115: Gaussian process fits for θ_t in the Southern Ocean. Vertical axis denotes latitude, whereas the horizontal axis denotes longitude. $N = 0.4°$, $n = 2$, for August 11–20.

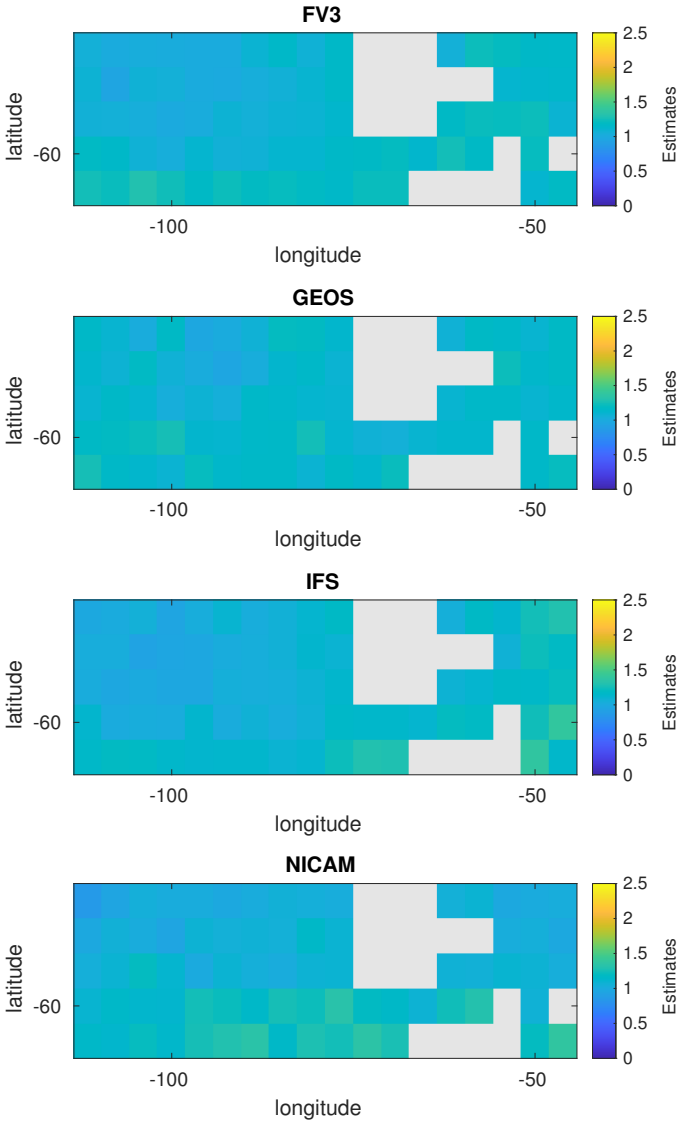

Figure A.116: Gaussian process fits for γ in the Southern Ocean. Vertical axis denotes latitude, whereas the horizontal axis denotes longitude. $N = 0.4°$, $n = 2$, for August 11–20.

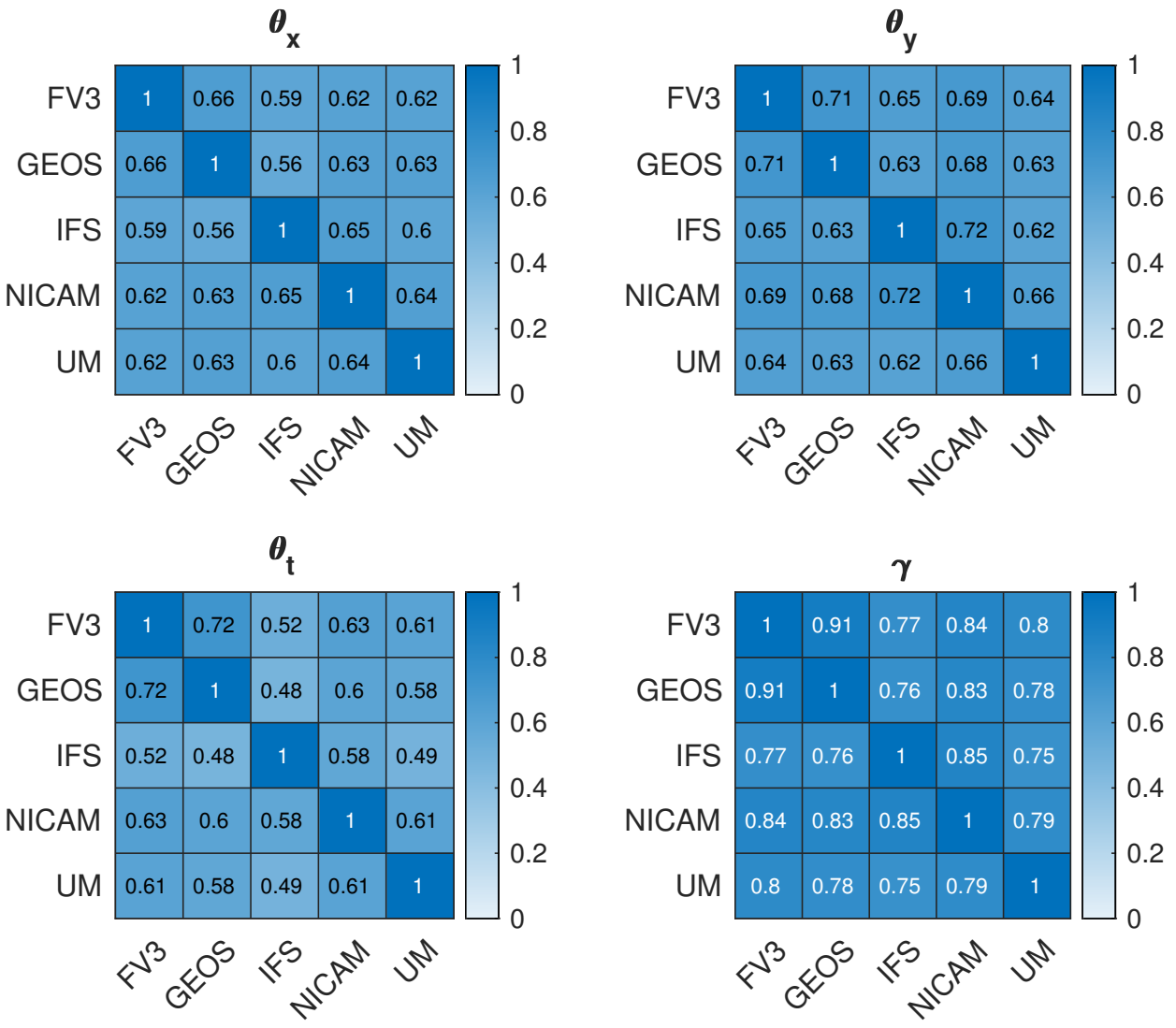

Figure A.117: Gaussian process fit correlations between different models for the Warm Pool.

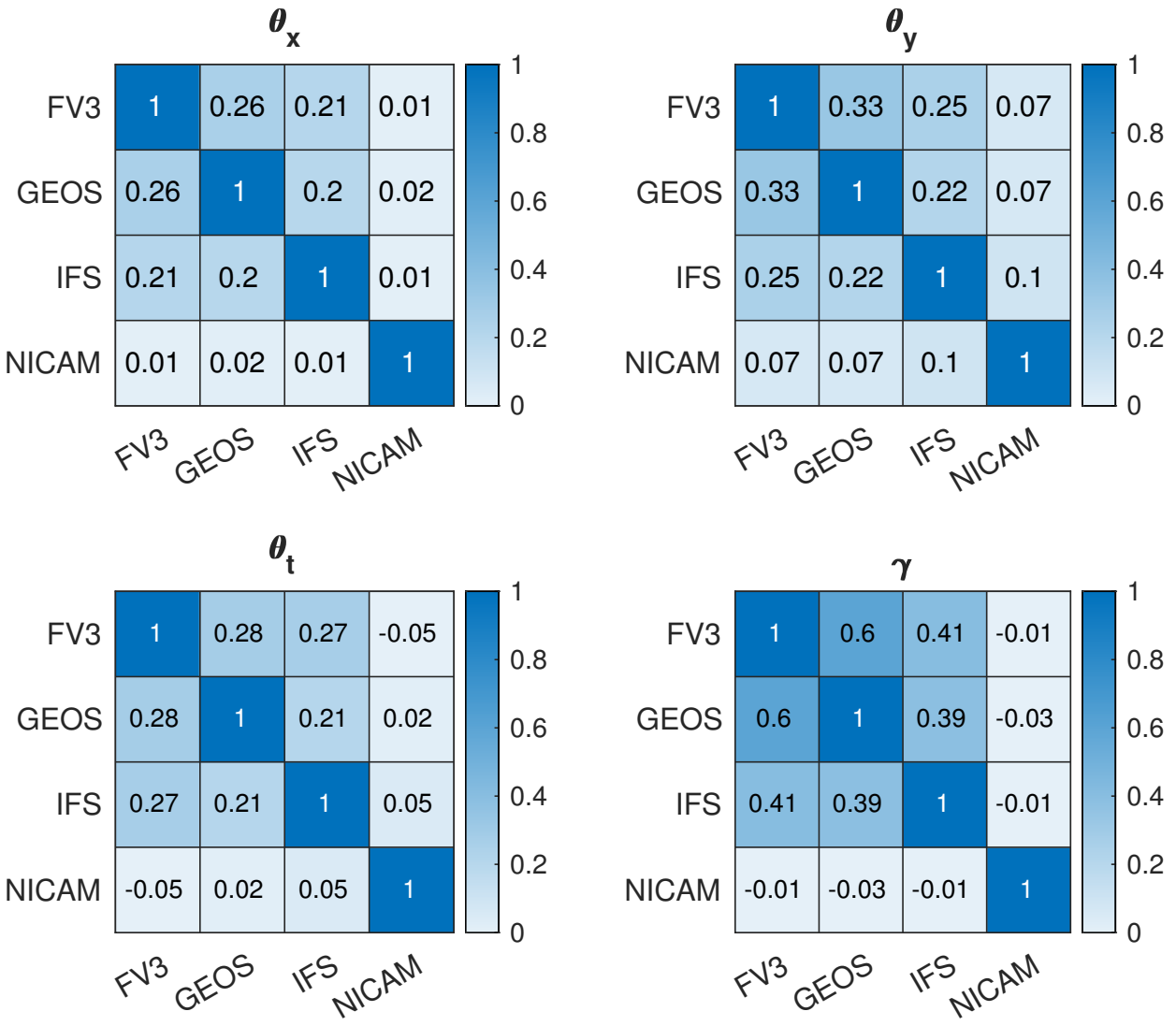

Figure A.118: Gaussian process fit correlations between different models for the subtropical Northeast Pacific.

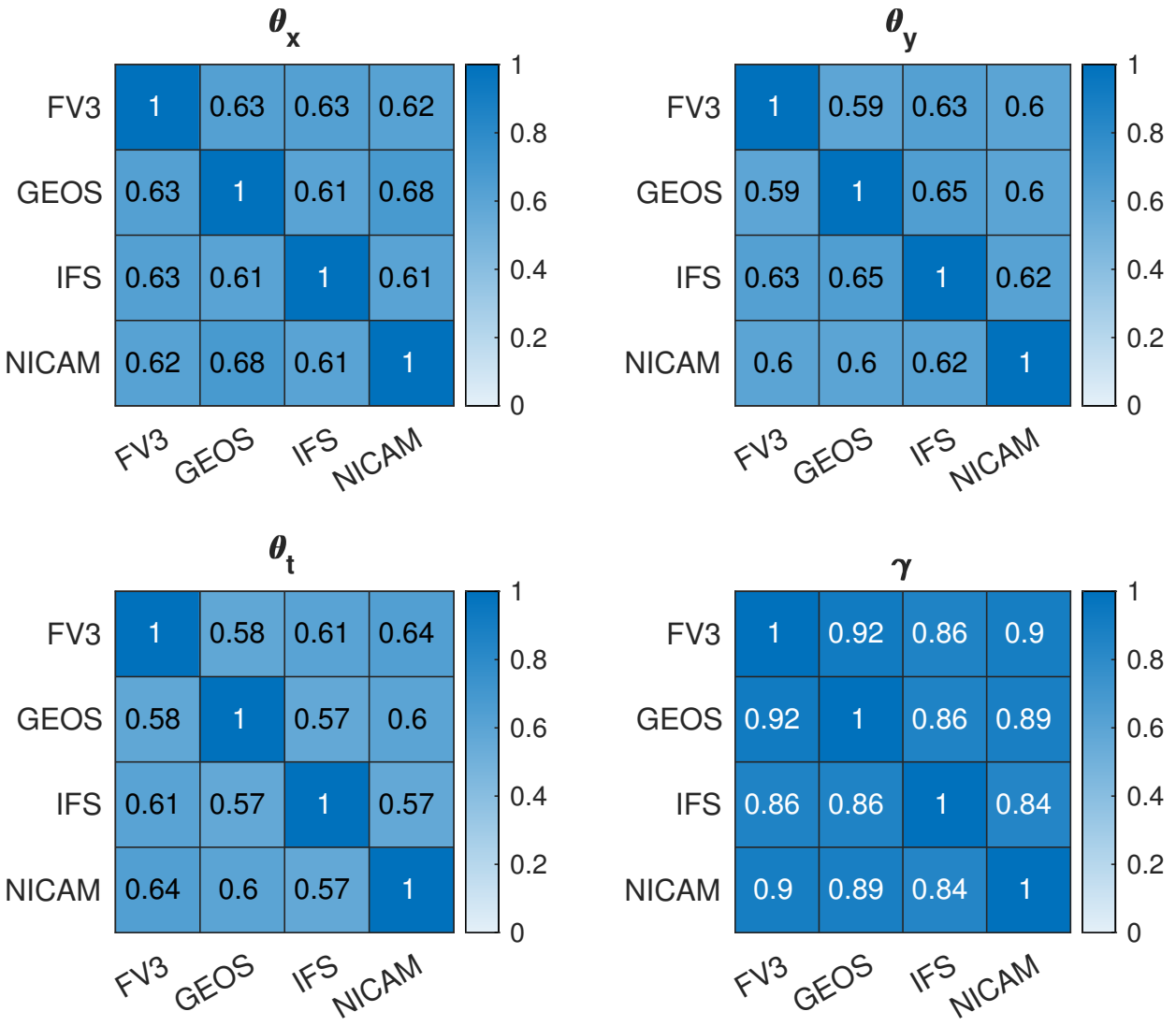

Figure A.119: Gaussian process fit correlations between different models for the subarctic Northeast Pacific.

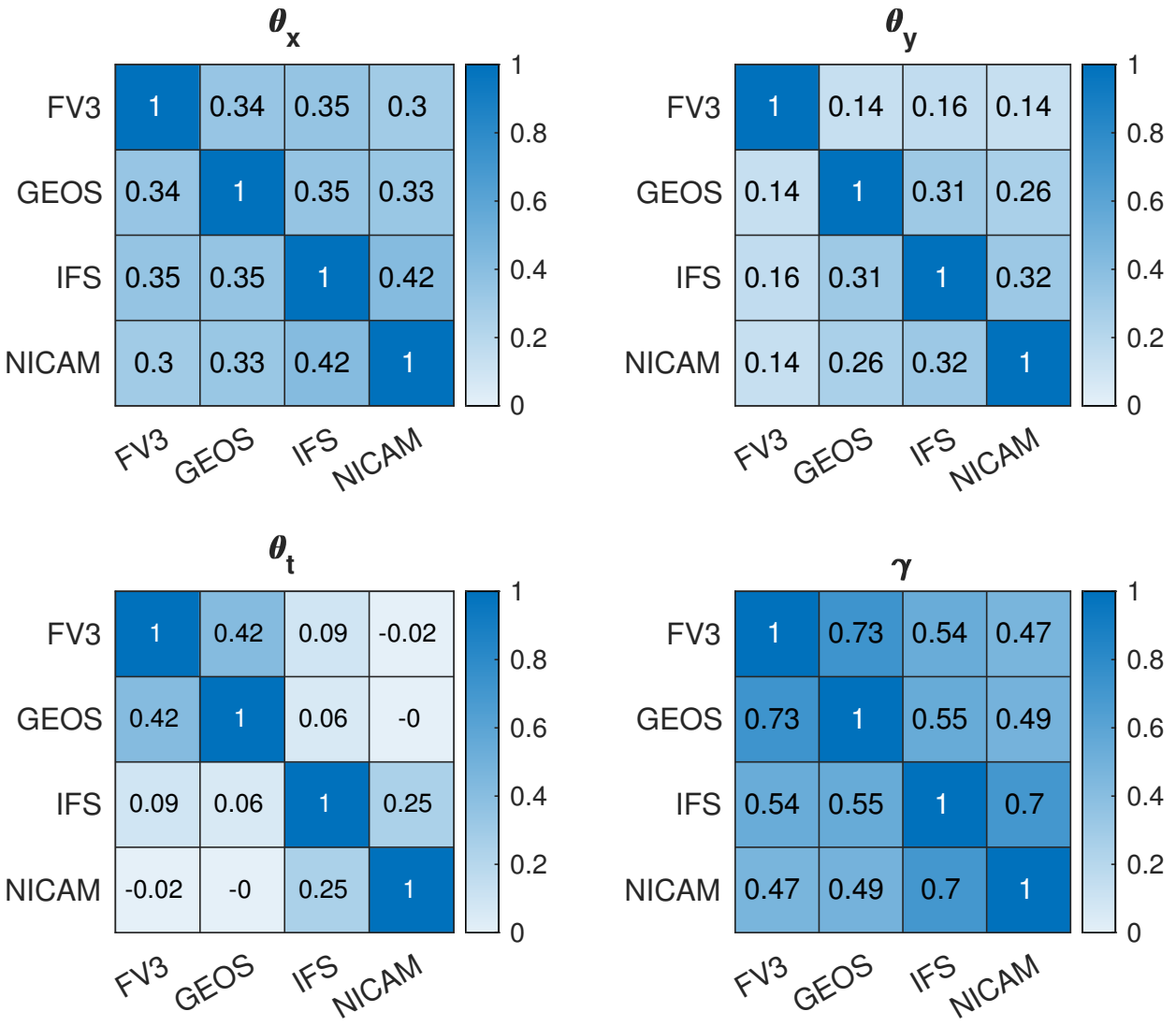

Figure A.120: Gaussian process fit correlations between different models for the Southern Ocean.

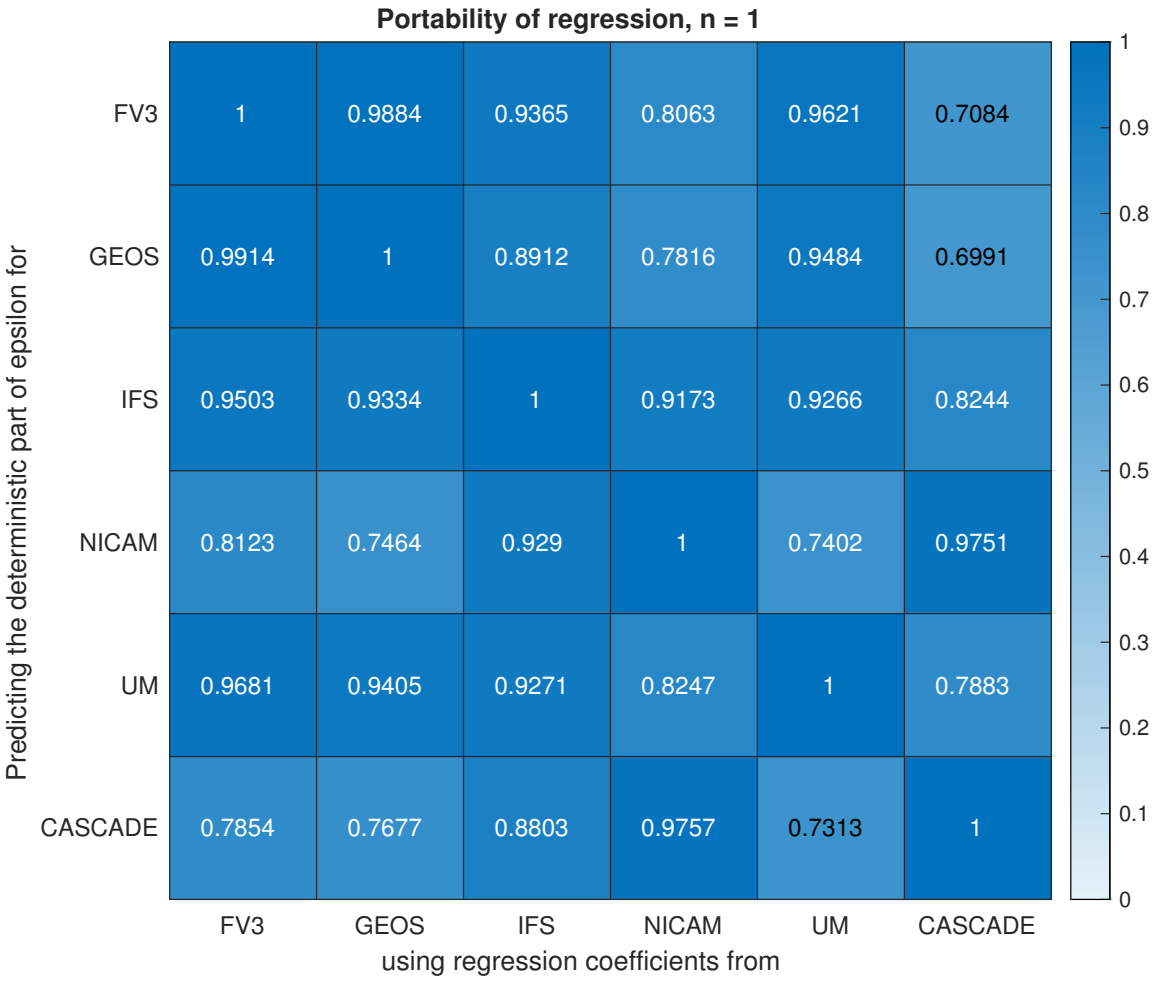

Figure A.121: Correlation of the deterministic part of the error process. The regression fit obtained from the model in the horizontal axis is applied to the variables obtained from the model in the vertical axis, and is compared to $\mu_{0.4^\circ,1}$ obtained from the regression and variables of the model in the vertical axis. $N = 0.4^\circ$, $n = 1$.

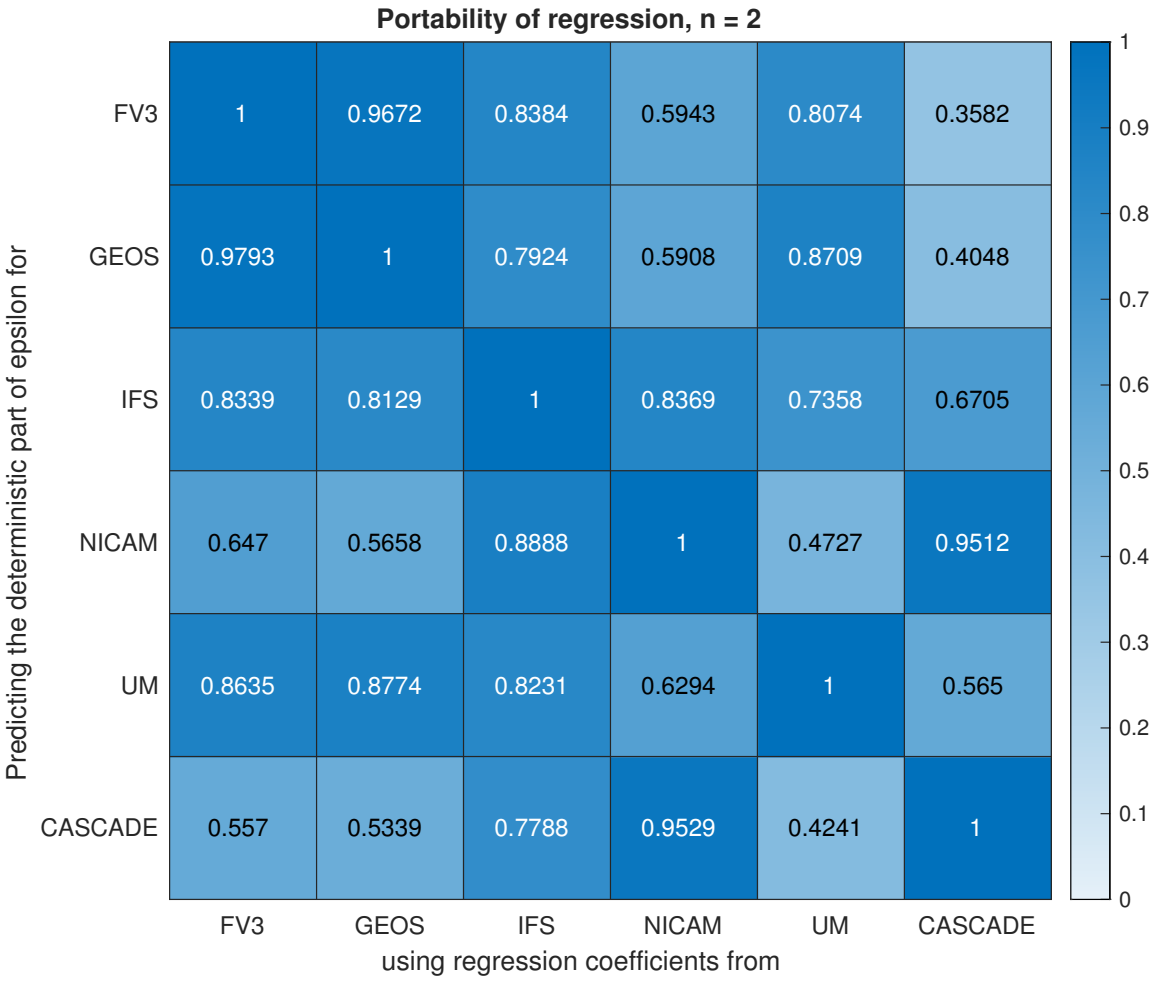

Figure A.122: Correlation of the deterministic part of the error process. The regression fit obtained from the model in the horizontal axis is applied to the variables obtained from the model in the vertical axis, and is compared to $\mu_{0.4^\circ,2}$ obtained from the regression and variables of the model in the vertical axis. $N = 0.4^\circ$, $n = 2$.

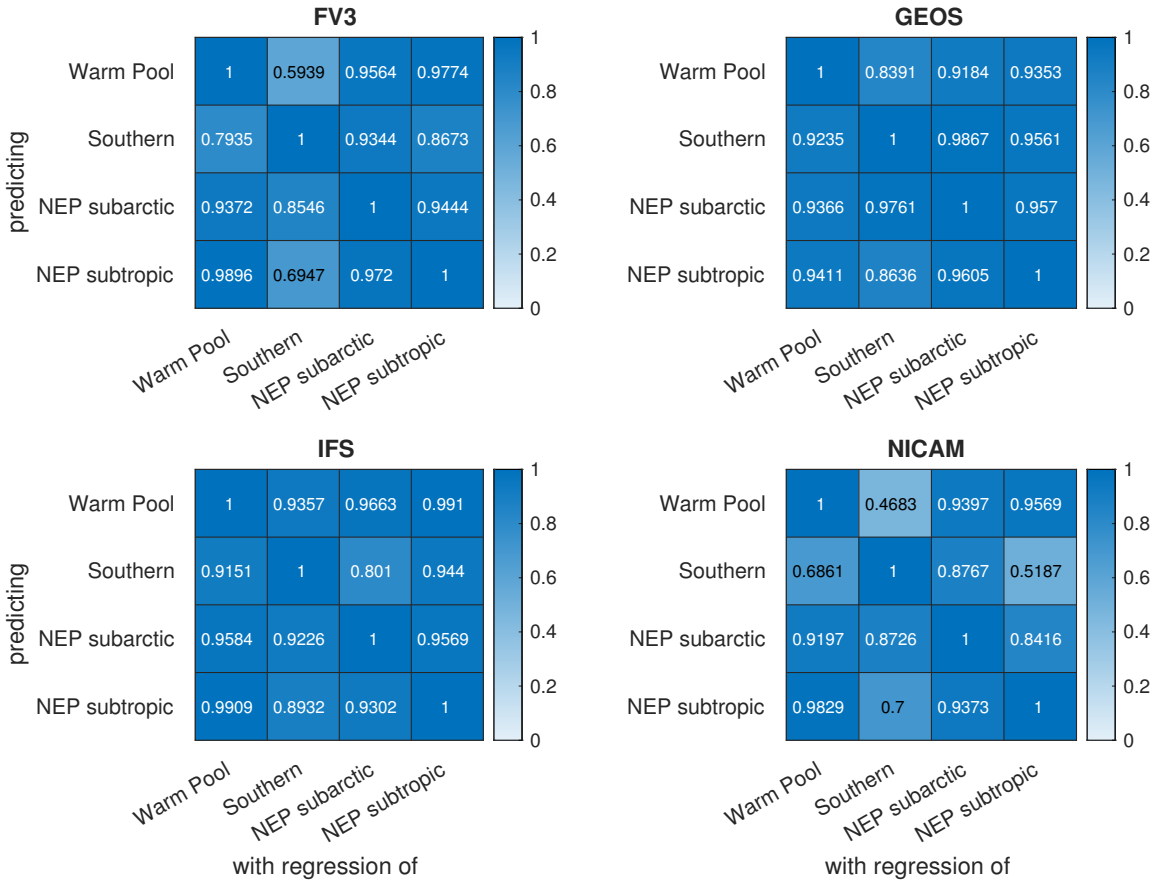

Figure A.123: Correlation of the deterministic part of the error process for portability across geographical regions, for each global model. The regression fit obtained from the region in the horizontal axis is applied to the variables obtained from the region in the vertical axis, and is compared to $\mu_{0.4^\circ,1}$ obtained from the regression and variables of the region in the vertical axis. $N = 0.4^\circ$, $n = 1$.

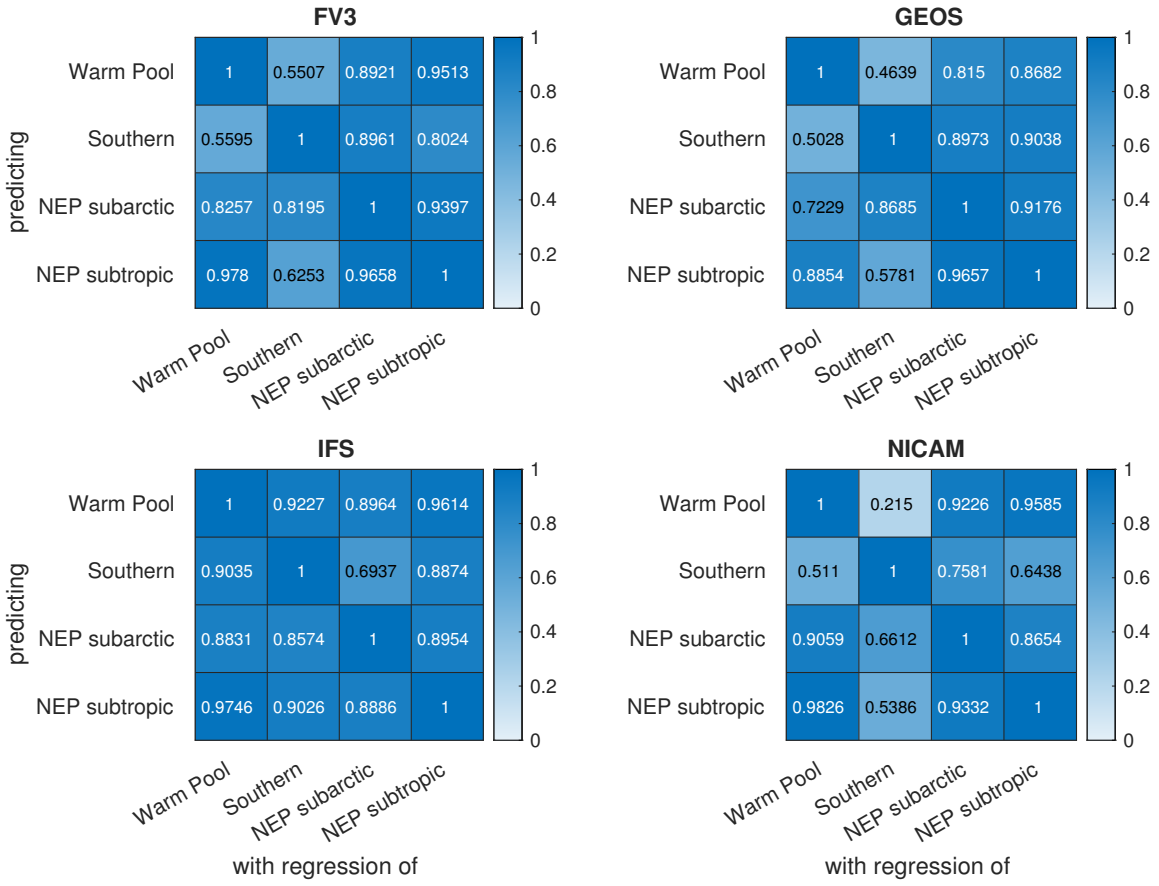

Figure A.124: Correlation of the deterministic part of the error process for portability across geographical regions, for each global model. The regression fit obtained from the region in the horizontal axis is applied to the variables obtained from the region in the vertical axis, and is compared to $\mu_{0.4^\circ,2}$ obtained from the regression and variables of the region in the vertical axis. $N = 0.4^\circ$, $n = 2$.

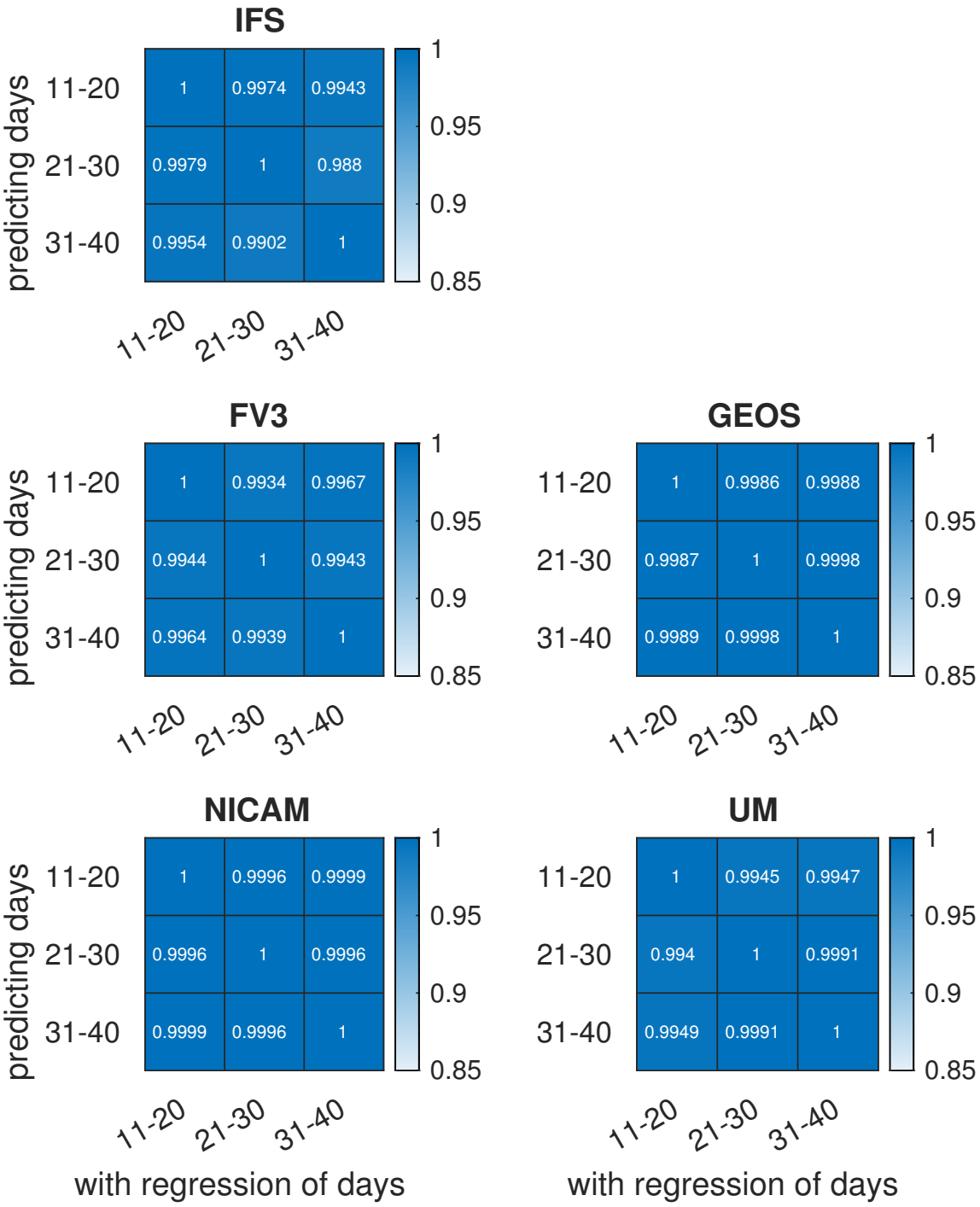

Figure A.125: Correlation of the deterministic part of the error process for three different ten-day periods, Warm Pool. The regression fit obtained from the time period in the horizontal axis is applied to the variables obtained from the time period in the vertical axis, and is compared to $\mu_{0.4^\circ,1}$ obtained from the regression and variables of the time period in the vertical axis. $N = 0.4^\circ$, $n = 1$.

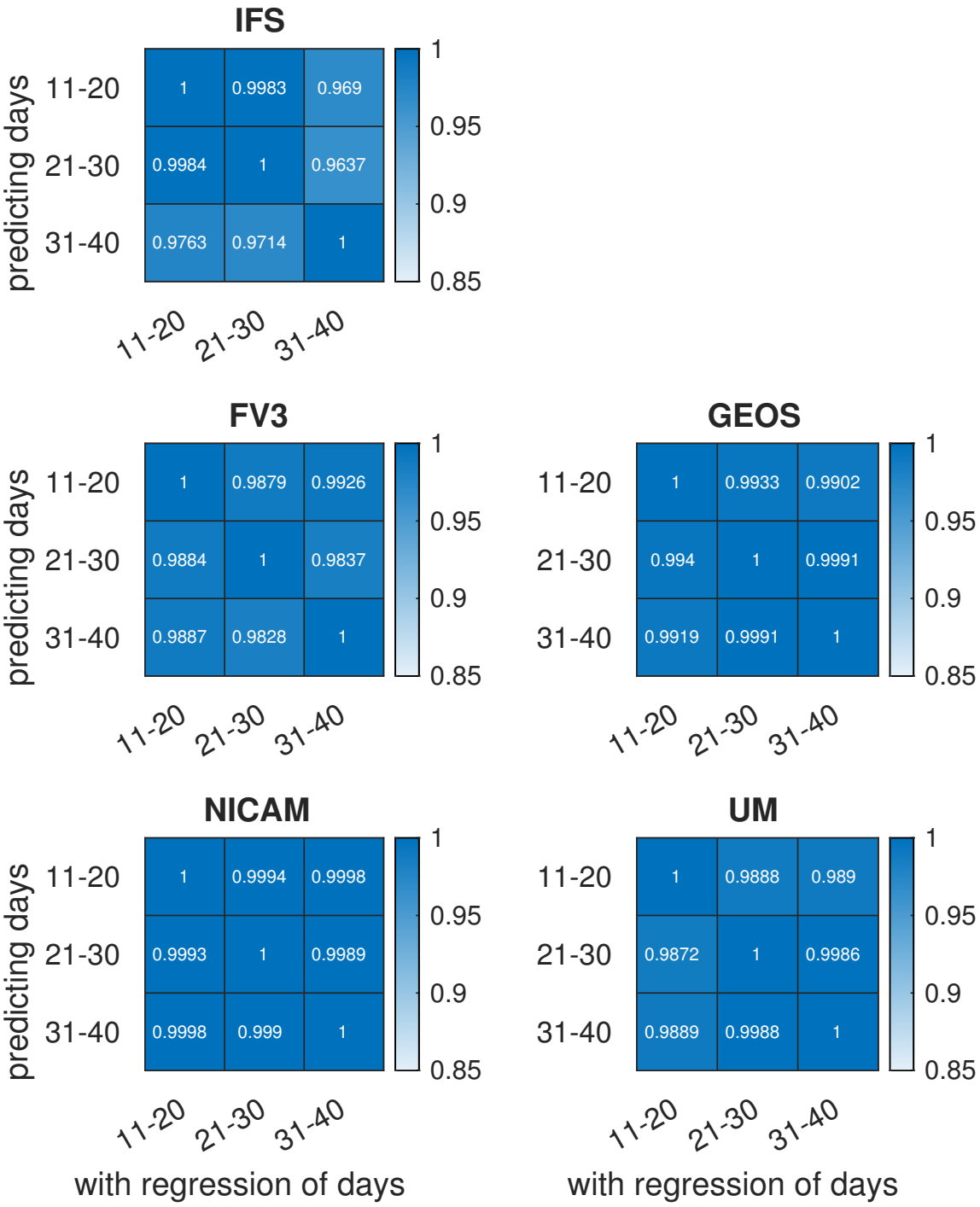

Figure A.126: Correlation of the deterministic part of the error process for three different ten-day periods, Warm Pool. The regression fit obtained from the time period in the horizontal axis is applied to the variables obtained from the time period in the vertical axis, and is compared to $\mu_{0.4^\circ,2}$ obtained from the regression and variables of the time period in the vertical axis. $N = 0.4^\circ$, $n = 2$.

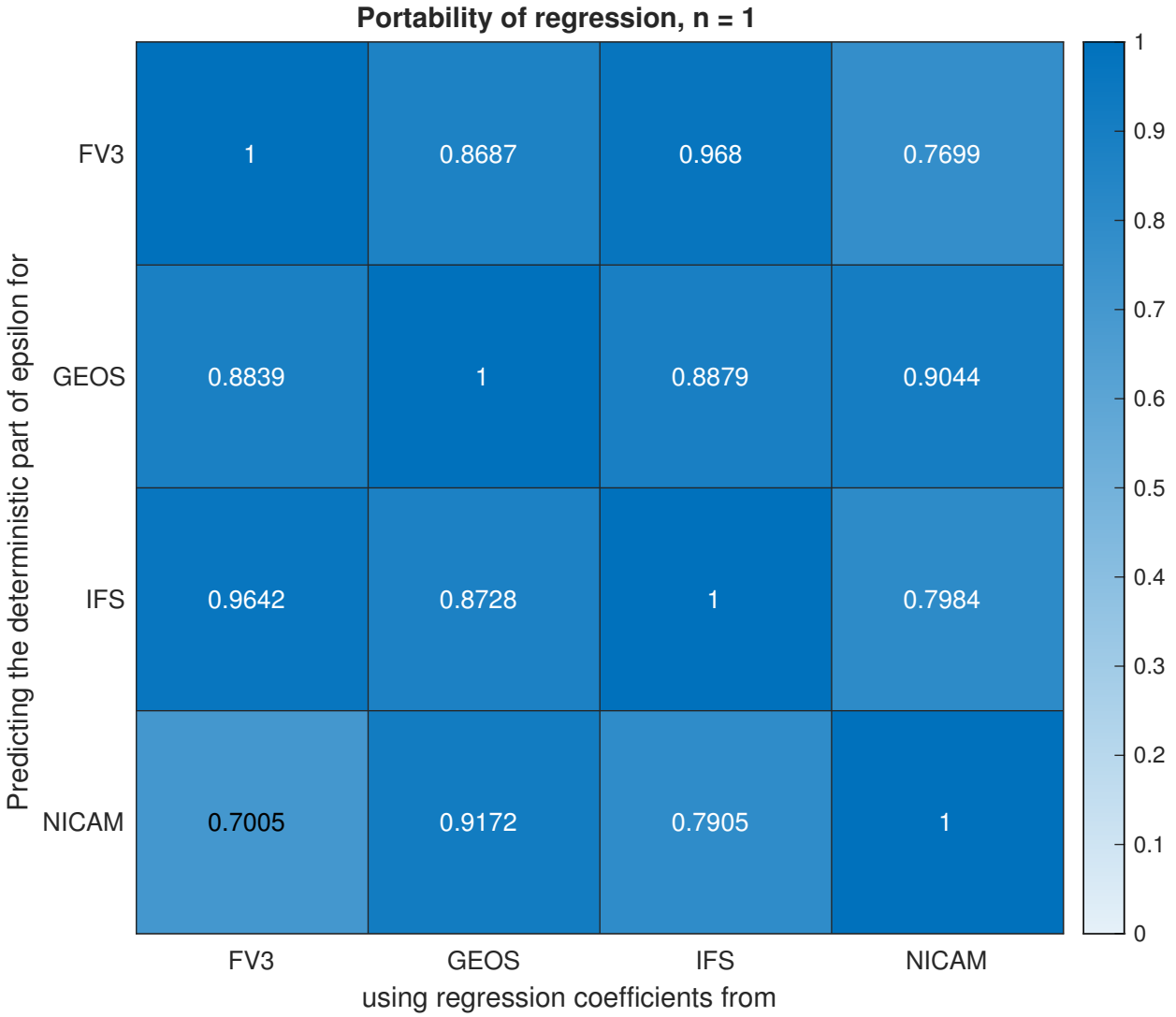

Figure A.127: Correlation of the deterministic part of the regression $\mu_{0.4^\circ,1}$ for the Southern Ocean, between models. The regression fit obtained from the model in the horizontal axis is applied to the variables obtained from the model in the vertical axis, and is compared to $\mu_{0.4^\circ,1}$ obtained from the regression and variables of the model in the vertical axis.

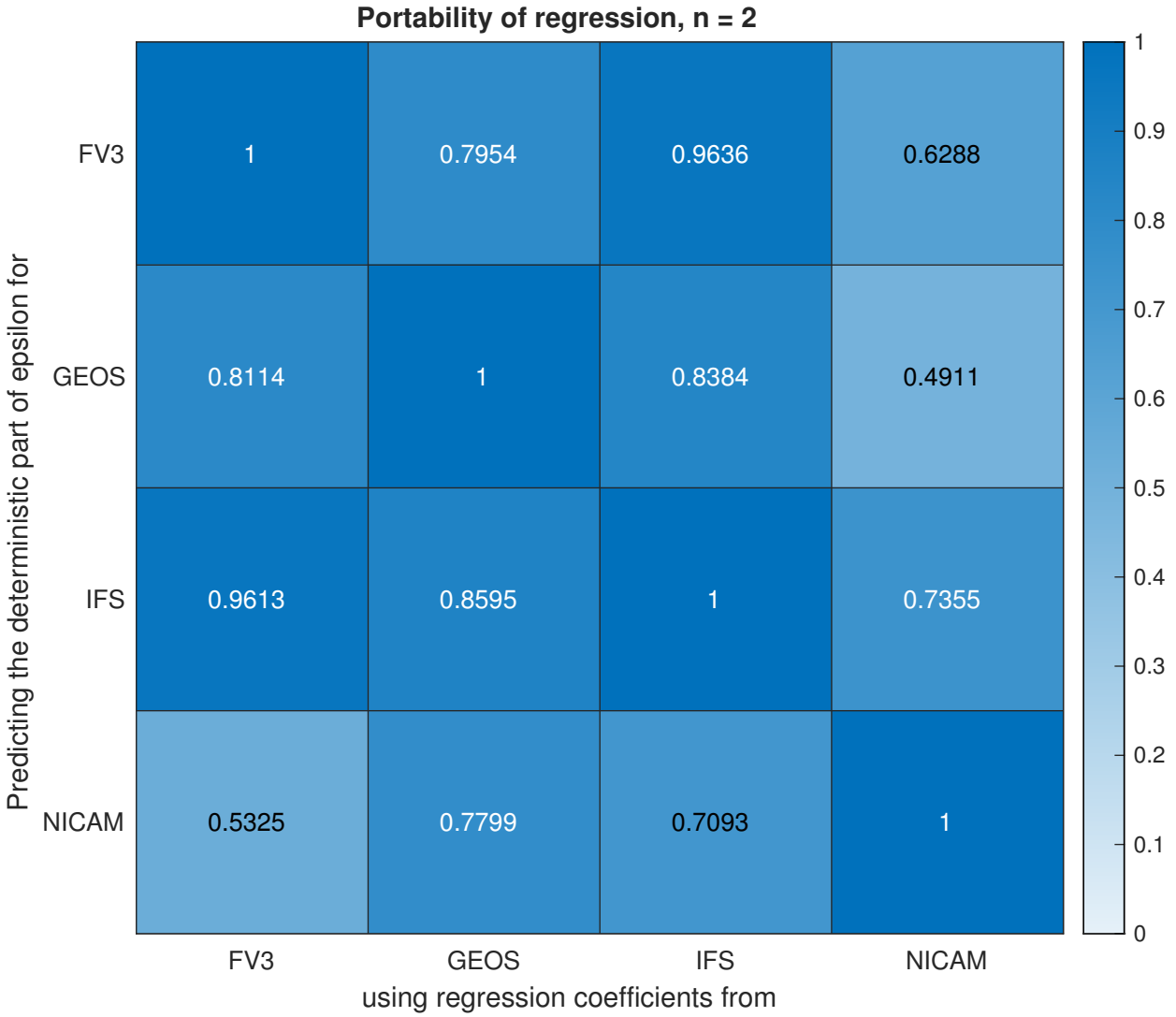

Figure A.128: Correlation of the deterministic part of the regression $\mu_{0.4^\circ,2}$ for the Southern Ocean, between models. The regression fit obtained from the model in the horizontal axis is applied to the variables obtained from the model in the vertical axis, and is compared to $\mu_{0.4^\circ,2}$ obtained from the regression and variables of the model in the vertical axis.

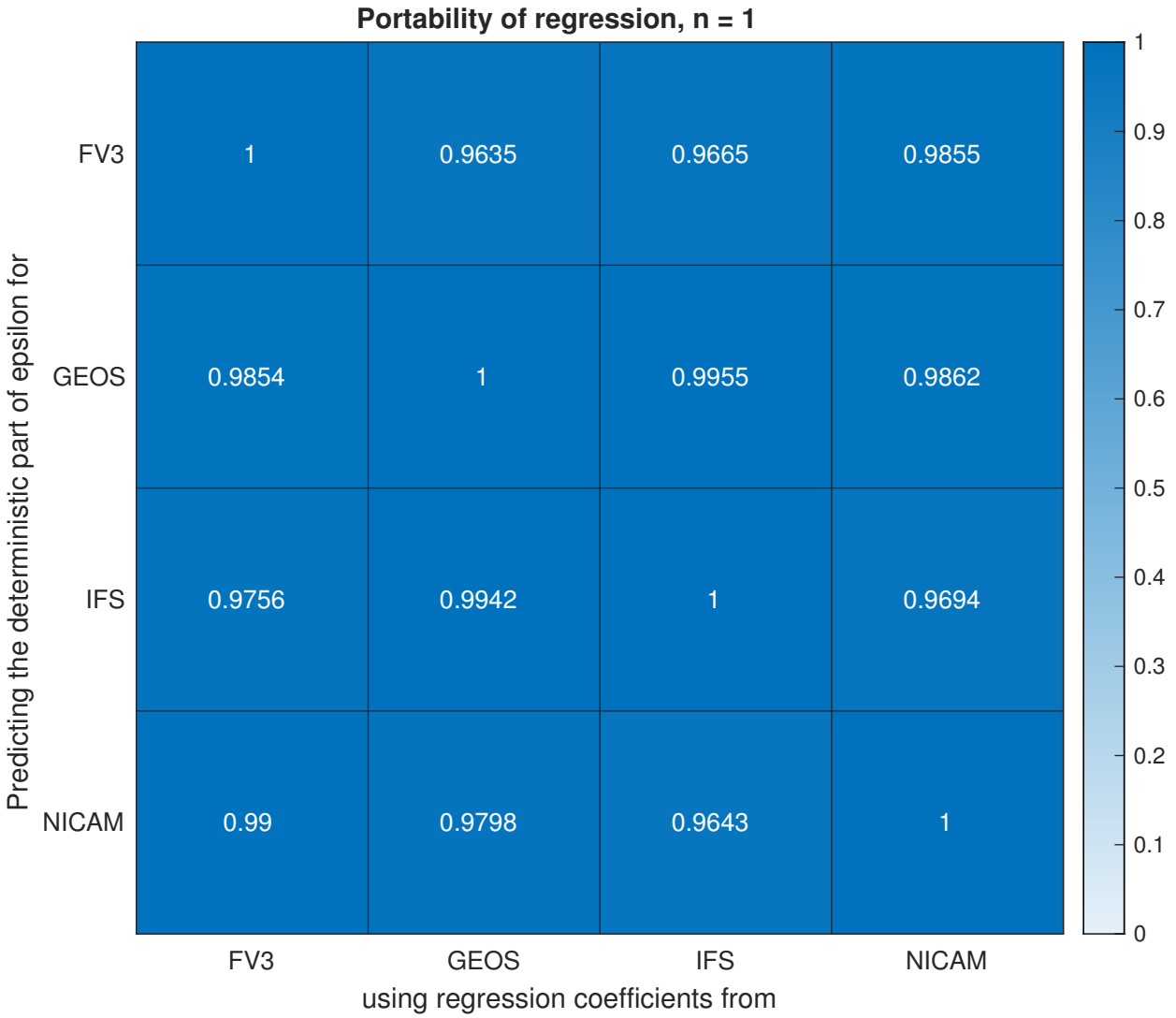

Figure A.129: Correlation of the deterministic part of the regression $\mu_{0.4^\circ,1}$ for the subarctic Northeast Pacific, between models. The regression fit obtained from the model in the horizontal axis is applied to the variables obtained from the model in the vertical axis, and is compared to $\mu_{0.4^\circ,1}$ obtained from the regression and variables of the model in the vertical axis.

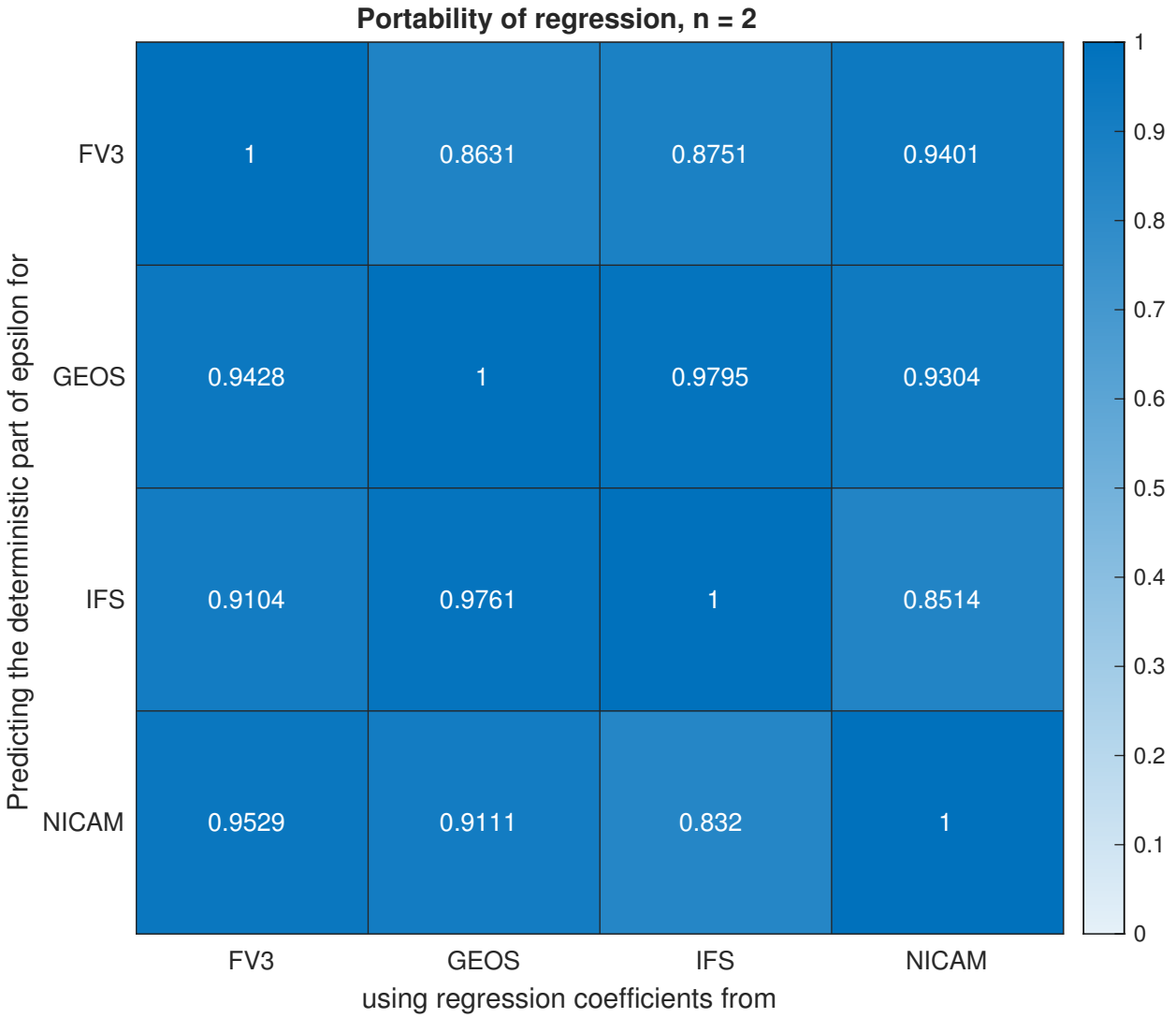

Figure A.130: Correlation of the deterministic part of the regression $\mu_{0.4^\circ,2}$ for the subarctic Northeast Pacific, between models. The regression fit obtained from the model in the horizontal axis is applied to the variables obtained from the model in the vertical axis, and is compared to $\mu_{0.4^\circ,2}$ obtained from the regression and variables of the model in the vertical axis.

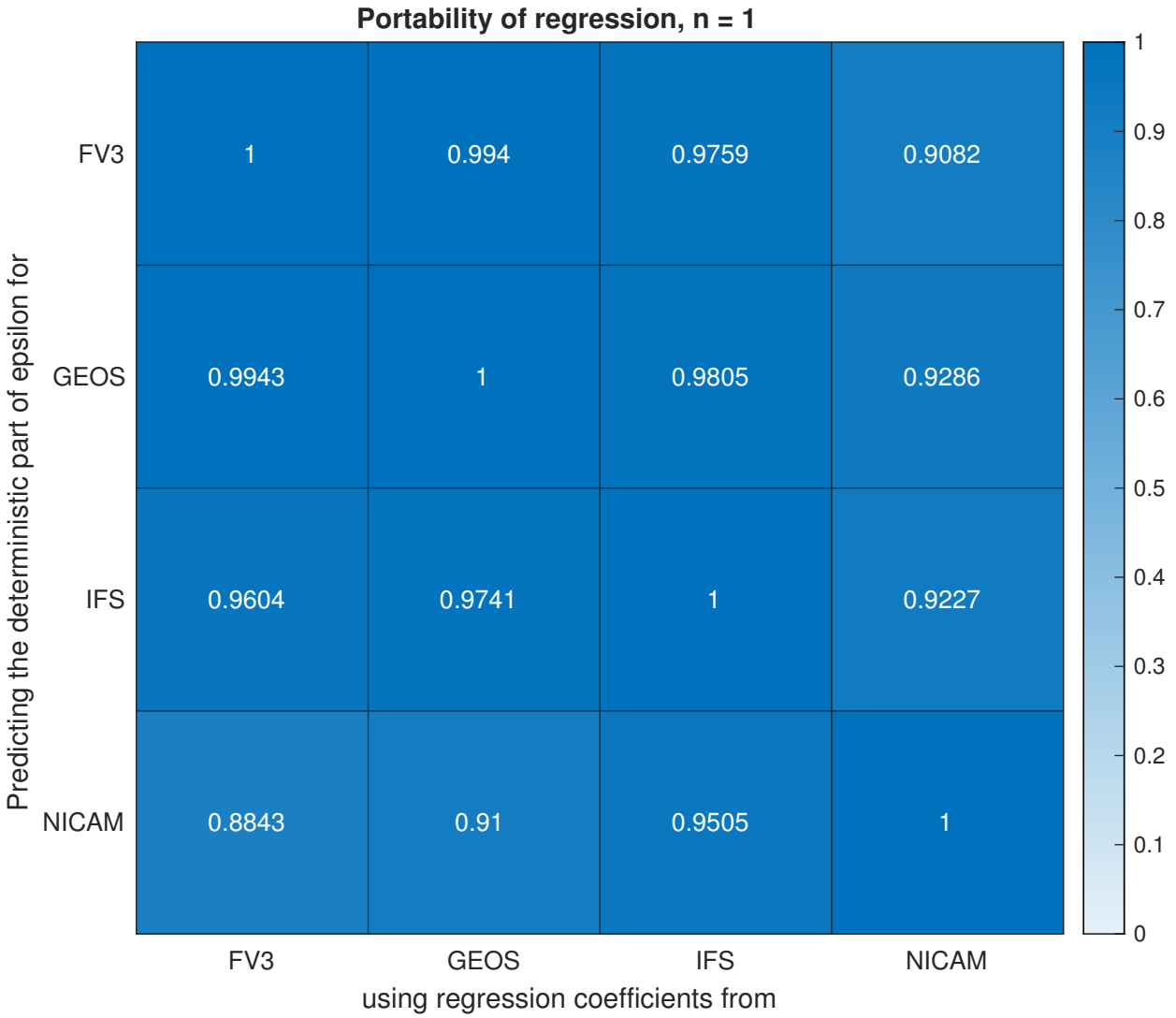

Figure A.131: Correlation of the deterministic part of the regression $\mu_{0.4^\circ,1}$ for the subtropical Northeast Pacific, between models. The regression fit obtained from the model in the horizontal axis is applied to the variables obtained from the model in the vertical axis, and is compared to $\mu_{0.4^\circ,1}$ obtained from the regression and variables of the model in the vertical axis.

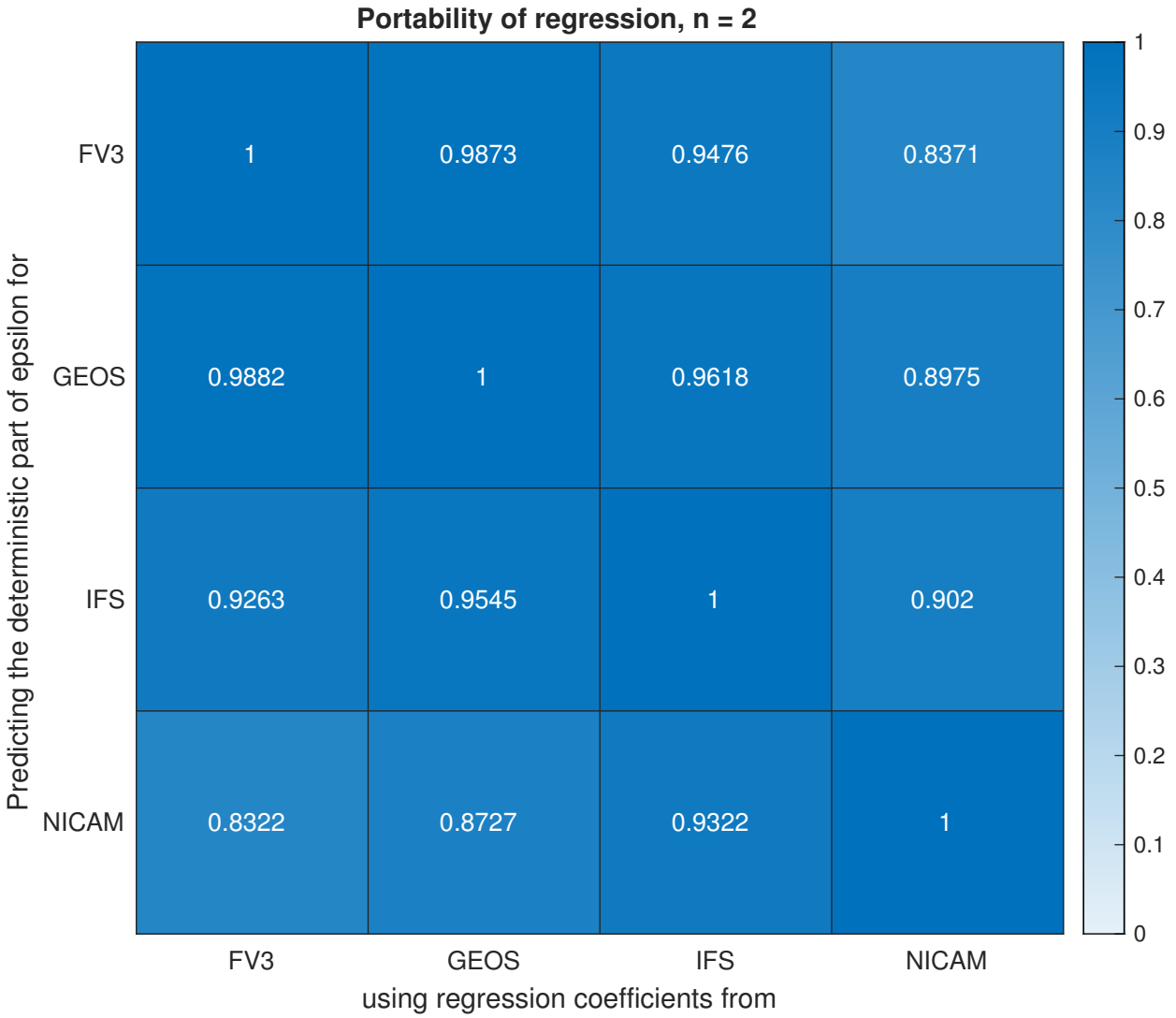

Figure A.132: Correlation of the deterministic part of the regression $\mu_{0.4^\circ,2}$ for the subtropical Northeast Pacific, between models. The regression fit obtained from the model in the horizontal axis is applied to the variables obtained from the model in the vertical axis, and is compared to $\mu_{0.4^\circ,2}$ obtained from the regression and variables of the model in the vertical axis.

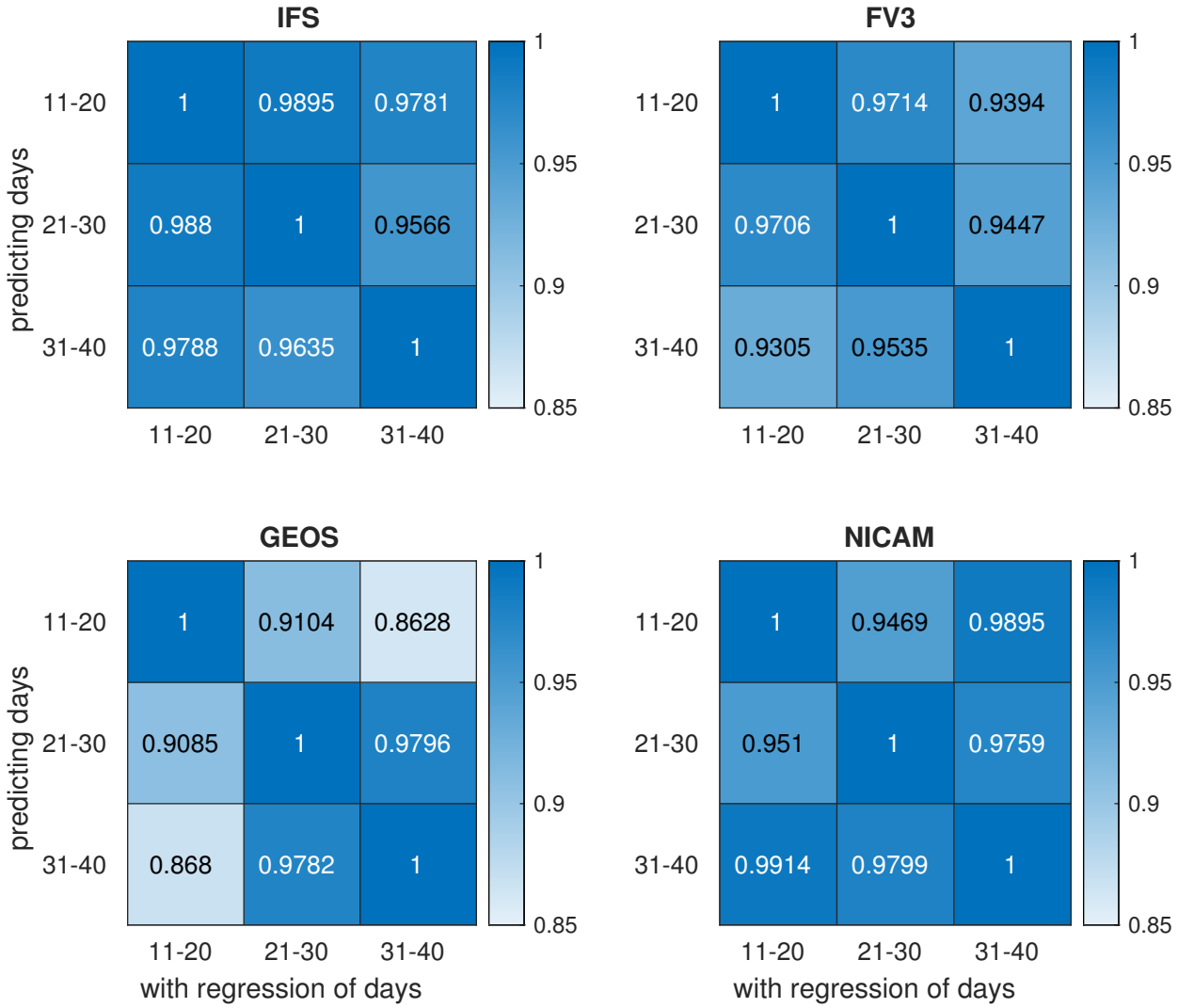

Figure A.133: Correlation of the deterministic part of the regression $\mu_{0.4^\circ,1}$ for the Southern Ocean, time periods. The regression fit obtained from the time period in the horizontal axis is applied to the variables obtained from the time period in the vertical axis, and is compared to $\mu_{0.4^\circ,1}$ obtained from the regression and variables of the time period in the vertical axis.

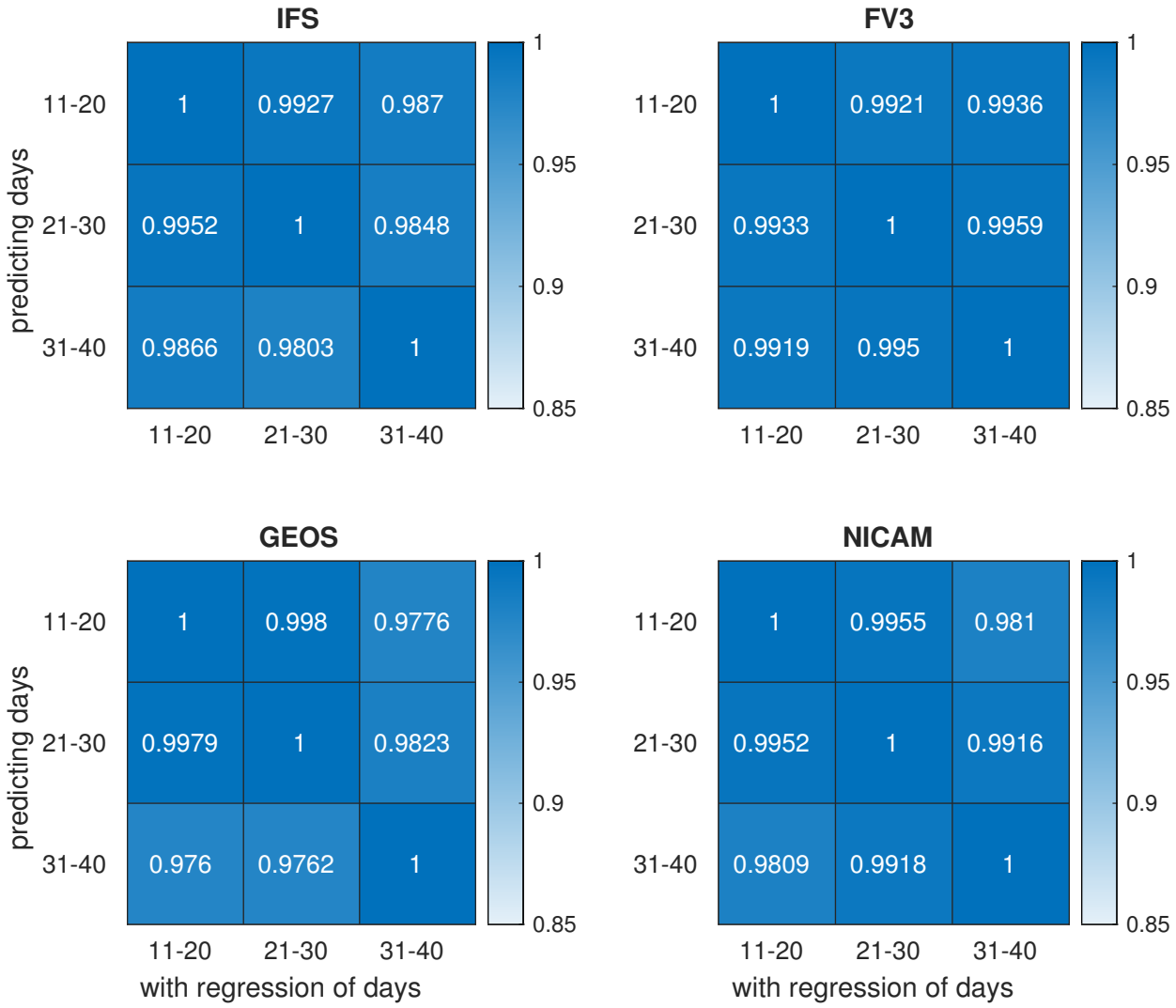

Figure A.134: Correlation of the deterministic part of the regression $\mu_{0.4^\circ,1}$ for the subarctic Northeast Pacific, time periods. The regression fit obtained from the time period in the horizontal axis is applied to the variables obtained from the time period in the vertical axis, and is compared to $\mu_{0.4^\circ,1}$ obtained from the regression and variables of the time period in the vertical axis.

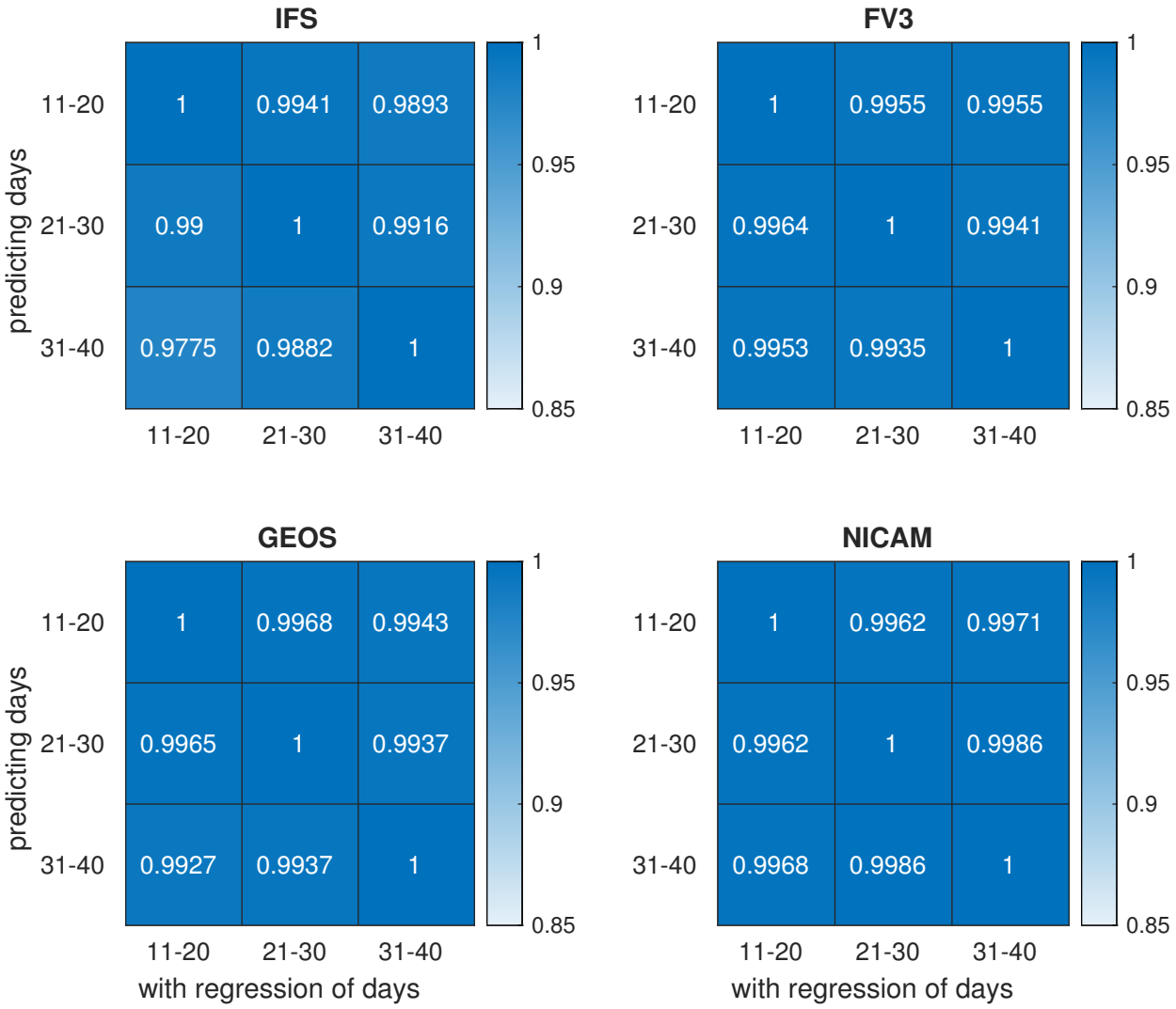

Figure A.135: Correlation of the deterministic part of the regression $\mu_{0.4^\circ,1}$ for the subtropical Northeast Pacific, time periods. The regression fit obtained from the time period in the horizontal axis is applied to the variables obtained from the time period in the vertical axis, and is compared to $\mu_{0.4^\circ,1}$ obtained from the regression and variables of the time period in the vertical axis.